

University of Nottingham
UK | CHINA | MALAYSIA

An Apoferritin-Based Drug Delivery System for Jerantinine A Acetate for Breast Cancer Treatment

School of Pharmacy

Haneen Abuzaid

BSc., MSc.

Thesis submitted to the University of Nottingham, United Kingdom for the degree of Doctor of Philosophy
February 2022

Abstract

Natural products have been a major and critically important source of anti-cancer drugs and inspiration for drug discovery. The *Aspidosperma* alkaloid Jerantinine A (JA) is a natural compound that possesses potent antiproliferative activity against various human-derived carcinoma cell lines. Jerantinines elicit potent but unselective effects by inhibiting tubulin polymerisation, polo-like kinase 1 (PLK1) and increasing ROS levels in treated cancer cells. Herein, we address the poor cancer-selectivity of JA acetate (JAa) and by developing an apoferritin (AFt) delivery vehicle for JAa, which can target transferrin receptor-1 (TFR1)-overexpressing breast cancer cells. The therapeutic benefits of AFt-JAa were evaluated in a panel of breast carcinoma cell lines. By optimising the pH-mediated reassembly method, a high yield was achieved with ~77% protein recovery. Following optimisation, ~120 molecules of JAa were successfully encapsulated within the AFt protein cavity. The AFt-JAa formulation has comparable size, charge and cage-integrity to AFt stock, as demonstrated by dynamic light scattering (DLS) and native polyacrylamide gel electrophoresis (PAGE). AFt- JAa was stable for ≥ 10 months of storage at T = 4 ºC and pH 7.4. Treatment of cells with AFt-JAa significantly enhanced breast cancer cell growth inhibition in cells with high TFR1 expression but not MRC-5 fibroblasts that express low TFR1 levels; TFR1 levels were detected with western blot and flow cytometry. Enhanced selectivity of encapsulated JAa in TFR1-overexpressing breast cancer cells was explained by enhanced internalisation of 5-carboxyfluorescein-conjugated-human-AFt compared to TFR1-low expressing cells (MRC-5 fibroblasts). Consequently, enhanced AFt-JAa nanoformulation potency (over naked JAa) was attributed to

greater intracellular accumulation of JAa in cells overexpressing TFR1 (SKBR-3, MDA-MB-231 and BT-474). Greater stability was observed for AFt-JAa in culture media under the treatment conditions (*T* = 37 ºC; ≤ 72 h) compared to the naked agent. The enhanced activity of AFt-JAa was supported by a greater reduction of colony formation in TFR1+ breast carcinoma cell lines SKBR-3, MDA-MB-468 and BT-474. Significantly lower number of viable cells, more profound cell cycle perturbation, including G2/M arrest, and increased apoptosis was evoked by AFt-JAa compared to JAa alone. Significant dose-dependent upregulation of biomarkers of apoptosis (cleaved PARP, decreased PLK1 and Mcl-1/Bcl-2 expression) further corroborates apoptosis. Treatment with naked and AFt-encapsulated JAa leads to the generation of ROS in MCF-7 and MDA-MB-231 cells, in addition to upregulating expression of WT p53 in MCF-7 cells, while repressing mutant p53 expression in both SKBR-3 and MDA-MB-231. These results indicate multiple cancer-related targets of JAa and confirm the natural product's rich and diverse pharmacology. AFt alone exerts negligible effects on cell growth or survival as indicated from MTT, cell count, clonogenic, cell cycle analysis, annexin V apoptosis assays; neither does AFt impact the expression of apoptotic/antiapoptotic proteins, as shown by western blot. Thus, AFt is a potentially biocompatible nanocarrier for targeted delivery of JAa to minimise its toxicity and enhance its activity in TFR1-overexpressing tumours.

Acknowledgements

All praises are to Allah, by whose Grace and Blessings have enabled me to complete my PhD study.

I would like to acknowledge and extend my deepest gratitude to my supervisor, Dr. Tracey Bradshaw, for giving me the opportunity to fulfil this project. Her guidance, patience and limitless support and kindness as a supervisor have made it possible to peruse this journey even during the most distressing times of this pandemic.

My gratitude should also go to Dr. Lyudmila Turyanska for her crucial contribution and invaluable comments she kept providing me throughout the study period. I would also like to thank Dr. Hilary Collins and Dr. Dong-hyun Kim for their continuous advice during my PhD.

I also would like to thank the following people who have contributed to this project. Dr. Kuan-Hon Lim for providing me with this precious compound, Dr. Salah Abdelrazig for conducting LC-MS studies, Lenny Ferreira for providing me human apoferritin, Ann Williams, Lee Hibbett and Paul Cooling for smoothly running our labs, David Onion and Nicola Croxall for their help with flow cytometry facility.

To all those in the cell culture lab who have helped me, especially: Kaouthar, José Junior and Lenny. And to my friends who helped me whenever I needed especially: Shahd, Alaa, Rasha, Sara and Rabab, thank you all.

I wish to expand my deepest gratitude and appreciation to my parents" Muneer and Majdah", my husband "Khaldoon" and to my little kid "Ziad", for their abundant support, patience, understanding, and their love. To my parents-in-law "Ziad and Maysoon" and my sisters and brothers, thank you all.

I also would like to thank my sponsor Al-Zaytoonah University of Jordan, Amman, Jordan for their generous funding and support.

List of Abbreviations

1° Ab	Primary antibody
2° Ab	Secondary antibody
ABC	ATP-Binding Cassette
AFt	Apoferritin
AIF	Apoptosis inducing factor
APAF1	Apoptotic peptidase activating factor 1
APC	Adenomatous polyposis coli
APS	Ammonium persulfate
ATCC	American Type Culture Collection
BCRP	Breast cancer resistance protein
BCT	Breast-conserving therapy
BER	Base excision repair
BSA	Bovine serum albumin
CDK	Cyclin-dependent kinase
CK	Casein kinase
CMF	Cyclophosphamide methotrexate fluorouracil
CXCR4	Chemokine (C-X-C motif) Receptor 4
d.H2O	Deionised water
DDS	Drug delivery system
DL	Drug loading
DLS	Dynamic light scattering
DMEM	Dulbecco's Modified Eagle's Medium
DMSO	Dimethyl sulfoxide
DPS	DNA-binding Protein from Starved cells
ECL	Enhanced chemiluminescence
ECM	Extracellular matrix
EE	Encapsulation efficiency
EGF	Epidermal growth factor
EGFR	Epidermal growth factor receptor
EPR	Enhanced permeability and retention
ER	Oestrogen receptors
FBS	Foetal bovine serum
FGFR1	Fibroblast growth factor receptor 1
Ft	ferritin
G1	Gap 1
G2	Gap 2
GF	Growth factors
GLUT1	Glucose transporter 1
GSH	Glutathione
GSK	Glycogen synthase kinase
H_2O_2	Hydrogen peroxide
H-AFt	Human apoferritin

HER2	Human epidermal growth factor receptor 2
HIF-1	Hypoxia-inducible factor 1
HPLC	High-performance liquid chromatography
IDC	Invasive ductal carcinoma
JA	Jerantinine A
JAa	Jerantinine A acetate
JAK	Janus Associated Kinases
JB	Jerantinine B
LC-HRMS	Liquid chromatography-high resolution mass spectrometry
M	Mitosis
mAb	Monoclonal antibody
MAPK	Mitogen activated protein kinase
MDR	Multi-drug resistance
MEM	Minimum essential medium
MOMP	Mitochondrial membrane permeabilisation
MPS	Mononuclear phagocytic system
MRP1	Multidrug resistance-associated protein 1
MS	Mass spectrometry
MTT	3-(4, 5-dimethylthiazol-2-yl)-2, 5-diphenyltetrazolium (MTT)
MWCO	Molecular weight cut-off
MWt	Molecular weight
NaOAc	Sodium acetate buffer
NEA	Non-essential amino acids
NMR	Nuclear magnetic resonance
NP40	Nonidet-P40
NPI	Nottingham Prognostic Index
NP	Nanoparticle
NRF2	Nuclear factor erythroid 2–related factor 2
P	Purification method
PAGE	Polyacrylamide gel electrophoresis
PARP	Poly-ADP ribose polymerase
PBS	Phosphate-buffered saline
PCR	Polymerase chain reaction
PE	Phycoerythrin
PEG	Polyethylene glycol
P-gp	Poly glycoprotein
PI	Isoelectric point
PI3K	Phosphatidylinositol 4,5-bisphosphate 3-kinase
PLK1	Polo-like kinase 1
PR	Progesterone receptor
PR%	Protein recovery percentage
PS	Phosphatidylserine
RB	Rhodamine B
Re-AFt	Reassembled AFt protein

ReM	Reassembly method
ROS	Reactive oxygen species
RT	Retention time
S	Synthesis
SAXS	Small-angle X-ray scattering
SDS	Sodium dodecyl sulphate
SF	Survival fraction
SF3B1	Splicing factor 3b subunit 1
SI	Selectivity index
snRNA	Small nuclear RNA
STAT	Signal transducers and activators of transcription
TBS-T	Tris-buffered saline – Tween-20
TEMED	Tetramethylethylenediamine
TFR	Transferrin receptor
TGI	Total growth inhibitory
TNBC	Triple-negative breast cancer
TNM	Tumour, lymph node involvement, metastasis
VCR	Vincristine
VEGF	Vascular endothelial growth factor
VR	Vincristine resistant
VVOs	Vesiculo–vacuolar organelles
WT	Wild type
ZP	Zeta potential

Table of Contents

1 Introduction 1

1.1 Cancer 1

1.1.1 Definition and epidemiology 1

1.1.2 Hallmarks of cancer 2

1.2 Breast cancer 13

1.2.1 Epidemiology 13

1.2.2 Histological classification of breast cancer 15

1.2.3 Molecular classification of breast cancer 15

1.2.4 Major signalling pathways in breast cancer development and progression 17

1.2.5 Other pathways and proteins in breast cancer 22

1.3 Breast cancer treatments 25

1.3.1 Breast surgery 25

1.3.2 Radiotherapy 26

1.3.3 Neoadjuvant/ adjuvant systemic treatment 26

1.4 Natural products and breast cancer treatment 34

1.4.1 Jerantinines 36

1.5 Drug delivery – nanotechnology and nanomedicine 38

1.5.1 Systemic delivery and biodistribution 39

1.5.2 Nanoparticle classes 41

1.5.3 Advantages and challenges of the nanoparticle driven delivery 43

1.6 Ferritin family proteins 48

1.6.1 Structure 48

1.6.2 Physiological role 49

1.6.3 Ferritin as a nanoparticle – Apoferritin 51

1.7 Aim and objectives of the study 55

2 Materials and methods 57

2.1 Encapsulation methods 57

2.1.1 Preparation of apoferritin 57

2.1.2 Jerantinine A acetate and stock solution 58

2.1.3 Encapsulation of jerantinine A acetate into apoferritin: The nano-reactor route 58

2.1.4 Encapsulation of jerantinine A acetate into apoferritin: The self-assembly route 59

2.2 Characterisation methods 60

2.2.1 Bradford assay 61
2.2.2 Native polyacrylamide gel electrophoresis 62
2.2.3 Sodium dodecyl sulphate polyacrylamide gel electrophoresis 63
2.2.4 Estimation of the protein recovery 66
2.2.5 Encapsulation efficiency and drug loading 66
2.2.6 Dynamic light scattering 67
2.2.7 Drug release study 69
2.2.8 Liquid chromatography-high resolution mass spectrometry 70
2.2.9 Stability study 71
2.3 *In vitro* cell culture assays 72
2.3.1 General cell culture 72
2.3.2 Mycoplasma assay 76
2.3.3 Western blot 78
2.3.4 The 3-(4, 5-dimethylthiazol-2-yl)-2, 5-diphenyltetrazolium dye reduction assay, cell growth inhibition assay 82
2.3.5 Cell counting assay 84
2.3.6 Clonogenic assay 85
2.3.7 Flow cytometry 87
2.3.8 Cellular uptake of free and encapsulated JAa 92
2.3.9 Measurement of reactive oxygen species 93
2.4 Statistical analyses 94
3 Encapsulation of jerantinine A acetate into apoferritin 96
3.1 Introduction 96
3.2 Chapter aims 97
3.3 Results and Discussion 98
3.3.1 Encapsulation of JAa through the nano-reactor route 98
3.3.2 Encapsulation of JAa through the self-assembly route 111
3.3.3 Validation of the optimised self-assembly method: encapsulation of vincristine and rhodamine B 135
3.3.4 Stability assay of AFt-JAa reassembled formulation 138
3.3.5 Release assay of JAa from AFt cages 139
3.4 Conclusion 144
3.5 Future work 146
4 Enhancing activity and selectivity of jerantinine A acetate in breast carcinomas upon apoferritin-encapsulation 147
4.1 Introduction 147

4.2 Chapter aims 149
4.3 Results and discussion 150
4.3.1 Expression of the transferrin receptor in breast cancer and non-transformed cell lines 150
4.3.2 *In vitro* growth inhibitory effects of JAa and AFt-encapsulated JAa on breast cell lines 155
4.3.3 *In vitro* cell viability effects of JAa and AFt-encapsulated JAa on breast cancer cell lines 168
4.3.4 Effects of JAa and AFt-encapsulated JAa on colony formation of breast cancer cell lines 170
4.3.5 Cellular uptake study 176
4.4 Conclusion 185
4.5 Future work 187
5 Free and apoferritin encapsulated jerantinine A acetate perturb cell cycle and induce cell death of breast carcinoma cells 188
5.1 Introduction 188
5.2 Chapter aims 190
5.3 Results and discussion 191
5.3.1 Free and encapsulated JAa perturb cell cycle progression of breast cancer cell lines 191
5.3.2 Free and encapsulated JAa induces apoptosis of breast cancer cell lines 199
5.3.3 Free and encapsulated JAa change the expression of apoptotic and anti-apoptotic protein biomarkers 205
5.3.4 Free and encapsulated JAa Induce reactive oxygen species in breast cancer cell lines 213
5.4 Conclusion 219
5.5 Future work 221
6 General discussion, conclusion and future directions 222
6.1 General discussion and conclusion 222
6.2 Future directions 230
7 References 232
8 Appendices 258
8.1 Appendix I 258
8.2 Appendix II 264

List of Figures

Figure 1.1: A schematic of the hallmarks of cancer. 2

Figure 1.2: Cell death classification. 5

Figure 1.3: The regulation of apoptosis by Bcl-2 family. 6

Figure 1.4: Homeostasis of angiogenesis. 9

Figure 1.5: Cancer incidence in 2020 worldwide among women 13

Figure 1.6: Estimated age-standardised incidence and mortality rates (World) in 2020. 14

Figure 1.7: HER2 and downstream signalling pathways: Ras/MAPK, PI3K/AKT, and JAK-STAT 20

Figure 1.8: Canonical Wnt/β-catenin signalling 22

Figure 1.9: Jerantinine A-G cytotoxic alkaloid compounds 37

Figure 1.10: Enhanced permeability and retention (EPR) effect 40

Figure 1.11: Classes of nanoparticles. 42

Figure 1.12: Commonly engineered NP surface properties 45

Figure 1.13: Timeline of the development of nanomedicines. 47

Figure 1.14: The spherical cage of native ferritin. 49

Figure 1.15: Intracellular Iron Homeostasis. 50

Figure 1.16: Internalisation of apoferritin into the cells through clathrin-coated pit-mediated endocytosis. 52

Figure 2.1: The nano-reactor encapsulation route of JAa inside AFt 59

Figure 2.2: Illustration diagram shows the reassembly encapsulation route of JAa inside the core of AFt cage. 60

Figure 2.3: The release study protocol of AFt-JAa. 70

Figure 2.4: Morphological appearance of cell lines used 75

Figure 3.1: DLS data recorded for AFt alone and AFt-JAa produced in Trial A and Trial B using the nano-reactor route. 99

Figure 3.2: DLS data recorded for AFt alone and AFt-JAa produced in Trial C ... 102

Figure 3.3: The integrity of AFt alone and AFt-JAa produced in Trial C..... 103

Figure 3.4: DLS data for AFt and AFt-JAa produced in Trial D using nano-reactor route. 105

Figure 3.5: Native and SDS-PAGE of AFt-JAa through the nano-reactor route and its AFt control..... 107

Figure 3.6: UV-Vis spectrophotometer data of JAa and standard curve of BSA. 108

Figure 3.7: Evaluation of the time needed to remove free (un-trapped) JAa molecules from the formulation using tabersonine as a model. 110

Figure 3.8: Polyacrylamide native gel electrophoresis of the disassembly of horse spleen AFt H-AFt at pH 2-2.5 114

Figure 3.9: Native PAGE of the AFt cage reassembly in one step vs two steps .. 116

Figure 3.10: Evaluating the time and speed needed to purify the reassembled formulation using spin filtration..... 126

Figure 3.11: Native PAGE gels following the purification of the reassembled AFt using 4 different methods 127

Figure 3.12: The encapsulation of JAa into AFt cages using the reassembly method. 131

Figure 3.13: DLS characterisation of AFt encapsulated JAa using dis-assemby method 133

Figure 3.14: Vincristine and rhodamine B structures and their 3D models 136

Figure 3.15: Stability study of AFt-encapsulated JAa 138

Figure 3.16: The release profile of JAa from AFt cargo in NaOAc (pH 5.3), and PBS (pH 7.4).. 140

Figure 3.17: Possible interaction of JAa and the interior surface of AFt. 142

Figure 3.18: LCMS profiles of detected peaks following the release of encapsulated JAa from AFt cage. 143

Figure 4.1: Expression of TFR1, TRF2 and SCARA-5 in cell lines using immunoblotting technique 151

Figure 4.2: Flow cytometric quantification of TFR1 expression in breast cell lines 153

Figure 4.3: Representative MTT graphs of AFt encapsulating JAa, JAa, and AFt alone on SKBR-3 and MDA-MB-231 cells 157

Figure 4.4: Summary of log GI50 values (μM) of JAa and encapsulated AFt-JAa on SKBR-3 and MDA-MB-231 cells at different exposure times 159

Figure 4.5: MTT graphs displaying comparative growth-inhibitory profiles in all studied cell lines after treating with JAa..... 161

Figure 4.6: Representative MTT graphs of AFt encapsulating JAa, JAa, and AFt alone in seven selected cell lines 166

Figure 4.7: Growth inhibitory activity of JAa and AFt-JAa in seven selected cell lines 167

Figure 4.8: Representative MTT graphs in all studied cell lines after treating with AFt-JAa..... 168

Figure 4.9: *In vitro* cell viability assays in SKBR-3 , MDA-MB-231 and MCF-7 170

Figure 4.10: Representative images of the clonogenic assays conducted on SKBR-3 and MDA-MB-468. 172

Figure 4.11: Representative images of the clonogenic assays conducted on BT-474 and MCF-7 174

Figure 4.12: Cellular uptake study in SKBR-3, MDA-MB-231, MRC-5, BT-474 and MCF-7 cells of 5-carboxyfluorescein-conjugated-H-AFt.. 178

Figure 4.13: Statistical analyses of H-AFt uptake with time of TFR1+ cells compared to TFR1-low expression. 179

Figure 4.14: Intra and extracellular levels of JAa and its hydrolysed form (JA) following 72 h exposure of free and AFt-encapsulated JAa in SKBR-3, MDA-MB-231 and BT-474 181

Figure 4.15: Levels of free and AFt-encapsulated JAa following incubation with different media.. 182

Figure 4.16: Cellular accumulation pattern of 5-carboxyfluorescein-conjugated-H-AFt for 24 h in TFR1+ cells and one TFR1-low expressing cells.. 184

Figure 5.1: The effects of JAa and AFt-JAa on the cell cycle of SKBR-3 cells..... 193

Figure 5.2: The effects of JAa and AFt-JAa on the cell cycle of MDA-MB-231 cells. 195

Figure 5.3: The effects of JAa and AFt-JAa on the cell cycle of MCF-7 cells 197

Figure 5.4: The effects of JAa and AFt-JAa on the apoptosis of SKBR-3 cells 201

Figure 5.5: The effects of JAa and AFt-JAa on the apoptosis of MDA-MB-231 cells. 203

Figure 5.6: The effects of JAa and AFt-JAa on the apoptosis of MCF-7 cells. 204

Figure 5.7: Apoptotic and antiapoptotic proteins expression in SKBR-3 cell lysates following 72 h exposure of cells to JAa, AFt-JAa at different concentrations. 207

Figure 5.8: Apoptotic and antiapoptotic proteins expression in MDA-MB-231 cell lysates following 72 h exposure of cells to JAa, AFt-JAa at different concentrations 209

Figure 5.9: Apoptotic and antiapoptotic proteins expression in MCF-7 cell lysates following 72 h exposure of cells to JAa, AFt-JAa at different concentrations. 211

Figure 5.10: ROS production following JAa and AFt-JAa exposure in MDA-MB-231 and MCF-7 cells 216

List of tables

Table 1.1: Molecular subtypes of breast cancer 17

Table 1.2: Summary of innate and modified AFt in cancer therapy as a nanocarrier 54

Table 2.1: Composition of the cathode, anode and loading buffers used in native PAGE 62

Table 2.2: Composition of the resolving and stacking gels used in SDS PAGE 65

Table 2.3: Composition of the running and loading buffers used in SDS PAGE ... 65

Table 2.4: Cell lines used and their supplemented media 74

Table 2.5: Antibodies used in western blot 81

Table 3.1: Drug encapsulation efficiency and drug loading of JAa encapsulated in AFt at three different ratios through the nano-reactor route 108

Table 3.2: A summary of published self-assembly methods 112

Table 3.3: Initial AFt protein concentration on the reassembly method 118

Table 3.4: Summary of dialysis and direct addition of buffer to restore AFt 119

Table 3.5: Optimisation of basic solutions/buffers used to reassemble AFt 123

Table 3.6: Summary of characterisation results for AFt-JAa produced via self-assembly route 134

Table 3.7: Results of encapsulating VCR and RB into AFt core and its DLS analysis summary. Results are shown in mean ± SD from two independent trials 137

Table 4.1: GI50, TGI, LC50a and selectivity index values of JAa and its encapsulated form AFt-JAa in all cell lines 163

1 Introduction

1.1 Cancer

1.1.1 Definition and epidemiology

Cancer is characterised by uncontrolled cellular growth associated with increases in size, disorganisation and malignancy [1]. Mutations in oncogenes and tumour suppressor genes are the main cause of tumours' initiation. The bidirectional interactions between the tumour cells and the extracellular matrix (ECM) regulate tumour survival, progression and metastasis [2].

Cancer is a global challenge and the second leading cause of death in the United States of America, with 599,274 deaths recorded in 2018 accounting for 21% of all deaths. In 2021, It is estimated that the number of new invasive cancer cases is 1,898,160 and 608,570 deaths. The highest number of deaths in men is from lung, prostate and colorectal cancers, and in women from lung, breast and colorectal cancers. [3]. According to GLOBOCAN 2020, in the United Kingdom, the estimated age-standardised incidence rate is 457,960 and 179,648 for mortality rate [4]. However, the number of avoidable cancer deaths is expected to increase considerably as a result of diagnostic delays due to the COVID-19 pandemic in the UK [4].

1.1.2 Hallmarks of cancer

Hanahan and Weinberg summarised the biological characteristics that tumour cells acquire during tumourigenesis - the so-called “hallmarks of cancer”, which include the following: sustaining proliferative signalling, evading growth suppressors, resisting cell death, enabling replicative immortality, inducing angiogenesis, activating invasion and metastasis, genome instability, inflammation, reprogramming of energy metabolism, and evading immune destruction (**Figure 1.1**) [5, 6].

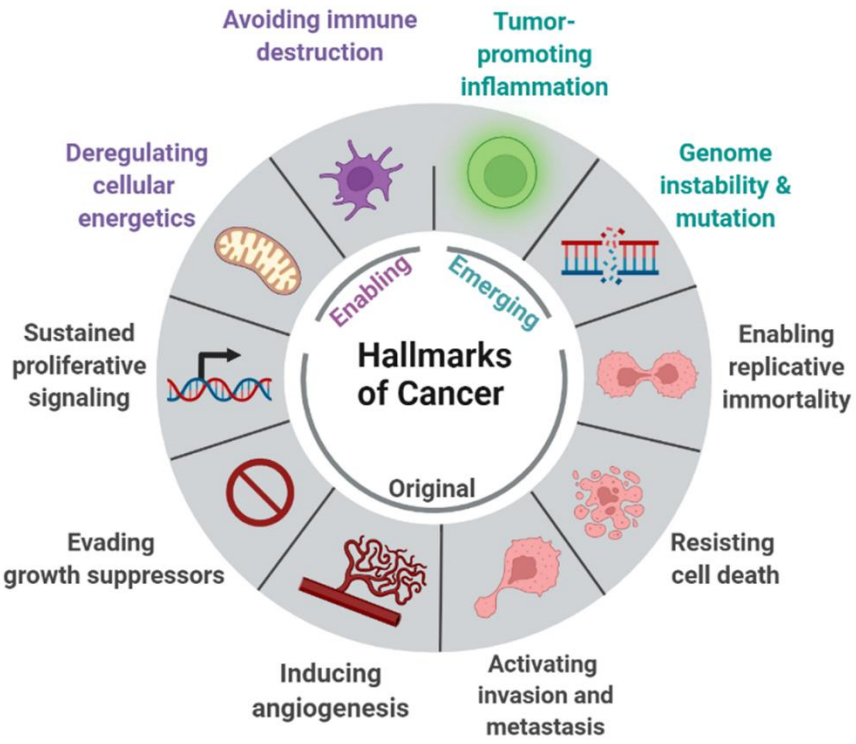


Figure 1.1: A schematic of the hallmarks of cancer. Reproduced from [7].

1.1.2.1 Sustaining chronic proliferation

Sustaining proliferation is one of the most important characteristics of cancer cells. Normal cells control their entry into the cell cycle by relinquishing their need

for growth-promoting signals. Cancer cells, deregulate growth signals and maintain continuous progression through various mechanisms [5]. For example, upon receiving growth factors (GF), cancer cells can enhance the response of GF receptors by elevating their expression on the cell surface. This hyperactivation can also result from mutations in the receptors' structure or their downstream pathways. The same outcome can result from mutations that disrupt negative feedback mechanisms. Alterations that occur in the structure of the receptor, can also change receptor activation to be independent of their cognate GF ligands. Moreover, cancer cells can also be independent of their environment, producing their own GFs and responding by expressing cognate receptors [5, 8].

1.1.2.2 Evading growth suppression

Normally, cells maintain homeostasis by limiting their growth through regulating tumour suppressor genes' activity. Cancer cells, however, proliferate by circumventing the activity of tumour suppressor genes [5]. *TP53* is a tumour suppressor gene that integrates signals from intracellular sources and regulates whether the cells enter cell cycle or, alternatively, trigger apoptosis if cell damage is irreparable [5]. In addition to its role in regulating apoptosis, p53 contributes to the maintenance of genome integrity by controlling the cell cycle and activating DNA repair proteins. p53 protein is negatively regulated by MDM2; MDM2 binds to p53 to stabilise it at low levels by making it detectable for Ubiquitination and protein degradation [9]. When cells are exposed to stress or damage, the binding ability of MDM2 to p53 is inhibited leading to an increase in p53 levels. Upon its activation, p53 prevents cell division until the damage is repaired [10] and stops

the damaged cells from transitioning from G1 to S and from G2 to M phases, as a result of cyclin-dependent kinase (CDK) inhibition. If the cell's damage cannot be repaired, p53 causes cell death mainly through apoptosis [11]. Defects in *TP53* and other suppressor proteins' normal function are associated with cell proliferation [5].

Evading growth suppression can be due to loss of contact inhibition, resulting in proliferation. Neurofibromatosis Type 2 (*NF2*) is a tumour suppressor that inhibits mitogenic signalling in response to cell contact. Merlin, a cytoskeleton scaffolding protein (product of the *NF2* gene), regulates pathways essential for proliferation and survival, such as inhibiting the activity of the epidermal growth factor receptor (EGFR) [12]. Therefore Merlin/*NF2* loss is associated with a more malignant phenotype in breast cancer [13, 14].

1.1.2.3 Resisting cell death

Cell death is an essential process to eliminate damaged cells and maintain homeostasis. There are several mechanisms of cell death including apoptosis, autophagy and necrosis [5]. More recently additional modes of cell death were identified, including entosis, methuosis, paraptosis, mitoptosis, parthanatos, ferroptosis, pyroptosis, NETosis and necroptosis [15]. Except for necrosis that results from unexpected injury, all other cell death modalities represent different types of programmed cell death (**Figure 1.2**) [16].

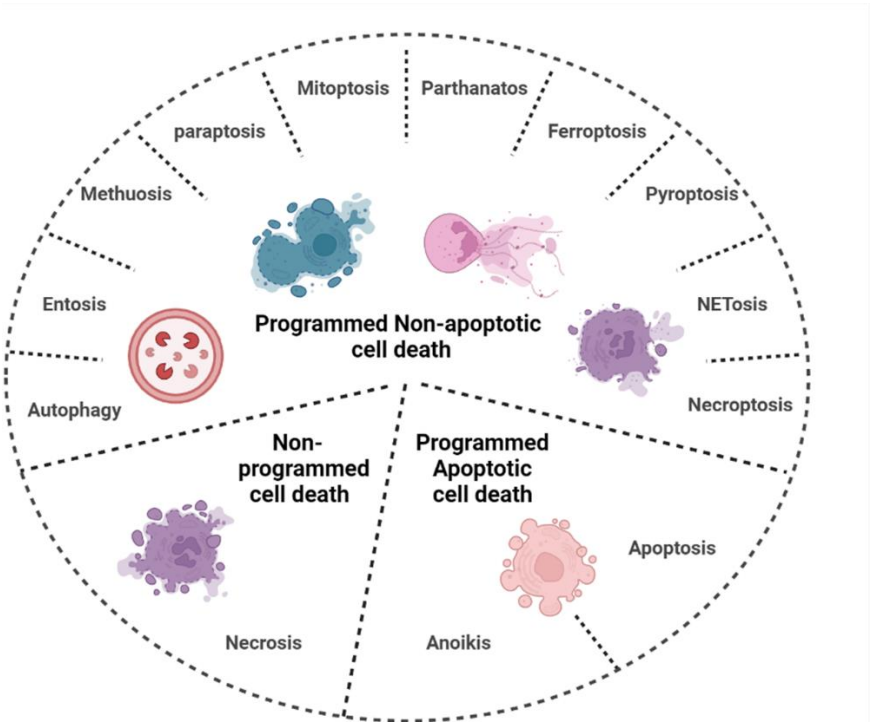


Figure 1.2: Cell death classification according to their signal-dependency, morphological characteristics and molecular mechanisms. Reproduced from [15].

Evasion from apoptosis in cancer cells is extensively reported [17] [R]. In normal cells, apoptosis is a strictly regulated mechanism that is triggered by both extrinsic signals (death receptors' pathway) and intrinsic signals (mitochondrial pathway). Both pathways lead to activation of cysteine-dependent aspartate-directed proteases (caspases), cell shrinkage, membrane blebbing, DNA fragmentation and condensation, and positional organelle loss [15, 17].

Bcl-2 family proteins play a crucial role in the mitochondrial apoptotic pathway. Pro-apoptotic (effectors) Bcl-2 proteins include BAX, BAK1, BIM, BID and BBC3 members, and antiapoptotic (inhibitors) include Bcl-2, Bcl-xL, Bcl-w, Mcl-1, A1. Moreover, PUMA gene encodes two of the BH-3 subclass of proapoptotic proteins, which can work as both activator and sensitiser to other Bcl-2 family members

[18]. When BH-3 only domain bind to Bcl-2 proapoptotic members [19, 20], or the anti-apoptotic subclass of Bcl-2 proteins, activators (such as BAX) dislocate from their binding groove resulting in apoptosis [19]. The activation of BAX monomer leads to its oligomerisation and conformational changes [21]. BAX oligomer clamp-like structure creates holes and induces outer mitochondrial membrane permeabilisation (MOMP), which is followed by releasing of cytochrome c into the cytosol (**Figure 1.3**). Cytochrome c is a proapoptotic signalling protein that activates, a cascade of caspases that possess proteolytic activities, this ultimately results in apoptotic cell death. In contrast, active anti-apoptotic members of the Bcl-2 family binding to the effectors' members inhibits the release of cytochrome c and subsequently apoptosis [21].

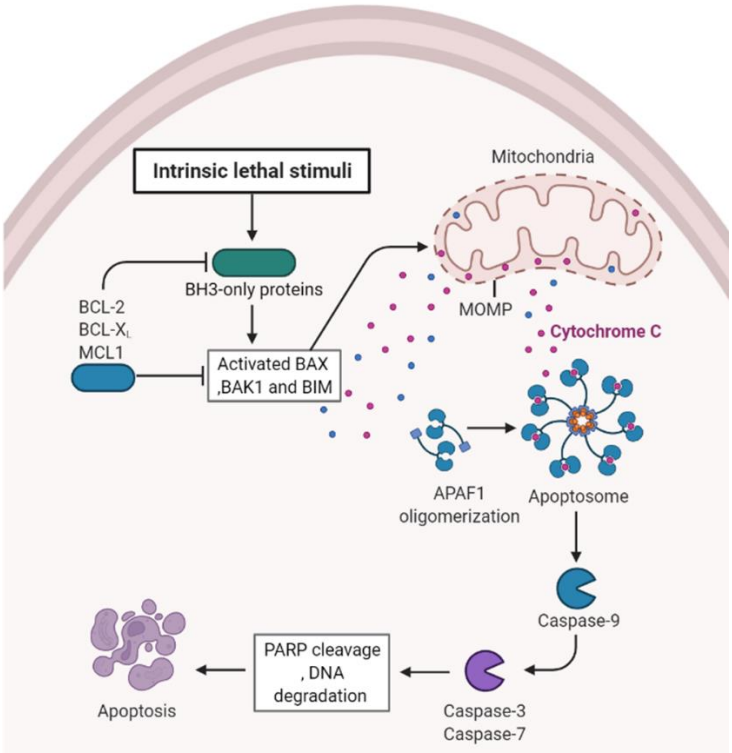


Figure 1.3: The regulation of apoptosis by Bcl-2 family. BAX, BAK1 and BIM= Pro-apoptotic proteins (effectors), Bcl-2, Bcl-xL and Mcl-1= antiapoptotic (inhibitors), BH-3= activator and sensitiser to other Bcl-2 family members, MOMP=

mitochondrial membrane permeabilisation, APAF1= apoptotic peptidase activating factor 1, PARP= poly-ADP ribose polymerase. Reproduced from [17, 22].

The expression (transcription) and activity of Bcl-2 proteins are regulated by other proteins, such as p53 and CDKs. Since the tumour suppressor p53 regulates cell death, it causes apoptosis in cancer cells by regulating the activity of the Bcl-2 proteins. *TP53* induces apoptosis by upregulating the expression of Noxa and Puma BH3-only proteins, which control the intrinsic pathway through the cytochrome c/ apoptotic peptidase activating factor 1 (APAF-1)–dependent pathway [11, 23]. Loss of p53 activity due to mutations is one of the main mechanisms in which cancer cells escape apoptosis [24]. The anti-proliferative Bcl-2 family proteins are elevated in certain tumours, making them promising therapeutic targets. However, other tumours can achieve proliferation by downregulating pro-apoptotic factors [25].

1.1.2.4 Enabling replicative Immortality

Immortalisation (unlimited cell division) is a main characteristic of cancer cells. Normally, cells can undergo a limited number of cell divisions before they senesce and undergo apoptosis; the number of divisions is defined by the presence of telomeres at the end of each chromosome [5]. Telomeres are DNA–protein complexes that protect the genome from degradation and interchromosomal fusion. In every cell division, chromosomes shorten at the telomeric DNA ends; incomplete synthesis of the lagging strand during DNA replication [26]. When telomeres reach the Hayflick limit and are no longer able to protect chromosomes,

the cell enters senescence (metabolically active, but no longer able to divide) and ultimately, apoptosis is triggered. In cancer cells, however, telomeres are lengthened enough to avoid triggering apoptosis. This is related to high levels of telomerase; a terminal transferase ribonucleoprotein that adds telomere segments to the ends of DNA [26].

1.1.2.5 Inducing Angiogenesis

Angiogenesis is the development of new blood vessels from pre-existing vasculature. In order to support neoplastic growth, tumour cells switch on and maintain the angiogenesis to provide required nutrients and oxygen and to remove the metabolic waste. Tumour angiogenesis enables metastasis through extravasation [27]. Normally, the process of angiogenesis is quiescent and activated when needed; during embryonic development, wound healing, and the menstrual cycle [5]. This process is strictly regulated through angiogenic stimulatory and inhibitory factors (**Figure 1.4**).

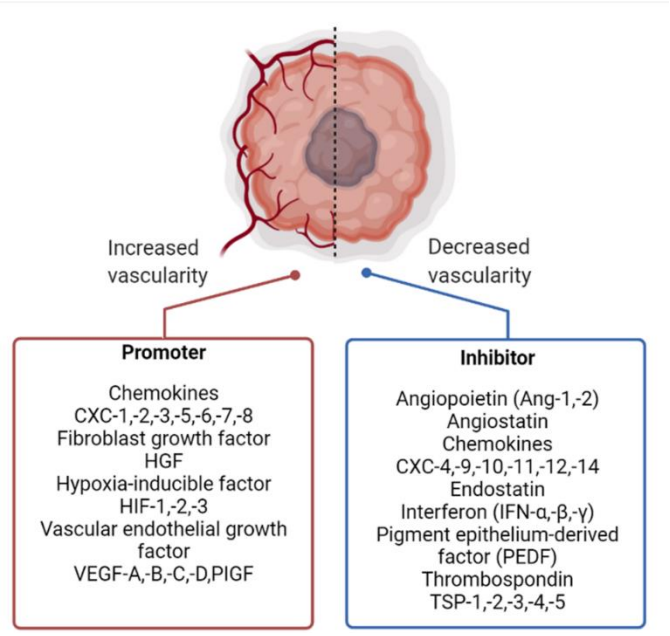


Figure 1.4: Homeostasis of angiogenesis results from an equilibrium between promotors and inhibitors of angiogenesis. Reproduced from [28].

In cancer, the state of relatively poorly blood-supplied hyperplasia and hypoxia causes an imbalance of inhibitory factors, thus inducing angiogenesis [29]. For instance, upregulated vascular endothelial growth factor (VEGF) increases angiogenesis. The upregulation of *VEGF* expression in response to hypoxia occurs through the transcription factor, hypoxia-inducible factor 1 (HIF-1) [30]. Oncogenic signals such as rat sarcoma (RAS) protein and other well-investigated GFs also contribute to the upregulation of *VEGF* and angiogenic switch [31, 32].

Antiangiogenic therapies have been developed such as small molecule tyrosine kinase inhibitors (e.g. sunitinib) to try to thwart tumour growth [33]. In addition, bevacizumab is an approved anti-VEGF monoclonal antibody (mAb) for the treatment of metastatic colorectal cancer in combination with chemotherapy. On the other hand, recruiting the impaired vasculature of tumour tissues to enhance the drug delivery is also widely investigated (Section 1.5) [34].

However, the process of angiogenesis in tumours results in the development of impaired vasodilation. The first angiogenic tumour vessel to form is the mother vessels, these originate from normal capillaries and venules. Mother vessels are known to be composed of thin, flattened and compressed endothelial cells that exhibit high permeability for bigger molecules up to 500 nm; depending on the gap size in the vessel wall. Impaired vasodilation plays a main role in enhanced permeability of the tumour-associated blood vessels to nanoparticles (NPs) [35-38].

1.1.2.6 Activating Invasion and Metastasis

Invasion and metastasis represent a key hallmark for malignancy and account for most cancer mortalities [39]. Metastasis is a multistep process known as the invasion-metastasis cascade that is initiated by local invasion of cancerous cells into the surrounding ECM. This is followed by intravasation into the tumour vasculature, into the bloodstream, from where cancer cells can extravasate into the parenchyma of distant tissues and form micro metastases, eventually, they colonise to form macroscopic metastases [40]. The capability of cancerous cells to dissociate from their place of origin is related to the loss of cellular adhesion. Downregulation or inactivation of molecules normally associated with cell-to-cell adhesion (e.g. E-cadherin), or upregulation of molecules normally associated with the cell migrations (e.g. N-cadherin) is detected in many invasive carcinomas [41]. While understanding the process of metastasis and the factors governing this hallmark is growing, no anti-metastatic drugs have been approved yet. Such therapy could potentially improve treatments and outcomes for patients with malignant cancers [42].

1.1.2.7 Deregulating cellular energetics

Deregulating cellular energetics, commonly termed metabolic reprogramming [5, 43, 44] is observed even in the presence of oxygen, where the energy metabolism production pathway is reprogrammed to aerobic glycolysis. Under normoxia, cells produce their energy by mitochondrial oxidative phosphorylation, which is ~15-times more efficient in producing ATP than glycolysis [44]. This energy metabolic reprogramming provides the cancer cells with glycolytic intermediates needed for

the biosynthesis of nucleosides and amino acids required for cancer proliferation [5]. Moreover, these intermediates themselves can be oncogenic by altering cell signalling and blocking cellular differentiation [43]. Cancer cells compensate for energy loss by upregulating glycolysis by upregulating glucose transporters (e.g., GLUT1) [45]. Upregulating glycolysis in cancer is related to the increase in the activity of HIF-1 or some oncogenes (e.g., RAS, a master regulator of cell cycle (MYC)) [46]. Glycolysis can also be activated following some mutations in tumour suppressors. In general, most mutations in *TP53* gene were found to increase glycolysis in cell culture in addition to its association with other hallmarks of cancer [47].

1.1.2.8 Evading Immune Destruction

Immune surveillance is a system able to recognise and eliminate emerging cancer cells. Cancer cells capable of evading detection or eradication by the immune system, grow into detectable tumours [5]. The relation between the defective immune system and the development of cancers is established [48-50], showing that immunocompromised individuals more often develop virus-induced cancers such as HIV-associated Kaposi sarcoma [50, 51]. Thus, the immune system acts as a barrier to tumour formation, progression, and invasion [50, 52].

1.1.2.9 Enabling hallmarks of cancer

For the hallmarks to emerge, two enabling characteristics have been recognised: development of genomic instability in cancer cells, and tumour-promoting inflammation [5].

Genome Instability and Mutation

Mutations in certain genotypes enable cellular growth. Mutability results from defects in the genomic maintenance and DNA repair machinery [5]. These defects can be generated through inactivation of mutations and epigenetic repression of these types of machinery, which may also be inherited. For example, in breast cancer, mutations in the suppressor breast cancer genes (BRCA-1 and BRCA-2) represent the largest proportion of inherited gene mutations and increase the lifetime risk for developing breast cancer by ~70% compared to non-carriers [4]. Moreover, inherited *TP53* mutations are found in 75% of patients with classic Li-Fraumeni syndrome, which is a cancer predisposition disorder associated with early-onset cancers in diverse tissues of origin [53].

Tumour-Promoting Inflammation

Tumour tissues are known to be infiltrated with different densities of immune cells. However, despite its attempt to eradicate some tumours, the inflammatory response itself can promote the development of incipient neoplasias into cancers through acquiring hallmarks capabilities [5]. This comes from the ability of Inflammation to supply the tumour microenvironment with the required bioactive molecules, such as GFs, angiogenesis-facilitating enzymes and reactive oxygen species (ROS) [5]. For example, Barratt's oesophagus and *Helicobacter pylori* infection are found to predispose oesophageal and gastric adenocarcinomas,

respectively. In both conditions, tumourigenesis is caused as a result of inflammation [54, 55].

1.2 Breast cancer

1.2.1 Epidemiology

Breast cancer is the most diagnosed cancer in the world (**Figure 1.5**). With an estimated 2.3 million new cases in 2020, breast cancer represents 11.7% of all cancer cases [56]. 88% higher incidence rates are reported in transitioned countries than in transitioning countries, corresponding to 56 and 30 individuals per 100,000, respectively. This is related to a greater prevalence of breast cancer risk factors, including lifestyle-related triggers such as higher levels of excess body weight and physical inactivity [57].

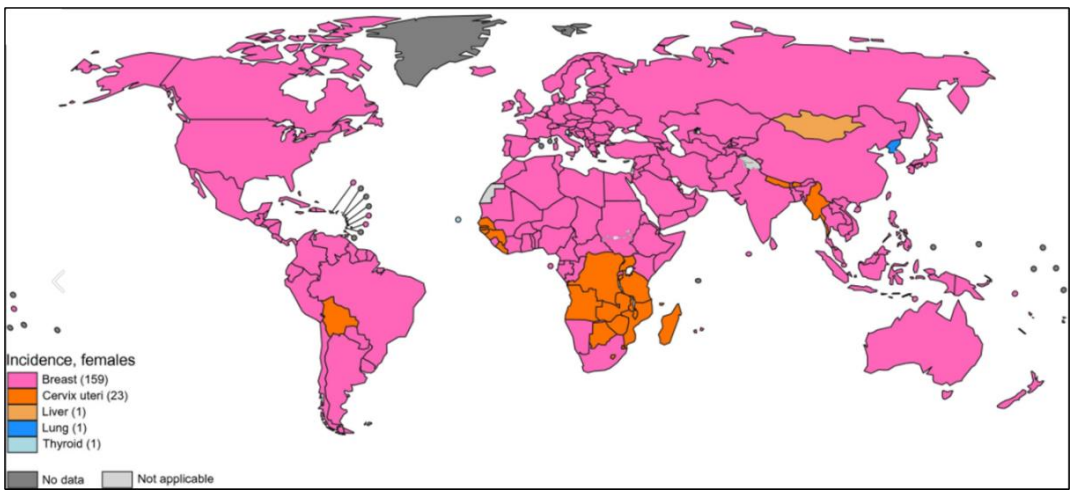


Figure 1.5: Most common type of cancer incidence in 2020 in each country among women [56].

In women, breast cancer is a leading cause of cancer death in 110 out of 185 countries across the globe [56]. In the UK, the estimated age-standardised incidence rate for breast cancer was the greatest among other cancers, with 53,889 female cases recorded in 2020 [58]. Breast cancer is the second-highest cause of cancer mortality in women in the UK after lung cancer (**Figure 1.6**). In 2020, 11,839 deaths due to breast cancer were recorded [58].

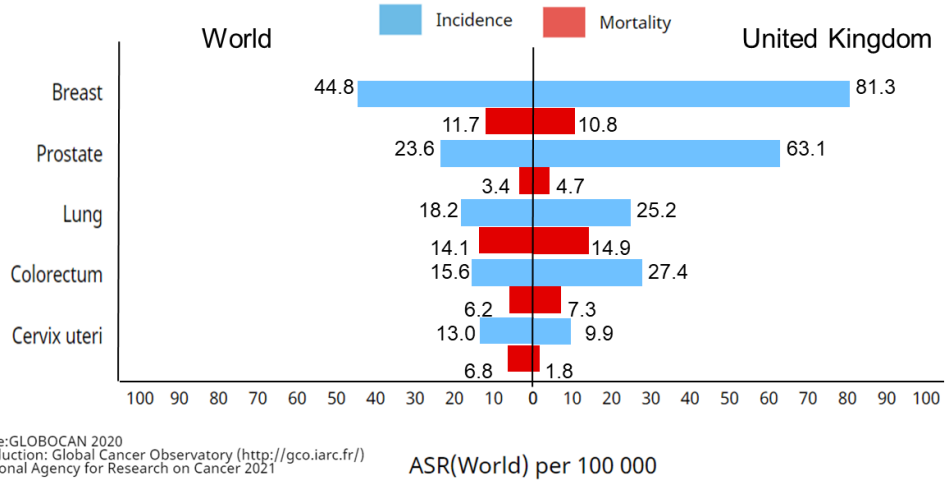


Figure 1.6: Estimated age-standardised incidence and mortality rates (World) in 2020, both sexes, all ages. Modified from GLOBOCAN 2020 [58].

The management of breast cancer is known to be multidisciplinary, and its effect varies from a curable disease when diagnosed at an early stage to incurable metastatic disease [59]. The management strategies including locoregional and systemic therapies differ according to the heterogeneity of breast cancer on the molecular level and the stage of the disease at diagnosis [60]. On the other hand, challenges facing the currently available chemotherapies including off-target effects and drug resistance have reduced the desired therapeutic outcome including improving patients' survival and quality of life [60-62].

Understanding the different classifications of breast cancer and the available treatments' challenges (briefed in Section 1.3) is essential to develop novel therapeutic approaches such as nano therapy to diminish its global burden.

1.2.2 Histological classification of breast cancer

The breast is a mammary gland composed of adipose tissue and glandular structures called lobules. The lobules are joined into lobes, which supply the ducts with milk [63]. Morphologically, breast cancers are classified according to their site of origin (ductal or lobular carcinoma) and depending on whether they invade the stroma or are limited to the epithelial component (invasive or non-invasive/in situ carcinoma) [64]. Up to 80% of the diagnosed invasive breast carcinomas are invasive ductal carcinoma (IDC). When IDC exhibit no specific morphological characteristics, they are classified into "no specific type" and constitute 40% to 75% of all invasive breast carcinomas [65].

1.2.3 Molecular classification of breast cancer

Breast cancer is known to represent a collection of biologically and phenotypically heterogeneous diseases. The heterogeneity affects the response to treatment and emergence of resistance [66]. Hence understanding the basic biology of the disease is crucial, yet it cannot be provided by the histopathological staging of breast cancer. Analysis of the molecular patterns of breast cancers can provide the data required for prognosis, predictive testing, and treatment planning, such as surgical decision-making to improve local-regional control [67].

Based on the results of microarray gene expression study by Perou et al. breast cancers are divided into five subtypes including luminal A, luminal B, basal-like, HER2 over-expression and normal-like. Recently another subtype, claudin-low, was added by Sorlie et al. [68-71]. This molecular classification is based on the presence of genes related to the expression of oestrogen receptors (ER), progesterone receptors (PR), human epidermal growth factor receptor-2 (HER2), and cell proliferation regulator (Ki-67) (**Table 1.1**) [72]. There is a strong link between the molecular subtype of breast cancer and the survival rate, with luminal A and B having a survival rate of more than 90% over 4 years, while other subtypes have lower survival rates [73]. Cells of different molecular subtypes also have a different response to therapy (**Table 1.1**). For instance, hormone receptor-positive and HER2-positive breast cancers respond to endocrine (Section 1.3.3.2) and anti- HER2 therapy respectively. On the other hand, breast cancers not expressing any of those receptors are treated with cytotoxic chemotherapy, targeted therapies such as poly-ADP ribose polymerase (PARP) inhibitors, and immunotherapy.

Evidence for molecular breast cancer heterogeneity continues to grow and to date, genome-wide studies have revealed the presence of over 300 mutations in the coding sequence per tumour and somatic mutations [64, 74]. The most frequently mutated and/or amplified genes are *TP53* (41% of tumours), PIK3CA (30%), MYC (20%), phosphatase and tensin homolog (PTEN, 16%), cyclin D1 (CCND1, 16%), HER2 (13%), fibroblast growth factor receptor 1 (FGFR1, 11%) and GATA Binding Protein 3 (GATA3, 10%), as reported for a series of early breast

cancers. A collective of low-penetrance mutations of these genes encodes cell-cycle modulators that either sustain proliferation and/or inhibit apoptosis [75].

Table 1.1: Molecular subtypes of breast cancer. Edited from [65, 70, 76].

Molecular Subtypes	**Luminal A**	**Luminal B**		**HER2 over-expression**	**Triple-negative**	
		HER-	**HER+**		**Basal-like**	**claudin-low**
Biomarkers	ER+ PR+ HER2- Ki67low	ER+ PR- HER2- Ki67high	ER+ PR-/+ HER2+ Ki67 low/ high	ER– PR– HER2+ Ki67 high	ER- PR- HER2- Ki67high	ER– PR– HER2– Ki67 low
Frequency of Cases (%)	40–50	20-30		15-20	15-20	
Histological grade	Well, Differentiated (Grade I)	Moderately Differentiated (Grade II)		Little Differentiated (Grade III)	Little Differentiated (Grade III)	
Response to therapies	Endocrine responsive, often chemotherapy responsive	Endocrine for ER+, target therapy for HER+, chemotherapy responsive		Target therapy for HER+, often chemotherapy responsive	Intermediate response to chemotherapy, PARP inhibitors	
Other features	Best prognosis	Lower survival than Luminal A, cytokeratin 8+		Worse prognosis than luminous subgroups	EGFR+ and/or cyto-keratin 5/6+	E-cadherin, claudin-3, claudinin -4, and claudinin -7 low
Example cell lines	MCF-7, T47D	ZR-75, BT-474	SKBR-3, MDA-MB-453	MDA-MB-468, SUM190	MDA-MB-231, BT549	

1.2.4 Major signalling pathways in breast cancer development and progression

As previously described in the hallmarks of cancer (Section 1.1.2), mutations in certain genes enable carcinogenesis. In breast cancer, various alterations affect the signalling pathways that govern cell proliferation, division, cell death, cell differentiation, and cell motility. Hyperactivation of proto-oncogenes and

inactivation of tumour suppressors in the predominant signalling pathways that regulate normal mammary gland development and breast cancer stem cell functions including, ER, PR, HER2, and canonical Wnt signalling are briefly described below [77].

1.2.4.1 Oestrogen receptors signalling in breast cancer

ERs (ERα, ERβ) are transcriptional factors that regulate the transcription of many genes upon ligand binding. These genes are crucial for cell division, and the development of the mammary gland, for example during the pubertal ductal elongation [78]. On the other hand, ER signalling is regulated by many co-activators and co-repressors; for example, *BRCA1*, acts partially by inhibiting ERα signalling [79].

ERα has been found to be expressed in 75% of breast cancers and plays an important role in the pathogenesis of the disease through different mechanisms. For instance, ERα increases the growth of breast tumour cells by promoting the transition of cells from the G1 into the S phase. This occurs following its binding to cyclin D1 which activate CDKs 4 and 6 that coordinate the G1-S transition [80].

1.2.4.2 Progesterone signalling in breast cancer

PR signalling in mammary epithelial cells is essential for ductal side branching and alveologenesis. PR can be either co-expressed or segregated from ER and extensive paracrine crosstalk between ER and PR signalling normally takes place. Using the same pathways, PR may cooperate with ER to drive malignant tumour progression [81]. PR signalling is known to affect signal transducers and activators

of transcription (STAT) downstream pathways. STAT proteins consist of three domains: a DNA binding domain, SH2/SH3 domains and a C-terminal transactivating domain. Following their activation, STAT members dimerise as a result of upstream regulators phosphorylation including janus associated kinases (JAK) and mitogen activated protein kinases (MAPKs) (**Figure 1.7**) [82, 83]. STAT dimers then translocate to the nucleus where the transcriptions of many genes associated with the mammary gland development take place [84]. Agreeing to its function, STAT members have been found to highly impact breast cancer development, ranging from potential tumour suppressor function of STAT1 in postmenopausal women to cancer-promoting effect as shown in triple-negative breast cancer (TNBC) [85, 86]. For instance, studies have suggested a positive correlation between active STAT3 and inducing genes required for proliferation, survival, and angiogenesis [87, 88], in addition to its constitutively active state in TNBC [89].

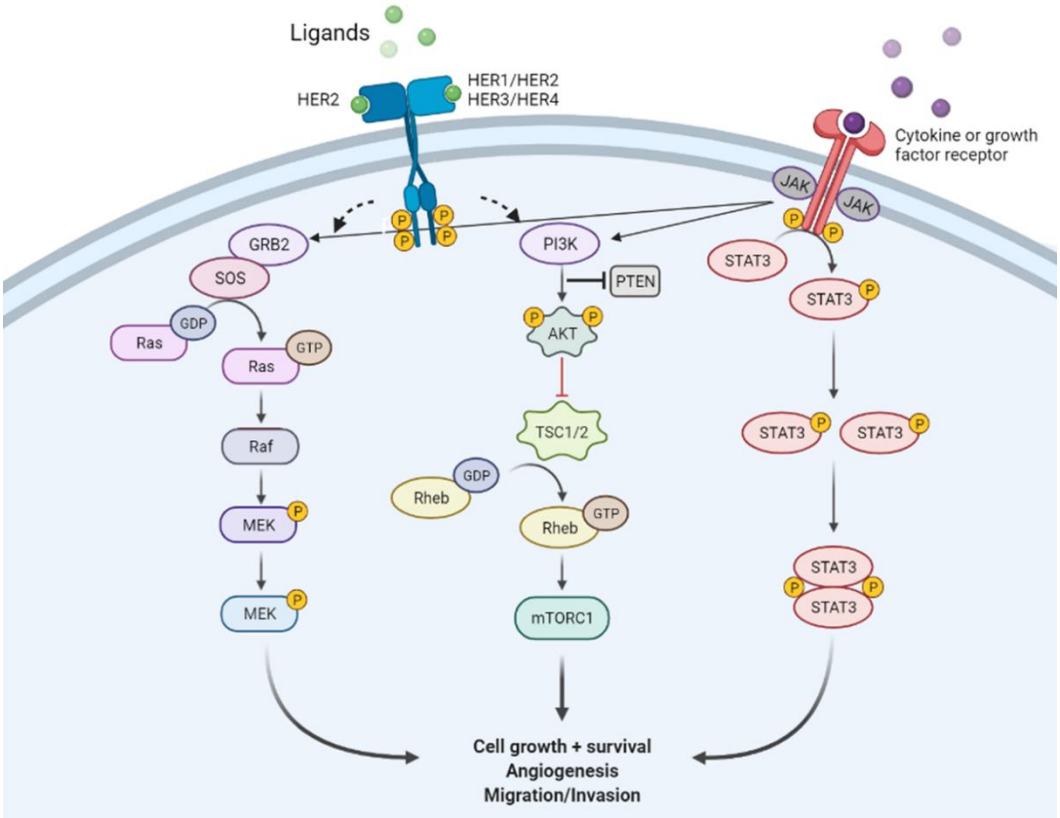


Figure 1.7: HER2 signalling pathway. Upon its response to various ligands, HER2 initiates downstream oncogenic signalling pathways such as Ras/MAPK, PI3K/AKT, and JAK-STAT pathway. Reproduced from [66, 90].

1.2.4.3 HER receptors in breast cancer

HER2/NEU, c-HER2 is a tyrosine kinase receptor belonging to the family of the human EGFRs, which constitute 4 family members [91]. EGFRs consist of three domains: an extracellular ligand-binding domain, a trans-membrane domain, and an intracellular domain [92]. Unlike other EGFRs, HER2 activity is independent of ligand-binding; HER2 dimerises with another HER2 molecule or other EGFR members and stimulates the phosphorylation of its intracellular tyrosine domain, resulting in activating multiple downstream signalling pathways that affect various cellular functions [93]. MAPK and the phosphatidylinositol 4,5-bisphosphate 3-kinase (PI3K) are two pathways that are highly associated with breast

tumourigenesis and activated as a result of HER2 dimerisation (**Figure 1.7**) [66]. As previously classified (**Table 1.1**), various breast cancer subtypes overexpress HER2 protein as a result of HER2 amplification, which is known to be linked to tumour proliferation and cancer progression and metastasis [94].

1.2.4.4 Canonical Wnt/b-catenin signalling in breast cancer

The β-catenin-dependent (canonical) route is one of the intracellular Wnt signalling cascades that is found to play critical roles in tumour cell proliferation, survival and metastasis [95]. When Wnt signalling is inactivated, the tumour suppressors glycogen synthase kinase 3β (GSK-3β) and casein kinase 1 (CK1) phosphorylate the cytoplasmic β-catenin proteins and form a complex along with Axin, and adenomatous polyposis coli (APC). This destruction complex leads to ubiquitination and proteolysis by proteasomes resulting in the inactivation of β-catenin signalling (**Figure 1.8**) [96]. On the other hand, binding of Wnt protein to its co-receptors (Frizzled (FZD1) and low-density lipoprotein receptor-related proteins 5 and 6 (LRP5, LRP6)) recruits many proteins including CK1 and Axin to the cell membrane. Dissociating the destruction complex results in inhibition of GSK-3b protein and thus β-catenin proteasomal degradation and accumulation [97, 98]. Following its accumulation in the cytoplasm and translocation into the nucleus, β-catenin acts as a co-transcriptional activator to regulate multiple downstream genes like C-MYC and cyclin D1, known oncogenes [99].

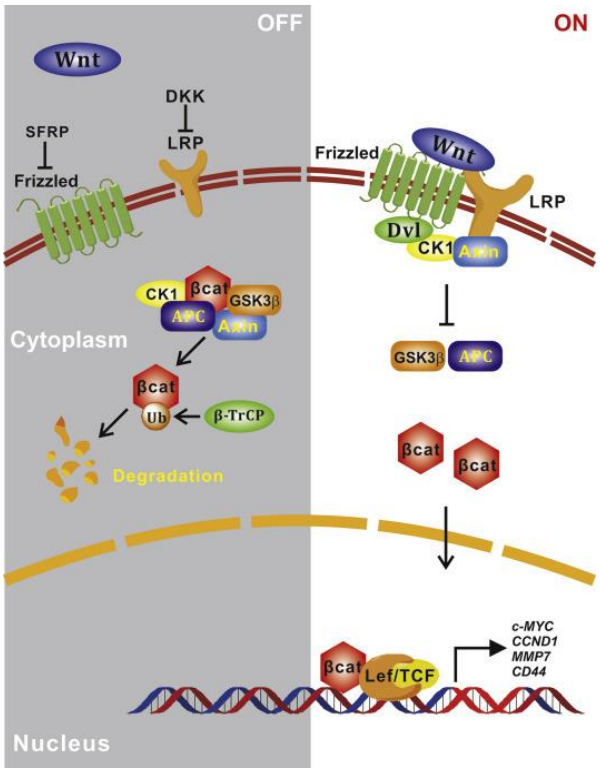


Figure 1.8: Canonical Wnt/β-catenin signalling [66].

Therefore, defects in the regulation of β-catenin target genes may result in tumour development. The prolonged activity of this signalling pathway is associated with clinical poor outcomes, metastasis, and resistance to chemotherapy [100-102]. For example, significant activation of Wnt/b-catenin pathway was reported in HER2-driven mammary tumours and TNBC. In basal-like breast tumours, nuclear localisation of β-catenin was associated with a worse prognosis [103-105].

1.2.5 Other pathways and proteins in breast cancer

In addition to the main pathway networks mentioned above, it is important to note that various signalling pathways affect normal mammary development and correspondingly breast cancer development when they are dysregulated. For example, CDKs, Notch, Sonic Hedgehog (SHH), PI3K [66]. On the other hand, the

upregulation and activation of receptors that promote the progression of breast cancer cells are not restricted to the ones that play roles in their major signalling pathways (e.g. ER) [106], but expand to include other proteins that are widely distributed in the body and participate in essential biological functions, for example, G protein-coupled- δ-opioid receptors and transferrin receptors (TFR) [107, 108].

1.2.5.1 Transferrin receptor

TFRs are transmembrane glycoproteins composed of a dimer of two identical subunits linked together by a disulfide bridge [109]. There are two subtypes of TFR: TFR1 which is expressed by most cells and TFR2 which is found on the surface of liver cells [110, 111]. TFR1 (also known as CD71) binds to transferrin and imports it inside the cells through clathrin-mediated endocytosis, where it releases its iron content under acidic conditions (pH ~ 5.5). This is followed by recycling the binding complex to the surface of the cell at physiological pH and releasing the empty transferrin [109-112]. It has been found that TFR1 also binds to ferritin (Ft) using the same described pathway [113]. As the gatekeeper of cellular iron uptake, TFR1 expression encoded by *TFRC* is precisely regulated by several genes whose activation is mediated by the iron needs of the cells expressing it [112]. TFR1 expression responds not only to the intracellular levels of iron but also to extracellular effectors such as hypoxia [114], inflammation [115] and oxidative stress [116]. Moreover, TFR1 expression is dysregulated in many cancers, indicating its participation in tumour onset and progression. It has been found that oncogenic C-MYC can induce the transcription of *TFRC* and contribute to its

overexpression [117]. In order to meet their excessive iron demands, overexpression of TFR1 has been found in many cancers including the brain [118], colorectal [119], hepatocellular carcinoma [120], prostate cancer [121], lung cancer [122], leukaemia [123], ovarian [124] and breast cancer [108].

In breast cancer, studies have shown that the expression of TFR1 can be an appropriate marker for diagnosis, prognosis, and a putative therapeutic target. In the ER+/luminal-like tumours, TFR1 overexpression was related to a higher grade of tumour and proliferation, and lower Nottingham Prognostic Index (NPI) score. The expression of TFR1 was also reported to be higher in patients with invasive breast carcinoma [125]. The study showed an association between the expression of TFR1 and the malignant transformation in breast tissues [126]. Moreover, the expression of TFR1 is proposed as an early detectable diagnostic biomarker in patients with ER+/PR+ invasive ductal breast cancer, where the study found that expression of TFR1 was significantly higher in those patients compared to matching controls [127]. The role of TFR1, as a signalling molecule in tumourigenesis, has been exposed in several studies. For instance, in breast cancer cells the phosphorylation of TFR1 at position 20 by Src tyrosine kinase was found to reduce apoptosis and enhance its survival [94].

1.3 Breast cancer treatments

Imaging and biopsy are routinely used for cancer diagnosis [128]. The treatment is based on the stage of the axilla and molecular profiling, and the best-individualised therapy depends on the stage of breast cancer according to the tumour, lymph node involvement, metastasis (TNM) system, the tumour grade and receptor status (ER, PR, and HER2). According to the TNM system, three clinical characteristics determine whether cancer cells have expanded into nearby tissue, into the lymph node, and metastasised beyond the breast [129]. Breast cancer stages are on a scale from 0 to IV, with stage IV describing invasive incurable cancers that have metastasised outside the breast to other parts of the body. Metastatic tumours of the breast commonly spread to the lung, liver, bone, adrenal glands and brain [130]. However, if the diagnosis confirmed non-metastatic breast cancer (stage 0-III), appropriate multimodal treatment with curative intent is then initiated, as briefly described below.

1.3.1 Breast surgery

Regardless of the molecular subtype of breast cancer, surgery of the primary tumour remains a cornerstone of locoregional therapy. Wide excision of the entire breast (mastectomy) was the typical surgery procedure, however, this was associated with a high rate of local recurrence and poor survival [131]. Breast conservation therapy (BCT) has substituted mastectomy without compromising survival, and become the primary surgical goal [132]. Compared with mastectomy, BCT renders equivalent overall survival in patients younger than 40 years of age

[133]. Following surgery, some form of systemic therapy is often given dependent on the risk of recurrence and other biomarkers [134].

1.3.2 Radiotherapy

Radiation is a valuable therapeutic option in the treatment of breast cancer [135]. In non-metastatic tumours, radiating the breast following BCT gives similar survival outcomes to those following mastectomy [133]. In addition, radiation therapy is associated with a lower risk of loco-regional recurrence by ~75% [136, 137]. Radiotherapy is also used in palliative therapy, as it can facilitate local control when surgical resection is not feasible and helps maintain or increase the quality of life [138]. In terms of treating distant metastases, radiotherapy is indicated following evaluation of benefits versus risk of toxicities; as treating distant metastases usually requires a high volume of radiation, increasing the risk to the lungs and heart. In this case, a strict adaptation of the irradiated volume is applied to shorten the duration of radiation therapy. This can be achieved by reducing numerical doses while slightly increasing the dosed fractions [139], indicating a boost dose to the primary tumour bed after BCT [140], or using a single intraoperative dose delivery during the surgical procedure [141]. As an alternative, adjuvant systemic therapy can also be indicated in some cases [142].

1.3.3 Neoadjuvant/ adjuvant systemic treatment

Surgery and radiotherapy are considered primary therapies and are usually combined with systemic therapy for patients with early breast cancer [143]. The

type of neoadjuvant and/or adjuvant therapy depends on the molecular subtype, tumour burden and risk of recurrence [144]. Usually, neoadjuvant therapy is used to reduce the tumour size before surgery or to evaluate the response of the tumour to additional adjuvant therapy. In HER2-positive breast cancers and TNBCs, neoadjuvant administration has become the standard [60]. Moreover, in clinically node-negative women, neoadjuvant chemotherapy has been found to significantly reduce the rate of axillary metastases [145].

On the other hand, adjuvant therapy is prescribed after surgical resection of the primary breast cancer to eradicate the residual micro-metastatic disease that may develop into frank metastatic disease if left untreated [146]. For early breast cancers, adjuvant chemotherapy and/or endocrine therapy decrease breast cancer mortality by up to 30% and reduce the risk of recurrence [147] - [148].

Although the selection of appropriate systemic therapies is based on individualised diagnoses, its implementation is hampered by access to the required medications and facilities [59]. The available systemic therapy for breast cancer can be categorised into cytotoxic chemotherapy and targeted therapy.

1.3.3.1 Cytotoxic chemotherapy

Usually, adjuvant chemotherapy is prescribed for most breast cancer patients, days to weeks after surgery and continued for months to years. The patient can be treated with a single agent or combination chemotherapy. Chemotherapy arrests the growth and causes death of the cancer cells. There are four phases of the cell cycle: G1 (gap 1), S (synthesis), G2 (gap 2), and M (mitosis). Chemotherapy

affects one of the phases (specific agents) or more (nonspecific agents). The commonly used chemotherapies for breast cancer treatment are discussed below.

Alkylating agents

Alkylating agents bind an alkyl group to a DNA during its synthesis in the S phase. molecule by a covalent bond and thus prevent the DNA from forming a double helix. This results in DNA strand breaks, the production of ROS and the inactivation of DNA polymerases which catalyse the synthesis of DNA molecules [149, 150]. Cyclophosphamide is the most commonly used alkylating agent in breast cancer treatment as a single agent or a combination therapy [151]. Despite these advantages, cyclophosphamide is associated with the highest risk of gonadotoxicity when treating breast cancer [152].

Platinum-based agents

Platinum-based agents are other non-phase specific agents (e.g., cisplatin, carboplatin) that are regularly prescribed in the treatment of breast cancer. These agents restrict DNA repair by forming DNA intra and inter strands crosslinks and DNA protein crosslinks [153]. Although effective, their adverse effects limit their use. The dose-limiting side effect for cisplatin is nephrotoxicity, for carboplatin it is myelosuppression. In breast cancer, platinum therapy is usually prescribed in combination with other agents to reduce the used dose and hence their adverse effects [154, 155]. For instance, in the guidelines for the treatment of HER2-positive early breast cancer, carboplatin is combined with docetaxel and anti-HER2 therapy in adjuvant therapy for one year [156].

Antimetabolites

Antimetabolites are agents that arrest cancer cells' DNA and RNA synthesis in the G1 phase resulting in starving cells of DNA building blocks, thus preventing the S phase. Due to their structure that mimics the building blocks of genetic material (e.g., nucleosides), they incorporate into DNA and RNA strands and act as chain terminators to inhibit DNA polymerase [157]. Gemcitabine, 5-fluorouracil, methotrexate, and capecitabine are antimetabolite agents that can be prescribed for the treatment of breast cancer in both early and advanced stages. 5-fluorouracil and methotrexate are usually combined with cyclophosphamide in the cyclophosphamide methotrexate fluorouracil (CMF) classic regime [155]. In premenopausal patients who had high-risk breast cancer, a significant improvement in disease-free survival and overall survival for at least 25 years is observed [158].

Antitumour Antibiotics

Anthracyclines are one class of antitumour antibiotics usually prescribed in breast cancer treatment. Anthracyclines' main antitumour effect is interfering with enzymes involved in uncoiling DNA during the cell cycle; topoisomerase II. This results in DNA strand breaks and apoptosis [159]. Other mechanisms include inhibiting DNA and RNA synthesis by intercalating their chromophore moiety between adjacent base pairs of DNA, or by adducting DNA by formaldehyde-releasing pro-drugs, resulting in blocking cell division and apoptosis. Anthracyclines are also known to produce ROS, resulting in oxidative stress, DNA damage, and lipid peroxidation triggering cell apoptosis [160]. Doxorubicin and Epirubicin are anthracycline anti-tumour antibiotics indicated in breast cancer. An

anthracycline - taxane regimen is recommended in luminal HER2-negative (HER-) early breast cancer, in addition to endocrine therapy depending on the individual risk of recurrence [161]. The anthracycline - taxane regimen is also indicated in the adjuvant treatment regime for HER2-positive (+) early breast cancer, and the preferred neoadjuvant chemotherapy in HER2+ early breast cancer and TNBC [60].

Microtubule inhibitors

Microtubule inhibitors are phase-specific agents that disrupt microtubule spindle formation during the M phase. Due to their key role in mitosis, stabilising (by taxanes) or destabilising (by vinca alkaloids) microtubules suppress their dynamics required for appropriate mitotic function, resulting in mitotic arrest, blocking cell cycle progression and ultimately causing apoptosis [162]. Taxanes (e.g., paclitaxel, docetaxel, and ixabepilone) and vinca alkaloids (e.g., vinblastine, vincristine (VCR), vindesine, and vinorelbine) are indicated in breast cancer during early and/or advanced stage [60]. For instance, adjuvant paclitaxel and trastuzumab are indicated for 1 year in patients with node-negative HER2+ tumours with size ≤ 3 cm, as it is associated with few recurrences [163]. In addition, For HER2+ advanced breast cancer previously untreated with trastuzumab, a combination of chemotherapy (e.g., docetaxel, paclitaxel) and anti-HER2 agents (trastuzumab) is the preferred first-line therapy option [164].

1.3.3.2 Targeted therapies

The expression of ER, PR, HER2 and Ki-67 subtypes that identify the molecular classification of breast cancer, can also be used as targets for specific treatments

[72]. Breast cancer-targeted agents work by interfering with the function of these proteins responsible for cancer proliferation and survival [165].

Endocrine treatment

Endocrine or hormonal therapy is the mainstay of treatment for patients with hormone-positive breast cancer (that is, all ER+ and/or PR+ tumours). They work by manipulating oestrogen signalling via ER which represents the driving transcription factor in around 70% of breast cancer [166], these include:

- **Tamoxifen** is a selective oestrogen receptor modulator that binds to the oestrogen binding domain of ER to block its effect, thus reducing the proliferation of tumour cells [167].
- **Aromatase inhibitors** (such as anastrozole, letrozole) are agents that stop oestrogen production from aromatase enzymes that convert androgens to oestrogen [168].
- **Fulvestrant** is a selective ER degrader. It binds to active ER and degrades it, resulting in losing its expression [169].

All patients with ER+ breast cancer, independent of PR/HER2 status, should receive endocrine therapy to block ER activity. In addition to breast cancer stage, the choice of endocrine therapy is also related to menopausal status. For instance, in early breast cancer with a low risk for recurrence, Tamoxifen can be indicated as a single agent for both pre- and postmenopausal patients for at least 5 years after surgery [60]. However, in postmenopausal women, aromatase inhibitors are the preferred choice over tamoxifen as the oestrogen is not mainly produced from

the ovary [170]. Patients with a high risk of recurrences are treated with endocrine therapy for up to 10 years along with appropriate chemotherapy [171].

Immunotherapy

Recombinant antibodies are also part of breast cancer treatment. Anti-HER2 mAb trastuzumab was the first approved mAb in 1998 for treatment of HER2(+) breast cancers [172]. Due to its overexpression in breast cancer, HER2 protein is considered a relevant biomarker for treatment. Trastuzumab binds to the extracellular domain of HER2 and inhibits its downstream signals. This results in blocking its action including proliferation and angiogenesis [173]. In HER2+ early breast cancer, neoadjuvant and adjuvant chemotherapy together with anti-HER2 therapy is used as standard therapy and correlates with decreased recurrence and improved disease-free survival and overall survival [172]. In HER2(+) advanced breast cancer, anti-HER2 therapy is also a standard in combination with other cytotoxic chemotherapy [60].

Other targeted agents

The conventional treatment for TNBC is chemotherapy including anthracyclines and taxanes. Although targeted therapies for TNBC have not yet been discovered, it may respond to PARP inhibitors targeted therapy [165]. Inhibition of PARP in BRCA-mutant cancers via the concept of synthetic lethality is well-established. Synthetic lethality occurs when two non-lethal genetic alterations contribute to lethality together (e.g., BRCA and PARP). In BRCA-mutant and BRCA-deficient (e.g., homologous recombination-deficient) tumours, PARP activity is essential in base excision repair (BER). Thus, BRCA-deficient tumours are acutely sensitive when

challenged with PARP inhibitors (that inhibit DNA BER), resulting in chromosomal instability, and selective cellular death with limited toxicity for the patient [165, 174, 175]. Thus, individuals with *BRCA* mutations in the breast cancer population including TNBC are potential targets for BRCA mutation-targeted therapies such as olaparib [176].

TNBC patients with high expression and/or functional activation of EGFRs represent a potential target for anti-EGFRs antibodies and/or small-molecule EGFR inhibitors [177]. However, due to the low response and high resistance, no EGFR therapies are currently approved for the treatment of TNBC [178]. On the other hand, EGFR therapies are effectively used in HER2(+) breast tumours. For example, gefitinib targets EGFR with high selectivity, lapatinib targets both EGFR and HER2 and neratinib targets multiple kinases [179].

1.3.3.3 Challenges associated with breast cancer treatment

Challenges associated with anticancer agents include innate or acquired drug resistance besides the previously mentioned significant toxicity (Section 1.3.3.1) which limits their overall clinical efficacy [155, 194]. Indeed, ~ 90% of chemotherapy fails at some point during invasion and metastasis of cancers, which are related to drug resistance [192]. In cancer cells, drug-resistant diseases result from their genome instability and mutation (Section 1.1.2.9).

The mechanisms of resistance are:

- Multi-drug resistance (MDR) develops when cancer cells can survive against a wide range of anti-cancer drugs as a result of increased drug efflux outside the cells and reduced drug uptake into the cells [191].

- Inactivation of anticancer drugs. Mechanisms include mutations, and changing the drug metabolism by down- or up-regulating the proteins and enzymes needed for activation or detoxification of anticancer agents respectively [192].
- Changing the anticancer drugs' targets. Mechanisms involve mutations in the structure of target proteins or changes in their expression levels, resulting in improper binding of the drugs to their targets [193].
- Enhancing the DNA repair mechanisms and inhibiting cell death can also result in resistance to chemotherapy [192].

1.4 Natural products and breast cancer treatment

Natural products have historically been a major and critically important source of therapy [180]. The earliest known prescriptions are recorded on Sumerian cuneiform clay tablets date back to ~2600 BCE [181]. The Ebers Papyrus is the largest and one of the oldest medical scrolls (c.1500 BCE), which documents over 700 plant-based remedies [182]. Ancient Egyptians were using castor oil, as a medicine, to eradicate tumours near the breast surface [183]. Exploiting natural products from different sources including plants has led to the discovery of many medicines. In one screening study for 32 plants from the rain Malaysian forests, 13 crude extracts from 11 plant species were found to possess an anti-proliferative activity in breast cancer cell lines [8]. Advanced technologies, such as high-performance liquid chromatography (HPLC), and nuclear magnetic resonance (NMR) coupled with mass spectrometry (MS)enabled purification, isolation, and

identification of the active component(s) responsible for the biological activity [184]. Following this, identified compound(s) are screened through the available natural product libraries (high-throughput screening) in order to predict their biological activity (de-replication) [185]. A panel of anti-cancer drugs related to natural products was identified, corresponding to 25% of all newly approved anti-cancer drugs between 1981 and 2019 [186].

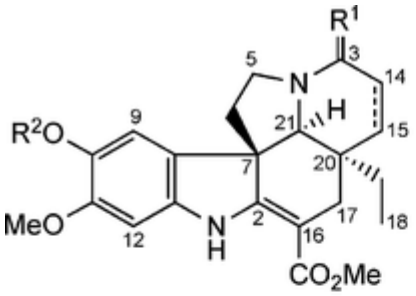
Among these are taxanes and vinca alkaloid anti-microtubules agents used as standard adjunct agents (Section 1.3.3.1) [187] Those plant-derived drugs that cause cell death in treated cancer cells, serve as standard adjunct agents in breast cancer treatment [162]. For instance, docetaxel demonstrates significant improvements in survival rates in high-risk breast cancer patients regardless of their prognostic factors. However, the potentially life-threatening adverse effects associated with taxanes (e.g. docetaxel) limit its use [188, 189]. In addition, acquired resistance to taxanes and other anticancer agents isolated from natural sources is reported in multiple types of solid tumours after long-term administration [190].

Challenges associated with anticancer agents (from natural sources and traditional systemic chemotherapy) including toxicity and drug resistance oriented the efforts toward the discovery of novel agents and strategies that may provide higher efficacy with limited toxicity along with overcoming innate or acquired drug resistance commonly associated with chemotherapeutic agents [162]. Among the efforts is re-examining the natural products as a rich reservoir of chemical diversity

[162, 195]. In addition, new strategies for safer delivery of available agents are being developed (e.g., nanomedicines) [196].

1.4.1 Jerantinines

Aspidosperma indole alkaloids, Jerantinines A-G, were first isolated and characterised in 2008 (**Figure 1.9**) [197]. Those alkaloids extracted from *Tabernaemontana corymbosa* leaves had shown *in vitro* cytotoxic activity in KB cells (IC_{50} < 1µg/ml) [197]. Subsequently, many jerantinines were tested for their *in vitro* antiproliferative activities. Jerantinines A (JA) and B (JB) have been found to display promising antiproliferative effects against many human cancer cell lines including breast (MCF-7, MDA-468), colorectal (HCT-116, HT-29), and lung (A549) carcinomas. JA and JB inhibit tubulin polymerisation leading to G2/M cell cycle phase arrest. Additionally, JB inhibits polo-like kinase 1 (PLK1; an early trigger for the G2/M transition) and increases ROS levels. Treatment with jerantinines results in cellular apoptosis, which is concentration- and time-dependent [198-203]. More recently, JA was shown to induce antiproliferative effects by targeting the spliceosome in breast cancer and causing abnormal splicing patterns that result in cell death. This is caused by stabilising the splicing factor 3b subunit 1 (SF3B1) protein and dissociating it from the nucleosome complex [204].



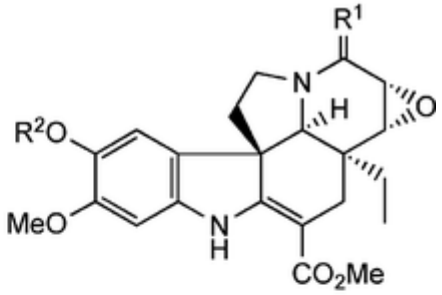
1 $R^1 = H_2$, $R^2 = H$, $\Delta^{14,15}$

3 $R^1 = O$, $R^2 = H$, $\Delta^{14,15}$

5 $R^1 = H_2$, $R^2 = H$

8 $R^1 = H_2$, $R^2 = OAc$, $\Delta^{14,15}$

10 $R^1 = H_2$, $R^2 = OMe$, $\Delta^{14,15}$

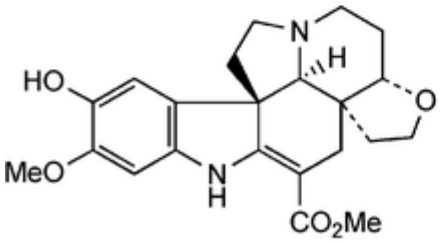


2 $R^1 = H_2$, $R^2 = H$

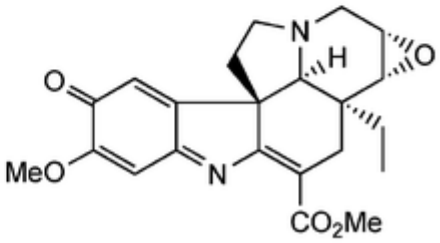
4 $R^1 = O$, $R^2 = H$

9 $R^1 = H_2$, $R^2 = OAc$

11 $R^1 = H_2$, $R^2 = OMe$



6



7

Figure 1.9: Jerantinine A-G cytotoxic alkaloid compounds isolated from Tabernaemontana corymbose. (1) jerantinine A, (2) jerantinine B, (3) jerantinine C, (4) jerantinine D, (5) jerantinine E, (8) jerantinine A acetate, (9) jerantinine B acetate, (10) 10-*O*-Methyl jerantinine A, (11) 10-*O*-Methyl jerantinine B [197].

Both JA and JB were found to evade poly glycoprotein (P-gp) mediated MDR induced by VCR in HCT-116 (colorectal cancer) cells [202, 203, 205-208]. P-gp is the first known ATP-binding cassette (ABC) transporter; also known as ABCB1. The contribution of ABC efflux pumps to drug resistance has been widely explored and the relationship between many MDR and ABC transporters has been established through their overexpression in different breast cancer cells [209-212]. P-gp, breast cancer resistance protein (BCRP), and MDR-associated protein 1 (MRP1) are the most prevalent ABC efflux transporters related to MDR in breast cancer [213]. P-gp is found to be overexpressed in breast cancer cell lines and its overexpression

is shown to be responsible for MDR in 41% of breast cancer patients [214-216]. A subsequent study has indicated that jerantinine may offer a potential alternative to VCR in the treatment of paediatric medulloblastoma [217]. With comparable antiproliferative effects to VCR, jerantinine activity is independent of intrinsic ABCB1 expression, thus avoiding MDR [217].

JA inhibited the growth of ER-positive MCF-7, TNBC MDA-MB-468 breast and HCT-116 colon cancer cells with GI_{50} values of <1 µM. JA acetate (JAa) which is a more stable derivative of JA has shown comparable activity in colon cancer cells and greater potency against A549 lung and HT-29 colon cancer cell lines [202]. The promising high potency, multi-target effects and ability to overcome MDR *in vitro* encourage the belief that jerantinines are worthy of preclinical development. However, JA has poor selectivity and exhibited cytotoxicity against non-cancerous normal lung fibroblast cells (MRC-5) with a GI_{50} = 1.72 µM [202]. Also, the availability of isolated natural agents is limited, hence the synthesis of jerantinines A and E using (-)-tabersonine as a precursor has been developed by John E. Moses and his co-workers [198-201].

1.5 Drug delivery – nanotechnology and nanomedicine

Nanomedicine is a developing field that applies nanotechnology to therapy. This research encompasses multiple disciplines including, biology, physics, chemistry, engineering, and mathematics [218, 219]. Nano-formulations are composed of NPs with a size of 1 - 1000 nm in which a drug or imaging agent is encapsulated, dissolved, entrapped or attached to its matrix [220]. The applications of

nanomedicine showed a notable enhancement in non-invasive cancer detection, imaging and treatment [221] and are expected to keep developing in the future [222].

1.5.1 Systemic delivery and biodistribution

The original concept of using nanoscale particles in cancer therapy is largely attributable to the enhanced permeability and retention (EPR) effect of impaired vasculature (section 1.1.2.5) that affects the biodistribution [223]. In tumour vasculature, some pre-existing venules contribute to the formation of the mother vessels, which enhance the permeability of the tumour microenvironment vasculature to NPs, due to their high permeable intercellular gaps [35-37]. In addition, big molecules can normally transfer through the capillary endothelial cells via vesiculo–vacuolar organelles (VVOs). VVOs that can be single or linked vesicles then discharge their cargo into the extravascular space [224], and represent a prominent structure and a primary pathway for NPs extravasation [225]. Enhanced permeability and mode for NP extravasation are illustrated in **Figure 1.10**.

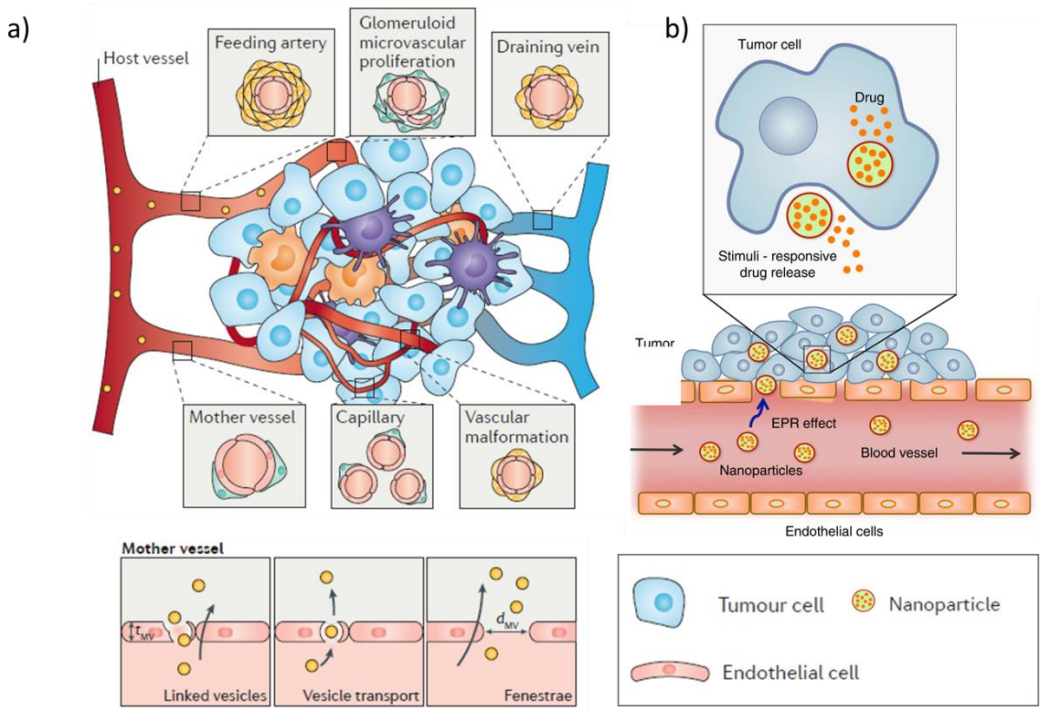


Figure 1.10: Schematic illustration of (**a**) tumour blood vessels and mode for nanoparticle extravasation in mother vessels and (**b**) enhanced permeability and retention (EPR) effect of vascular malformations. dMV= the intercellular gap distance in mother vessels, tMV= the thickness of endothelial cells lining the mother vessels. Modified from [226, 227].

On the other hand, the leakiness of tumour vasculature allows plasma and blood proteins to extravasate into the tumour microenvironment resulting in more viscous blood. This ultimately enhances the efficiency of NPs' ability to permeate porous vasculature as it slows the blood flows (also known as flow reversal) and gives more time for NPs to permeate out of the tumour vasculature [228].

As a result of the tumour pathophysiological features; the leakiness of tumour vasculature, tumour microenvironment interactions, and poor lymphatic drainage, NPs preferentially extravasate the tumour vasculature and accumulate in the tumour microenvironment. This is then followed by the uptake of NPs by the tumour cells [223, 229, 230].

Modifying the biodistribution and enhancing the tumour's accumulation of anticancer agents using nanomedicine, have been successfully used to improve efficacy and reduce toxicity in clinical practice [231]. In addition, NPs have been used to enhance the physical properties of pharmaceutical agents including solubility and stability, as was demonstrated for Ibuprofen and nucleic acids [232-234].

1.5.2 Nanoparticle classes

The composition of the nano formulation matrix is of high importance, as it affects the biological biodistribution and the physical properties of the NPs [235], as well as the efficiency of cargo delivery and patient response [236]. The following NPs are considered for drug delivery:

Lipid-based nanoparticles

Lipid-based NPs are mostly spherical particles composed of lipid bilayer(s) surrounding an aqueous compartment (**Figure 1.11**). They can be modified to entrap more than one drug even with opposite lipophilicity [237]. Liposomes are the most common class of FDA-approved nanomedicines due to their formulation simplicity and modification capability; allowing enhanced biological stability of the cargo [238, 239].

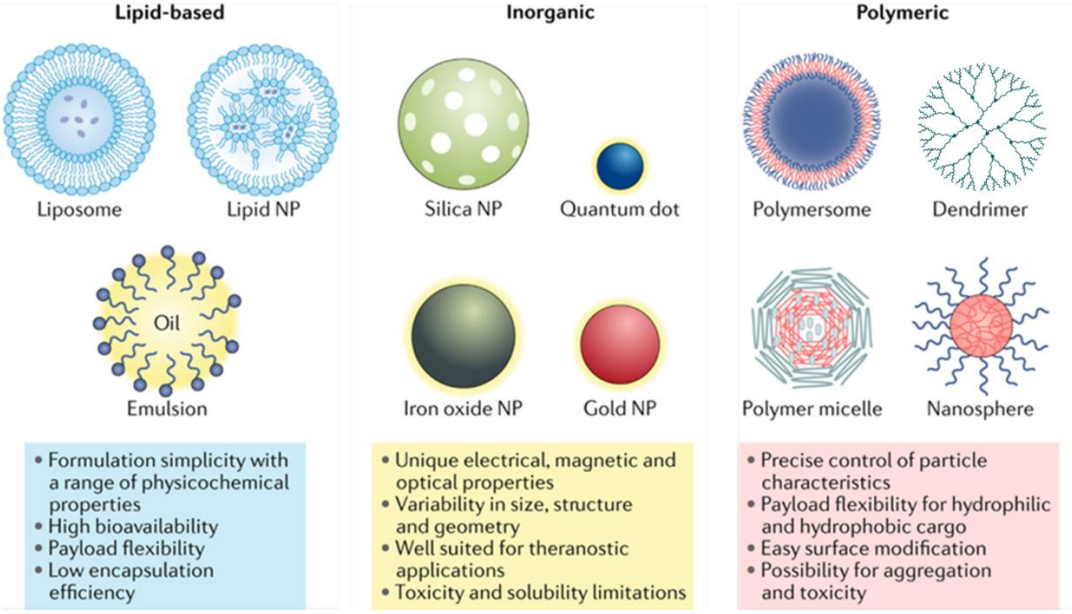


Figure 1.11: Classes of nanoparticles according to their composition including the most common advantages and disadvantages for each. Modified from [236].

Inorganic nanoparticles

Inorganic NPs, for example, gold, iron and silica NPs, are used for drug delivery (**Figure 1.11**) [240]. Inorganic NPs can have specific physical, magnetic and optical properties, depending on their composition, that enables their use in diagnostics, imaging and photothermal therapies [241]. Moreover, inorganic NPs can be engineered with different sizes and geometries, which is known to affect their delivery [240]. Gold NPs and iron oxide are two commonly studied inorganic NPs with FDA approval for the latter for iron-deficiency management [236].

Polymer-based nanoparticles

Polymer-based NPs are colloidal systems that can be synthesised from natural or synthetic polymers (**Figure 1.11**). The polymeric NPs nanocapsules/nanospheres are divided according to their shapes into polymersomes, micelles and dendrimers

[242]. The therapeutic agent can be encapsulated, entrapped, or even conjugated to the polymer during synthesis, allowing this NP to hold molecules with various biological characteristics [243-245]. Moreover, the feasibility for scaling up and high stability in the biological system are two significant advantages over other lipid-based and inorganic nanocarriers [246]. However, NPs encounter disadvantages related to poor encapsulation efficiency (EE) and high biodistribution to the liver and spleen, as seen with lipid NPs [247], and solubility related to the inorganic NPs especially when using heavy metals [248], in addition to aggregation problems encountered with polymeric NPs, and reported toxicity [236].

1.5.3 Advantages and challenges of the nanoparticle driven delivery

The biodistribution of systemically-administered NPs can be affected by several biological factors, including interaction with plasma proteins, blood circulation time and clearance, in addition to uptake by cancer cells [249]. Once inside the circulation, NPs are covered with a corona - a shell formed as a result of adsorbing mainly plasma proteins and to a lesser extent carbohydrates and lipids onto the NPs' surface [250]. The formation of a corona can be irreversible and depends on the NP physicochemical properties, exposure time, the protein source and its concentration. The presence of a corona can change the NP interactions in a biological environment [250-252] and its toxicity [253].

The interaction of the NP with the environments can be modified by their size, shape, surface charge and composition. For example, when opsonin binds to the surface of positively charged NPs as part of the corona, it triggers the mononuclear phagocytic system (MPS) that might cost NPs their targeting capability [254]. The MPS is rich in resident phagocytic cells, mainly from the liver and spleen that identify, sequester and eliminate NPs as foreign substances [255]. Although the toxicological investigations of NPs on the targeted organs have not been fully addressed, the fact that NPs accumulate in the main organs including the liver, kidney and lung provides the necessary information needed to control NPs toxicity before transiting them into the clinic [256].

In general, the properties of NPs can be altered during synthesis to optimise their *in vitro* and *in vivo* stability [236], targeting properties, biodistribution, loading efficacies and release kinetics [257] (**Figure 1.12**) [235].

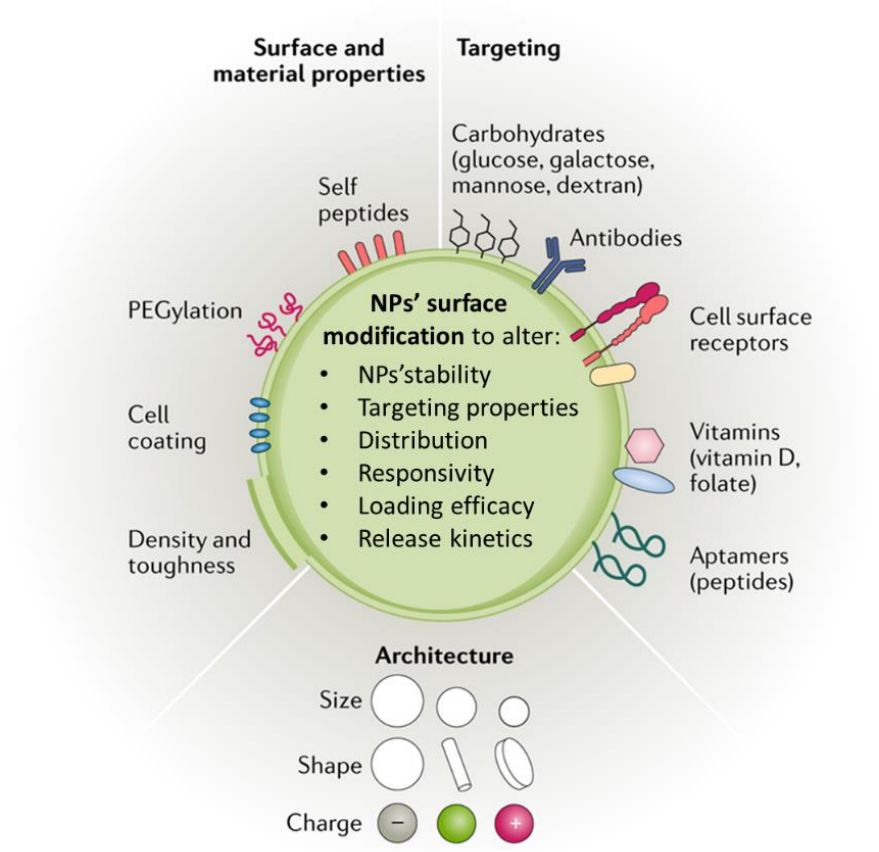


Figure 1.12: Commonly engineered NP surface properties that allow for enhanced delivery. Modified from [236].

The NP size plays an important role when being developed for specific tumours. For example, tumour vessels that grow in cranial environments or regressing tumours after hormone withdrawal, have a smaller pore cut-off size compared to other tumours including the subcutaneous ones that normally range from 200 nm to 1.2 µm [258]. Hence the size of the NPs used should be within this range to enable efficient delivery. When the size of the molecule is considerably smaller than the pore cut-off size, the permeability becomes independent of pore size [258]. Moreover, The NP's size is crucial for clearance from the body. When NPs successfully pass bypass sequestering by MPS and renal system filtration by having

a size bigger than glomerular filtration cut-off ~ 5.5 nm, they will have opportunity to reach and interact with the tumour tissue [259, 260]

Successful modifications of the NP surface properties to enhance delivery have been made. To prevent non-specific distribution, Active targeting of NPs by modifying their surface using targeting moieties including antibodies [261], glucose [262] and other ligands [263] has been made to direct their delivery (**Figure 1.12**). These targeting moieties interact with cognate molecules on the target cell's surface, such as receptors. Attempts to reduce the protein interaction with NPs, including covering NPs with polyethylene glycol (PEG), reducing their recognition by MPS and lengthening their half-life in the circulation by up to 2 days by avoiding MPS clearance [264].

On the other hand, reducing toxicity, protein interaction and enhancing the biocompatibility of exogenous materials have been achieved by coating their surface with endogenous materials [265]. Successful NPs surface modification by applying a membrane made of self-peptide, leukocytes, erythrocytes, or platelets enhanced the biocompatibility of NPs, reduced their MPS recognition and ultimately lengthened circulation half-life [266-269].

While many promising preclinical studies are reported, only a few have been approved for clinical use [270]. PEGylated liposomal doxorubicin was the first approved NP for the treatment of various cancers. this was followed by the approval of many NPs' medicines formulated into PEGylated and non-PEGylated liposomes, in addition to albumin-particle bound paclitaxel and others as shown in **Figure 1.13** [271].

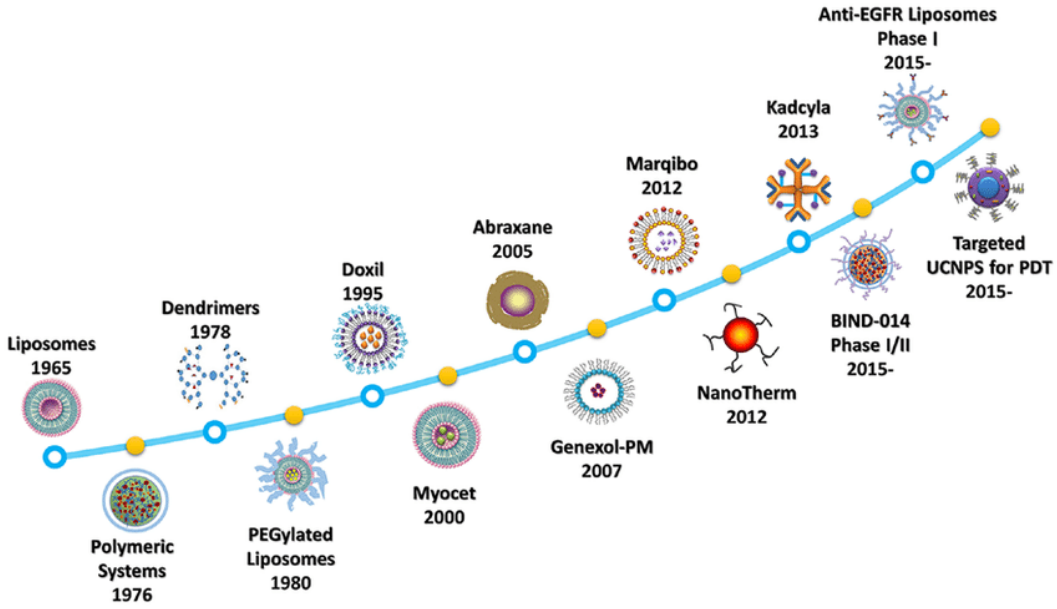


Figure 1.13: Timeline of the development of nanomedicines. Doxil (doxorubicin, non-PEGylated liposome Myocet (doxorubicin) (155), albumin-based nanoparticle (NP) Abraxane (doxorubicin), PEG-PLA polymeric micelle Genexol-PM (paclitaxel), vincristine sulfate liposome (Marqibo), the iron oxide NP (NanoTherm), targeted ado-trastuzumab emtansine (DM1) liposome (Kadcyla), PEG-PLGA polymeric NPs (BIND-014), up conversion nanoparticles (UCNPs) used in photodynamic therapy (PDT) [272].

On the other hand, using endogenous materials as nanocarriers for cancer therapy not only enhances biocompatibility but also biodegradability Peptides have been used as nanocarriers, however, their poor stability, solubility and membrane permeability presented challenges [273]. Using proteins as nanocarriers has been shown to overcome these obstacles, making them very promising nanocarriers for cancer therapy [273].

1.6 Ferritin family proteins

1.6.1 Structure

Ft proteins are the main storage proteins for iron in human tissues, microorganisms, and even plants. The superfamily of Ft consists of three members; the classic Ft which is found in eukaryotes and some types of bacteria, bacterio-Ft found in other types of bacteria and archaea and DNA-binding protein from starved cells (DPS) which plays an important role in protecting chromosomes from being oxidised and eventually damaged [274].

Mammalian Ft consists of 2 polymer chains, the H-chain (also known as the heavy chain) consists of 182 amino acids and has a molecular weight (MWt) of 21,000 d. H-chain contains the active “ferroxidase” site where oxidation of iron takes place. The L chain is a “light” chain composed of 174 amino acids and has a MWt of 18,500 d; it facilitates the mineralisation process of iron ions (**Figure 1.14**). Other Ft types also contain the ferroxidase site with some differences in the structure of H and L chains [275, 276]. The H-chain was originally named after being isolated from the heart where it is predominant, whereas the L-chain is predominant in liver tissue. Moreover, the predominance of H and L subunits varies according to the pathological condition and each is encoded by separate genes [277, 278]. The 24 subunits of Ft are arranged in octahedral (432) symmetry to form a spherical cage with an outer and inner diameter of 12 nm and 8 nm, respectively, capable of storing ~4500 iron atoms (**Figure 1.14**) [279, 280]. The inner cavity of Ft is connected to the external environment through eight hydrophilic triple-axis

channels and six hydrophobic quadruple axis channels with sizes between ~0.3 and ~0.5 nm. Those are necessary for the iron in- and out-diffusion [281, 282].

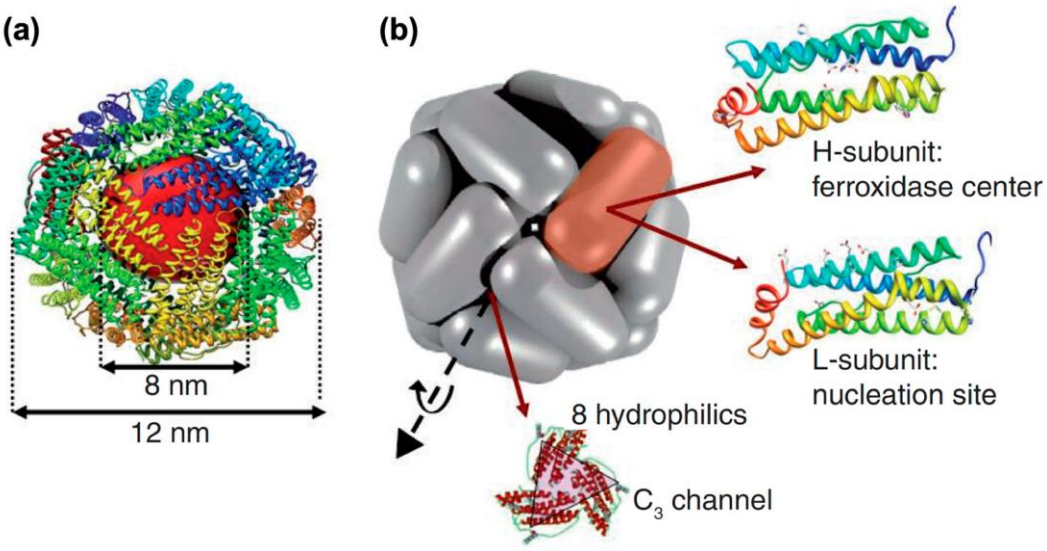


Figure 1.14: **(a)**The spherical cage of native ferritin with an outer and inner diameter of 12 nm and 8 nm and iron core of ferritin. **(b)** ferritin is composed of 24 oligomers; H chain subunits and L chain subunits with 8 hydrophilic channels [283].

1.6.2 Physiological role

Ft function is crucial for iron homeostasis (**Figure 1.15**). As an iron storage protein, Ft captures free iron (FeII) and sequesters it inside its mineral core in the form of ferrihydrite phosphate ([FeOOH] 8[$FeOPO_3H_2$]. This protects the tissues from the accumulation of free iron. Free iron ions are very toxic to cells as they can form free radical species that directly bind to and damage DNA, lipids and even proteins in a process known as peroxidative damage. The stored (FeIII) iron ions are not toxic and can be released from Ft when needed [279, 280, 284-286].

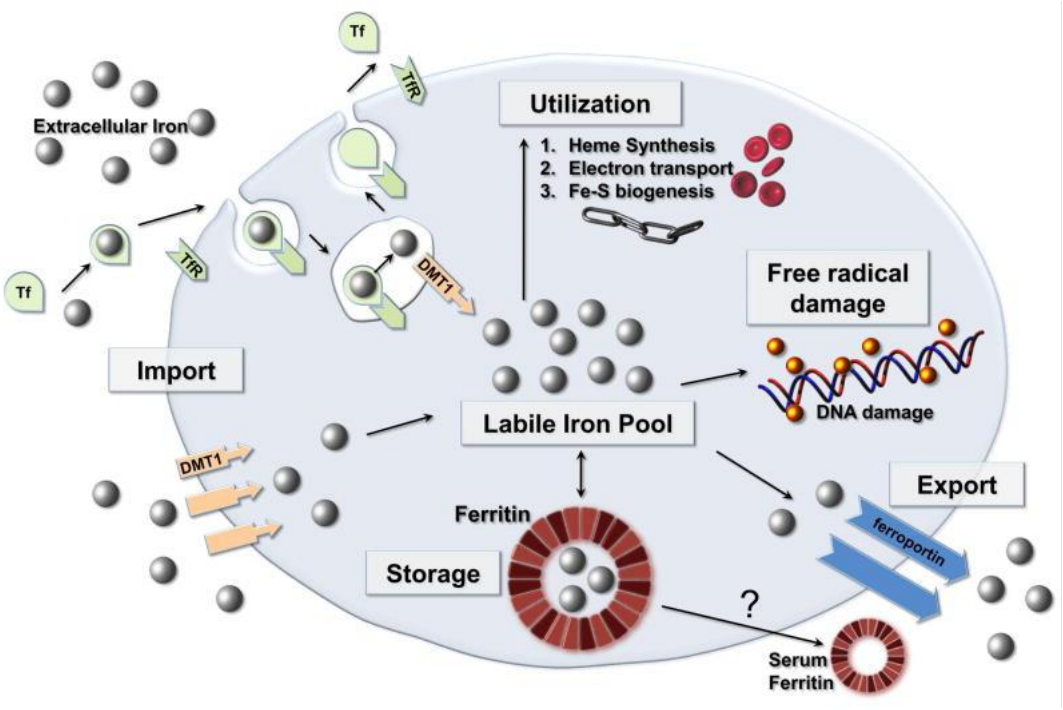


Figure 1.15: Intracellular Iron Homeostasis and the role of Ferritin in storing iron (FeIII) inside its mineral core. DMT1 = divalent metal ion transporter 1, Tf = Transferrin, TFR = Transferrin receptor [287].

Cellular Ft is mainly located in the cytoplasm, however, it can be also found in the nucleus and in mitochondria, where its expression is controlled post-transcriptionally by iron levels inside the cells [288]. Cellular Ft is overexpressed in many cancerous tissues, including hepatocellular, breast and pancreatic carcinoma. The overexpression of cellular Ft reflects the integral role of iron. Indeed iron is essential for all cells as it plays a critical role in cellular respiration by converting oxygen into ATP (the usable energy form in cells) [287]. It is needed for the formation of iron-containing proteins necessary for oxygen transport [289]. Moreover, iron is a co-factor for many enzymes such as ribonucleotide reductase which is necessary for DNA synthesis [290].

Although mammalian Ft is normally found in high levels inside the cells, it is also present extracellularly within the serum. Here it can deliver iron to different tissues in the case of transferrin depletion; transferrin is the main iron transport protein in the blood [287]. Unusually high levels of extracellular Ft have been detected in different fluids including cerebrospinal, synovial fluid and serum. The raised levels are related to iron overload, inflammation, or even some malignancies including hepatocellular, pancreatic, breast and many other carcinomas [291-294]. In addition to iron storage, transport and protection roles, Ft has a role in dietary iron absorption [295].

1.6.3 Ferritin as a nanoparticle – Apoferritin

The relationship between cancer and TFR1 made it a valuable target for therapy. For example, mAb against TFR1, competes with transferrin binding to TFR1, resulting in the intracellular iron deprivation and death of cancer cells overexpressing TFR1 [296]. On the other hand, due to its upregulation in cancer cells, targeting TFR1 with specific nanocarriers (such as Ft) is another developing therapy option [297].

Iron-free Ft is called apoferritin (AFt), it is a colourless, spherical hollow polypeptide cage. AFt was prepared from Ft first by Granick and Michaelis in 1940 [298, 299]. Besides being biocompatible (non-toxic), AFt is a stable protein under different environmental conditions. It is stable at high temperatures up to 75 ºC, in various denaturants such as urea and within a wide pH range (2 - 10). AFt has a self-assembly property; it dissociates under acid/alkaline pH (≤2.0 or ≥11.0) into its 24 subunits and restores its nano-spherical shape at physiological pH (7.5). In

addition, it has been found that TFR1 is responsible for AFt uptake into cells, by selectively binding to its H subunit. AFt is taken up by clathrin-coated pit-mediated endocytosis and trafficked through the cells by endosomes and lysosomes similar to transferrin (**Figure 1.16**) [113, 300].

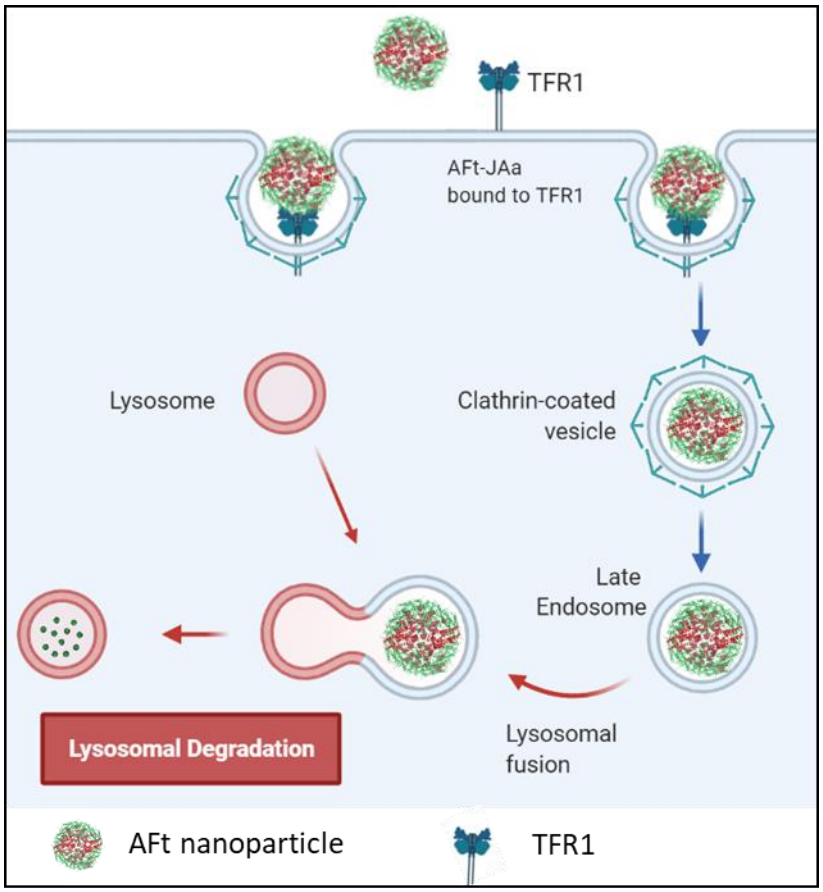


Figure 1.16: Internalisation of apoferritin = AFt into the cells through clathrin-coated pit-mediated endocytosis following its recognition by transferrin receptor 1= TFR1.

Adding to their biocompatibility, biodegradability and selective uptake, which make proteins the most attractive endogenous nanocarriers, the self-assembly property presents interesting opportunities for the encapsulation of different agents inside its hollow core [279, 285, 301-303].

Using the self-assembly method in 2005, Ece H. Simsek et, al. were the first to encapsulate an anti-tumour agent (doxorubicin-HCl) inside AFt [304]. Although doxorubicin is a quite large molecule ~ 544 g/mol, 28 molecules were successfully entrapped inside the AFt core [305]. Subsequently, many successful encapsulation studies have been achieved by exploiting the self-assembly property of AFt at different pH values [266-270]. More recently, the encapsulation of therapeutic agents into AFt core was achieved through "the diffusion method". This was done by exploiting the hydrophilic channels of AFt to entrap small MWt agents [118, 306-309].

To date, a number of studies have been reported to develop AFt as a tumour-targeted NP [44]. Indeed, AFt has been exploited as a nanocarrier for many cancer therapies including; chemotherapy, gene therapy, photothermal therapy and photodynamic therapy [310]. Due to its innate tumour-targeting capability, AFt is superior to other nanocarriers (that depend only on the EPR effect to enhance tumour selectivity), further reducing the undesirable effects of the enclosed agent [273]. In addition to its high stability feature, exploited to enhance the chemical instability of encapsulated agents, AFt has been investigated to enhance poor solubility. This is due to its excellent water solubility signified by its positive charge at neutral pH [311, 312]. Besides doxorubicin, other compounds (synthetic and those isolated from natural sources) have been successfully encapsulated inside AFt, for example, epirubicin, paclitaxel, gefitinib, curcumin and olaparib [306, 312-315].

The AFt surface can be modified chemically or genetically for active tumour-targeting to minimise nonspecific binding. Functionalised AFt may be developed for dual targeting - to TFR1 as well as another protein expressed in tumours (e.g. HER2). This is achievable by modifying the amine groups on the outer surface of AFt and binding it with small molecules [313], antibodies [316], or peptides [314, 317]. Furthermore, an interesting study has shown the possibility of incorporating two anticancer agents (doxorubicin and docetaxel) inside the core of one AFt molecule and their successful intracellular delivery [318]. AFt has also shown its ability to translocate into the nucleus following the DNA damage, thus delivering anticancer agents attempted for DNA targeting [319]. **Table 1.2** shows some recent studies of innate and modified AFt used to overcome some issues related to anticancer agents' utilisation.

Table 1.2: Summary of innate and modified AFt in cancer therapy as a nanocarrier.

AFt used	Advantages	References
Innate AFt	Treat multidrug-resistant tumours with temozolomide, Cu(II), and doxorubicin	[118, 320, 321]
Innate AFt, ERK-Peptide-Inhibitor-Modified Ferritin	Enhance efficacy of temozolomide, paclitaxel, olaparib, Cu(II), and artesunate	[118, 314, 315, 320, 322]
Innate AFt, GKRK-peptide-modified AFt	Facilitate brain-targeted delivery of vincristine sulfate, doxorubicin, and mAbs	[317, 323, 324]
Innate AFt	Enhance chemical stability of curcumin	[312]
Innate AFt	Enhance solubility of 5F 203, and curcumin	[307, 312]

1.7 Aim and objectives of the study

The overall aim of this study was to develop a new therapy with enhanced antitumour activity and reduced toxicity for breast cancer patients, which represents the first leading cause of cancer death in women globally [56]. This can be achieved by delivering existing antitumour agents within an appropriate nano vehicle. As one of the most attractive endogenous nanocarriers, AFt protein was used in our study to encapsulate and deliver JAa to breast cancer cells [279, 285, 301-303]. AFt can be targeted to the tumour tissues due to its recognition by TFR1 which is overexpressed by tumour cells. Like other tumours, breast cancer upregulates TFR1, and while its overexpression can serve as a marker for diagnosis and prognosis, it can also be used as a valuable therapeutic target [125-127]. On the other hand, jerantinines, alkaloids isolated from *T. corymbosa* have been found to display a promising potency against various human cancer cell lines, while evading one of the main obstacles associated with chemotherapeutic agents; MDR conferred by P-gp expression [202, 203, 205-208]. However, the main obstacle facing jerantinines is their poor selectivity and cytotoxicity against non-cancerous cells e.g. MRC-5 fibroblasts [202]. Therefore, the development of AFt as a nanocarrier and delivery agent for JAa has been set as the main purpose of this study.

To achieve this major aim, the research project was undertaken with the following specific objectives:

1. Optimisation of JAa encapsulation into the AFt core using nano-reactor and self-assembly routes. Following encapsulation, characterisation of the new

formulations with respect to protein recovery (PR%), AFt-integrity, stability, size, charge, and MWt. The results associated with this objective are discussed in Chapter 3.

2. Evaluation of targeting distinct molecular subtypes of breast cancer versus non-transformed phenotypes with AFt by determining TFR1 expression in each breast cancer cell line using western blotting and flow cytometry techniques. The results associated with these objectives are discussed in Chapter 4.
3. Evaluation of the effect of AFt encapsulation on the toxicity and selectivity of JAa in treated cell lines by conducting various *in vitro* assays including MTT, viable cell counting and clonogenic assays. In addition, evaluation of the biocompatibility of empty AFt against the selected treated cell lines. The results associated with these objectives are discussed in Chapter 4.
4. Evaluation of the possible molecular targets of JAa and the effect of AFt encapsulation on these targets by investigating their cell cycle perturbation effect, apoptosis-inducing effect and the expression of some proteins that play a role in apoptosis and survival in selected breast cancer cell lines. The results associated with these objectives are discussed in Chapter 5.
5. Investigating the correlation between cellular response to AFt-JAa, cellular expression of TFR1 and uptake of AFt and encapsulated JAa. The results associated with these objectives are discussed in Chapter 4.

2 Materials and methods

2.1 Encapsulation methods

2.1.1 Preparation of apoferritin

AFt preparation method was adopted and modified from the original publication by Granick and Michaelis [298].

Materials

All chemicals were purchased as listed below and used without further purification: horse spleen Ft (Sigma-Aldrich, product code (PC)-1002315752) stored at 4 ºC; freshly prepared sodium acetate buffer (NaOAc, 100 mM, pH 5.5); 98% mercaptoacetic acid (ACROS, PC-125430010) stored at 4 ºC; dialysis bags (Fisherbrand, PC–2115210), with a molecular weight cut-off (MWCO) 3.5 KDa, stored at 4 ºC.

Method

AFt was prepared from Ft by dissolving the iron-core. First, mercaptoacetic acid (2 mL) was added dropwise over 15 min to the freshly prepared NaOAc buffer (2 L). Ft solution (10 mg/mL) was prepared using the same buffer and dialysed for 2 h. Afterwards, the outer buffer system was supplied with additional mercaptoacetic acid (1 mL) and dialysed for an additional 1 h. The dialysis bag was then transferred into fresh NAoAC buffer, and the process was repeated 5 times (over 3 days). The

resulting colourless protein was then dialysed against fresh NaOAc buffer for 24 h (T = 4 ºC) with continuous stirring to remove any mercaptoacetic acid residue. The AFt was then purified using 0.2 mm filters (Minisart), split into 1 mL aliquots, and stored at -20 ºC.

2.1.2 Jerantinine A acetate and stock solution

JAa, a more stable form of JA (**Figure 2.1**), was provided by Dr Kuan-Hon Lim, School of Pharmacy, UNM (University of Nottingham, Malaysia). JAa was reconstituted with Dimethyl sulfoxide (DMSO) to make a 10 mM stock solution. Stocks were then stored at -80 ºC in 10 µL aliquots to avoid freeze/thaw cycles.

2.1.3 Encapsulation of jerantinine A acetate into apoferritin: The nano-reactor route

Encapsulation of JAa inside the core of AFt was achieved using the diffusion methods described earlier with some modifications [118, 307]. First, we tried to encapsulate JAa in different ratios and conditions (see Section 3.3.1). The optimised encapsulation of JAa was performed at a ratio of 1:200 of AFt: JAa (*T* = 4 ºC). First, AFt stock was diluted using NaOAc (100 mM, pH 5.5) to reach a final protein concentration of 2 mg/mL (measured using Bradford assay as described in Section 2.2.1) and kept under continuous stirring. The aliquotes of JAa (10 µL, 10 mM) in DMSO were added at 30 min intervals until the required amount was achieved. After the final addition, the solution was stirred for an additional 30 min. The resulting solution was then purified through Amicon Ultra-4 centrifugal filter (MWCO 30 KDa) for 4 min (4000 rpm) to remove any unencapsulated JAa

molecules. Encapsulation, purification and storing of the formulations were performed at 4 ºC to minimise deterioration of AFt protein and degradation of JAa.

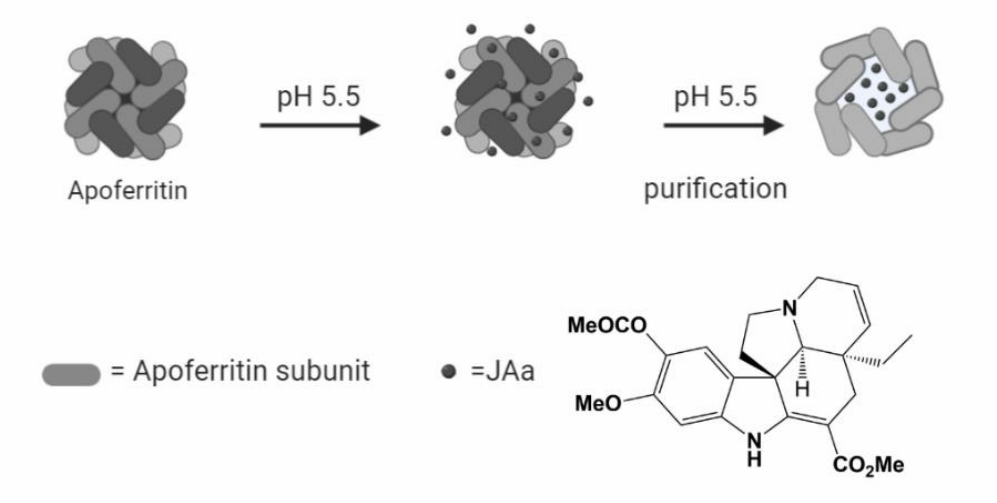


Figure 2.1: Schematic diagram of the nano-reactor encapsulation route of JAa inside the core of AFt protein.

2.1.4 Encapsulation of jerantinine A acetate into apoferritin: The self-assembly route

The self-assembly method was optimised to enhance PR% and EE%. AFt stock was diluted with ultrapure water to a concentration of 2-2.5 mg/mL (see section 2.2.1). The self-assembly route involves two main steps, the disassembly and the re-assembly of AFt. Dis-assembly of AFt to its 24 subunits was achieved at pH 2. The pH of the AFt solution was adjusted by adding HCl solution (1 M) dropwise at 4 ºC. After 30 min of continuous stirring, JAa (10 µL, 10 mM) was added gradually, along with the addition of NaOAc buffer (30 µL, 100 mM, pH 4) every 15 min. The addition of JAa and NaOAc was stopped at pH 4 and when the required ratio of 150 JAa molecules to each AFt molecule was achieved. The resulting solution was stirred continuously at 4 ºC for another 60 min. Full re-assembly of the AFt cage

was achieved at pH 7.4 by adding tris-acetate buffer (100 mM, pH 7.4) at 4 ºC with continuous stirring overnight. Aggregated protein and unencapsulated drug molecules were then purified by centrifuging the solution for 15 min (3000 rpm, 4 ºC) using Amicon® Ultra Centrifugal Filters (MWCO 100 KDa). Lastly, to desalt the protein formulation and to remove any remained unencapsulated JAa molecules, the AFt-JAa formulation was dialysed overnight against tris-acetate buffer (25 mM, pH 7.4) and then stored at 4 ºC (**Figure 2.2**).

The pH of the solution was measured after each addition, and all measurements were done using a Mettler Toledo pH meter. The pH meter was calibrated using a range of Metler Toledo standard buffers (pH: 2.00, 4.01, 7.00, and 10.01) to cover all different pH values used during the encapsulation. The calibration of the pH meter was done before each encapsulation experiment to ensure sensitive and reliable measurements.

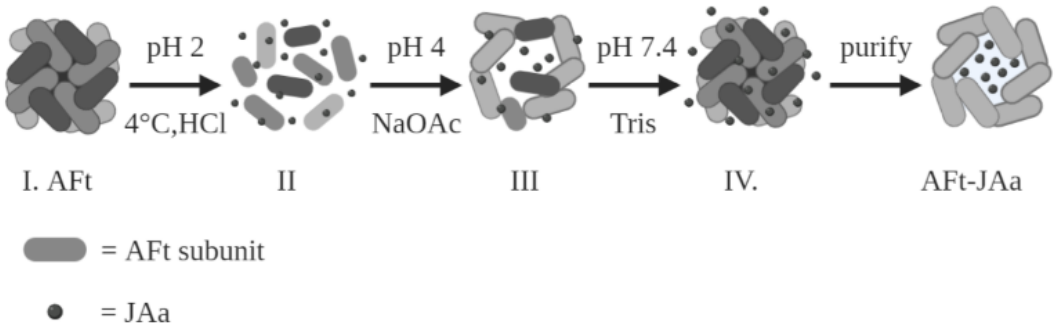


Figure 2.2: Illustration diagram shows the reassembly encapsulation route of JAa inside the core of AFt cage.

2.2 Characterisation methods

Several characterisation methods were used to assess the composition/integrity, size and stability of AFt cage during and after the encapsulation of JAa.

2.2.1 Bradford assay

To equalise the concentration of loaded proteins, the sample concentrations were quantified using the Bradford protein assay [325]. In the Bradford assay, a change in the colour of Coomassie Brilliant Blue G-250 dye upon its binding to a protein causes a shift of colourimetric absorbance. The shift of absorbance (from 465 to 595 nm) is then measured and is proportional to the concentration of protein in the sample [325].

Materials

Bradford reagent (Sigma-Aldrich, PC-B6916) stored at 4 ºC; bovine serum albumin (BSA; VWR, PC-421501J) stored at 4 ºC; ultrapure water (18.2 MΩcm).

Method

The Bradford protein assay was used to measure the concentration of proteins used in this study based on a BSA calibration curve. In a 96-well microtiter plate, 10 µL of 6 serially diluted concentrations (1.0 mg/mL, 0.8 mg/mL, 0.6 mg/mL, 0.4 mg/mL, 0.2 mg/mL, and 0.1 mg/mL) of BSA were diluted in 90 µL of ultrapure water and shaken in a plate shaker (Amersham)® for 1 min. From each dilution, 10 µL was then mixed with 140 µL of Bradford reagent and shaken again for 5 min in dark conditions at room temperature. Absorbance readings at 595 nm were recorded using a Perkin Elmer plate reader followed by the generation of a calibration curve. The absorbance of other proteins of interest was recorded using the same method and their concentration was calculated based on the equation obtained from BSA calibration curves (n = 3, for > 3 replicates). Ultrapure water was used as a negative control in each measurement.

2.2.2 Native polyacrylamide gel electrophoresis

Native polyacrylamide gel electrophoresis (PAGE) was performed to separate proteins based on their shapes and sizes under non-denaturing (non-reducing) conditions [326]. Native PAGE does not give reliable indications of molecular weight, however, changes in detected bands' molecular weight were used to detect any conformational fluctuations in AFt protein resulting from the encapsulation of JAa.

Materials

Gradient native PAGE 4-16% Bis-Tris gel electrophoresis (Invitrogen)® stored at 4 ºC; NativeMark™ Unstained protein standard (Invitrogen)® stored at -20 ºC; TRIS (Sigma-Aldrich, PC-B9754) stored at room temperature; Tricine (Sigma-Aldrich, PC-T0377) stored at room temperature; Coomassie Brilliant Blue G-250 solution (G-BIOSCIENCES, PC-786-498) stored at room temperature.

All buffers used in the native PAGE were pre-prepared and stored at 4 ºC as described in **Table 2.1**. The cathode and anode buffers were diluted to their working concentrations 1X with deionised water (d.H_2O) on the day of the experiment.

Table 2.1: Composition of the cathode, anode and loading buffers used in native PAGE

Buffer used	**10X Cathode buffer, pH 7.0**	**10X Anode buffer, pH 7.0**	**4X loading buffer, pH 6.8 (10 mL)**
Composition	500 mM Tricine; 150 mM Bis-Tris/HCl	500 mM Bis-Tris/HCl	Glycerol (4 mL); 1M Tris-HCl, pH 6.8 (2.4 mL); Bromophenol blue (4 mg); d.H2O (3.1 mL)

The required pH was adjusted using HCl (1 M) and pH measurements were done using a pre-calibrated Mettler Toledo pH meter.

Samples loading and native gel electrophoresis method

Protein samples (30 µg in a final volume of 15 µL) were stained with 5 µL of 4X loading buffer and loaded in the cassette fixed into an electrophoresis tank. After loading the samples, cathode buffer (between gels' compartments), and anode buffer (outside of gels' compartments), the native gel was run at 175 mV for 2 h. Preparation of samples, samples loading, and gel electrophoresis were performed at 4 ºC to keep the protein samples from denaturing. The protein bands were either visualised directly under UV light or after staining with Coomassie Brilliant Blue staining G-250 solution for 1 h.

2.2.3 Sodium dodecyl sulphate polyacrylamide gel electrophoresis

The separation of proteins based on their MWt under denaturing and reducing conditions was performed using sodium dodecyl sulphate (SDS)-PAGE [327].

Materials

Protein MWt markers (Thermo-Scientific, PC–26619) stored at -20 ºC; Tris (Sigma-Aldrich, PC - T6066) stored at room temperature; glycerol (Sigma-Aldrich, PC-G5516) stored at room temperature; β-mercaptoethanol (Sigma-Aldrich, PC-M6250) stored at room temperature and handled under the fume hood; SDS (Sigma-Aldrich, PC-L3771) stored at room temperature; ammonium persulfate (APS, Sigma-Aldrich, PC-A3678) stored at room temperature; acrylamide/bis acrylamide stock solution (Sigma-Aldrich, PC-A2917) stored at 4 ºC; N, N, N', N'-

tetramethylethylenediamine (TEMED, Sigma-Aldrich, PC-T9281) stored at room temperature and handled under the fume hood; gel cassette 1.5 mm (Invitrogen UK, PC-NC2015); isopropanol (Sigma-Aldrich, PC-563935).

Preparation of polyacrylamide gels method

Polyacrylamide gels with different ratios of acrylamide to bisacrylamide (in the resolving gel) were prepared to separate different MWt proteins. The higher the ratio of acrylamide to bisacrylamide, the larger the pore size of the gel, and the higher MWt of protein to be separated [328]. The preparation of any required gel was started with making the resolving gel followed by 5% stacking gel. The resolving gel was prepared following the recipe described in **Table 2.2** based on the required gel ratio. The resolving gel was then poured inside the gel cassette and set for the polymerisation process to complete in 30 min. Isopropanol (~ 100 µL) was added on top of the resolving gel to protect the polymerisation reaction from being inhibited by molecular oxygen. After resolving gel polymerisation, isopropanol was removed and 5% stacking gel (following the recipe described in **Table 2.2**) was poured on top of the resolving gel and covered immediately by a comb. The polymerisation of the gels was initiated by the addition of APS. TEMED was used to stabilise polymerisation.

Table 2.2: Composition of the resolving and stacking gels used in SDS PAGE

Resolving gel				Stacking gel	
Reagent	**8% (10 mL)**	**10% (10 mL)**	**12% (10 mL)**	**Reagent**	**5% (4 mL)**
H2O	4.6	4.0	3.3	**H2O**	2.7
30% w/v acrylamide	2.7	3.3	4.0	**30% w/v acrylamide**	0.67
1.5 M Tris, pH 8.8	2.5	2.5	2.5	**1.0 M Tris, pH 6.8**	0.5
10% SDS	0.1	0.1	0.1	**10% SDS**	0.04
10% APS	0.1	0.1	0.1	**10% APS**	0.04
TEMED	0.006	0.004	0.004	**TEMED**	0.004

Stocks of 4X loading buffer and **10X** running buffer were pre-prepared and stored at room temperature as described in **Table 2.3**. The required pH was adjusted using HCl (1 M) and pH measurements were done using a pre-calibrated Mettler Toledo pH meter.

Table 2.3: Composition of the running and loading buffers used in SDS PAGE

Buffer used	**10X Running buffer, pH 7.0 (500 mL)**	**4X Loading buffer, pH 6.8 (10 mL)**
Composition	Tris (21.2 g); Glycine (72.06 g); SDS (5 g); d.H2O (up to 500 mL)	Glycerol (4 mL); 1M Tris-HCl, pH 6.8 (2.4 mL); Bromophenol blue (4 mg); 0.8 g SDS; d.H2O (3.1 mL)

Samples loading and SDS gel electrophoresis method

Protein samples were mixed at a ratio of 3:1 with the loading buffer (pre-mixed with β-mercaptoethanol at a ratio of 19:1 just before loading with the protein samples). Samples in Eppendorf tubes were heated in a heating block at 95 ºC for 5 min to denature the proteins. After loading the samples (30-40 µg/well, 18 µL) with the molecular marker (5 µL), 1X running buffer was added to the tank and samples were run at 90 V (~20 min) followed by 30-40 min at 140 V. The gel was

then stained with Coomassie Brilliant Blue staining G250 for 1 h or used in western blotting without staining.

2.2.4 Estimation of the protein recovery

The PR% was calculated to assess and optimise the encapsulation method through the reassembly method. The weight of the formulation was obtained before and after the purification step. The protein concentration of the formulation was measured before and after the purification (see Section 2.2.1). The purification of the formulation samples was done using the Amicon Ultra-2 Centrifugal Filter Unit (Millipore®, PC-UFC210024) with MWCO 100 KDa. The protein concentrate was collected, and its recovery was calculated by Equation (2.1):

$$concentrate\ recovery\% = \frac{W_c * C_c}{W_0 * C_0} 100\% \quad (2.1)$$

where W_c is the weight of the formulation after purification, C_c is the concentration of the formulation after purification, W_0 is the weight of formulation before purification and C_0 is the concentration of the formulation before purification.

2.2.5 Encapsulation efficiency and drug loading

EE% is defined as the percentage of drug that is successfully encapsulated in the formulation. While drug loading (DL%) is defined as the amount of drug-loaded inside the NPs per unit weight. EE% and DL% are elementary measurements for drugs encapsulation in NPs [329-332]. The concentration of encapsulated JAa was calculated using a calibration curve of JAa. The absorbance spectra of JAa with

known concentrations (200 µM, 100 µM, 50 µM, 25 µM, 12.5 µM, 6.2 µM, 3.1 µM) were measured using Varian Cary50, UV-Vis Spectrophotometer over a range of wavelengths (200-800 nm) in 0.5 mL quartz cuvette. Subsequently, a calibration curve of JAa with R^2 > 0.99 was generated at measured λ_{max}=330 nm. The absorbance of encapsulated samples was then measured and both EE% and DL% were calculated using Equations (2.2) and (2.3), respectively.

$$EE\% = \frac{molar\ concentration\ of\ encapsulated\ drug}{molar\ concentration\ of\ added\ drug} 100\% \quad (2.2)$$

$$DL\% = \frac{weight\ of\ encapsulated\ drug}{weight\ of\ encapsulated\ nanoparticles(AFt+encapsulated\ drug)} 100\% \quad (2.3)$$

2.2.6 Dynamic light scattering

Dynamic light scattering (DLS) is a powerful analytical tool used to characterise NPs in a solution in terms of their particle size and surface charge [333-335]. In the DLS technique, the detected scattered light in all directions is related to the diffusion characteristics (e.g. size and shape) of the macromolecules. The DLS technique was developed after establishing the relation between the diffusion of moving particles and their radius. This was followed by the Stokes-Einstein relationship (Equation (2.4)) that combines the diffusion behaviour including the speed of particles and the particle size, where the speed of the particles is given by the translational diffusion coefficient, *D*. The Stokes-Einstein equation also includes other parameters that are directly related to the particle movement; the viscosity of the dispersant and the temperature [336].

$$D = \frac{k_B T}{6\pi\eta R_h} \quad (2.4)$$

where D is the translational diffusion coefficient [m²/s], k_B is the Boltzmann constant [m²kg/Ks²], T is the temperature [K], η is the viscosity [Pa.s], R_h is the hydrodynamic radius [m].

Zeta potential (ZP) is the potential at the surface of the hydrodynamic shear plane that can be measured using an electrophoretic field. ZP can be used to describe the electrostatic repulsion between particles in the colloidal solution. This is to assess the charge and stability of nanomaterials; high ZP means high solution stability and a low degree of aggregation. [336, 337]. Generally, particles with ZPs within the range of ±30 mV are considered unstable; in addition, values within the range of ±5 mV are considered unstable, where rapid coagulation or flocculation happen in the solutions [338].

Equipment

ZetaSizer Nano ZS, (Malvern Instruments) equipped with a 633 nm laser at a fixed angle of 173º; folded capillary zeta cell (Malvern, PC-DTS1070); 40 µL cuvette (Malvern, PC-ZEN0040).

Method

The protein concentration in the AFt-JAa formulation and its AFt reference was equalised after Bradford measurements (see Section 2.2.1). Samples were then dialysed against the same buffer (phosphate-buffered saline (PBS) or Tris-acetate). The samples were then diluted in 1:10 with ultrapure water. Samples were filtered to remove dust by 0.2 mm filters before measurement. DLS analyses were carried

out at 25 ºC using a 40 µL cuvette. The full particle size distribution was reported as the volume and number averages of NP, which are modelled from Intensity distribution measurements. ZPs were measured using folded capillary zeta cell and reported by mean ± SD after triplicate internal measurements.

2.2.7 Drug release study

Materials

Slide A-Lyzer® MINI dialysis device (Thermo Scientific, PC-8840, 0.5mL) with MWCO 10 KDa; NaOAc (100 mM) adjusted to pH 5.3 by acetic acid; PBS (pH 7.4)

Methods

The release study was performed to assess the time by which JAa releases from the AFt cage. Release of JAa from the AFt formulation was evaluated in physiologically relevant conditions (T = 37 ºC, pH 7.4) and endosomal and lysosomal relevant conditions (T = 37 ºC, pH 5.3). The formulation (n = 3) was placed into the dialysis device and direct and indirect samples were collected at different time intervals (0 h, 1 h, 3 h, 6 h, and 24 h, as illustrated in **Figure 2.3**). The concentration of the drug was estimated using liquid chromatography-high resolution-MS (LC-HRMS).

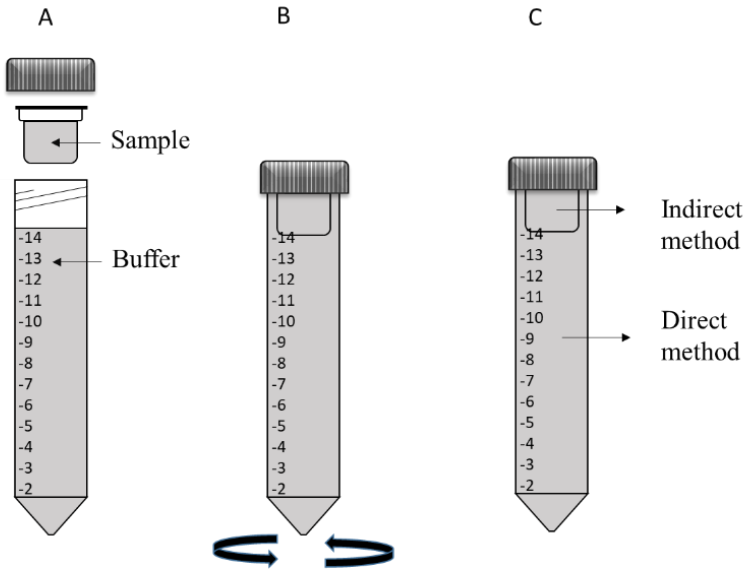


Figure 2.3: Illustration of the release study protocol. **(a)** Samples were placed in the device and dialysed against NaOAc (pH 5.3) or PBS (pH 7.4) that fill the conical tube. **(b)** The device was shaken gently at 37 ºC for 24 h. **(c)** Samples were taken directly (from the conical tube) and indirectly (from the device) at specific times (1 h, 3 h, 6 h, and 24 h) for further LC-HRMS analysis.

For direct samples, the concentration of released JAa was measured using EQMS after samples were taken directly from the outer buffer system. For indirect samples, the concentration of released JAa was estimated after measuring JAa concentrations remaining in the dialysis device. First, samples were treated with 1:5 methanoic acid: methanol to precipitate and open the AFt cage. Samples were then centrifuged (13,000 rpm; 10 min) and the supernatant was measured using EQMS.

2.2.8 Liquid chromatography-high resolution mass spectrometry

Materials

Dionex U3000 UHPLC system (Thermo Fisher Scientific, Hemel Hempstead, UK); ZIC-pHILIC column (4.6 × 150 mm, 5 µm particle size, Merck Sequant, Watford, UK); orbital trap mass spectrometer (QExactive-Orbitrap, Thermo Fisher Scientific, Hemel Hempstead, UK).

Methods

LC-HRMS was performed using Dionex U3000 UHPLC system on a ZIC-pHILIC column. The column was maintained at 45 ºC and a flow rate of 300 µL/min. Mobile phases used were: (A) 20 mM ammonium carbonate and (B) acetonitrile. The gradient started with 20% (A) and increased to 95% (A) over 8 min then the composition was returned to 20% (A) in 2 min at 400 µL/min and then the column was left to re-equilibrate at the initial gradient conditions for 5 min (15 min total time). The injection volume was 5 µL and samples were maintained at 4 ºC during the analysis. An orbital trap mass spectrometer was used in simultaneous ESI+ and ESI- modes for full LC-MS profiling. The operational parameters were: spray voltage 4.5 kV (ESI+), 3.5 (ESI-), capillary voltage 20 V (ESI+), -15 V (ESI-), sheath, auxiliary and sweep gas flow rate were: 40, 5 and 1 (arbitrary unit), respectively, for both modes. Capillary and heater temperatures were maintained at 275 ^{o}C and 150 ^{o}C, respectively. Data were acquired in full scan mode with resolution 70,000 from *m/z* 70-1050.

2.2.9 Stability study

The stability of the AFt-JAa formulation was assessed upon its storage at 4 ºC. DLS was used to measure the changes in the size and the charge of the formulation

over 10 months (see Section 2.2.6). The stability of encapsulated JAa was assessed using a UV-Vis spectrophotometer over 5 weeks of storage (see Section 2.2.5). Particle sizes, ZPs, and JAa concentrations were compared before and after storing at 4 ºC.

2.3 *In vitro* cell culture assays

Cell lines are the most valuable *in vitro* model used for cancer research and drug development studies. Good culture techniques and recommended guidelines are followed to avoid ethical issues associated with *in vitro*, *in vivo* and clinical studies [339, 340]. Here, we used different breast cancer, ovarian cancer, and non-transformed cell lines to conduct our studies.

2.3.1 General cell culture

Materials

All cell lines used were purchased from American Type Culture Collection (ATCC), and subcultured according to the ATCC protocol (**Table 2.4**); T25 cm^2 tissue culture flasks with 0.2 µm vented cap (Corning, PC–3056); RPMI-1640 medium (Sigma-Aldrich, PC-R8758), stored at 4 ºC; minimum essential medium (MEM, Sigma-Aldrich, PC-M2279), stored at 4 ºC; McCoy's 5a medium modified (Sigma-Aldrich, PC-9309) stored at 4 ºC; Dulbecco's Modified Eagle's Medium (DMEM) - high glucose (Sigma-Aldrich, PC-D5671) stored at 4 ºC; DMEM/F12 (Invitrogen, PC-11330-032) stored at 4 ºC; heat inactivated foetal bovine serum (FBS, Sigma-Aldrich, PC-F9665), stored at -20 ºC; penicillin-streptomycin (Sigma-Aldrich, PC-

P4333), stored at -20 ºC; horse serum (Invitrogen, PC-16050-122) stored at 4 ºC; epidermal growth factor (EGF, Sigma-Aldrich, PC-E1257) stored at -20 ºC; hydrocortisone (Sigma-Aldrich, PC-H0888) stored at -20 ºC; insulin (Sigma-Aldrich, PC-I6634) stored at -20 ºC; sodium bicarbonate (Sigma-Aldrich, PC-S8761) stored at 4 ºC; non-essential amino acids (NEA, Sigma-Aldrich, PC-M7145) stored at 4 ºC; HEPES (Sigma-Aldrich, PC-H0887) stored at 4 ºC; L-glutamine (Sigma-Aldrich, PC-G7513) stored at 4 ºC; PBS (Sigma-Aldrich, PC- P4417), stored at room temperature; trypsin-EDTA (Sigma-Aldrich, PC-T4174), stored at -20 ºC; freezing medium (95% FBS and 5% DMSO), freshly prepared; cryopreservation vials (Thermo-Scientific, PC-10440613).

Cell lines

For breast cell lines, one of each molecular subtype was chosen based on their genetic expression classification by Perou et al., and Sorlie et al., [70, 71]. MCF-7 for luminal A, BT-474 for luminal B, MDA-MB-468 for TNBC basal-like, SKBR-3 for HER2 overexpression, MDA-MB-231 for TNBC claudin-low, and MCF-10A for a non-transformed epithelial phenotype. In addition, MRC-5 (normal lung foetal fibroblasts) were used for comparison purposes, as a model representing a non-tumour cell line. (**Table 2.4**). All cell lines were also tested regularly for mycoplasma infection (see Section 2.3.2).

Table 2.4: Cell lines used and their supplemented media

Cell line	Clinical property [76]	Subtype and primary features [71, 76]	Culture media
MCF-7	Breast-invasive ductal carcinoma	Luminal A (strongly ER+ and PR+)	RPMI-1640 supplemented with 10% FBS
BT-474	Breast-invasive ductal carcinoma	Luminal B (lower ER, PR expression, and HER2+)	DMEM-high glucose supplemented with 10% FBS
SKBR-3	Breast-adenocarcinoma	HER2 overexpression (ER–, PR–, and HER2+)	McCoy's 5a supplemented with 10% FBS
MDA-MB-468	Breast-adenocarcinoma	Basal-like (EGFR+ and TNBC – ER-, PR-, HER2-)	MEM supplemented with 10% FBS
MDA-MB-231	Breast-adenocarcinoma	Claudin-low (EGFR+, ER-, PR-, HER2-)	MEM supplemented with 10% FBS
MCF-10A	Breast-Fibrocystic disease	Non-transformed epithelial phenotype	DMEM/F12 supplemented with • 20 ng/mL EGF • 2.5% Horse serum • 0.5 mg/mL Hydrocortisone • 10 µg/mL insulin • 1% Penicillin-streptomycin
MRC-5	Normal	lung foetal fibroblasts	MEM supplemented with • 10% FBS • 1% 1 M HEPES • 1% 200 mM L-glutamine • 1% 0.1 mM NEA • 7.5% Sodium bicarbonate • 1% Penicillin-streptomycin

2.3.1.1 Passaging of cells

Subculture of cells in T25 cm^2 culture flasks was done using their appropriate media (**Table 2.4**). Cells were split continuously upon reaching 70% confluence (**Figure 2.4**). That was achieved by passaging all cell lines once (or twice) a week. Complete growth medium was aspirated, and sterile PBS (1 mL) was used to wash the cells. Trypsin-EDTA solution (1mL; 1X) was added to cover all cells, which were then incubated at 37 ºC for several minutes until the cell layer had detached. Complete culture medium (3 mL) was added to the cell suspension to deactivate

the trypsin-EDTA solution. Subsequently; the cell suspension of MCF-7 (0.1 mL), BT-474 (0.8 mL), MDA-MB-468 (0.5 mL), SKBR-3 (0.5 mL), MDA-MB-231 (0.4 mL), MCF-10A (0.2 mL) and MRC-5 (0.1 mL) were transferred to new T25 cm^2 flasks with their appropriate media (7 mL). Flasks were labelled with the date, name, and passage number and then incubated at 37 ºC in an atmosphere of 5% CO_2 and humidity of 95% incubator until the next passaging date. All cell lines were passaged a maximum of 30 times to minimise phenotypic drift. All cell culture techniques were carried out in class II biological safety cabinet. The cabinet and all other tools used were decontaminated using 70% industrial methylated spirit (IMS) before use.

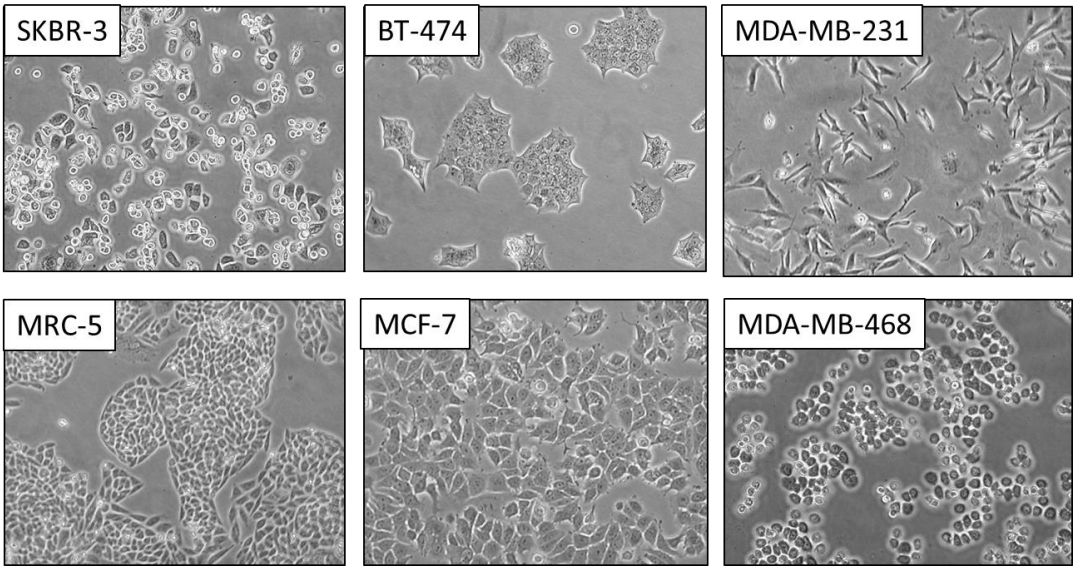


Figure 2.4: Morphological appearance of cell lines used in this study in phase-contrast microscopy at confluency 50-80%.

2.3.1.2 Freezing and defrosting cells

Cells were cryopreserved in liquid nitrogen for long term storage. Cells at 70% confluence in T25 cm^2 culture flasks were washed with pre-warmed PBS (1 mL),

trypsinised using 1X trypsin-EDTA (1 mL), collected after deactivation of trypsin with complete growth medium (7 mL). Subsequently, the cell suspension was centrifuged at 1200 rpm for 5 min and the supernatant layer was discarded. Cell pellets were then re-suspended in 1 mL of freshly prepared freezing medium (95% FBS and 5% DMSO) and transferred to labelled sterile cryogenic vials. Vials were kept overnight at -20 ºC, followed by 1 day at -80 ºC before being transferred to the liquid nitrogen at -196 ºC for long term storage.

To defrost cells, vials were retrieved from liquid nitrogen. The cryovial was quickly but not completely defrosted in a water bath (pre-heated at 37 ºC) for not more than 30 seconds. The cryovial was then decontaminated with 70% IMS. The thawed cells were re-suspended in T25 cm^2 culture flasks with 9 mL of pre-warmed complete growth medium suitable for each cell line (**Table 2.4**).

2.3.2 Mycoplasma assay

Microbial contamination is an important widespread problem when working with cell lines. Mycoplasma is serious and rapidly-transmissible contamination that affects the genotype, phenotype and behaviour of cells. Data produced from experiments conducted using contaminated cells are invalid and should be repeated using non-infected cells [341]. For this reason, cells need to be checked for mycoplasma infection regularly with sensitive tests such as polymerase chain reaction (PCR)-based assays [340].

Materials

Mycoplasma assays for qPCR Kit (Microsart®, PC-SMB95-1005) were stored at 4 ºC before opening and -20 ºC after opening. The kit contains Mycoplasma Mix, Positive Control, Rehydration Buffer and PCR grade water.

Methods

Reconstitution of the mycoplasma kit was done before preparing the samples. First, the mycoplasma mix and positive control were centrifuged at 13000 rpm for 5 sec. The mycoplasma mix was then diluted with 600 µL of rehydration buffer, while the positive control was diluted by adding 300 µL of PCR grade water. Both were kept at room temperature for 5 min, vortexed at 13000 rpm for 5 sec, aliquoted, and then stored at -20 ºC to be used on the day of testing.

Cells at 90 to 100% confluence in T25 cm^2 culture flasks were ready for mycoplasma testing. Culture media were retained for subsequent testing of floating cells. Cells were washed with PBS, detached from flasks by trypsinisation, then combined with the non-adherent cells from the culture flasks. Culture media and cells were tested together to detect both extra- and intracellular mycoplasma. A sample of cell suspension (500 µL) was then transferred to a sterile Eppendorf tube. All samples were subsequently heated for 10 mins at 95 ºC on a heat block. Samples were then centrifuged briefly at 13000 rpm for 5 sec to pellet the cell debris. The supernatants were then transferred to new Eppendorf tubes and stored at 4 ºC to analyse within a month.

In the PCR reaction tubes, the mycoplasma mix (23 µL) was mixed either with PCR grade water (2 µL); for negative control tubes, or with positive control DNA (2 µL); for positive control tubes, and 2 µL of pre-prepared cells to be tested. PCR tubes

were briefly centrifuged before loading. Samples were run in 45 cycles; each cycle is started with a denaturing stage (95 ºC for 30 sec), followed by annealing (55 ºC for 30 sec) and extending stage (60 ºC for 45 sec). The internal amplification control was detected at 610 nm (ROX™ channel) and the mycoplasma-specific amplification was detected at 520 nm (FAM™ channel). Cycle threshold (Ct) values were then automatically obtained to detect positive from negative samples.

2.3.3 Western blot

Western blotting is a semi-quantitative analysis technique used to detect the expression of specific proteins in cell lysates. The recognition of the protein of interest depends on its binding with a specific matched antibody [342, 343]. The technique consists of several steps:

2.3.3.1 Preparation of protein lysates

Materials

Nonidet-P40 (NP40) lysis buffer was pre-prepared and stored at 4 ºC and contains: 100 µL NP40 (Fluka, PC-74385) stored and handled under the fume hood; NaCl (1.5 mL, 1 M); Tris (500 µL, 1 M, pH 8.0); d.H_2O (7.9 mL); 1 tablet of protease inhibitors (Roche, PC-05892791001); 1 tablet of phosphatase inhibitors (Roche, PC-04906845001).

Methods

Cells at a density of 1 x 10^5 were seeded in 6 well plates and allowed to attach overnight. Cells were treated with the required concentrations of the test

compounds and incubated at 37 ºC, 5% CO_2 for desired exposure times. Subsequently, growth medium/floating cells were aspirated and collected in pre-labelled falcon tubes and kept on ice. Cells were then trypsinised, deactivated with their respective pre-collected growth media, and centrifuged at 1200 rpm for 5 mins, 4 ºC. The pellets were re-suspended in 10 mL of ice-cold PBS and centrifuged as before. Cell pellets were then lysed using ice-cold NP40 lysis buffer (100 µL) and transferred to labelled 1.5 mL Eppendorf tubes and kept on ice for 30 mins with flicking from time to time. Afterwards, Eppendorf tubes were centrifuged at 13,300 rpm for 10 mins at 4 ºC. The supernatants (lysates) were then collected and transferred to new labelled Eppendorf tubes and stored at -80 ºC.

2.3.3.2 Protein separation methods

Cell lysates thawed on ice, each containing 40 µg protein (see Section 2.2.1) in a volume of 20 µL were run using the SDS PAGE (see Section 2.2.3).

2.3.3.3 Protein blotting

Following gel electrophoresis, separated proteins were transferred to a nitrocellulose membrane using a transfer buffer and a transfer system.

Materials

Nitrocellulose membrane (Bio-Rad, PC-162-0115); blotting paper (Whatman, PC -3030 672); 10X Transfer buffer was pre-prepared and stored at room temperature. The Transfer buffer contained: Tris Base (12.11 g); Glycine (56.3 g) and d.H_2O (500

mL). The transfer buffer was diluted to its working concentration of 1X with (350 mL d.H_2O, 50 mL 10X transfer buffer, and 100 mL methanol).

Methods

Following SDS-PAGE electrophoresis, the blots were transferred onto a solid nitrocellulose membrane by the semi-dry technique. The nitrocellulose membrane and eight chromatography papers in a comparable size to the gel were cut and placed in the transfer buffer for 5 mins. The gel was then placed over the nitrocellulose membrane and assembled between 4 chromatography papers on each side. Protein transfer was carried out using the Trans-Blot Turbo Transfer System (Bio-Rad) under the following conditions: 2.5 A, 25 V, 45 min).

2.3.3.4 Membrane blocking and incubation of antibodies

Materials

Non-fat milk (10%; 5.0 g non-fat dried milk in 50 mL TBS-T); Tween-20 (Fisher Scientific, PC-10485733) stored at room temperature; 1X Tris-buffered saline – Tween-20 (TBS-T) was adjusted to pH 7.6 by HCl (1 M) and stored at room temperature. TBS-T contains: 0.5 mL Tween-20 (Fisher Scientific, PC-10485733); NaCl (8.0 g); Tris (2.42 g) and d.H_2O (1 L).

Antibodies: The antibodies (Abs) used in this study are summarised in **Table 2.5** along with supplementary information detailing dilution, in addition to suppliers and catalogue numbers.

Table 2.5: Antibodies used in western blot.

Antibody	Dilution used	Supplier	Catalogue number
Primary antibody (1° Ab)			
Anti- GAPDH (housekeeping gene)	1:1000	**Cell Signaling Technology**	5174
Anti-TFR1			13113
Anti-HER2			2242
Whole PARP			9532
Cleaved PARP			5625
Mcl-1			4572
Bcl-2			2876
PLK-1			4513
Anti-TFR2		Abcam	ab80194
Anti- SCARA5		R&D systems	MAB4754
Secondary antibody (2° Ab)			
anti-rabbit/mouse IGg	1:4000	Dako	PO448 / PO447

Methods

After protein transfer, the nitrocellulose membrane was blocked using TBS-T containing 10% non-fat milk for 1 h at room temperature with gentle shaking followed by washing 3 times for 5 mins with TBS-T. The blocking was done to prevent non-specific binding of antibodies to the membrane in the subsequent step. To identify the expression of certain proteins on the nitrocellulose membrane, after washing, the membrane was incubated overnight with a specific 1º Ab away from light with gentle shaking at 4 ºC (**Table 2.5**). The membrane was washed 3 times with TBS-T for 5 mins each before incubating with an appropriate 2° Ab for 1 h at room temperature with gentle shaking. This was followed by washing the membrane with TBS-T, 3 times, as before.

2.3.3.5 Detection and analysis of proteins bands

Following the final washing step, the nitrocellulose membrane was soaked in a 1:1 mixture of Enhanced chemiluminescence (ECL) western blotting detection reagent

(GE Healthcare Life Sciences; Amersham ECL, PC-RPN2209) reagent (1.5 mL) for 5 min at room temperature away from light to enable detection. The membrane was scanned using a densitometer (GS-800, Bio-Rad) in grayscale using the quality one software version 4.6.5. Densitometry analysis was carried out to quantify the intensity of the bands of the proteins of interest using FIJI software. Densitometry was initiated by detecting the linear line of the proteins of interest followed by subtracting the background and then normalising their intensities to the housekeeping gene (GAPDH). Statistical analysis was performed using Graph Pad Prism v.9.1.0 and the student t-test was conducted to assess differences between samples.

2.3.4 The 3-(4, 5-dimethylthiazol-2-yl)-2, 5-diphenyltetrazolium dye reduction assay, cell growth inhibition assay

The 3-(4, 5-dimethylthiazol-2-yl)-2, 5-diphenyltetrazolium (MTT) assay is a robust, reproducible, easy and quick *in vitro* growth inhibitory / cytotoxicity assay that allows a large number of tests to be carried out at the same time. The active mitochondrial enzymes (of viable cells) convert the MTT reagent into violet formazan crystals, the intensity of which (following solubilisation) correlates to the number of viable cells [344].

Materials

MTT (2 mg/mL in sterile PBS, Sigma-Aldrich, PC-M2128), stored at 4 ºC in the dark for 1 month; DMSO (Sigma-Aldrich, PC-D5879), stored at room temperature;

EnVision 2105 Multimode Plate Reader (PerkinElmer); 96 well microtiter plates (Thermo scientific).

Methods

Cells at 70-80% confluence were trypsinised, resuspended in their appropriate growth medium, and counted using a haemocytometer.

Cells with a density of 3-5 x 10^3 per well were seeded in 96 well microtiter plates. In triplicate, 180 µL of the desired cell density from the cell suspension was transferred using a multichannel pipet. All columns were seeded with cells except for columns 1 and 12 which were supplied with 180 µL of growth medium only. A separate plate comprising 2 columns (16 wells) of cells from each cell line used was seeded at the same cell density to measure the absorbance of cells at the time of treatment (T0). Plates were incubated at 37 ºC in an atmosphere of 5% CO_2 and humidity of 95% for 24 h. Afterwards, 50 µL of pre-warmed MTT reagent was added to the T0 plate and incubated for 3 h. Thereafter, the growth medium with MTT reagent was carefully aspirated from wells and the formed purple MTT-formazan crystals were dissolved with 150 µL DMSO. The absorbance values were recorded at 570 nm using Perkin Elmer Envision plate reader after shaking for 5 min using a plate shaker (Amersham). At the same time, all other plates were treated with the desired test agent along with appropriate negative and positive controls. When testing encapsulated agent, the naked agent was considered the positive control, and the empty capsules (AFt vehicle) were considered the negative control. The test agent was diluted in a complete growth medium to prepare 8 different concentrations at 10X the final concentrations. Cells were fed

with 20 µL of the desired test agent to get a final 1X concentration, while control wells were fed with medium only (20 µL) and incubated for 72 h, 48 h, or 24 h. After the desired incubation time the absorbance values were recorded after adding MTT and DMSO as described with T0 plates. A DMSO control was also performed to exclude its inhibition effect on cells. Growth inhibition curves were represented using Graph Pad Prism v.9.1.0. Test agent concentration required to achieve 50% growth inhibition, GI_{50}, values were calculated from measured absorbance using Equations (2.5) and (2.6):

$$AGI_{50} = \frac{A_1 - A_0}{2} + A_0 \tag{2.5}$$

$$GI_{50} = \left(\frac{A_H - AGI_{50}}{A_H - A_L} * (C_H - C_L) \right) + C_L \tag{2.6}$$

where AGI_{50} is the absorbance of GI_{50}, A_1 is the absorbance in control (untreated) wells, A_0 is the absorbance at T0, A_H is one absorbance higher than AGI_{50}, A_L is one absorbance lower than AGI_{50}, C_H is one concentration higher than GI_{50}, C_L is one concentration lower than GI_{50}.

2.3.5 Cell counting assay

To validate the results obtained from the MTT assays, *in vitro* viable cell counting assays were conducted. The reduction of MTT reagent and thus the absorption spectrum of MTT-formazan may be affected by cell number and the pH of tested samples. Failing in controlling these conditions during MTT assay can result in underestimation of chemo-sensitivity [345]. MTT assay can also show false

positive results upon the treatment with natural products with intrinsic reductive potential [346].

Materials

0.4% Trypan blue solution (Gibco, PC-15250061)

Methods

Cells were seeded at a density of 2 x 10^4 for SKBR-3, MDA-MB-231 and MCF-7 in 6 well plates and incubated overnight. On the next day, cells were treated with JAa, AFt-JAa (0.2 µM JAa), AFt (0.0017 µM) or appropriate media alone for 48 h. Cells were harvested using trypsin-EDTA (300 µL), pooled together with the appropriate medium (700 µL). Cell suspensions were then stained with trypan blue with a ratio of 1:1 and viable cells counted using a haemocytometer. The trypan blue azo dye is used to label dead cells exclusively being able to permeate the compromised cell membrane and stain cells dark blue [347]. The percentage of viable cells was then calculated, decreasing number of viable cells reflected growth inhibition and toxicity caused by the test agent. Thus, this assay was conducted to corroborate MTT assay results.

2.3.6 Clonogenic assay

The clonogenic assay is a cell sensitivity assay used to evaluate the ability of single cells to survive a brief challenge with a test agent and to form progeny colonies [348]. The clonogenic assay is often adopted to discriminate between test agent cytotoxicity (reduced colony numbers) and cytostasis (smaller colonies, but little/no reduction in colony numbers) [349].

Materials

Methylene blue (0.05%) in a 1:1 solution of d.H_2O: MeOH stored at 4 ºC; 6-well plates (Corning Costar)®

Methods

Cells were harvested and counted as described; following optimisation, SKBR-3 (700 cells), BT-474 (700 cells), MCF-7 (250 cells) and MDA-MB-468 (400 cells) were seeded in 6 well plates and allowed to attach overnight. Thereafter, BT-474 cells were treated for 72 h, while other cells were treated for 48 h with JAa, AFt-JAa (0.2 µM and 0.4 µM JAa), AFt (0.0033 µM; equivalent to the highest concentration of AFt used in this assay) and appropriate medium alone. Afterwards, cells were washed with sterile PBS (1 mL) and supplied with fresh pre-warmed medium (3 mL). Cells were then incubated at 37 ºC in an atmosphere of 5% CO_2 and humidity of 95%. Assays were terminated when colonies containing ≥ 50 cells had formed in the control wells (between 7-30 days). Colonies were then washed twice with PBS (1 mL), fixed with 100% methanol (1 mL) for 15 min, and stained with 0.05% methylene blue (0.5 mL) for 15 min. colonies were counted to calculate their percentage plating efficiency and survival fraction (*SF*%). plating efficiency (*PE*%) and *SF*% were calculated using equations 2.7 and 2.8 respectively and results were presented in Figures prepared using Graph Pad Prism v.9.1.0.

$$PE\% = 100 * \frac{Number\ of\ colonies\ counted}{Number\ of\ cells\ plated} \quad (2.7)$$

$$SF\% = 100 * \frac{PE\ of\ treated\ sample}{PE\ of\ control} \quad (2.8)$$

2.3.7 Flow cytometry

Flow cytometry is a powerful and widely used laser technique to evaluate single cells suspended in a solution. In the flow cytometry technique, the analysis of scattered visible light or the fluorescence of pre-stained cells provides unique knowledge for individual cells (events) in cell biology studies [350].

2.3.7.1 Cell cycle analysis

The effect of JAa and its encapsulated form to perturb each phase of the cell cycle was evaluated by measuring the DNA content in thousands of individual cells. Propidium iodide staining is used to stain the DNA of cells, therefore, fluorescence is proportional to the DNA content in each cell, thereby indicating the cell cycle phase of each cell under scrutiny [351, 352]. Cell cycle is divided into three main subpopulations if the cells are in exponential growth status. The main cell cycle phases detected are G1/G0 phase (2N and known as diploid), the S phase (> 2N and known as hyperploid) and the G2/M phase (4 N and known as tetraploid) [353]. In addition to pre-G1 (< 2N and known as hypoploid) and super G2 (> 4N number and known as hypertetraploid or aneuploid). As tetraploid cells have twice the amount of DNA of diploid cells, the detected fluorescence intensity of DNA stains is collected on a linear scale. The signals are then processed with special programs with appropriate algorithm capable of precisely fitting the population peaks into cell cycle phases by using either parametric or nonparametric approaches [354]. Triton was used as a detergent to allow the penetration of propidium iodide through the cell membrane. Ribonuclease A was used to remove double-strand RNA and inhibit its interaction with propidium iodide [355].

Materials

Hypotonic fluorochrome solution was prepared in PBS to contain:

- 50 µg/mL Propidium iodide (Sigma-Aldrich, PC-81845) stored at 4 ºC.
- 0.1 mg/mL ribonuclease A (Sigma-Aldrich, PC-R4642) stored at -20 ºC.
- 0.1% v/v Triton X-100 (Sigma-Aldrich, PC-X100) stored at room temperature.
- 0.1% w/v sodium citrate (Sigma-Aldrich, PC-1613859) stored at room temperature.

Methods

Cells, at a density of 1 x 10^5 per well were seeded in 6 well plates and allowed to attach overnight. The cells were then treated with JAa, AFt-JAa (0.2 µM and 0.4 µM JAa), AFt (0.0033 µM) and appropriate media alone for 48 h. After treatment, Cells were trypsinised and, once detached, pooled together with the appropriate medium (and floating cells). Cells were then pelleted in a Beckman Coulter Allegro centrifuge at 1200 rpm for 5 min at 4 ºC. The pellets were then washed with ice-cold PBS (1 mL) and pelleted again to remove the remaining medium. The pellets were then re-suspended in cold hypotonic fluorochrome solution (0.5 mL) and incubated overnight in the dark, 4 ºC. The samples were run on a Beckman Coulter FC500 flow cytometer using channel FL2 and events (10,000 or 20,000) were gated to count only single cells. Cell cycle analysis was done using FlowJo version 10 and the statistical analysis was performed using Graph Pad Prism version 9.1.0.

2.3.7.2 Annexin V-FITC and propidium iodide apoptosis assays

The annexin V-FITC/ propidium iodide assay is used to distinguish between early and late apoptotic, and non-apoptotic (e.g., necrotic cells). Annexin V-FITC is used to bind to the phosphatidylserine (PS) phospholipid on the outer plasma membrane of apoptotic cells. While propidium iodide is used to bind to the DNA of necrotic cells after penetration through the porous late apoptotic/necrotic cell membranes [356].

Materials

Annexin V-FITC apoptosis detection kit (BD Pharmingen, PC-556547) stored at 4 ºC. The kit contains:

- FITC-annexin V.
- Propidium iodide staining solution.
- Binding buffer 10X (diluted in d.H_2O to make 1X).

Methods

The cells were seeded, treated, harvested, and pelleted as described previously for the cell cycle assay (Section 2.3.7.1). After the pellets were washed with ice-cold PBS and pelleted again, each sample was re-suspended in 1X annexin binding buffer (100 µL) and annexin V-FITC (5 µL). The samples were vortexed and kept in the dark at room temperature for 15 min. Afterwards, annexin binding buffer (400 µL; 1X) and propidium iodide solution (10 µL) were added to each tube, vortexed, and kept in the dark for another 10 min to be analysed within 1 h of preparation. The samples were analysed by Beckman Coulter FC500 flow cytometer using channels FL2 and FL3 and events were gated to count only single cells (20,000

events per sample were analysed). Quadrant plot analysis was evaluated using Kaluza software v.2.1 and its statistical analysis was performed using Graph Pad Prism v.9.1.0.

2.3.7.3 Assessment of TFR1 expression

Accurate quantitative flow cytometry analysis was performed to assess TFR1 expression levels on the surface of studied cell lines [357]. The analysis was done after labelling the TFR1 on the cell surface with human phycoerythrin (PE)-conjugated anti-CD71 that can be detected by flow cytometry.

Materials

Human PE-conjugated anti-CD71 (Invitrogen) prepared at a concentration of 2% in blocking buffer; blocking buffer (1% FBS diluted in PBS); paraformaldehyde 3.7% (Sigma-Aldrich, PC-P6148) diluted in PBS.

Methods

The cells at a density of 1 x 10^5 for each cell line were seeded in 6 well plates. The cells were allowed to attach overnight, harvested by trypsin, pooled together with the appropriate medium (and floating cells) as described before. The cell suspension was then pelleted in a Beckman Coulter Allegro by centrifuging at 1200 rpm for 5 min, 4 ºC. Pellets were washed with PBS (1 mL) and pelleted again. The pellets were resuspended in the blocking buffer (1 mL) and incubated for 30 min at room temperature and pelleted as before. To remove any remaining blocking buffer, pellets were washed with PBS (1 mL) and pelleted again. Cells were then labelled with anti-CD71 primary antibody (1º Ab, 80 µL) for 45 min at 4 ºC, washed

with the blocking buffer and pelleted again. Cells were fixed with formaldehyde (500 µL) for 5 min at room temperature, pelleted again, and resuspended in PBS (1 mL) for analysis. The samples were analysed by Beckman Coulter FC500 flow cytometer using channels FL2 and events were gated to count only single cells (10,000 events per sample were analysed). The shifts in signals of labelled cells compared to the control (unlabelled cells) were evaluated using FlowJo version 10. Statistical analysis was performed using Graph Pad Prism version 9.1.0.

2.3.7.4 Cellular uptake studies

Cellular uptake of human apoferritin

The uptake study of human AFt (H-AFt) was performed to correlate cellular uptake to the TFR1 expression on the surface of selected cell lines. Cells were seeded in 12-well plates at a density of 5 x 10^4 and allowed to attach overnight. Thereafter, the cells were exposed to 5-carboxyfluorescein-conjugated H-AFt at a concentration of 40 nM (equivalent to the highest concentration of AFt used in the MTT assay) and incubated at 37 ºC for the desired time (1 h, 2.5 h, 4 h, and 24 h). The treated cells and their controls (untreated cells) were then harvested after trypsinisation and pelleted in a Beckman Coulter Allegro centrifuge at 1200 rpm for 5 min, 4 ºC. The cell pellets were then washed with PBS (1 mL) before pelleting and fixing with 3.7% formaldehyde/PBS (0.5 mL) for 5 min at room temperature. Cells were pelleted again and suspended in PBS (0.5 mL) before analysis. The samples were analysed by Beckman Coulter FC500 flow cytometer using channels FL1 and events were gated to count only single cells (10,000 events per sample

were analysed). Signal graphs and their shifts were evaluated using FlowJo version 10. Statistical analysis was performed using Graph Pad Prism v.9.1.0.

- 5-carboxyfluorescein-conjugated H-AFt was kindly provided by Lenny Ferreira, Biodiscovery Institute, University of Nottingham, UK.

2.3.8 Cellular uptake of free and encapsulated JAa

To correlate cellular uptake of AFt-encapsulated agent to the detected enhanced activity, SKBR-3, MDA-MB-231, BT-474 and MCF-7 cells at a density of 2 x 10^6 were exposed to JAa, AFt-JAa (0.4 µM JAa), AFt (0.0033 µM) or appropriate media alone for 72 h (*n* = 6). After treatment, growth medium/floating cells were collected (1 mL) for all treated conditions (*n* = 6), frozen down promptly, and stored at -80 ºC for further extracellular samples` preparation. For intracellular samples` preparation, media was removed from six dishes and cells were washed with pre-warmed PBS (3 mL). The cells were then quenched with pre-cooled methanol (1 mL, ≤ - 48 ºC), scraped, and transferred into pre-cooled tubes (4 ºC). The cell extracts were vigorously vortexed for 1 h and then centrifuged in HERAEUS-Fresco 17 centrifuge (Thermo Election Corporation) at 13300 rpm for 10 min at 4 ºC. The supernatants were transferred into pre-cooled tubes and completely dried under vacuum using Jouan vacuum concentrator. The samples were then reconstituted with methanol (70 µL) and centrifuged again. The supernatants were transferred into pre-labelled auto-sampler vials and stored at -80 ºC before analysis using LC-HRMS. For extracellular samples preparation, pre-collected spent media samples were thawed on ice and centrifuged at 13300 rpm for 10 min at 4 ºC. Supernatants (250 µL) were mixed with precooled methanol (750 µL, -20 ºC) and incubated for

20 min (-20 ºC) to precipitate proteins. the samples were centrifuged at 13,300 rpm for 10 min at 4 ºC, and supernatants were transferred into pre-labelled auto-sampler vials and stored at -80 ºC before analysis.

2.3.9 Measurement of reactive oxygen species

ROS are highly reactive radicals, ions or molecules that derived from oxygen and are necessary for normal signal transduction [358, 359]. However, Uncontrolled high levels of ROS may damage proteins, DNA and sometimes contribute to tumourigenesis [360]. Measuring the change in the cellular levels of ROS in cancer cells following the treatment is valuable, as some chemotherapeutic agents excessively increase the intracellular ROS levels which lead to cell cycle arrest and thus kill cancer cells [361].

Hydrogen peroxide (H_2O_2) is the most eminent ROS that regulates the cell cycle, and its detection in biological systems is important to provide a better understanding of several pathological events [362]. Moreover, a change in H_2O_2 levels can reflect an overall change in ROS levels [363]. Measuring the levels of ROS was done using the ROS-GloMT H_2O_2 kit (Promega) ® kit. The kit contains H_2O_2 substrate that reacts with H_2O_2 in cell culture to produce a luciferin precursor. Upon adding the ROS-Glo™ substrate detection solution, the luciferin precursor is converted to luciferin which reacts with the provided Ultra-Glo™ luciferase to produce a luminescent signal that is proportional to the level of H_2O_2 in the cells.

Materials

96 opaque white plates (Corning, PC-353296); ROS-Glo H_2O_2 assay kit (Promega, PC-G8820) stored at -20 ºC. The kit contains: H_2O_2 substrate (40 µL,10 mM); H_2O_2 substrate dilution buffer (2 mL); Lyophilised luciferin detection reagent; Reconstitution buffer (10 mL); D-cysteine (100 µL, 100X); Signal enhancer solution (100 µL).

Method

Cells were seeded in an opaque white 96-well plate with a density of 5 x 10^3 and a volume of 70 µL. Following the attachment, cells were treated with 10 µL of JAa, AFt-JAa (0.4 µM JAa), AFt (0.0033 µM) and appropriate media alone for 24 h. Subsequently, a freshly diluted H_2O_2 substrate (125 µM) was made using a chilled H_2O_2 substrate dilution buffer. For the final 6 h of treatment, cells were treated with the freshly prepared H_2O_2 substrate solution (20 µL per well). Freshly prepared ROS-Glo™ substrate detection solution (mixture of 1 mL reconstituted lyophilised luciferin detection reagent with 10 µL of D-cysteine and 10 µL of signal enhancer solution) was added 20 min before sample readings with a volume of 100 µL per well. Luminescent signals were measured using a Perkin Elmer plate reader and statistical analysis was performed using Graph Pad Prism v.9.1.0.

2.4 Statistical analyses

Data were evaluated using Graph Pad Prism version 9.1.0. Representative Figures are shown as mean ± standard deviation (SD), except for flow cytometry represented by median ± SD. T-test, one and two-way ANOVA statistical analyses

were used, and Sidak's multiple comparisons test was used to assess significant differences with control samples and defined as * ($P < 0.05$), ** ($P < 0.01$), *** ($P < 0.001$), **** ($P < 0.0001$). Further comparison between naked JAa and its encapsulated form was done and defined and shown in brackets. All experiments were repeated ≥ 3 times with internal replicates of $n \geq 3$.

3 Encapsulation of jerantinine A acetate into apoferritin

3.1 Introduction

AFt is a nanoscale spherical protein [279, 298, 299, 301], with outer and inner diameters of 12 nm and 8 nm, respectively. Due to its recognition by cellular TFR1 [113] that is overexpressed by tumourigenic tissues [373, 374], AFt has been considered a possible drug delivery vehicle. The encapsulation into AFt has been performed through two main methods: diffusion (nano-reactor route) [118, 306-309] and self-assembly methods [375-379], which could suffer from low yields [375, 380]. To date, there are no established general AFt-encapsulation protocols, necessitating protocol optimisation for each encapsulated agent. This presents limitations to the translation of AFt as a clinical drug delivery system (DDS) [310]. However, AFt has beneficial stability, biodegradability and biocompatibility, hence was chosen to achieve targeted delivery and to address the putative cytotoxicity of jerantinines. The activity of AFt encapsulated JAa was then assessed in non-cancerous as well as breast carcinoma cell lines.

3.2 Chapter aims

- Optimise the encapsulation route of JAa into the AFt core using both the nano-reactor and self-assembly methods, specifically to enhance the reassembly yield/ PR%.
- Evaluate the protein integrity, size, and charge for the AFt-JAa produced using the reassembly route.
- Study the storage stability of AFt-JAa formulations.
- Assess the release of JAa from the AFt cage under physiologically relevant conditions.
- Validate the optimised self-assembly method by encapsulating other Large MWt agents such as VCR and rhodamine B (RB).

3.3 Results and Discussion

3.3.1 Encapsulation of JAa through the nano-reactor route

3.3.1.1 The theory of optimisation

The encapsulation of JAa into horse spleen AFt through the nano-reactor route was established and optimised taking into consideration the theoretically calculated pKa of JAa (~7). According to the Henderson–Hasselbalch equation [381], > 99% of JAa molecules are ionised at a pH of two units lower than its calculated pKa. Thus, the encapsulation was performed at pH 5.5 to allow the protonation of the amino group in JAa molecules. We theorised that positively charged JAa molecules would be attracted to the negatively charged AFt interior and enhance the encapsulation [382]. Moreover, compared to physiological conditions (pH ~7.4), the more acidic pH of 5.5 will lead to relaxation of the AFt capsule and might further facilitate in-diffusion JAa through ionic channels in the AFt [380].

3.3.1.2 Optimisation of the nano-reactor method

The following parameters were considered in addition to changing the pH of the solution during the encapsulation process: 1) the volume of added JAa, 2) the time intervals at which JAa was added, 3) the temperature of stored AFt before encapsulation and 4) the molar ratio of JAa to AFt.

In Trial A, JAa (20 µL, 10 mM) was added gradually every 15 min to a solution of AFt (~2.5 mg/mL) in a ratio of 1:200 (AFt: JAa) at *T* = 4 ºC. The DLS measurements were then used to assess the hydrodynamic size of the AFt before and after the encapsulation. The results for samples prepared in Trial A are presented in **Figure 3.1**.

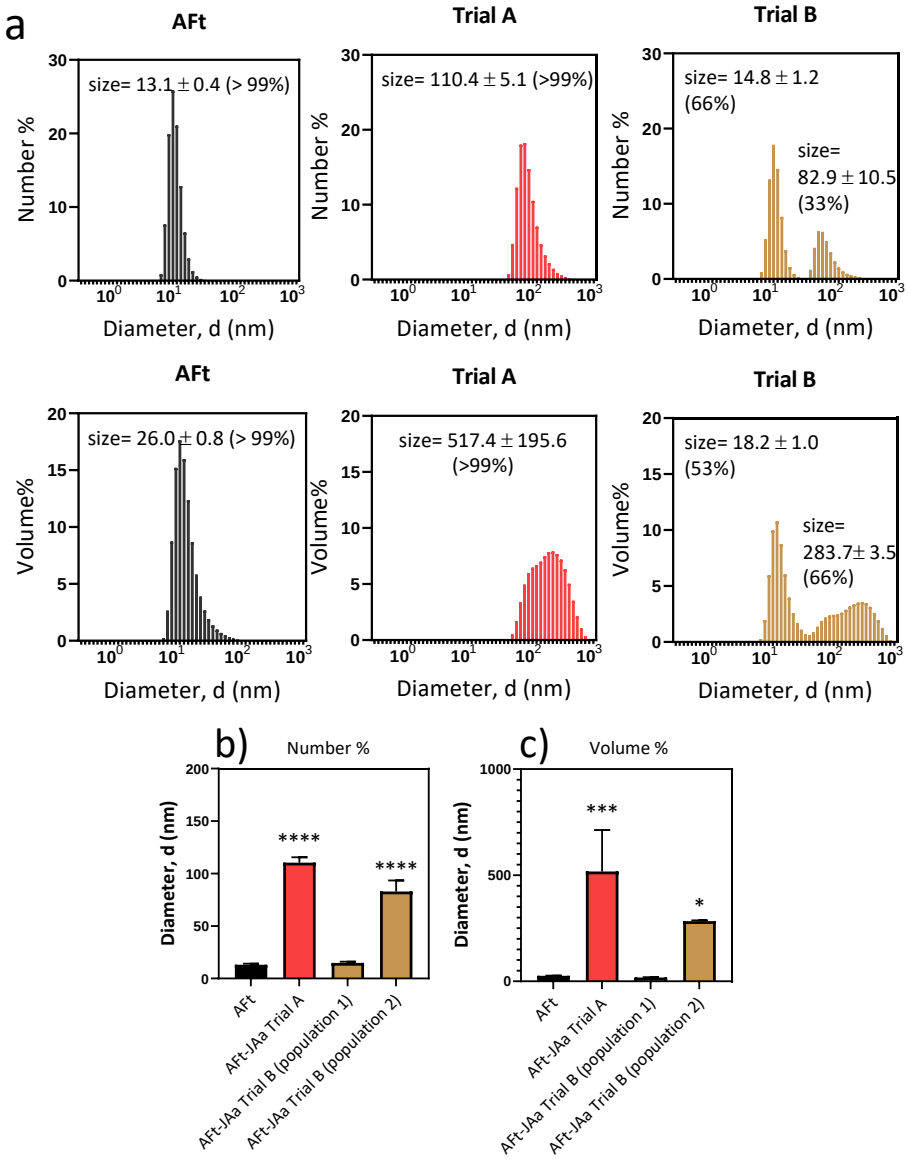


Figure 3.1: **(a)** DLS data recorded for AFt alone and AFt-JAa produced in Trial A and Trial B using the nano-reactor route. **(b)** Native AFt stock was used as a control to evaluate the changes in the nanoparticle size after the encapsulation. Hydrodynamic sizes of all studied agents were estimated from the DLS

measurements by number and **(c)** volume ± SD for 3 repeats. Significant differences are expressed as *P < 0.05, ***P < 0.001 and ****P < 0.0001.

After JAa-encapsulation, the hydrodynamic size of AFt increased from ~13 nm to ~110 nm and from ~26 nm to ~517 nm, as assessed by number and by volume averages, respectively (**Figure 3.1**). The significant increase of the particle size after the encapsulation of JAa ($p < 0.001$) indicates aggregation/precipitation of the protein in this formulation. Although some precipitation is commonly observed for small NPs and polymer-based NPs [236, 310, 380], further optimisation is needed to minimise this aggregation.

In Trial B, JAa was added after longer intervals and in lower volumes (10 µL, 10 mM, every 30 min). We reasoned that longer times intervals might be needed for JAa to enter the AFt capsule through its hydrophilic channels. This method resulted in two populations observed in the DLS studies with ~ 66% (by number) and ~53% (by volume) of the NPs with sizes comparable to that expected for the AFt (12 nm) (**Figure 3.1**). Hence, JAa likely needed more time to diffuse through small channels into the AFt cavity (~ 0.3-0.5 nm) [383]. Allowing more time for diffusion would have reduced the possible unwanted intramolecular and intermolecular interactions which were reflected by marked reduction of aggregation/ precipitation of AFt-JAa. However, over 30% of the population was still significantly larger than the expected size of AFt as reported by both number ($p < 0.001$) and volume averages ($p < 0.05$).

In Trial C, The AFt stock was used directly after defrosting on ice to reduce the precipitation/aggregation of the final formulation. Moreover, in this Trial, higher

ratios of JAa to AFt were used in the encapsulation process: molar ratios of AFt: JAa = 1:400 and 1:800. The integrity and size of the final formulations were assessed using native PAGE and DLS measurements respectively (**Figure 3.2**). The hydrodynamic sizes measured for the formulations with higher AFt: JAa ratios of 1:400 and 1:800 are $d_{AFt\text{-}JAa}$ = 10.7±2.8 nm and 14.4±1.1 nm, respectively, comparable to that of AFt alone d_{AFt} = 12.1±0.4 nm. DLS measurements by number revealed that >99% of the population has average size comparable to that expected for AFt, hence showing benefits from using freshly defrosted AFt stock.

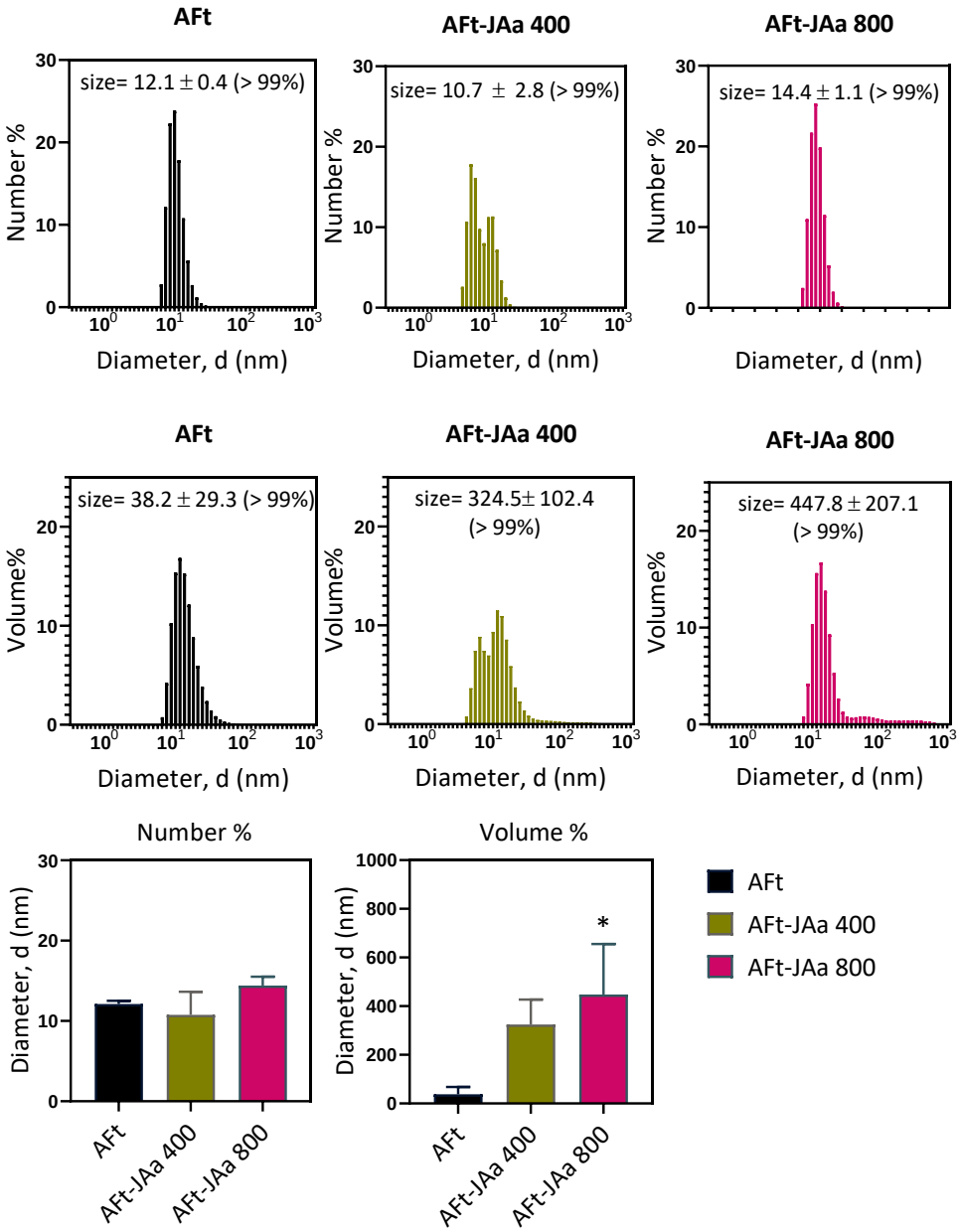


Figure 3.2: (a) DLS data recorded for AFt alone and AFt-JAa produced in Trial C in different ratios (1:400; 1:800) using nano-reactor route. **(b)** Native AFt stock was used as a control to evaluate the changes in the nanoparticle size after the encapsulation. Hydrodynamic size of all studies agents, estimated from the DLS measurements by number and **(c)** volume ± SD for 3 repeats. Significant differences are expressed as *P < 0.05.

Native PAGE was used to evaluate the integrity of the AFt protein in non-denaturing conditions [384]. The native PAGE revealed the presence of a band at 480 KDa for both 1:400 and 1:800 (AFt: JAa) formulations, similar to that observed for the AFt control (**Figure 3.3a**). The charge and stability of nanoformulations were assessed by measuring their ZP values [336, 337]. In NaOAc buffer (100 mM, pH 5.5), ZP was measured to be $\zeta = -12.9 \pm 0.7$ mV and -12.3 ± 1.0 mV for the ratio of 1:400 and 1:800, respectively, which is comparable to that of AFt alone $\zeta = -12.4 \pm 1.0$ (**Figure 3.3b**).

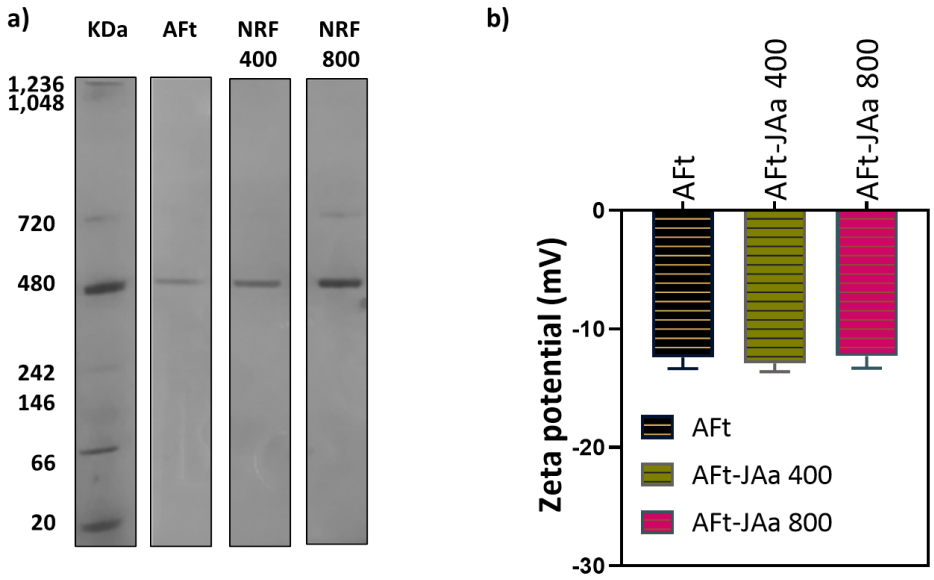


Figure 3.3: Characterisation of the integrity of AFt alone and AFt-JAa produced in Trial C in different ratios (1:400; 1:800) using nano-reactor route. (**a**) Using (4-16%) native PAGE and **(b)** ZPs. Data are reported as mean ± SD and show no significant difference.

Comparable MWt, size and ZP for AFt encapsulated JAa give convincing evidence that the integrity of AFt cage was preserved. Despite these promising results, the DLS measurements revealed larger hydrodynamic sizes by ~7-fold for 1:400 and ~10-fold for 1:800 formulations compared to AFt alone (**Figure 3.2**). The higher

volume average sizes with AFt: JAa ratios (1:400 and 1:800) suggest that some aggregation is still taking place in these formulations. In agreement, the ZP measurements of AFt-JAa formulations ~-12 mV, suggest problems with dispersion stability. Particles with ZPs within the range of ±30 mV are usually considered unstable [338]. This instability indication can be due to the pH change in the encapsulation solution. It has been reported previously that the isoelectric point (PI) of AFt is 4.1- 5.1; the point at which proteins carry both negative and positive charges and thus tend to aggregate [385]. As the nano-reactor encapsulation was performed at pH 5.5 (near the PI), we envisage that the un-encapsulated (excess) JAa molecules could interact with AFt and further reduce its stability within its PI value.

Additionally, another possible reason for aggregation is related to excess JAa molecules in the solution, as a greater proportion of the particles with size expected for AFt was observed for the lower ratio of AFt: JAa = 1:400. To assess this, encapsulation was performed using a lower molar ratio of 1:200, which is discussed below.

3.3.1.3 Characterisation of AFt-encapsulated JAa through the optimised nanoreactor route

To further enhance the stability of the final formulation, Trial D was performed with molar ratio of AFt: JAa = 1:200. The AFt stock was used immediately after defrosting on ice. JAa (10 µL, 10 mM) was added gradually, every 30 min, until the required ratio was obtained. Encapsulation was performed at 4 ºC. To further

enhance its stability, the final formulation was dialysed against PBS at pH 7.4 (outside the PI range of AFt).

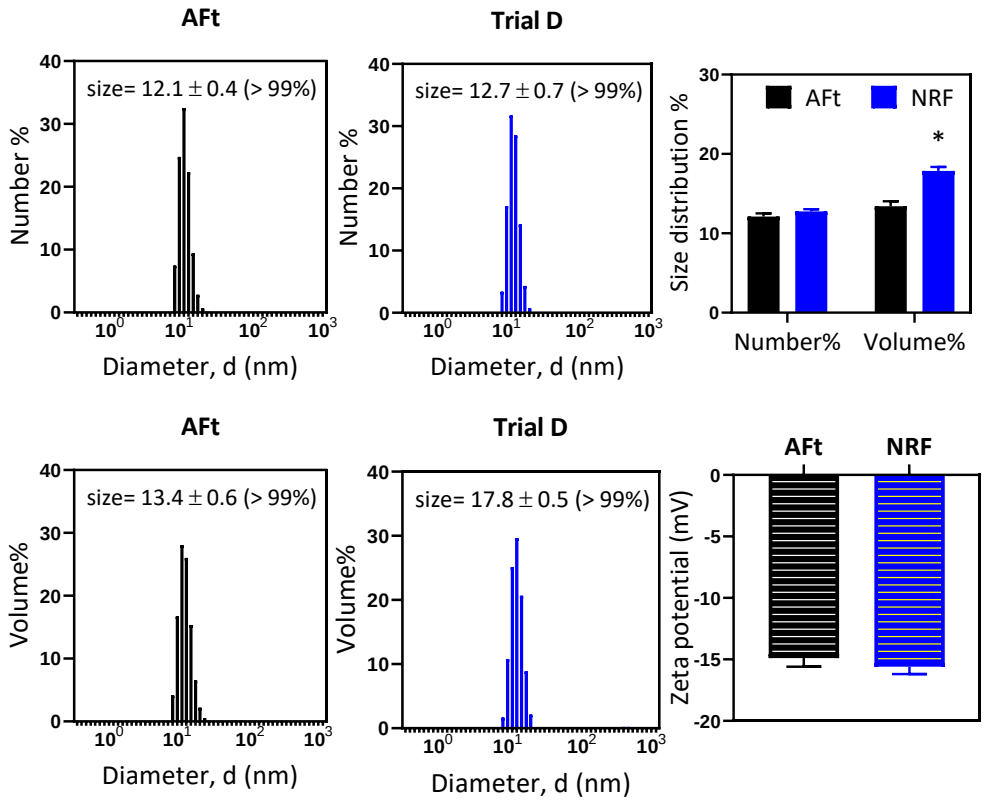


Figure 3.4: DLS data recorded for AFt alone and AFt-JAa nano-reactor formulation produced in Trial D. Native AFt stock was used as a control to evaluate the changes in the NPs' size and ZPs after the encapsulation. Hydrodynamic size of all studied agents, estimated from the DLS measurements by number and volume. Data are reported as mean ± SD for 3 repeats and no significant differences.

The DLS results of the optimised nano-reactor route formulation (**Figure 3.4)** show comparable size for AFt before (d_{AFt} = 12.1 ± 0.4 nm) and after the encapsulation ($d_{AFt\text{-}JAa}$ = 12.7±0.7 nm), as reported by number averages. The hydrodynamic size reported by volume shows an increase from d_{AFt} = 13.4±0.6 nm to $d_{AFt\text{-}JAa}$ = 17.8 ± 0.5 nm. Interestingly the volume average size of AFt-JAa at a ratio of (1:200) was ~17-fold and ~24-fold smaller than the size of AFt-JAa produced with molar ratios

of 1:400 and 1:800, respectively. This indicates that lowering the ratio of JAa during the encapsulation and retaining the formulation outside its PI value were beneficial and significantly enhanced the stability ($p < 0.0001$).

ZPs studies were performed in PBS (pH 7.4) and comparable values were measured for AFt, $\zeta = -14.9 \pm 0.7$ mV, and AFt-JAa, $\zeta = -15.6 \pm 0.6$ mV (**Figure 3.4**). The reduction in the measured ZP from ~ -12 mV at pH 5.5 (near the PI of AFt) to ~-15 mV at pH 7.4 (outside the PI range of AFt) provides evidence of enhanced formulation stability at pH 7.4. It might be argued that at a pH = 7.4, the net charge of the AFt outer surface is negative, which can enhance its binding to free positive JAa molecules. However, the physiological pH is slightly higher than the theoretically calculated pKa of JAa (~7) and none of the JAa molecules is expected to be protonated. These results suggest that optimal storage of the final formulation is at physiological pH.

To further assess the integrity and composition of AFt protein before and after the encapsulation, AFt protein was separated using PAGE under non-denaturing (using native PAGE) and denaturing (using SDS PAGE) conditions as described in Sections 2.2.2 and 2.2.3. Comparable bands' MWt (~480 KDa) and composition of encapsulated AFt with native AFt were demonstrated by native and SDS PAGE respectively (**Figure 3.5**).

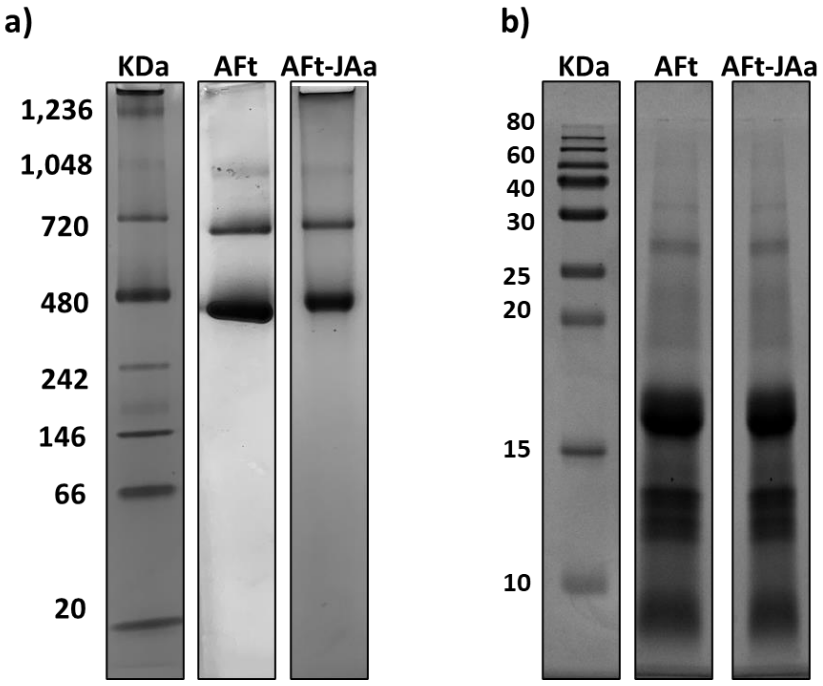


Figure 3.5: **(a)** Blue (4-16%) polyacrylamide native gel electrophoresis of AFt-encapsulated-JAa (AFt-JAa) through the nano-reactor route and its AFt control, the AFt band is shown at 480 KDa. **(b)** Sodium dodecyl sulfate-polyacrylamide gel electrophoresis (SDS-PAGE) on 15% polyacrylamide gel stained by coomassie blue G250.

Subsequently, all formulations produced using different molar ratios (Trial C and Trial D) were assessed for EE% and DL% values (see Section 2.2.5). Absorption of JAa at 330 nm was measured (**Figure 3.6a**) and its integrated intensity was calibrated to the amount of JAa. A calibration curve (**Figure 3.6b**) was used to quantify AFt-encapsulated JAa.

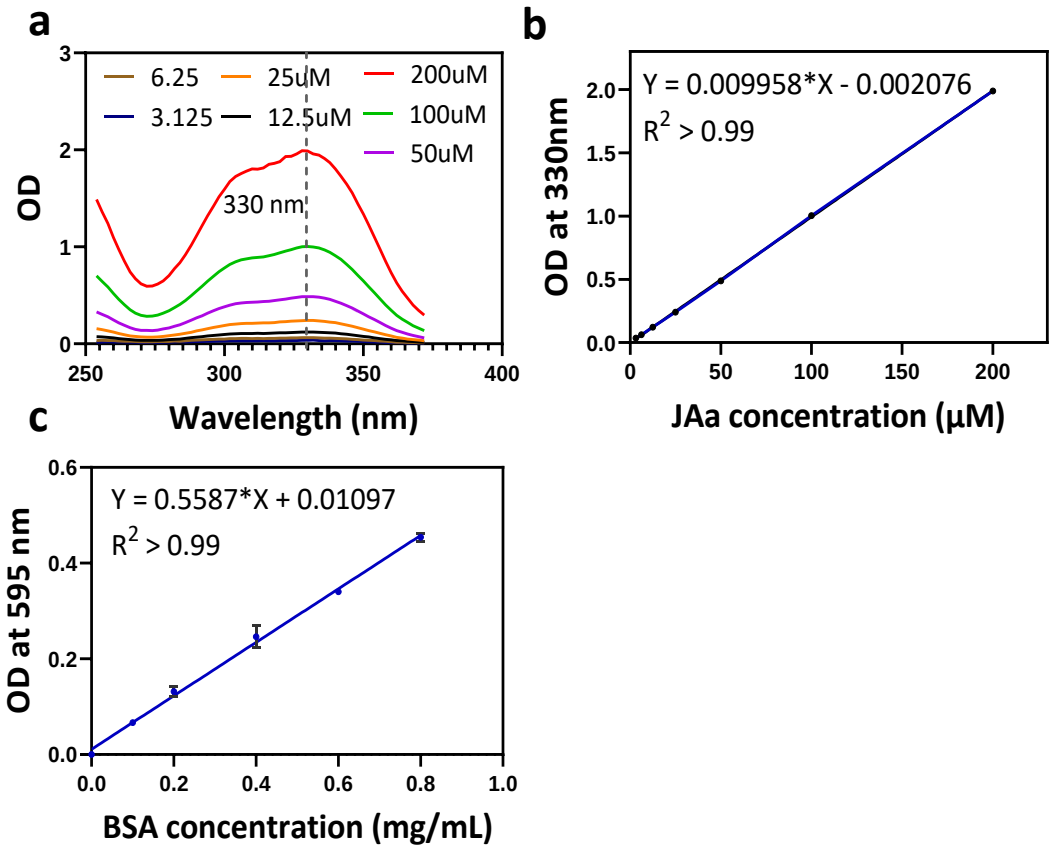


Figure 3.6: UV-Vis spectrophotometer data. **(a)** Absorbance spectra of JAa at different concentrations; maximum absorbance (λ_{max}) of JAa was detected at 330 nm. **(b)** The standard curve of JAa at λ_{max}. **(c)** Standard curve of BSA measured using Bradford assay. Measurements are reported as the mean of absorbance ± SD for > 3 repeats.

Our results indicate that the nano-reactor route resulted in the encapsulation of 118, 161 and 399 molecules of JAa from added 200, 400, and 800 molecules per cage of AFt, respectively (**Table 3.1**).

Table 3.1: Drug encapsulation efficiency (EE) and drug loading (DL) of JAa encapsulated in AFt at three different ratios through the nano-reactor route (*n* = 2).

	AFt: JAa molar ratio		
	1:200	**1:400**	**1:800**
Encapsulation efficiency (EE)%	59 ± 10	40 ± 6	50 ± 5
Drug loading (DL)%	10 ± 1.5	13 ± 2	27 ± 2

No. of molecules encapsulated per AFt cage	118 ± 20	161 ± 26	399 ± 41

The highest EE% = ~59% was achieved with 1:200 ratio, followed by ~50% for 1:800 ratio and ~ 40% for 1:400 ratio. The trend of the EE% and DL% does not increase with increasing JAa ratio as expected, thus, further investigation was needed. To assess if this was related to the presence of excess un-encapsulated JAa in the solution, different filtration times were used to remove the un-encapsulated JAa. Tabersonine (a natural product precursor of JAa) was used as a model in this experiment due to JAa's stock limit [201]. Tabersonine and JAa possess the same structural backbone with lateral dimensions of 0.97 x 0.96 nm and 1.26 x 0.96 nm, respectively as shown in the 3D model (**Figure 3.7**). This, suggests that JAa and tabersonine, which have similar sizes, diffuse into, and are released from the AFt cage with comparable time profiles. A ratio of 1:200 (AFt: tabersonine) was mixed and purified immediately. Samples from the mixture were collected during the process (0 min, 2 min, 4 min, 6 min, 8 min and 10 min), and the release pattern of un-trapped tabersonine molecules is illustrated in **Figure 3.7.** The release profile of tabersonine (similar to the release profile of JAa observed in our previous trials) shows a plateau between 8 and 10 min of filtration. The graph shows that ~ 40% of the test compound was still inside the AFt after 4 min of spinning filtration at 4000 rpm (using 30 K filters); time used to purify JAa after AFt-encapsulation using the nano-reactor route. Therefore, we conclude that the time to remove un-encapsulated JAa should be increased to ~ 10 min.

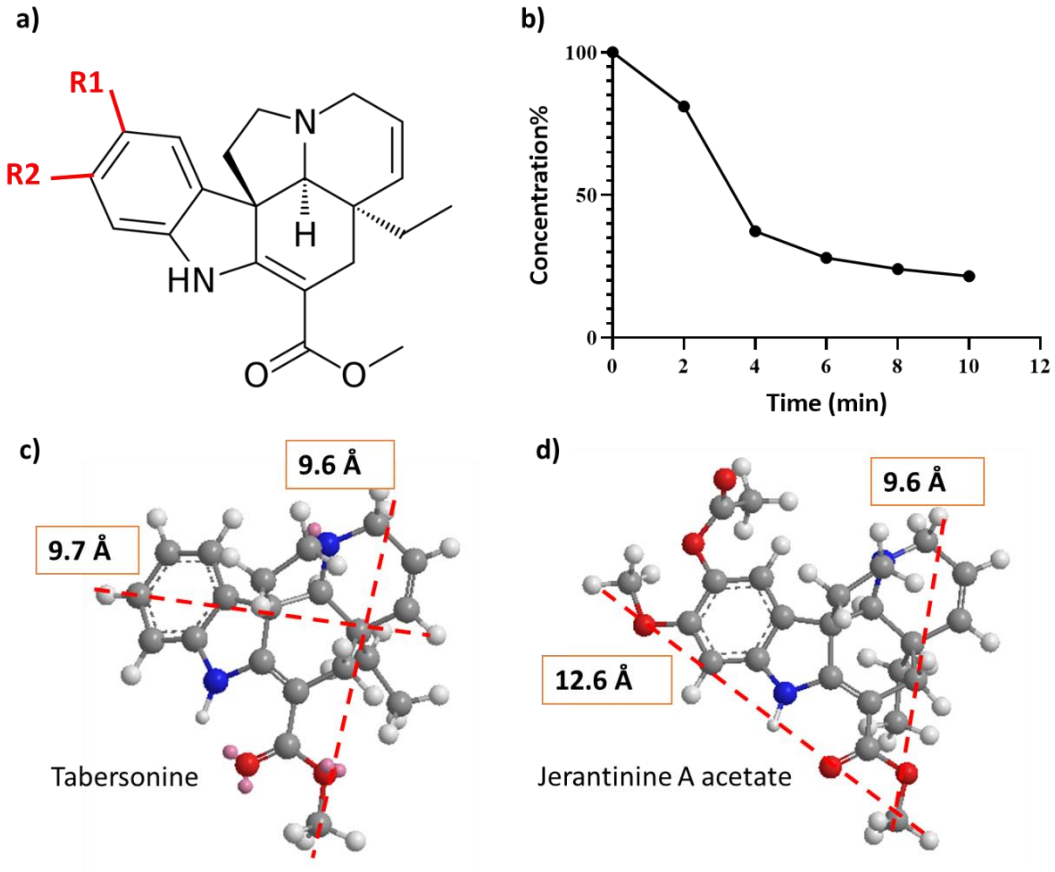


Figure 3.7: Evaluation of the time needed to remove free (un-trapped) JAa molecules from the formulation using tabersonine as a model. **(a)** The shared structure of JAa and tabersonine is shown in black, where R1: MeOCO, R2: MeO for JAa and R1: H, R2: H for tabersonine. **(b)** The concentration of tabersonine remaining entrapped with AFt at different filtration times using ultracentrifugation filters at 4000 rpm is represented as mean ± SD (*n* = 3). **(c)** Tabersonine in the 3D model with lateral dimensions of (0.96 X 0.97 nm). **(d)** The 3D model of jerantinine A acetate (JAa) with estimated lateral dimensions of (0.96 X 1.26 nm) using 3D ChemDraw.

Our results corroborate the findings of the previous encapsulation using the nano-reactor route, that this method has a minimum effect on the composition/integrity of AFt cage [118, 308]. Our optimisation succeeded in reducing the precipitation associated with the small NPs [386]; however, a small fraction of aggregated sample was still detected by DLS (~ 17.8 ± 0.5 nm as measured by volume) (**Figure 3.4**).

Despite the promising results and advantages of the nano-reactor method, the question remains whether JAa was efficiently entrapped into the core of AFt or not. Taking into account the estimated dimensions of JAa (0.96 X 1.26 nm), JAa diffusion through the AFt's pores (0.3-0.4 nm) is challenging [387]. Although Yang *et al.* succeeded in using this method for maltose (approximate dimension 1.3 nm), they used the proton NMR relaxation method and ferric ions which served as a paramagnetic relaxation agent to achieve this encapsulation [309]. The majority of reported successful encapsulations through the nano-reactor route were achieved for relatively small MWt (< 250) agents, such as antitumour benzothiazoles and temozolomide [118, 307], or agents that possess lateral dimensions ≤ 0.3 nm e.g. gefitinib [306]. Therefore, these findings strongly support investigating the self-assembly method to encapsulate JAa to further decide which route to adopt for JAa encapsulation.

3.3.2 Encapsulation of JAa through the self-assembly route

3.3.2.1 The theory of optimisation

To ensure successful entrapment of JAa inside the core of AFt, the self-assembly property of AFt was also exploited. In this method, AFt is disassembled into its sub-units and re-assembled using pH change. However, because of the low yield of the reassembled AFt (Re-AFt) formulations, the optimisation of the self-assembly route was required to encapsulate JAa [310, 375, 380].

3.3.2.2 Optimisation of the self-assembly method

Optimisation of this route was carried out after examining several published self-assembly methods. To ensure reliability, In these studies, horse spleen-AFt was used for the encapsulation. Many agents were successfully encapsulated using different dis-assembly methods as summarised in (**Table 3.2**).

Table 3.2: A summary of published self-assembly methods

	Cargo				
	Epirubicin [388]	**Verapamil** [389]	**Vincristine** [317]	**Doxorubicin-HCl** [304, 375]	**Neutral red, platinum anticancer drugs, and Desferrioxamine** [379, 390-392]
Concentration of AFt	1 mg/mL	3.7 mg/ mL	10 mg/ mL	2.5 mg/mL	10-50 mg/mL
Disassembly method (at pH 2)	HCl (1M) for 20 min at 8 ºC	HCl (0.1 M)	HCl (0.1 M)	Glycine acetate buffer for 5 min on ice	HCl (1M) for 20 min
Reassembly method (at pH 7.4)	One step (1S); Direct addition slowly to pH 7.4 using NaOH (1 M), stirred for 2 h at room temperature (RT)	1S; Direct addition slowly to pH 7.4 using NaOH	1S; Direct addition slowly to pH 7.4 using NaOH (0.1 M)	Two steps (2S); slowly to pH 4 with Trizma-base solution (4 M). followed by dialysis with Trizma-acetate buffer (20 mM) overnight	1S; NaOH
Purification method	Dialysis with PBS (25mM, pH 7.4, 24 h) at RT	NA	Dialysis against 0.9% NaCl solution	Purified through the reassembly method	Centrifugation
Yield	NA	NA	NA	58% and 64% with and without cargo respectively	NA

The self-assembly methods summarised in **Table 3.2** were compared. The clear differences between the methods used are seen, such as concentration of AFt

used, disassembly and reassembly methods, solution, and time, in addition to the purification method and time, and thus support the importance of the validation and optimisation required for this route.

The encapsulation was performed at 4 ºC, to avoid deterioration of the protein and seven different parameters were considered in the optimisation process:

3.3.2.2.1 Evaluating the disassembly methods used to dissociate the AFt cage

Disassembly of the AFt protein is the first step in the self-assembly method. Under extreme conditions (outside the range of pH 2-10) AFt is dissociated into its 24 subunits [282]. In horse spleen AFt, the dissociation will produce two H-chain (composed of 182 amino acids) and 22 L-chain (composed of 174 amino acids) [275]. Here, the dissociation was performed under acidic conditions (pH 2) comparing two methods described previously: using (1) HCl [317, 379, 388-392] and (2) glycine acetate buffer [304, 375, 393]. In addition to horse spleen AFt, recombinant H-AFt was used to further validate the disassembly process under the same conditions. After the disassembly step, samples were loaded onto native PAGE to confirm the absence of the intact AFt cage. For disassembled protein, the native gel revealed no band at ~480 KDa expected for intact AFt (**Figure 3.8a**), suggesting successful disassembly of the horse spleen AFt to its subunits when using HCl but not glycine acetate (**Figure 3.6b**). multiple lower bands are observed on the native gel after using both HCl and glycine acetate buffer, confirming presence of proteins with lower MWt, hence indicating partial disassembly of H-AFt protein under both used conditions (**Figure 3.6a**, **b**).

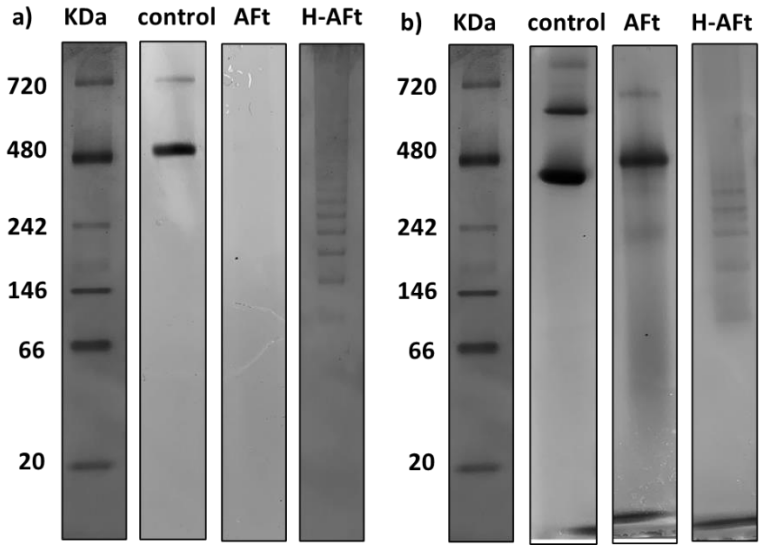


Figure 3.8: Blue (4-16%) polyacrylamide native gel electrophoresis of **(a)** the disassembly of horse spleen AFt and human recombinant AFt (H-AFt) to its building subunits at pH 2-2.5 using direct addition of HCl along with native AFt control, or **(b)** dialysis against glycine acetate buffer. Native AFt control band is shown at ~480 KDa.

As seen from the native PAGE (**Figure 3.8**), HCl was more efficiently able to disassemble the horse spleen AFt cage. A possible explanation is related to the salting-in and salting-out effect of proteins. When a small amount of salt is added to a protein solution, it enhances its solubility by reducing its electrostatic energy; the salting-in effect [394]. However, when the concentration of salts highly increases, it adversely affects the protein's solubility by reducing its electrostatic energy resulting in aggregation; the salting-out effect [394]. Besides, ionic strength and composition play important roles in this effect. According to Hofmeister, ions can be ordered by their ability to salt in (structure-breaking ions) or salt out (structure-making ions) proteins. Based on the strength of hydration ordering, acetate is a better structure-making ion than Cl^-. Accordingly, Cl^- is better in structure-breaking due to its higher ability to salt in AFt subunits and therefore

keeping AFt subunits separate at pH 2. On the other hand, the disassembly of H-AFt, but not horse spleen AFt by acetate-based method indicates its relatively lower stability. This further supports the need for L-rich AFt (horse AFt) for more extreme conditions to denature compared to H-AFt, and that the stability of H homopolymers of AFt can be enhanced if some are substituted with L-chain residues [395].

Previously, Kilic *et al*. (2012) optimised the self-assembly method to obtain one of the highest PR% values; 64% [375]. They proposed using glycine acetate buffer (at pH 2.5) to disassemble AFt cages to avoid the possible precipitation of AFt when using other acidic alternatives that contain phosphoric acid and anions such as OH− and Cl−. However, in our study, the weak disassembly seen in native gels upon using glycine acetate buffer opposes its use to efficiently dissociate the horse spleen AFt (**Figure 3.8b**).

3.3.2.2.2 Evaluating the reassembly methods used to restore the AFt cage at physiological pH: raising the pH in one step versus raising the pH in two steps

Following unfolding of the AFt cage, different methods to refold the cage were evaluated. Two of the most widely used reassembly methods were evaluated: raising the pH (from pH 2 to pH 7.4) in one step (1S method) [379, 392] and raising the pH in two steps (2S method) (from pH 2 to pH 4 and then from pH 4 to pH 7.4) [304, 375]. The reassembly of the AFt cage in 1S-method was done by dialysis against glycine NaOH buffer (25 mM, pH 7.4, 4 ºC) overnight. Raising the pH in 2S method was done by directly adding Trizma-base solution (4 M, 1 h) to raise the

pH from 2 to 4 (several minutes), followed by dialysis against glycine NaOH buffer (25 mM, pH 7.4, 4 ºC) overnight. The reappearance of the AFt band at ~480 KDa on the native gel, gives evidence of AFt reassembly. The native gel shows a more intense AFt band at 480 KDa (50% more) when using 2S method compared to the AFt band obtained using 1S reassembly method. These results reflect better PR% and cage reformation (**Figure 3.9**). This finding was also reported by Kilic *et al*. [375].

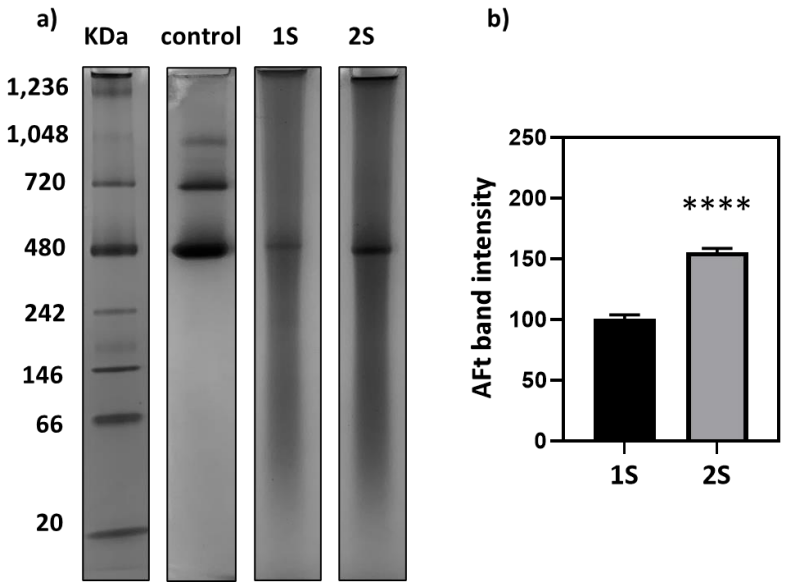


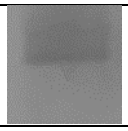
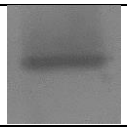
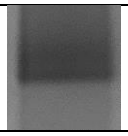
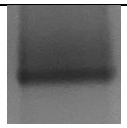
Figure 3.9: Blue (4-16%) polyacrylamide native gel electrophoresis of **(a)** the AFt cage reassembly in one step (1S) from pH 2 to pH 7.4 vs raising the pH in two steps (2S) from pH 2 to pH 4 and then from pH 4 to pH 7.4; AFt control band is shown at ~480 KDa. **(b)** Densitometry measurements of AFt band intensity. Intensity is reported as mean ± SD in 3 repeats and a significant difference is expressed as ****P < 0.0001.

3.3.2.2.3 Evaluating the initial concentration of AFt used.

The initial concentration of AFt previously used varied from 1 mg/mL to 50 mg/mL (**Table 3.2**), thus its effect on the yield of reassembled protein was evaluated. Using the same reassembly method (ReM), AFt at concentrations of 5 mg/mL (ReM-1) versus 2.5 mg/mL (ReM-2) was disassembled as described earlier and reassembled by 2S method by quickly adding (several minutes) NaOAc (100 mM, pH 4) to raise the pH from 2 to 4, followed by dialysis against Trizma-acetate buffer (1 M, pH 7.4, 4 ºC) overnight. Native PAGE was used to evaluate AFt-reformation after the first step of the reassembly process at pH 4 (partial reassembly) and after full reassembly at physiological pH.

Native PAGE shows that reassembly of AFt at a concentration of 5 mg/mL resulted in a less intense AFt band at 480 KDa at both pH 4 and pH 7.4 compared to reassembly at an initial AFt concentration of 2.5 mg/mL (**Table 3.3**). The PR% was also calculated as described in Section 2.2.4 after spin filtration using 2000 rpm for 10 min and 1 min reverse. The results show a non-significant lower PR% produced with higher AFt concentration ($p > 0.05$). Pictures taken for both formulations also show more turbidity of reassembled protein when using a higher concentration of 5 mg/mL (**Table 3.3**).

Table 3.3: Summary of the study of the effect of initial AFt protein concentration on the outcomes of the reassembly method.

	AFt initial concentration and method	
	ReM-1 (5 mg/mL)	**ReM-2 (2.5 mg/mL)**
Buffer used: (pH 2 to pH 4)	100 mM NaOAc (pH 4, quick addition)	100 mM NaOAc (pH 4, quick addition)
Native gel PAGE (pH 4)		
Buffer used (pH 4 to pH 7.4)	1M Trizma- acetate buffer (pH 7.4, quick addition)	1M Trizma- acetate buffer (pH 7.4, quick addition)
Native gel PAGE (pH 7.4)		
Protein recovery%	23%	26%
Final formulation		

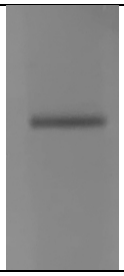
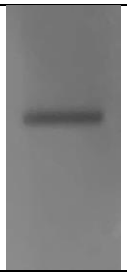
Hence, we conclude that better reassembly with higher PR% and lower aggregation of the final Re-AFt is obtained with a lower protein concentration of 2.5 mg/mL.

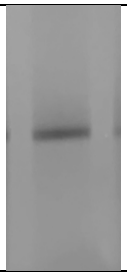
These findings conflict with the previously reported statement that the effect of the initial protein concentration is negligible on the yield of the formulation [375]. Observations further suggest a correlation between the initial AFt concentration and the precipitation/aggregation of the final formulation (**Table 3.3**) and agree with the finding of Stefanini et al. [393], who suggested keeping the initial concentration of AFt < 3 mg/mL for the self-assembly method to reduce its precipitation.

3.3.2.2.4 Effect of pH change methods: dialysis vs direct addition.

Based on the literature, methods of adjusting the pH for reassembly were performed by either quick addition of basic buffer/ solution or after the dialysis process (**Table 3.2**). To evaluate the effect of the method to change pH on the reassembly process, AFt (2.5 mg/mL) was disassembled using HCl and the subunits were then restored using the 2S method by adding 4 M Trizma base solution (within minutes) followed by either dialysis overnight (ReM-3) or quick addition, within few minutes (ReM-4) of 20 mM Trizma-acetate buffer (pH 7.4). The native PAGE of Re-AFt (at pH 4 and physiological pH), the PR% following purification by spin filtration (2000 rpm for 10 min and 1 min reverse), and the measurements of hydrodynamic size were used to evaluate the final reassembled protein (**Table 3.4**).

Table 3.4: The investigation of dialysis and direct addition of buffer to restore AFt protein cage.

	Reassembly method	
	ReM-3	**ReM-4**
Buffer used (pH 2 to pH 4)	4 M Trizma base solution (quick addition)	4 M Trizma base solution (quick addition)
Native gel PAGE (at pH 4)		
Buffer used (pH 4 to pH 7.4)	20 mM Trizma-acetate buffer (pH 7.4, dialysis	20 mM Trizma-acetate buffer (pH 7.4, quick addition)

Native gel PAGE (at pH 7.4)		
Protein recovery%	37%	58%
Hydrodynamic size (by number average)	7.6 ± 1.9 nm (93%)	18.1 ± 5.4 nm (90%)
Hydrodynamic size (by volume average)	6.8 ± 1.6 nm (>99%)	15.3 ± 4.0 nm (>99%)

The presence of a band at 480 KDa in native gels reflects refolding of AFt protein to expected MWt (**Table 3.4**). The hydrodynamic sizes measured for AFt are d_{AFt} = 15.3 ± 4.0 nm and 18.1 ± 5.4 nm as reported by number and volume respectively for the direct addition method, comparable to those of AFt ~12 nm. While for the dialysis method, the hydrodynamic sizes for AFt measured d_{AFt} = 6.8 ± 1.6 nm and 7.6±1.9 nm as reported by number and volume respectively (**Table 3.4**). The shift of hydrodynamic size from the expected AFt indicates the presence of unfolded AFt subunits when using the dialysis method. This was further corroborated by calculating the PR% after the purification of unfolded protein subunits, which were calculated as 58% and 37% for direct addition and dialysis methods respectively. Moreover, more smearing of AFt band (at ~480 KDa) in the native PAGE following the dialysis method reflects greater heterogeneity, or dissociated protein samples [396, 397], which further contribute to lowering PR% (37%) and the smaller hydrodynamic size of the reformed AFt cage seen with the dialysis method.

These results suggest that using the direct addition method to adjust pH during the reassembly results enhances PR% and produces a greater fraction of reassembled protein with particle sizes expected for AFt. A possible explanation for this might be related to the time that AFt subunits remain within the PI range of the AFt (4.1- 5.1) during dialysis, suggesting that the success of the reassembly process is reduced with a longer time AFt is at PI range. According to Stefanini *et al.* [393] ~ 70-90% of precipitated AFt within its PI can restore its reassembly property at physiological pH. This further implies that up to 30% of the proteins might be losing their ability to restore their original form, in agreement with our findings. Based on these observations and that the reassembly process does not take place at the PI, rapid addition of buffers to raise the pH of the solution was adopted for further studies.

Nevertheless, the differences in ionic strength of the reassembly buffer used to raise pH from 4 to 7.4 should be considered. In ReM-3, the ionic strength of 4 M Trizma base solution (pH 4) was diluted through dialysis with 20 mM Trizma-acetate buffer (pH 7.4). While in ReM-4, the direct addition of 20 mM Trizma-acetate buffer preserved the ionic strength of the reassembly solution. The effect of ionic strength on the reassembly of the AFt cage can be clarified by the salting effect on proteins. It can be argued that at a high salt strength the salting-out emerges and affects the stability of the AFt protein; however, according to the salting-out effect, at high salt concentration, the hydrophobic forces of protein increase as a result of increasing surface tension [398]. It is known that the disassembly of AFt protein resulted from breaking the non-covalent forces such as hydrogen and hydrophobic bonds between its 24 subunits [282]. Therefore,

increasing the intermolecular hydrophobic forces between the AFt subunit is crucial to retain its original form, and using a high strength of buffer/basic solution during the reassembly of AFt will ensure its successful reassembly.

All previous investigations established the fundamental steps from which to conduct further optimisation. Accordingly, all experiments performed thereafter were consistent: using 1) HCl (1 M) to disassemble the horse spleen AFt cage, 2) 2S method to raise the pH to reassemble the AFt cage, 3) initial AFt concentration of 2.5 mg/mL to reduce the aggregation/ precipitation of the formulation and 4) direct addition of buffers/ basic solution during the reassembly to enhance both the reassembly and PR%.

It is interesting to note that two of the previously conducted experiments; ReM-2 (**Table 3.3**) and ReM-4 (**Table 3.4**) produced a noticeable difference in the PR% with 26% and 58% respectively. Both experiments were conducted using the same conditions for disassembly and reassembly except for the buffer type and strength in the reassembly step. This finding further supported investigating the buffer types used in each step during the reassembly process.

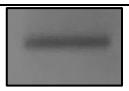
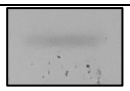
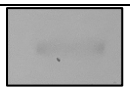
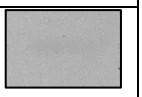
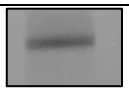
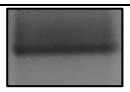
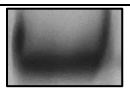
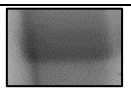
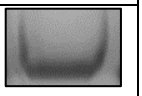
3.3.2.2.5 Investigating the buffers / basic solutions used to reassemble the AFt cages

Several different buffers/basic solutions (e.g., Trizma-acetate, Trizma base, glycine-acetate, NaOH, and NaOAc were tested for efficient reassembly and PR% as described in **Table 3.5**.

ReM-5-10 were evaluated by native PAGE after the first (at pH 4) and the second (at physiological pH) steps of the reassembly, to ensure correct reassembly of the

AFt. The hydrodynamic sizes of reformed AFt were reported by number and volume, in addition to the calculated PR% after purification by spin filtration using 2000 rpm for 10 min and 1 min reverse spin filtration (**Table 3.5**).

Table 3.5: Optimisation of basic solutions/buffers used to reassemble horse spleen AFt.

Reassembly method	**ReM5**	**ReM6**	**ReM7**	**ReM8**	**ReM9**	**ReM10**
buffer used (pH2 to pH4)	4 M Trizma base solution (quick addition)	200 mM Glycine acetate (pH 4, quick addition)	100 mM sodium acetate buffer (pH 4.0, quick addition)	100 mM sodium acetate buffer (pH 4.0, gradual addition)	5 N NaOH (quick addition)	5 N NaOH (quick addition)
Native gel (at pH 4)						
buffer used (pH 4 to 7.4)	20 mM Trizma-acetate buffer (pH 7.4, quick addition)	4 M Trizma-base solution (quick addition)	5 N NaOH (quick addition)	1 M Trizma-acetate buffer (pH 7.4, quick addition)	5 N NaOH (quick addition)	1 M Trizma-acetate buffer (pH 7.4, quick addition)
Native gel (at pH 7.4)						
Protein recovery%	58%	90%	28%	43%	32%	24%
Diameter represented by volume%	18.1 nm ± 5.4 (90%)	11.8 nm ± 3.4 (>99%)	12.5 nm ± 2.4 (96%)	12.8 nm ± 2.2 (98%)	12 nm ± 3.1 (90%)	14.2.0 nm ± 3.4 (>98%)
Diameter represented by number%	15.3 nm ± 4.0 (>99%)	9.5 nm ± 2.3 (>99%)	11.7 nm ± 2.1 (>99%)	12.1 nm ± 2.0 (>99%)	10.8 nm ± 2.5 (>99%)	12.6 nm ± 2.7 (>99%)

All investigated methods in **Table 3.5** resulted in different degrees of AFt reassembly, represented by a band at 480 KDa with various intensities. All methods used showed more intense band of AFt (at ~480 KDa) at physiological pH than the band seen after the 1S of reassembly (at pH 4) for the same used method.

These results are in agreement with those obtained by Crichton *et al.* [399] and Stefanini *et al.* [393] that reported ~ 50% of AFt reassembly occurs at pH 4, and this partial reassembly is followed by a full assembly of the cage at physiological pH.

The hydrodynamic sizes measured for the formulations with ReM-5, ReM-8 and ReM-10 were comparable to the expected size of ~12 nm, reflecting correct assembly of the cage. On the other hand, the DLS measurements in ReM-6, ReM-7 and ReM-9 demonstrated hydrodynamic size < 12 nm and revealed that using a basic solution instead of buffers in step 2 of reassembly (at physiological pH) failed to restore the required particle size (~12 nm) in these experiments. The native gels in the later experiments also show weak and smeared bands of AFt compared to the AFt reassembly methods using buffers, which as mentioned earlier, reflect heterogeneity or dissociated protein samples [396, 397].

Our data corroborate the importance of using buffers to control the pH of the solution, which results in a better reformation of AFt cages to their expected size and agrees with conclusions drawn by Zbacnik *et al* [400]. Besides the role of buffers to regulate shifts in pH, the authors reviewed the mechanisms through which buffers can stabilise proteins. Specifically, buffers increase the conformational stability of proteins by preferentially binding to their native form, with no impact on the denatured or unfolded state. This can be crucial for efficient AFt refolding, as during the reassembly process, AFt subunits need to be free from any binding except for the intramolecular forces (hydrogen and hydrophobic) to retain the native shape of their cage. Enhancing intramolecular forces between

subunits was achieved by increasing the ionic strength of the solution and gaining the salting-out effect on proteins (see Section 3.3.2.2.4). On the other hand, the desired refolded AFt during the reassembly process is stabilised by the added buffer. All together this reveals the considerable effect of using a buffer with high ionic strength to control the pH of the solution, refold and stabilise the AFt protein.

It is interesting to note that the imperfectly reformed AFt cage in ReM-9 (using HCl to unfold the AFt cage and NaOH to refold it) supports evidence from previous observations of Mihee *et al.* upon using the same method. The authors found that AFt failed to fully reassemble as was shown by synchrotron small-angle X-ray scattering (SAXS) [380]. However, we do not agree with the authors' conclusion in the previous study that AFt fails to fully reassemble at physiological pH. As in the previous study, the author neglected the importance of using buffers to stabilise proteins, and their conclusion could have been prematurely generated, as it was based on the use of one method to reassemble the AFt cage using NaOH basic solution only. Our findings, furthermore, emphasise the importance of using buffers to stabilise AFt and fully reassemble its cage.

ReM-5 and ReM-8, which were successful in yielding the correct capsule diameters and the highest PR% with ~58% and ~43% respectively, were chosen for further optimisation and evaluation.

3.3.2.2.6 Evaluating the purification process used to discard the un-reformed AFt subunits: dialysis and centrifugation.

The method and time needed to purify the formulation from the un-reformed AFt subunits were further evaluated. First, AFt protein reassembled using ReM-5 was

used to evaluate the time and speed needed for the purification using spin filtration. The final formulation at physiological pH was spin filtered using I) 10 min at 2000 rpm, II) 15 min at 3000 rpm. The native PAGE results are shown in **Figure 3.10**.

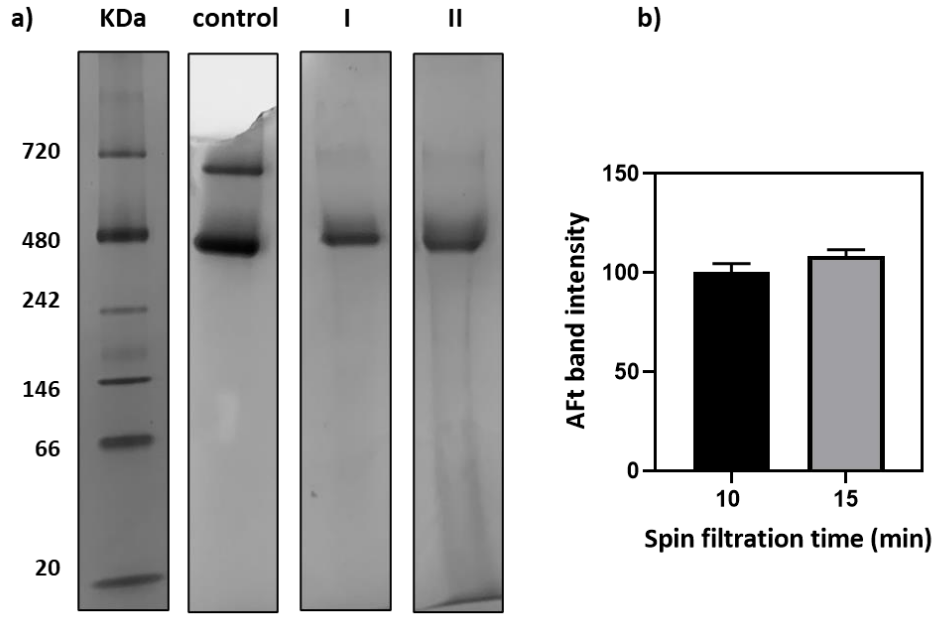


Figure 3.10: Evaluating the time and speed needed to purify the reassembled formulation using spin filtration. **(a)** AFt reassembled using ReM-5 and spin filtered for 10 min at 2000 rpm (I) or 15 min at 3000 rpm (II). Native PAGE performed using Blue (4-16%) gel, and AFt band is shown at ~480 KDa. **(b)** Densitometry measurements of AFt band intensity. Intensity is reported as mean ± SD in 3 repeats and shows no significant difference.

Native PAGE shows the same AFt band intensity at 480 KDa regardless of the time and speed used for the purification by spinning filtration. Using more extreme purification conditions (from 10 min at 2000 rpm to 15 min at 3000 rpm) might be more efficient to eradicate unfolded AFt subunits, however, resulted in smearing that suggests the need for further optimisation. Besides, the purification for a longer time resulted in some curving in AFt band, indicating high salt

concentration in the samples, and further highlights the importance of investigating the dialysis effect to desalt the final formulation.

Further optimisation of the purification process was performed using ReM-8. As shown in **Table 3.5**, among all methods, ReM-8 produced the least protein smearing in the native gel after refolding at physiological pH and produced the second-highest PR% (~43%). In this experiment, Re-AFt was purified using four different methods and the resulting native gel of each is represented in **Figure 3.11**. The purification techniques aimed to remove the unfolded AFt subunits and remove the salting effect seen previously upon concentrating the formulation after the spinning filtration for 15 min (**Figure 3.10**).

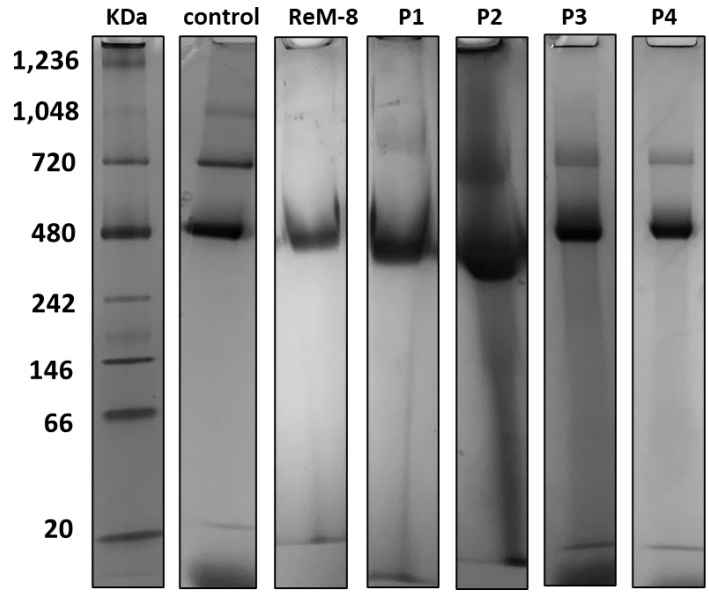


Figure 3.11: The native gels show the purification of the reassembled AFt (Re-AFt) using 4 different methods. ReM-8 AFt was spin filtered for 15 min (P1), dialysed against 25 mM Trizma-acetate buffer then spin filtered for 15 min at 3000 rpm (P2), spin filtered for 15 min at 3000 rpm then dialysed against (100 mM) glycine NaOH buffer at pH=8.6 (P3) or spin filtered for 15 min then dialysed against 25 mM Trizma-acetate buffer at pH=7.4 (P4). AFt control band is shown at 480 KDa.

The Re-AFt band using the ReM-8 without any purification was shown as a control. Purification 1 method (P1) was conducted using spin filtration for 15 min at 3000 rpm (P1). AFt shows a similar but more intense (more concentrated) band compared to the control and the salting effect was still clearly obvious with minimum smearing. In the purification 2 method (P2), overnight dialysis against 25 mM Trizma-acetate buffer was performed to de-salt the refolded AFt protein. This was followed by spin filtration for 15 min at 3000 rpm to remove the unfolded AFt subunits. The native gel clearly shows more smearing compared to the control, suggesting greater heterogeneity in the protein sample [396, 397]. A possible explanation might be that, after full reassembly had taken place using direct addition of buffer, the remaining unfolded AFt subunits incorrectly interacted with each other at low ionic strength (25 mM Trizma-acetate buffer) overnight to produce the observed heterogeneity. These results provide further support for the conclusion drawn from Section 3.3.2.2.4, where less PR% and more smearing of the reformed AFt was produced with dialysis compared to the direct addition of buffer.

Subsequently, two purification methods were conducted by first spin filtration for 15 min at 3000 rpm, followed by dialysis against glycine NaOH buffer (pH 8.6) or Trizma-acetate buffer (25 mM, pH 7.4); purification methods P3 and P4 respectively. The resulting AFt bands at ~480 KDa were neat for both methods used. These results support the use of dialysis only to de-salt the final formulation after discarding all unfolded AFt subunits to prevent them from wrongly folding during overnight dialysis. Furthermore, the native gel of AFt purified after dialysis with glycine NaOH buffer shows more smearing compared to using Trizma acetate

buffer, which was the only difference between the two self-assembly methods used.

According to our observations, we can conclude that the smearing of the native gels (resulting from imperfect AFt reassembly) is not related to the amount of loaded protein (**Table 3.2**) or the time needed for the purification (**Figure 3.10**). The smearing is correlated to the buffers (composition and ionic strength) used to reassemble AFt, in addition to their effect on the PR%. This further supports the previously reported influence of buffers' composition on the reassembly process [383, 393, 401].

3.3.2.2.7 Evaluating the time needed to reassemble the AFt cages.

One final optimisation parameter was the evaluation of the time needed to reassemble the AFt cage after reaching physiological pH. Using ReM-8 and the purification method (P4). Increasing the time of reassembly after direct addition of Trizma acetate buffer (25 mM, pH 7.4) from 4 h to overnight robustly enhanced PR% from~43% to 77%. Indicating that allowing more time for the AFt subunits to reassemble was beneficial and enhanced the PR%.

The optimisation process of the self-reassembly method of AFt resulted in a fully reassembled protein using ReM-8 with an expected hydrodynamic diameter of ~12 nm (**Table 3.5**), MWt of ~480 KDa (**Figure 3.11**) and a robust PR% of 77±5%.

Moreover, during the self-assembly optimisation process, measuring the pH of the solution after each addition was done using a pH meter (Mettler Toledo). Failing to pre-calibrate the pH meter before each encapsulation produced inconsistent results regarding the PR%. Upon completion of optimisation process, JAa was

encapsulated using the optimised method, and the effect of its encapsulation on the integrity of the AFt cage was further evaluated.

3.3.2.3 Characterisation of AFt-encapsulated JAa through the optimised the self-assembly route

Following optimisation, the encapsulation of JAa was performed at a ratio of 1:150 (AFt-JAa). Addition of JAa was done gradually along with adjusting the pH to 4 with NaOAc in the first step of reassembly. The encapsulation method of JAa through the optimised self-assembly method is fully described in Section 2.1.4.

To assess the effect of encapsulating JAa using our optimised method, the AFt-JAa formulation at a ratio of 1:150 (AFt-JAa) has been characterised for its size, stability, and integrity (**Figure 3.12**). Characterisation of AFt-JAa was performed together with the empty Re-AFt protein which was prepared under the same buffer conditions and diluted at the same conditions for analysis. Results were also compared with the AFt control taken directly from our AFt stock.

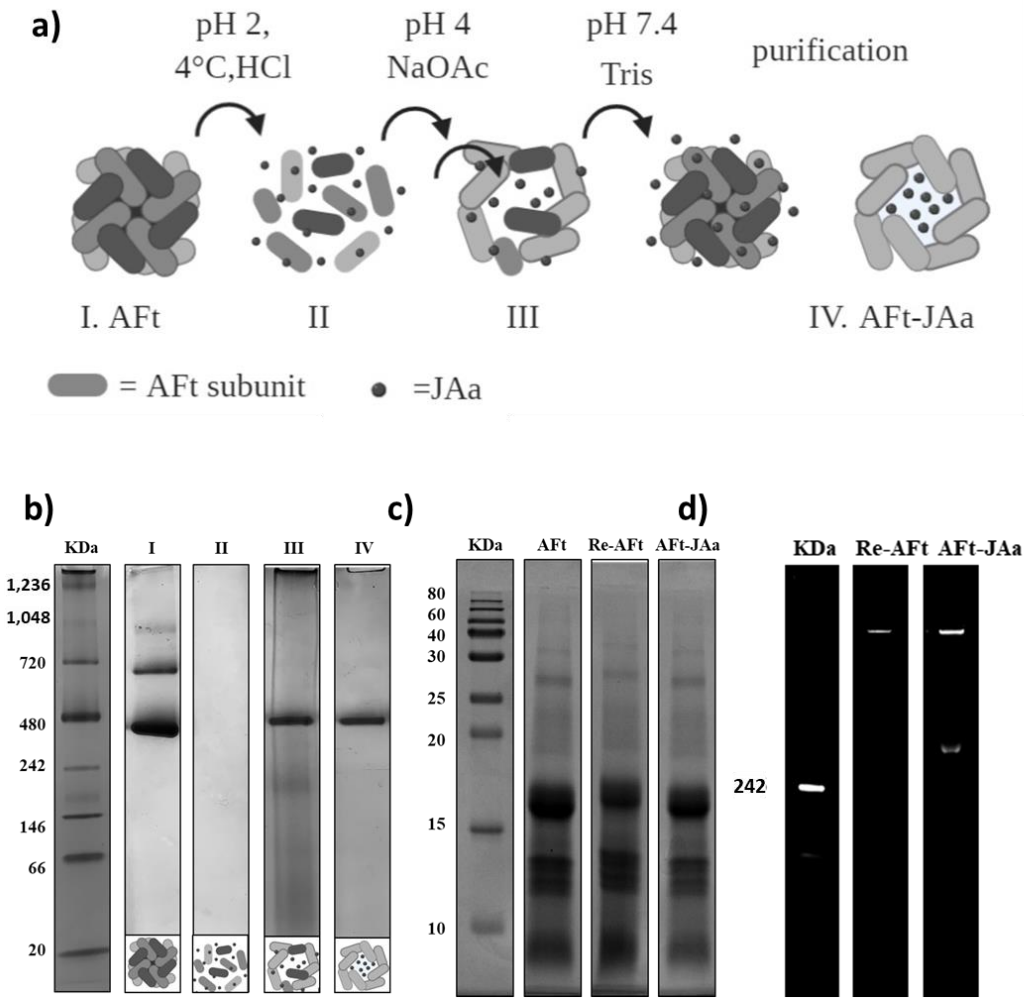


Figure 3.12: The encapsulation of JAa into AFt cages using the reassembly method. **(a)** Illustration of JAa encapsulation by the reassembly method performed at 4 ºC. **(b)** Native PAGE of each step of the reassembly method. **(c)** SDS PAGE shows the composition of AFt encapsulating JAa (AFT-JAa), empty reassembled AFt protein (Re-AFt), and stock AFt control. **(d)** The native PAGE of AFt-JAa and empty Re-AFt under the UV light.

AFt was evaluated after each step of self-assembly during the encapsulation process using blue native PAGE. The native gel revealed no band at ~480 KDa expected for intact AFt, indicating successful disassembly of the horse spleen AFt represented at pH 2.5 after the addition of HCl for 30 min. During reassembly, JAa (10 µL; 10 mM) was added gradually along with NaOAc, the resulting solution remained very clear even after resting the formulation for 1 hr at 4 ºC. The native

gel band at ~480 KDa indicates obvious reassembly of AFt cages at pH 4 after gradual addition of NaOAc with JAa. The smearing at pH 4 in the native gel is proof of only partial reassembly of the cage at this stage. The clear AFt band at physiological pH at ~ 480 KDa following the purification process reflects the full and successful reassembly of the AFt-JAa formulation. This suggests that the integrity of AFt protein after encapsulation of JAa was preserved as demonstrated by native gel in **Figure 3.12b**. Additionally, the successful entrapment of JAa was evaluated by using UV light to illuminate the native PAGE protein bands after the purification process (**Figure 3.12d**). Illumination of native gel was conducted after ensuring illumination of JAa in a stock of 10 mM along with the AFt-JAa formulation in their original Eppendorf tubes. The dialysis process was performed originally to desalt the protein, to further ensure that the detected concentration of JAa in the formulation is not related to any attached molecules on the surface of AFt. At a loading of 50 µg protein/well, the AFt-JAa but not empty AFt protein shows a UV absorption band at ~480 KDa. Therefore, this band is concordant only with JAa encapsulation within AFt but not AFt protein. Both AFt-JAa and empty Re-AFt shows a band in the loading wells, which could be related to some precipitation of AFt due to the high amount of loaded protein.

Under denaturing conditions, the composition of AFt-JAa formulation and empty Re-AFt along with AFt control was assessed under denaturing and reducing conditions using SDS PAGE [327]. SDS PAGE demonstrated indistinguishable secondary structure composition of AFt protein of all tested samples, this further confirms that our optimised reassembly method succeeded to restore the AFt cage after disassembly, with and without JAa entrapment (**Figure 3.12c**).

The hydrodynamic sizes were measured for AFt, Re-AFt and AFt-JAa and reported by number and volume respectively along with the ZPs (**Figure 3.13**).

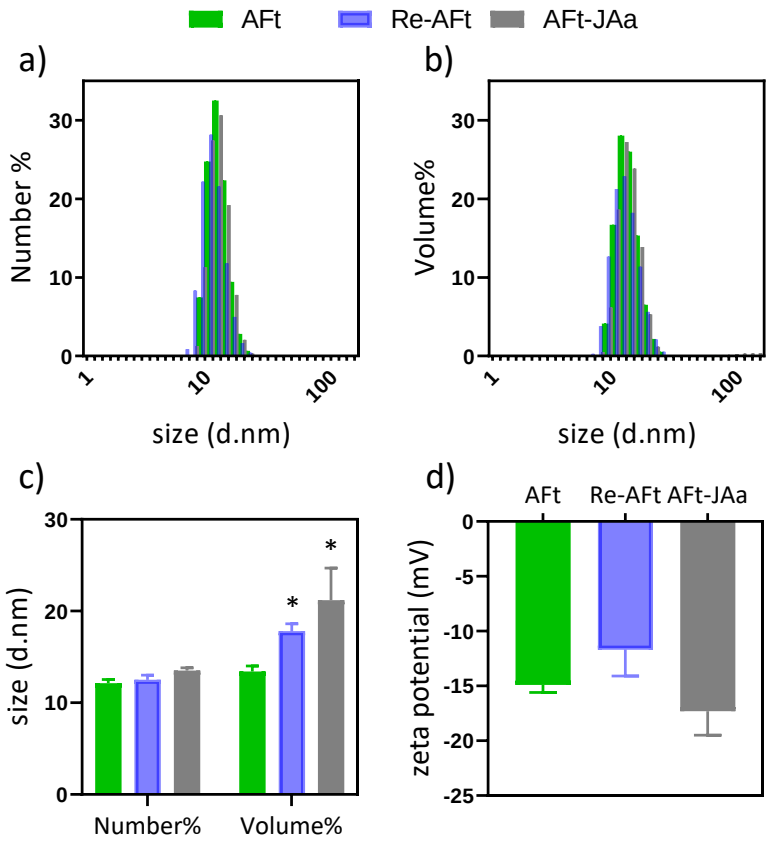


Figure 3.13: DLS characterisation of AFt encapsulated JAa (AFt-JAa). Data compares the size of the nanoparticles to the empty reassembled AFt protein (Re-AFt), and stock AFt in both **(a)** number and **(b)** volume averages, along with **(c)** their statistical analysis. **(d)** Measured ZPs show no significant difference in all tested samples. Data are reported as mean ± SD. Significant differences are expressed as *P < 0.05.

The hydrodynamic size of AFt-JAa $d_{AFt\text{-}JAa}$ = 13.5±0.3 nm and $d_{AFt\text{-}JAa}$ = 21.2±3.3 nm to AFt d_{AFt} = 12.13±0.4 nm and d_{AFt} = 13.4±0.6 nm reported by number and volume respectively (**Figure 3.13**, **Table 3.6**). The sizes presented by% volume still reflect the presence of some unavoidable precipitation usually accompanying small NPs

[386, 397]. However, the hydrodynamic size presented by the average number shows a non-significant difference in the particle size in both the empty AFt and AFt-JAa ($p > 0.05$).

To evaluate the effect of the reassembly process and JAa encapsulation on the stability of AFt, ZP values were measured in Trizma acetate buffer (25mM, pH 7.4). The measured ZPs $\zeta = -11.7 \pm 2.4$ mV and -17.3 ± 2.2 mV for Re-JAa and AFt-JAa respectively compared to $\zeta = -14.9 \pm 0.7$ mV of AFt.

The change of ZPs was non-significant for AFt-JAa and Re-AFt compared to the stock AFt ($p > 0.05$) (**Figure 3.13d**, **Table 3.6**). These observations reflect preservation of AFt cage stability after the reassembly process with and without encapsulation of JAa.

Table 3.6: Characterisation summary of encapsulated JAa into AFt core through the self-assembly route. Results are shown as mean ± SD from three independent trials.

	AFt stock	**Reassembled AFt reference**	**AFt-JAa (1:150)**
Size by number (nm)± SD	12.13±0.4	12.5±0.5	13.5±0.3
Size by volume (nm)± SD	13.4±0.6	17.8±0.8	21.2±3.3
Zeta potential (mV)± SD	-14.9±0.7	-11.7±2.4	-17.3±2.2
Protein recovery%	NA	77 ± 5	69 ± 7
Encapsulation Efficiency (EE)%	NA	NA	80 ± 7
No. of molecules encapsulated per AFt cage	NA	NA	120 ± 10

Table 3.6 provides the results in terms of EE% and the number of JAa molecules encapsulated per AFt cage for the AFt-JAa formulation. We achieved ~80% EE upon encapsulation of JAa into AFt core through the self-assembly method. This encapsulation achieved entrapment of ~ 120 molecules of JAa inside each AFt

capsule. **Table 3.6** also compares the PR% obtained from the self-assembly of the empty AFt cage and with AFt-JAa. The most striking result to emerge from the data is the PR%, which reached 77% without adding JAa and dropped to ~ 70% upon the addition of JAa. Adding JAa during the reassembly process reduced the PR% but not significantly ($p > 0.05$). Our method was superior to the best-optimised method reported in the literature, where PR% of 64% and 58% have been reported for AFt alone and encapsulated doxorubicin respectively [375]. The successful encapsulation of JAa into AFt addressed the main drawback of using the self-assembly AFt-encapsulation method and further supports adoption of this method for encapsulation of other agents with high MWt.

Thus, successful encapsulation of JAa was achieved through both the nano-reactor and the self-assembly methods. Both encapsulation methods preserved the size, integrity and charge of AFt's cage upon encapsulation of JAa. However, due to its high MWt of 424, JAa may not diffuse efficiently through the channels of AFt and thus AFt-JAa obtained from the self-assembly method was used in further *in vitro* assessment.

3.3.3 Validation of the optimised self-assembly method: encapsulation of vincristine and rhodamine B

Following the promising characterisation results of AFt-encapsulated JAa achieved through the self-assembly method, the applicability of using the method to encapsulate other high MWt agents was investigated. VCR with MWt of 825 and lateral dimensions of 1.0 X 1.45 nm and RB with MWt of 479 and lateral dimensions of 1.05 X 1.44 nm were encapsulated through our optimised

reassembly method (**Figure 3.14**). VCR has been encapsulated previously inside the core of AFt [317], a successful entrapment of such a big molecule (double the MWt of JAa) will be beneficial to validate our method. RB is a xanthene fluorescent dye frequently used to stain biological samples [402, 403]. Successful encapsulation of RB inside the core of AFt can be used to track AFt uptake/ localisation by measuring its fluorescence signal. VCR was encapsulated in a ratio of 1:100 (AFt: VCR) and RB was encapsulated in a ratio of 1:200 (AFt: RB).

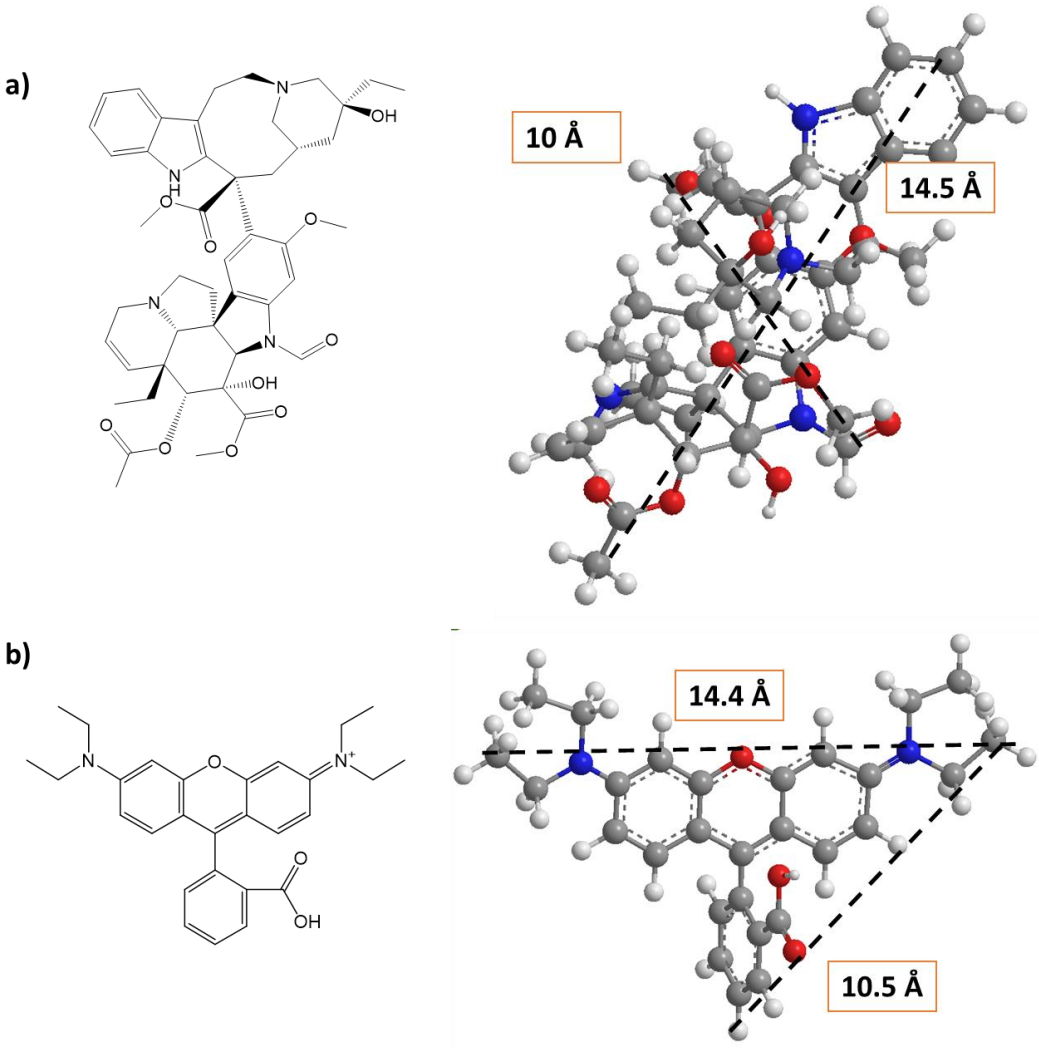


Figure 3.14: Vincristine structure and 3D model with lateral dimensions of (1.0 X 1.45 nm) (a). The structure and 3D model of rhodamine B (RB) with lateral dimensions of (1.05 X 1.44 nm) (b).

Following encapsulation through our optimised self-assembly method, AFt-VCR and AFt-RB were characterised along with their AFt stock and Re-AFt controls for their size and stability using DLS measurements. Results are described in **Table 3.7.**

Table 3.7: Results of encapsulating VCR and RB into AFt core and its DLS analysis summary. Results are shown in mean ± SD from two independent trials.

	AFt stock	**Reassembeled AFt**	**AFt-VCR (1:100)**	**AFt-RB (1:200)**
Size by number (nm)± SD	11.9±1.3	12.9±1.3	11.7±0.7	11.8±1.2
Size by volume (nm)± SD	19.1±1.3	20.1±1.2	18.5±0.2	17.6±0.8
Zeta potential (mV) ± SD	-12.5±0.9	-11.7±0.9	-10.3±0.5	-9.6±0.7
Protein recovery%	NA	77 ± 5	65±5	79±6
Encapsulation Efficiency (EE)%	NA	NA	30±3	4.5±1
No. of molecules encapsulated per AFt cage	NA	NA	30±3	9±2

The hydrodynamic size of both formulations revealed indistinguishable sizes to AFt ~12 nm ($p > 0.05$). Moreover, ZPs measured $\zeta = -10.3 \pm 0.5$ mV and -9.6 ± 0.6 mV for AFt-VCR and AFt-RB respectively compared to $\zeta = -11.7 \pm 0.9$ mV of empty Re-AFt stock. Reduction in the ZPs was not significant following the encapsulation of VCR ($P > 0.05$). However, a significant reduction in the ZP upon the encapsulation of RB ($p < 0.05$) might be related to the binding of RB on the surface of AFt. AFt successfully entrapped ~30 molecules of VCR with EE% of 33%. Previously VCR was encapsulated inside the core of horse-AFt with an average EE% of ~40%. However, authors from the previous study did not report the% weight of VCR to AFt, so a comparison of the EE% could not be drawn with our data [317]. On the other hand, AFt entrapped ~7 RB molecules, which might need further investigation to enhance its EE%. Of interest, the recovered protein measured ~65% and 79% after

the encapsulation of VCR and RB respectively. The successful refolding of AFt to its expected size ~12 nm confirmed the superiority of our optimised method to efficiently recover AFt upon the disassembly process and further support its use to encapsulate high MWt agents.

3.3.4 Stability assay of AFt-JAa reassembled formulation

The stability of reassembled AFt-JAa formulation at 4 ºC was assessed over 10 months. The changes in size and charge of AFt-JAa in Trizma-acetate buffer (25 mM, pH 7.4) with time are shown in **Figure 3.15**.

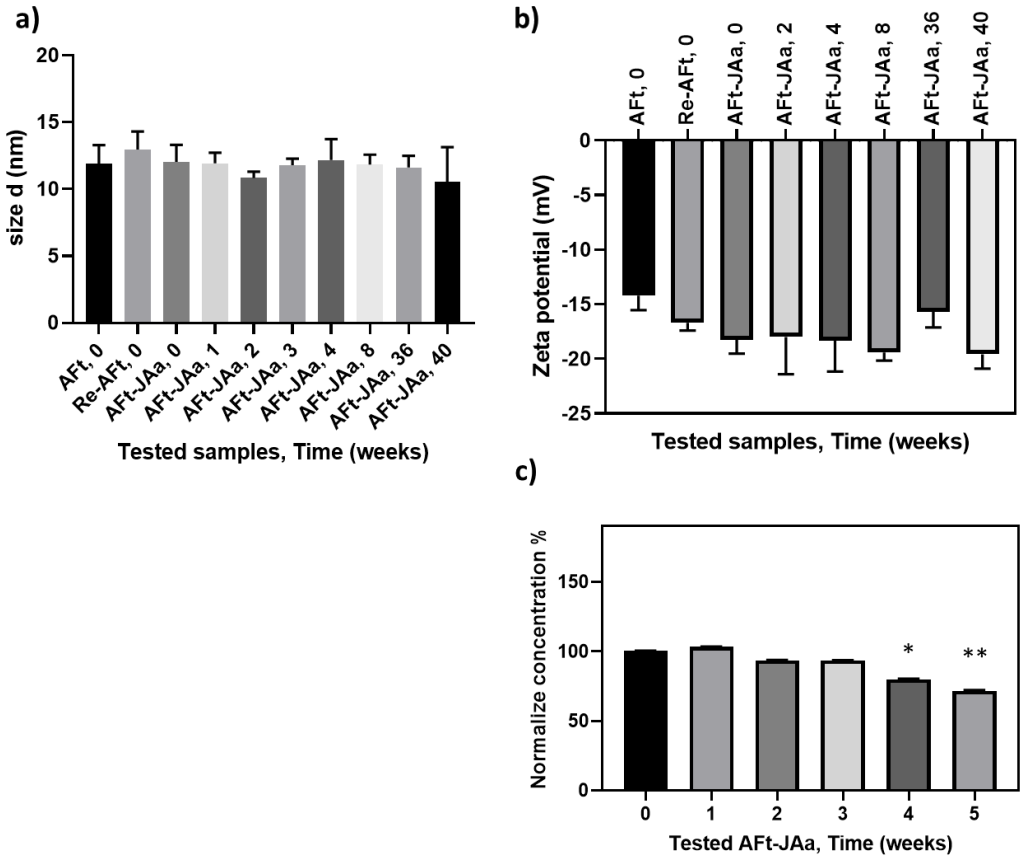


Figure 3.15: Stability study of AFt-encapsulated JAa through the self-assembly method monitored at storage conditions (*T = 4* ºC; pH 7.4). **(a)** Hydrodynamic size and **(b)** ZP were measured using Malvern zeta sizer Nano ZS. Measurements of AFt-JAa were conducted along with empty reassembled AFt (Re-AFt) and AFt stock

controls. **(c)** The stability of encapsulated JAa was assessed by measuring its concentrations by UV-Vis spectroscopy at 330 nm over 5 weeks.

At storage conditions (*T* = 4 ºC; pH 7.4), the hydrodynamic sizes of AFt-JAa were statistically comparable to the AFt stock and empty Re-AFt over 10 months of storage ($p > 0.05$). Moreover, ZP values did not change significantly ($p > 0.05$) over 10 months of storage. Reflecting the stability of reassembled AFt-JAa formulation at storage conditions over the experiment time (10 months). The stability of the encapsulated JAa was also evaluated using a UV-Vis spectrophotometer to detect changes in JAa concentration over 5 weeks. JAa started to degrade after 4 weeks of synthesis. Acetate derivatives of jerantinines were synthesised to enhance their stability [202]. This stability of JAa is seen over the first 3 weeks of storage at 4 ºC, followed by partial degradation with time. Due to partial degradation of JAa, fresh formulations of AFt-JAa were prepared every month for *in vitro* assessments. Regardless of the stability of the encapsulated agent (JAa), our reassembled AFt formulation remained stable over the whole time of assessments (10 months) and further supported the high stability of native AFt [395]. Certainly, retaining the stability of NPs is essential [404], and preserved stability was efficiently achieved through our optimised reassembly method of AFt.

3.3.5 Release assay of JAa from AFt cages

Encapsulation of JAa within the core of AFt was followed by evaluation of its release from cages under physiologically-relevant conditions (*T* = 37 ºC, pH 7.4). In addition, the release of JAa was assessed at endosomal- and lysosomal-relevant

conditions (*T* = 37 ºC, pH 5.3). it is known that after being recognised by TFR1 membrane receptors, AFt is taken up by clathrin-coated pit-mediated endocytosis and trafficked through the cells by endosomes and lysosomes [113, 405]. Therefore, it is important to evaluate JAa release under these conditions, to ensure its release inside the cells (and molecular-target - tubulin dimers' accessibility) [202]. Under both conditions, samples were collected over 24 h and the concentration of released JAa was used to derive release profiles (**Figure 3.16**).

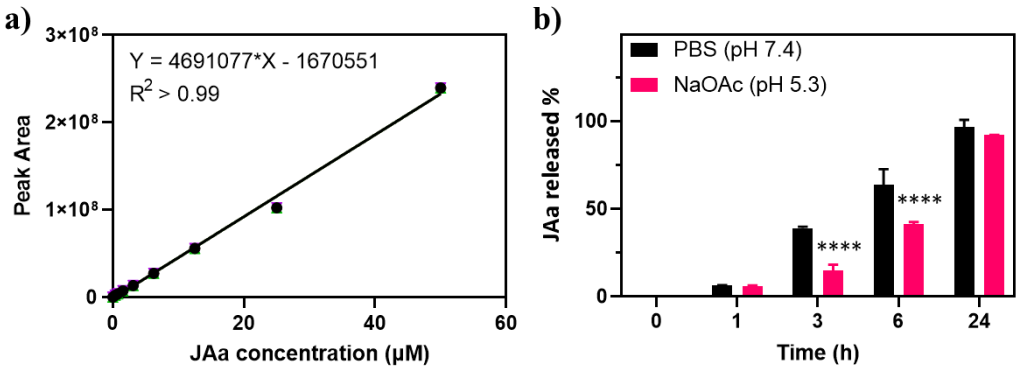


Figure 3.16: **(a)** The standard curve of JAa obtained from LCMS. **(b)** The release profile of JAa from AFt cargo (24 h, at 37 ºC) in NaOAc (pH 5.3), and PBS (pH 7.4) in four independent trials, statistical analysis of released JAa under both conditions for the same time point, where data are reported as mean ± SD (*n* = 3). Significant differences between both conditions are expressed as ****P < 0.0001.

Although the release of JAa under both conditions (pH 5.3 and pH 7.4) follows a similar pattern (**Figure 3.16b**), the results show ~23% slower release rate at pH 5.3 compared to pH 7.4 within the first 3 h and 6 h of the study. Moreover, A fast-release pattern was seen following the first 6 h of the study with ~60% at pH 7.4 and ~40% at pH 5.3. This was followed by a slower release rate up to 24 h. After

24 h, some JAa was still inside the AFt cage with ~5% at pH 7.4 and ~10% at pH 5.3. A relationship between JAa release from AFt cages and the pH of the outer environment can also be concluded from these data. At pH 5.3, the slower release suggests greater entrapment of JAa molecules inside the core of AFt at lower pH, at first consideration, perhaps contrary to expectations, as the AFt capsule is expected to be more relaxed at lower pH, facilitating more ready release of an entrapped agent. However, the observed slower release can be related to the structure of AFt and its possible interactions with cargo. AFt can form hydrogen bonds with loaded non-ionic molecules [406], and electrostatic attractions with ionic molecules due to its highly active inner surface [382, 406, 407]. Thus, we propose that at pH 5.3, the positively charged JAa molecules are trapped inside the highly reactive negatively charged AFt interior through ionic interactions [407]. Due to this strong electrostatic interaction, positively charged JAa is better entrapped than the uncharged JAa molecules at physiological pH 7.4 and thus show a slower release (**Figure 3.17**).

An explanation of the two-phased release pattern could be related to the distance of JAa molecules cargo from the inner surface of AFt. This is illustrated using the actual relative size of AFt along with JAa (**Figure 3.17**). In the first release phase (up to 6 h), rapid release may be due to unbound JAa molecules that exist in the centre of AFt's core (distant from the interactive inner surface of AFt) which are less likely to be entrapped through ionic or hydrogen bonds. In the second release phase (from 6 h to 24 h), more steady release may be due to the entrapped JAa molecules through stronger ionic (at pH 5.3) or weaker hydrogen (at pH 7.4) bonds.

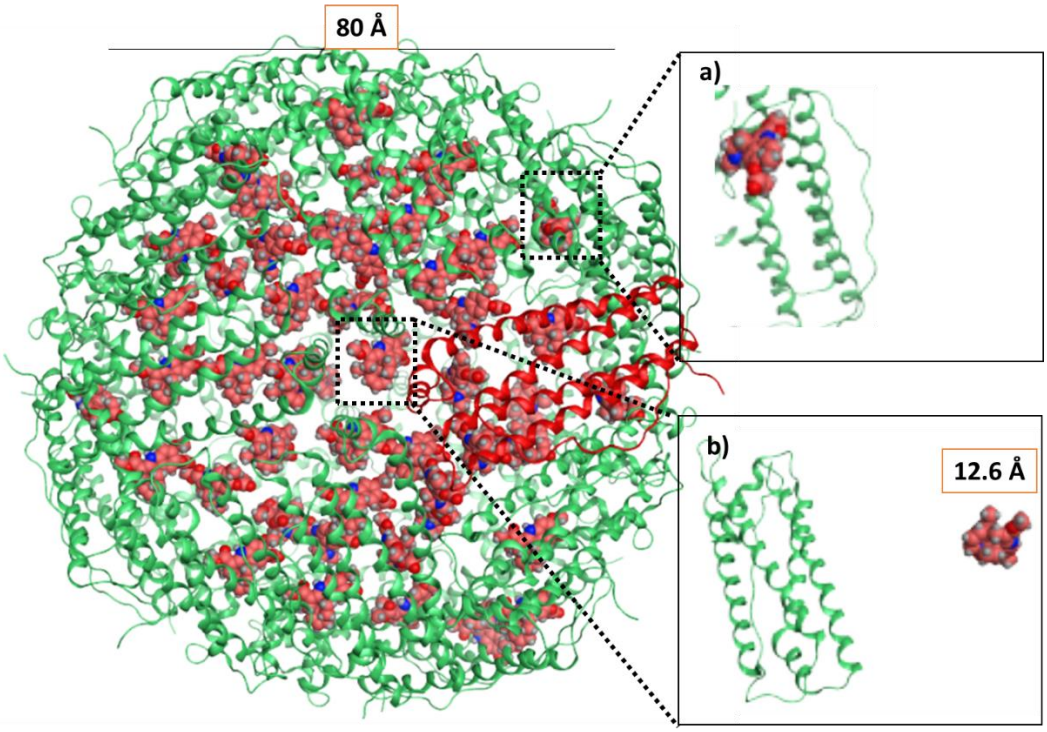


Figure 3.17: Illustration of possible interaction of JAa and the interior surface of AFt showing its inner diameter of 8 nm. **(a)** Possible ionic interaction of positively charged JAa molecules at pH 5.3 or hydrogen bond interaction of uncharged JAa molecules at pH 7.4 **(b)** At proximity, fewer possible interactions of JAa molecules in the centre of the core and inner surface of AFt. Structure generated from Molecular Operating Environment (MOE) software.

LC-MS analysis was beneficial to enable the detection of any possible JAa degradation in samples. Detection of one peak at retention time (RT) ~3.8 with MWt of 424 for JAa but not at RT ~3.5 for JA confirmed that JAa was not degraded/hydrolysed during the processes of encapsulation or release (**Figure 3.18**).

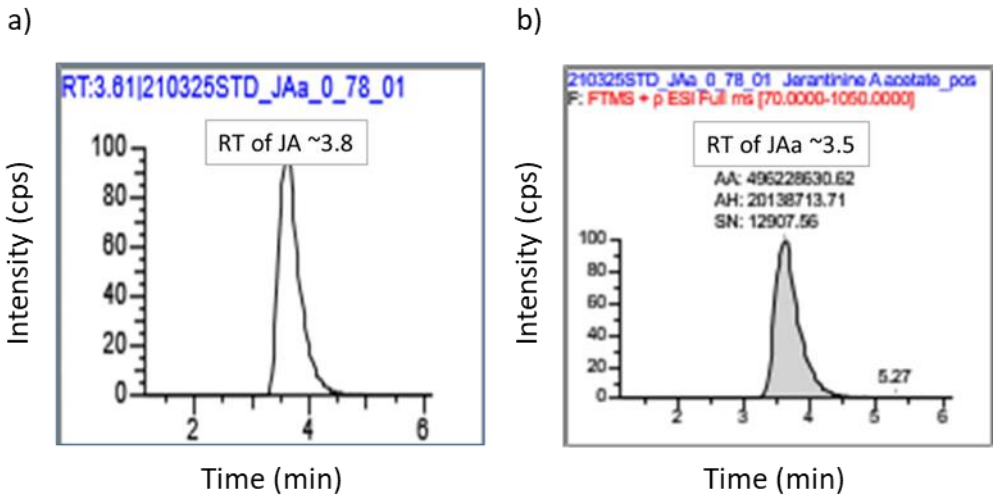


Figure 3.18: LCMS profiles of detected peaks following the release of encapsulated JAa from AFt cage under physiological pH (7.4). **(a)** Peak was not detected at retention time (RT) ~3.8 of JA, **(b)** while the peak of JAa at RT ~ 3.5 was detected for the same sample.

3.4 Conclusion

This Chapter was undertaken to develop and determine the best method to encapsulate JAa inside the core of horse spleen AFt; multiple parameters that contribute to optimised encapsulation were evaluated. The optimisation process of JAa encapsulation through both the nano-reactor route (diffusion method) and the self-assembly route highlighted many parameters to be considered before selecting the best encapsulation route for JAa cargo. Our findings support the use of the nano-reactor route (the diffusion method) to preserve the integrity and characteristics of the AFt cage [118, 308]. However, when choosing the nano-reactor route to encapsulate agents, it is important to consider the lateral dimensions of the agent to be encapsulated. The nano-reactor method is best suited for encapsulation of small MWt molecules or those having a lateral dimension < 0.4 nm [118, 306, 307] but not JAa (dimensions 0.96 nm x 1.26 nm). The encapsulation of cargo through the nano-reactor route is guided not only by cargo size but also by its ionisation state which can easily be manipulated according to the pH of the solution; positively charged molecules are drained through the channels of AFt into the negatively charged interior [407]. We thus optimised the self-assembly method for AFt-encapsulation of JAa with robust and reproducible results. Our observations addressed the conflicts related to the unclear protocols associated with the preparation of AFt formulations which represent a major obstacle to the translation of AFt from experimental to clinical DDS [310]. Our study supports both the previously successful and failed methods of AFt reassembly and identifies the critical component behind the observed

conflict - the buffer composition and its ionic strength. Our validated optimised self-assembly method also resolved the main disadvantage to its use, the low yield of the formulation [375], and recovered ~77% of protein. Characterisation of AFt-JAa has been performed demonstrating the robustness and reproducibility of the method developed and produced a cage with comparable hydrodynamic size, charge and integrity to native AFt. The successful encapsulation of 120 molecules of JAa within horse spleen AFt cavity and PR% of ~70% were achieved by the self-assembly method, with minimum precipitation and high stability over 10 months of storage.

3.5 Future work

1. Future studies need to be carried out to validate our reassembly method on H-AFt to further progress pre-clinical (and eventual clinical) studies.
2. The future study should be tested using both the non-glycosylated and glycosylated H-AFt as the half-life of glycosylated Ft is ten times longer than non-glycosylated Ft which may impact the final formulation kinetic profile in future clinical studies [408].
3. The encapsulation of large molecules through the nano-reactor route should be investigated by relaxing the cage using the proton NMR relaxation method [309] and using *Archaeoglobus fulgidus* Ft, which possesses wider channels ~4.5 nm [409].

4 Enhancing activity and selectivity of jerantinine A acetate in breast carcinomas upon apoferritin-encapsulation

4.1 Introduction

Jerantinines exhibit potent antitumour activity against diverse carcinoma cell lines including colorectal (HCT-116, HT-29), breast (MCF-7, MDA-MB-468), lung (A549) and pancreatic (MIA PaCa-2) cancer models [202, 203]. Jerantinines may also represent a potential alternative therapy in carcinoma cells that possess acquired drug resistance. This was exemplified in KB cells with (IC_{50} < 1µg/ml) [197], and paediatric medulloblastoma [217]. In addition to its potential use in human-derived colorectal (HCT- 116) cells that developed MDR upon long term exposure to escalating VCR concentrations [203].

Being indole alkaloids, jerantinines share a similar structure and main mechanism of action to vinca alkaloids (e.g, VCR) by inhibiting microtubules' polymerisation [202, 203, 410], However, the tubulin-binding site is distinct from VCR, jerantinines bind to colchicine binding site as reported previously in X-ray crystallography studies [201].

The non-selective activity of jerantinines reported following the treatment of MRC-5 normal fibroblasts might anticipate systemic toxicity and thus restrict its prospective treatment use [202, 203]. Thus, the need for caution regarding toxicity

to normal cells has led to consideration of development of a vehicle to deliver JAa selectively to cancer cells [411].

In an attempt to enhance cancer patients' quality of life and reduce mortality, the development of therapies such as targeted delivery of NPs has been successfully reported to reduce drug resistance and toxicities in different cancer types including breast cancer [213, 412-414]. NPs' enhanced activity of several anticancer agents has been reported in many *in vitro* [415-417] and *in vivo* studies [418-423]. Similar to other NPs, AFt was successfully employed for targeted delivery of chemotherapeutic agents due to its biocompatibility, biodegradability and self-targeting property through selective binding of its H subunits to TFR1 that is overexpressed by tumour cells [113, 279, 285, 301-303, 374, 424]. As TFR1 is also overexpressed in breast cancer cells, AFt represents a promising excellent DDS in the treatment of breast cancer [113].

4.2 Chapter aims

The goals of research described within this Chapter include:

- Evaluation of targeting distinct subtypes of breast cancer (MCF-7 - luminal A, ER+; BT-474 - luminal B, HER2+; SKBR-3, HER2 overexpression; MDA-MB-468 - basal-like, TNBC; MDA-MB-231 - claudin-low, TNBC) versus non-transformed phenotypes (MCF-10A breast cells besides MRC-5 foetal fibroblasts) with AFt by determining TFR1 expression in each breast cancer cell line.
- Evaluation of the biocompatibility of AFt against the aforementioned cell lines.
- Evaluation of the effect of naked JAa and AFt-encapsulated JAa in terms of toxicity and selectivity in the cell lines by conducting MTT assays and validating the results with other *in vitro* viable cell counting and clonogenic assays.
- Assessment of AFt cellular uptake to determine whether intracellular accumulation of AFt correlates with TFR1 expression levels, and thus the changes in the JAa's activity following its encapsulation.

4.3 Results and discussion

4.3.1 Expression of the transferrin receptor in breast cancer and non-transformed cell lines

To examine the possibility of targeting breast cancer cells using AFt NPs, the expression of TFR1 was investigated in the seven selected cell lines. AFt is mainly but not exclusively sequestered through TFR1; SCARA-5 and TFR2 proteins also contribute to the intracellular uptake of Ft through the recognition of L-chain and H-chain respectively [111, 425]. Thus, their cellular levels were also evaluated alongside the levels of TFR1 in whole-cell lysates. Using the western blotting technique (see Section 2.3.3), cell lysates containing 40 µg protein determined by the Bradford assay (see Section 2.2.1) were loaded and run by SDS PAGE. Western blots detected diverse expressions of TFR1 in all breast cancer cell lines, whereas, in MRC-5 fibroblast lysates, expression of TFR1 was below detectable levels (**Figure 4.1a**). Significant differences in the expression of TFR1 in lysates of MCF-7, BT-474, MCF-10A and SKBR-3 cells were detected compared to MRC-5 lysates ($P < 0.0001$) (**Figure 4.1b**). While a non-significant difference in the expression of TFR1 from MRC-5 in the lysates of triple-negative cells; MDA-MB-231 and MDA-MB-468 ($p > 0.05$). Lysates of MDA-MB-231 and MRC-5 containing 50 µg protein were also evaluated by western blot for the expression of TFR1 (**Figure 4.1c)**.

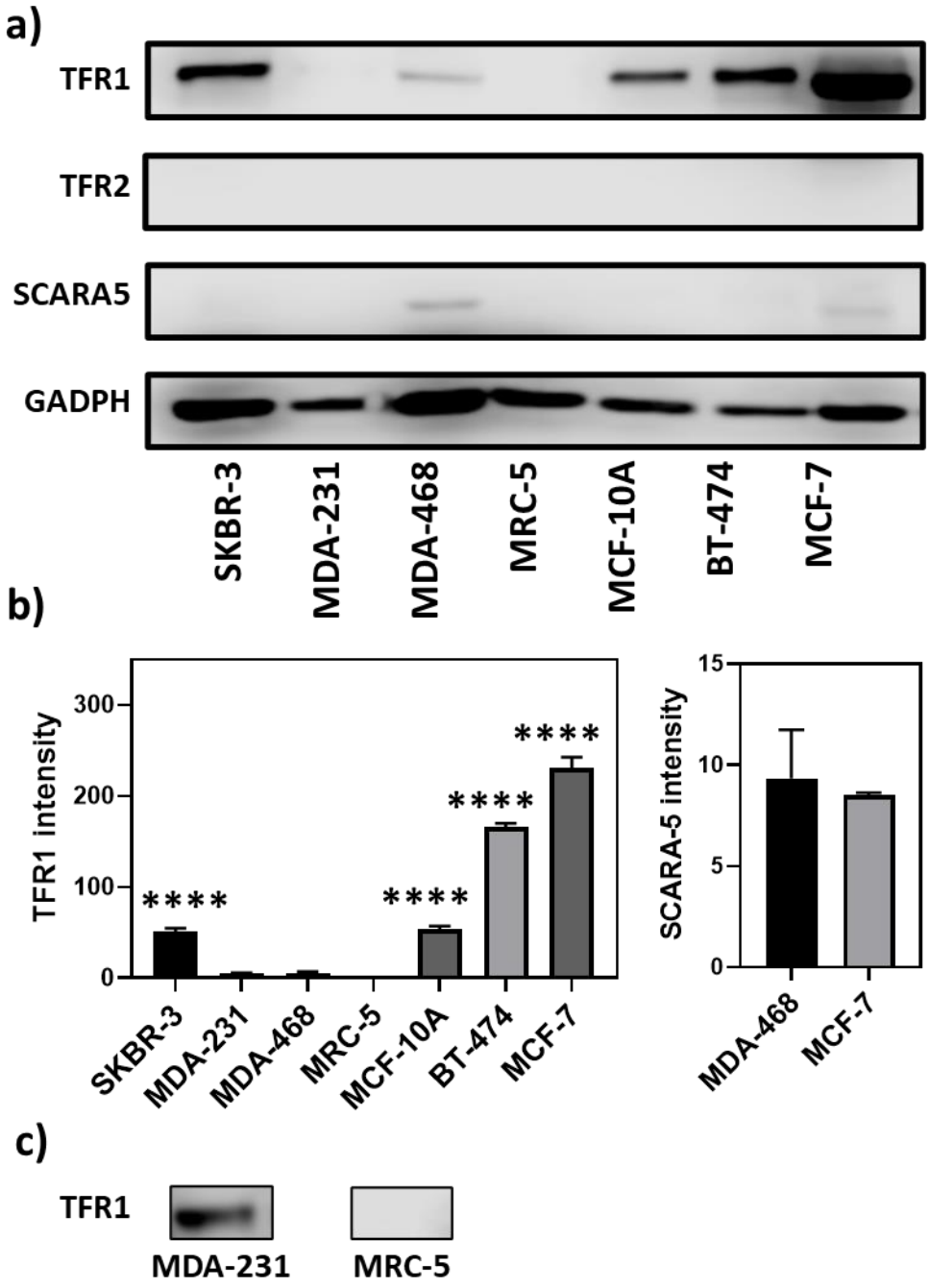


Figure 4.1: **(a)** Expression of TFR1, TRF2 and SCARA-5 in cell lines using immunoblotting technique of cell lysates containing 40 µg protein. **(b)** Densitometry analysis of TFR1 and SCARA-5 proteins normalised to the housekeeping gene (GAPDH). **(c)** Expression of TFR1 in MDA-MB-231 and MRC-5 lysates containing 50 µg protein. Values are reported as mean ± SD for 3 independent trials. Significant differences from MRC-5 are expressed as ****P < 0.0001.

Weak expression of SCARA-5 in MDA-MB-468 and MCF-7 lysates and undetectable expression levels of TFR2 are seen in all tested cell lines (**Figure 4.1a**). Thus, suggesting that the uptake of AFt is primarily *via* TFR1 in tested cell lines.

In western blot, despite a) loading the same amount of protein per lysate and also b) comparing expression to a house-keeping protein (GAPDH), the signal generated by protein detection is not linear across the concentration range of samples, thus data are typically considered to be semi-quantitative [342]. Thus, western blot detection of TFR1 was followed by quantitative flow cytometry analysis of TFR1 on the surface of all tested cell lines [357].

In flow cytometric analysis, cells were stained with a human PE-conjugated anti-CD71 1^{o} Ab and analysed using channels FL2 along with the control for the same cell type (non-labelled cells). The expression of membrane-bound TFR1 was obtained from the shift in fluorescence signals of 10,000 gated single cells for each cell line compared to their control (See Section 2.3.7.3).

The representative flow cytometry plots show a significant shift in TFR1 after binding of PE-Anti-TFR1 in breast cancer cell lines in blue (SKBR-3, MDA-MB-231, MDA-MB-468, MCF-10A, BT-474, and MCF-7) compared to their controls ($P < 0.0001$), reflecting its high expression in these cells (**Figure 4.2**). In contrast, the shift in the signal of labelled MRC-5 cells was indistinguishable from the control non-labelled cells ($p > 0.05$), hence MRC-5 cells were thus termed TFR1-low cells.

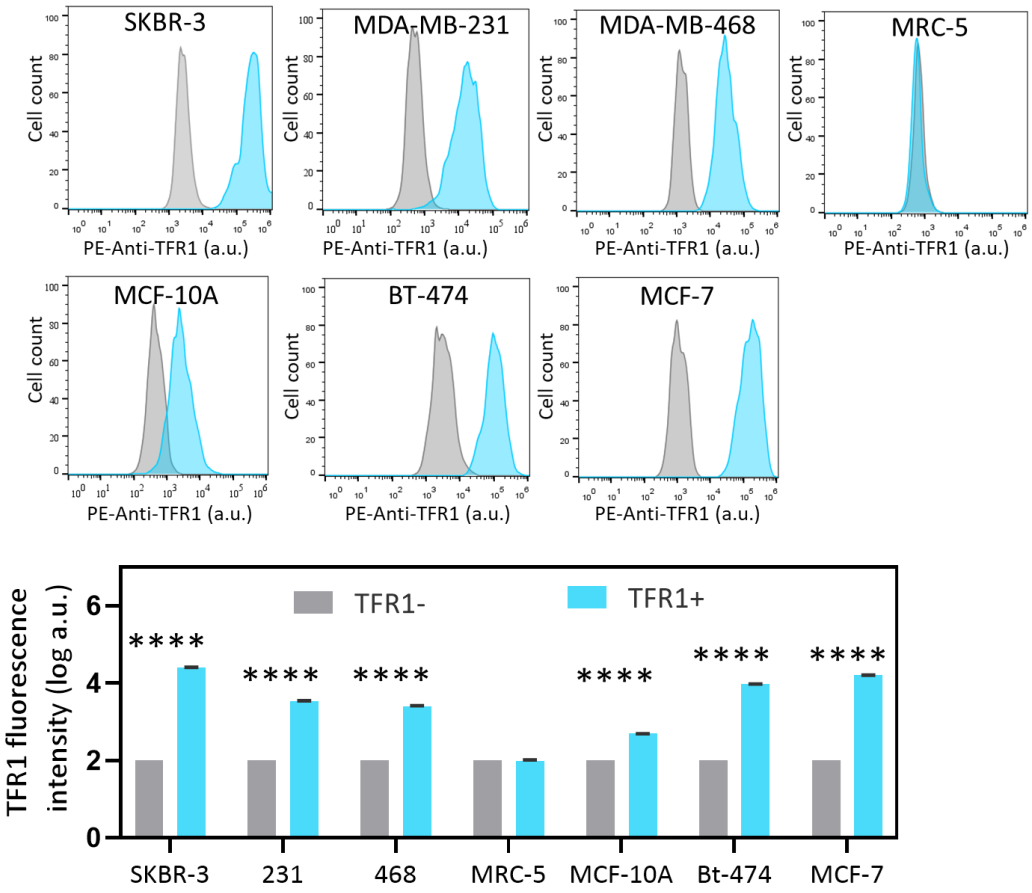


Figure 4.2: Flow cytometric quantification of TFR1 expression in SKBR-3, MDA-MB-231, MDA-MB-468, MRC-5, MCF-10A, BT-474 and MCF-7. Graphs represent median values ± SD (*n* = 3) for 2 independent trials. Significant expressions from control un-labelled cells were expressed as ****P < 0.0001.

Of note, results obtained for the expression of TFR1 from the WB and flow cytometry analysis show no correlation for some cell lines. For instance, in TNBC (MDA-MB-231 and MDA-MB-468) cells show a weak band for TFR1 in western blots but a significant shift in their signals with the flow cytometry analysis. The opposite is seen with MCF-10A cells. An explanation might be related to the differences in the ratio of intracellular to extracellular levels of TFR1, which can be detected only with whole lysates evaluated by western blot. Therefore, the detected weak western blot signals in cells with high shifts in flow cytometry indicate lower total TFR1 in these cell lines, however more (active) membrane-

bound TFR1, as flow cytometry only detects intact, properly folded, surface-exposed protein and thus functional TFR1 levels [357]. These results further support the previously-detected high ratio of TFR1 to intracellular organelles, as a consequence of spontaneous endocytosis and recycling [426].

High expression of TFR1, confirmed in breast cancer cells by both immunohistochemical semi-quantitative analysis and flow cytometric analysis, provides an exceptional opportunity for active targeting by AFt [113, 374, 427]. As mentioned earlier (Section 1.2.5.1), high levels of active TFR1 seen in carcinoma cells may be related to (and a consequence of) high iron demand, inflammation, oxidative stress, and hypoxia associated with cancer microenvironments [116, 427-429]. In addition to its participation in tumour onset and progression. The high level of TFR1 in MCF-7 cells was found to be caused by the high expression level of *TFRC* [430] and might serve as a biomarker for early detection of ER+/PR+ ductal breast cancer due to its high expression level compared to control signals [127]. Previous findings also highlighted the positive correlation between upregulation of TFR1 and oncogenic EGFR and HER2 found in aggressive breast cancers. In TNBC (associated with poor prognosis), where EGFR acts as an oncogenic protein [431], a positive correlation between membrane TFR1 expression and EGFR activation has been reported. It has been shown that EGFR is required for cellular iron import by binding to and regulating the subcellular distribution of TFR1 [432]. In HER2-expressing cell lines (BT-474 and SKBR-3), the higher HER2 activity increases the rate of HIF-1α synthesis [433], which binds to specific promoter elements leading to overexpressed *TFRC* to promote iron-import [434].

All tested breast cell lines including non-transformed MCF-10A measured significantly higher levels of surface-exposed functional TFR1 levels compared to normal MRC-5 fibroblasts ($P < 0.0001$). Thus, MRC-5 cells provide appropriate negative control for our studies. Although previous immunohistochemical studies reported significantly higher levels of TFR1 with breast carcinoma in situ, invasive breast carcinomas and higher breast tumour grade compared with normal or benign breast tissues [126, 435], upregulation of TFR1 expression may also be associated with benign proliferative pathologies such as mammary gland fibrocystic disease as exemplified by non-tumourigenic MCF-10A cells [436].

4.3.2 *In vitro* growth inhibitory effects of JAa and AFt-encapsulated JAa on breast cell lines

The effect of JAa and its AFt-encapsulated form, in addition to the empty AFt protein on the growth of cells, was initially assessed using two selected cell lines; HER2-overexpressing SKBR-3 and TNBC MDA-MB-231 that highly expresses EGFR [437]. The anti-proliferative effects of the above-mentioned test agents were first evaluated using the MTT assay (see section 2.3.4). This assay is based on the conversion of yellow water-soluble tetrazolium-based MTT reagent into purple formazan crystals through the mitochondrial dehydrogenases of viable cells; the intensity of formazan is directly proportional to the number of viable cells [438]. The *in vitro* MTT assay was adopted in accordance with previous studies conducted to evaluate the activity of jerantinines on cancer cells' growth and viability [202, 203].

Cells were evaluated by MTT assays after being exposed to JAa, AFt-JAa (0.02 – 5 µM JAa), and AFt (0.17- 40 nM) equivalent to its concentrations in the formulation for 24 h, 48 h, and 72 h.

In **Figure 4.3**, growth inhibition profiles for both cell lines show time- and concentration-dependent reduction in the growth of the cells treated with naked JAa. The growth inhibitory effect of JAa was detected at lower concentrations in SKBR-3 cells than MDA-MB-231: ~60% growth inhibition of SKBR-3 cells was detected following their exposure to 0.5 µM JAa at both 48 h and 72 h (**Figure 4.3**), while in MDA-MB-231 cells, the growth was comparable to the control cells under the same treatment conditions. These results demonstrate JAa's s disparate activity against the two breast cancer cell lines, higher sensitivity of SKBR-3 and more resistance of TNBC MDA-MB-231 to JAa treatment at low concentrations and corroborate JAa's s high anticancer potency as a natural alkaloid derivative [202, 203].

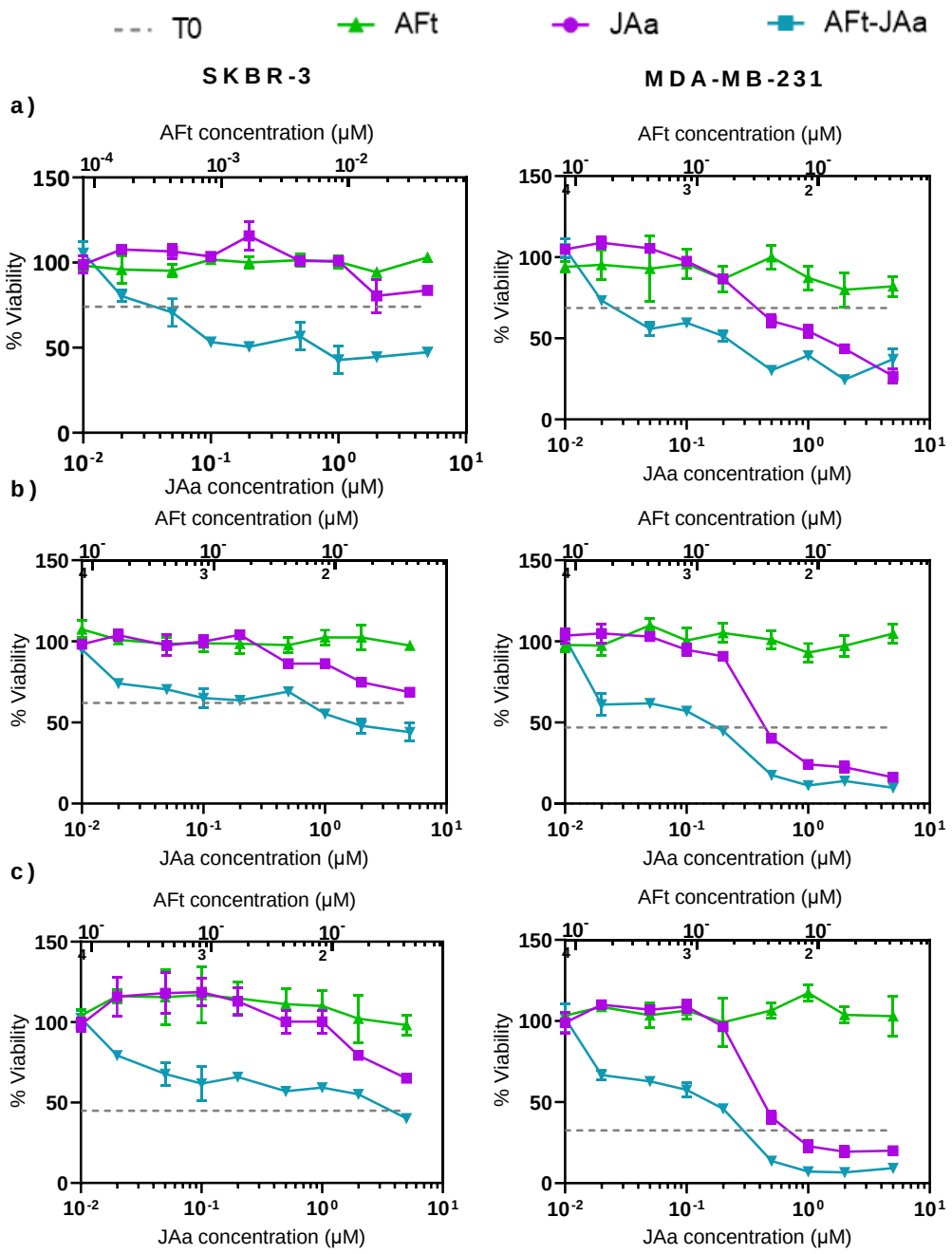


Figure 4.3: Representative MTT graphs displaying the growth inhibitory properties of AFt encapsulated JAa, JAa, and AFt alone on SKBR-3 and MDA-MB-231 cells. Cells were seeded in 96-well plates at a density of 4 x 10^3 cells/well. After allowing to adhere (24 h), cells were treated and incubated for **(a)** 24 h, **(b)** 48 h, and **(c)** 72 h. Mean ± SD of representative experiments are shown (n ≥ 3 per trial); MTT assays were repeated 3 times.

Interestingly, both SKBR-3 and MDA-MB-231 cells were more sensitive to JAa at all used concentrations (≥ 0.02 μM) when it was delivered to the cells within AFt nanocapsules at all tested time points (24 h, 48 h, and 72 h). For example, AFt-JAa (0.5 μM JAa) inhibited the growth of SKBR-3 cells by ~82% and ~86% and MDA-MB-231 by 31% and 43% following 48 h and 72 h exposure respectively (**Figure 4.3**). The growth of cells was also evaluated following treatment of cells with DMSO vehicle at its highest-used concentration in MTT assays (0.05%); no effect on absorbance readings in either cell line was detected (data not shown). These observations demonstrate that the activity of JAa is enhanced following its encapsulation within the core of AFt and again demonstrate the higher sensitivity of SKBR-3 to the treatment. AFt, at all concentrations (≤ 40 nM) has no effect on the growth of cells, reflecting its biocompatibility, corroborating previous findings [118].

To evaluate and compare the activity of both naked and encapsulated JAa, estimated GI_{50} values were calculated; the concentration of the test agent that inhibits the growth of cells by 50% (see Section 2.3.4). Log GI_{50} is shown in **Figure 4.4** for better presentation due to high variants between GI_{50} values.

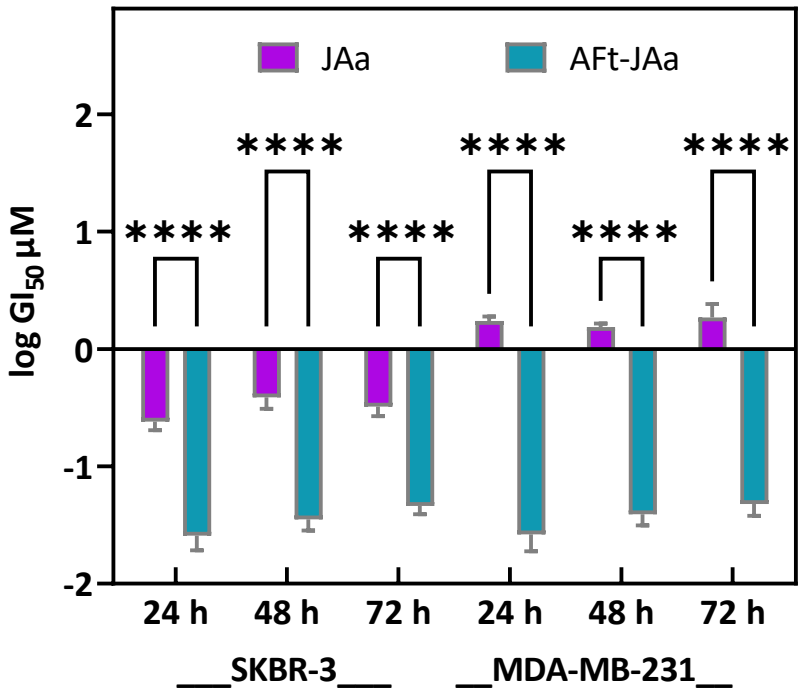


Figure 4.4: Summary of log GI_{50} values (µM) of JAa and encapsulated AFt-JAa on SKBR-3 and MDA-MB-231 cells at different exposure times. Cells were seeded in 96-well plates (n ≥ 3) at a density of 4 x 10^3 cells/well. Cells were treated incubated for 24 h, 48 h, and 72 h after allowing them to adhere for 24 h. Data points represent log GI_{50} mean ± SD (n ≥ 3); representative of 3 independent trials. Significant differences are expressed as ****P < 0.0001.

JAa revealed high potency with GI_{50} ~ 0.20 – 0.45 µM in SKBR-3 cells and ~1.4 – 2.4 µM in MDA-MB-231 cells (24 h – 72 h). Treatment with encapsulated JAa clearly shows greater potency than naked JAa, represented by a significant reduction in GI_{50} values at all different exposure times (P < 0.0001).

The high potency of JAa seen with our data agrees with the previously reported for JA and JB that showed a high potency (GI_{50} values of <1 µM) against two breast cancer cell lines: MCF-7 (ER+, luminal A subtype) and MDA-MB-468 (TNBC, basal-like subtype) [202, 203]. In addition, previously when treating Mia PaCa-2 cells

with JB, cells appeared to have greater growth after a 72 h (compared to 24 h) exposure to JB at 1x GI_{50}; some ability to recover was speculated [439].

Subsequent assessment of the growth of all studied breast cancer cell lines was conducted using MTT assays. One breast cell line for each subtype was used for this evaluation: MCF-7 for luminal A (strongly ER+ and PR+), BT-474 for luminal B (lower ER, PR expression, and HER2+), SKBR-3 for HER2 overexpression (ER–, PR–, and HER2+), MDA-MB-468 for basal-like (EGFR+), MDA-MB-231 for claudin-low (EGFR+), and MCF-10A for non-tumourigenic phenotype [70, 71]. MRC-5 fibroblasts were used as TFR1-low expressing cells (as described previously in Section 4.3.1). The assessment was done using AFt-encapsulated freshly reconstituted JAa stock, naked JAa, and AFt alone following 48 h exposure, except for BT-474 cells which were treated for 72 h; to allow time for a minimum of one cell cycle division.

Upon the treatment with naked JAa (0.02 – 5 μM JAa), clear concentration-dependent growth inhibition was detected in all tested cell lines (**Figure 4.5**), providing evidence of JAa's activity in breast carcinomas regardless of subtype. A comparison of the growth inhibition between the two most sensitive breast carcinoma cell lines (SKBR-3 and MDA-MB-468) and MRC-5 normal fibroblasts with JAa (5 μM) shows comparable growth inhibition by ~91%; indicating non-selective inhibition (**Figure 4.5.b**).

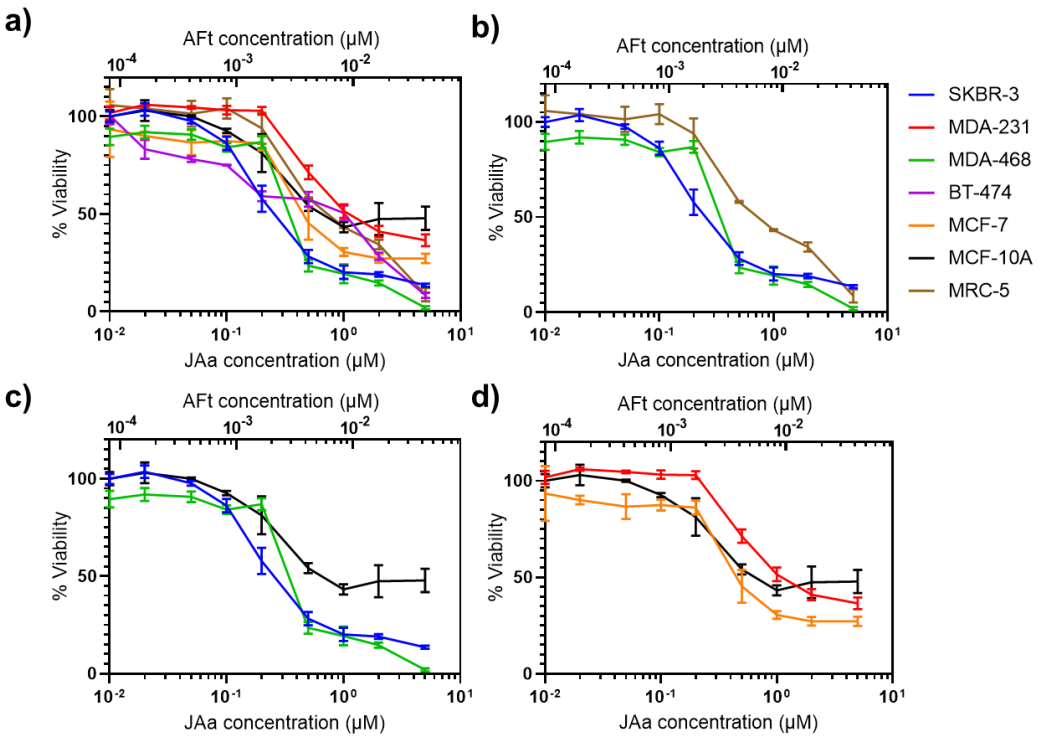


Figure 4.5: Representative MTT graphs displaying **(a)** comparative growth-inhibitory profiles in all studied cell lines after treating with JAa. **(b)** Comparative growth-inhibitory profiles of SKBR-3, MDA-MB-468, and normal MRC-5. **(c)** Comparative growth-inhibitory profiles of SKBR-3, MDA-MB-468, and normal MCF-10A. **(d)** Comparative growth-inhibitory profiles of MCF-7, MDA-MB-231 and normal MCF-10A. Cells were seeded in 96-well plates at a density of 3-5 x 10^3 cells/well. After allowing to adhere (24 h), all cell lines were treated and incubated for 48 h, except for BT-474 which was treated for 72 h and excluded from this comparison. Mean ± SD of representative experiments are shown (n ≥ 3 per trial); MTT assays were repeated 3 times.

To support previous observations, selectivity indices (SI) were calculated to demonstrate the selectivity of JAa for breast cancer cell lines compared to non-cancerous lung (MRC-5) fibroblasts (**Table 4.1**). The SI was calculated by dividing the GI_{50} value in MRC-5 cells by the GI_{50} in the particular breast cancer cell line; SI values > 3 were considered as high selectivity [440]. Except for BT-474, JAa shows low selectivity for breast cancer cells over non-transformed foetal fibroblasts as reflected by SI < 3. The low selectivity of JAa reflected by SI values in all TFR1+ cell

lines supports: i) previous data indicating non-selective growth inhibition of MRC-5 cells when treated with JB and JA [202, 203]; ii) our quest to exploit and target TFR1 overexpression in breast cancer cell lines to deliver the AFt protein nanocarrier and its cargo to breast cancer cells.

Table 4.1: GI_{50}, *TGI*, LC_{50}[a] and selectivity index (SI)[b] values of JAa and its encapsulated form AFt-JAa in all cell lines.

	Cell lines						
	SKBR-3	**MDA-MB-231**	**MDA-MB-468**	**MRC-5**	**MCF-10A**	**BT-474**	**MCF-7**
				GI_{50}			
JAa	0.19± 0.04	0.38± 0.10	0.28± 0.04	0.56± 0.15	0.36± 0.05	0.14± 0.02	0.37± 0.03
AFt-JAa	0.04± 0.02	0.12± 0.07	<0.02	0.53± 0.04	0.03± 0.01	<0.02	0.15± 0.06
				TGI			
JAa	0.30± 0.09	1.15± 0.21	0.48± 0.02	4.10± 0.11	>5.00	1.35± 0.04	0.79± 0.04
AFt-JAa	0.13± 0.02	.53± 0.07	0.21± 0.06	>5.00	1.06± 0.04	0.17± 0.02	0.75± 0.05
				LC_{50}			
JAa	0.22± 0.04	0.58± 0.03	0.35± 0.04	0.68± 0.07	0.27± 0.04	0.36± 0.03	0.30± 0.03
AFt-JAa	0.04± 0.04	0.06± 0.05	<0.02	0.48± 0.05	<0.02	0.05± 0.02	0.14± 0.02
				SI			
JAa	2.9	1.4	1.9	-	1.5	24.4c	1.5
AFt-JAa	13.5	4.6	26.7	-	18	64.5c	3.5
TFR1 expression	250	33	24	NA	4	92	158

[a] GI_{50}, *TGI* and LC_{50} values are presented as mean ± SD from three independent MTT assays (n = 3).

[b] SI values > 3 were considered high selective [440].

[c] GI_{50} values of BT-474 to MRC-5 after 72 h exposure were considered to calculate SI values.

[d] TFR1 expression from flow cytometry data was calculated in fold-increase in comparison to the normalised fluorescence signal from labelled MRC-5 cells (TFR1-).

On the other hand, comparative growth inhibition curves between cancerous breast cell lines and non-cancerous MCF-10A show growth inhibition of MCF-10A by ~52% and greater growth inhibition of MDA-MB-468 and SKBR-3 by 98% and ~86% respectively with JAa treatment at a concentration of 5 µM (**Figures 4.5c**). At the same concentration, JAa inhibited the growth of MCF-7 by ~72% and MDA-

MB-231 by ~63% (**Figures 4.5d**). These observations reflect some selectivity of JAa for cancerous breast cell lines over non-cancerous MCF-10A cells at high concentrations only (> 2 μM) and corroborate a previous report of the selectivity of JA for two breast cancer cells (MDA-MB-468, and MCF-7) over non-cancerous MCF-10A cells [204]. In the previous study, a combined proteomic and functional genomic analysis showed that JA exerts its antitumour activity by modulating spliceosome activity, in addition to its reported targeting of tubulin polymerisation. JA was found to upregulate SF3B1 and SF3B3 proteins in MCF-7 and MDA-MB-468 by enhancing their stability rather than transcriptional activation and induced dissociation of the protein from the nucleosome complex in both breast cell lines but not in MCF-10A cells. The induction of SF3B1 further impaired mRNA splicing activity and induced specific apoptosis in breast cancer cells**.** However, as selectivity was detected only at a high concentration of JAa, and as using high concentrations of antitumour agents anticipates more systemic toxicity, the development of a vehicle to deliver JAa selectively to cancer cells is necessitated [411].

Following treatment of cells with AFt-JAa (0.02 – 5 μM JAa) and AFt (0.17- 40 nM), the specific growth inhibition profiles for each cell line following all different treatment conditions including naked JAa is shown in **Figure 4.6**.

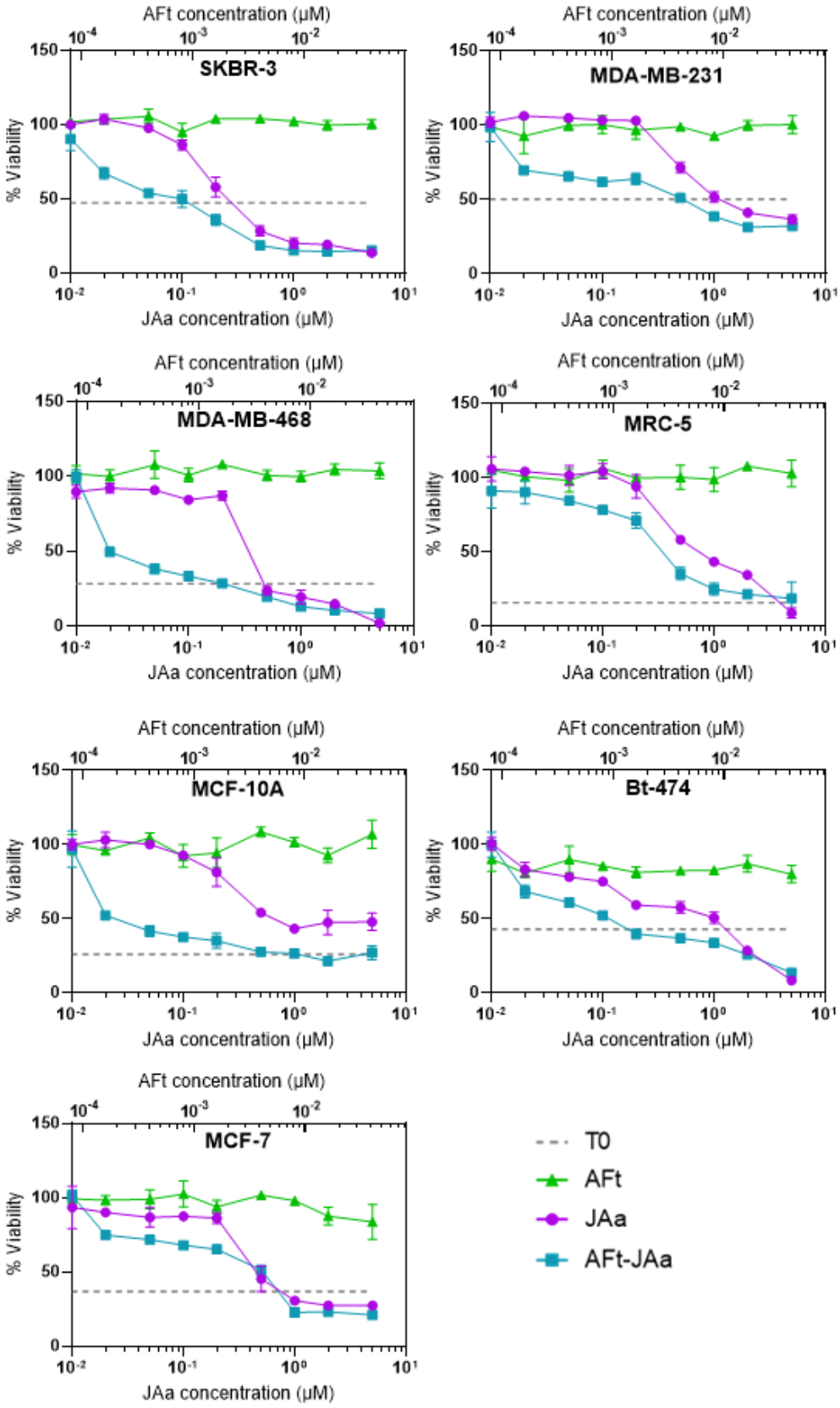

AFt concentration (μM)
SKBR-3
MDA-MB-231
MDA-MB-468
MRC-5
MCF-10A
Bt-474
MCF-7
% Viability
JAa concentration (μM)
T0
AFt
JAa
AFt-JAa

Figure 4.6: Representative MTT graphs from a single trial displaying the growth inhibitory properties of AFt encapsulating JAa, JAa, and AFt alone in seven selected cell lines. Cells were seeded in 96-well plates at a density of 3-5 x 10^3 cells/well. After allowing to adhere (24 h), cells were treated and incubated for 48 h. BT-474 was incubated for 72 h. All cell lines show a reduction in growth when treated with JAa and AFt-JAa. AFt did not affect the growth of the cells. Mean ± SD of representative experiments are shown (n ≥ 3 per trial); MTT assays were repeated 3 times.

AFt alone demonstrated a non-detrimental effect on the growth of cells at all concentrations (≤ 40 nM), confirming its biocompatibility (**Figure 4.6**). Interestingly, greater growth inhibition was evident in all cell lines following the delivery of JAa through AFt NPs even at the lowest-used concentration of 0.02 µM (**Figure 4.6**) reflecting its higher potency. Compared to treatment with naked JAa, a significant reduction in GI_{50} values was detected following treatment with AFt-JAa in all used breast cell lines ($P < 0.05$), thus indicating significantly enhanced activity following AFt-encapsulation (**Figure 4.7**).

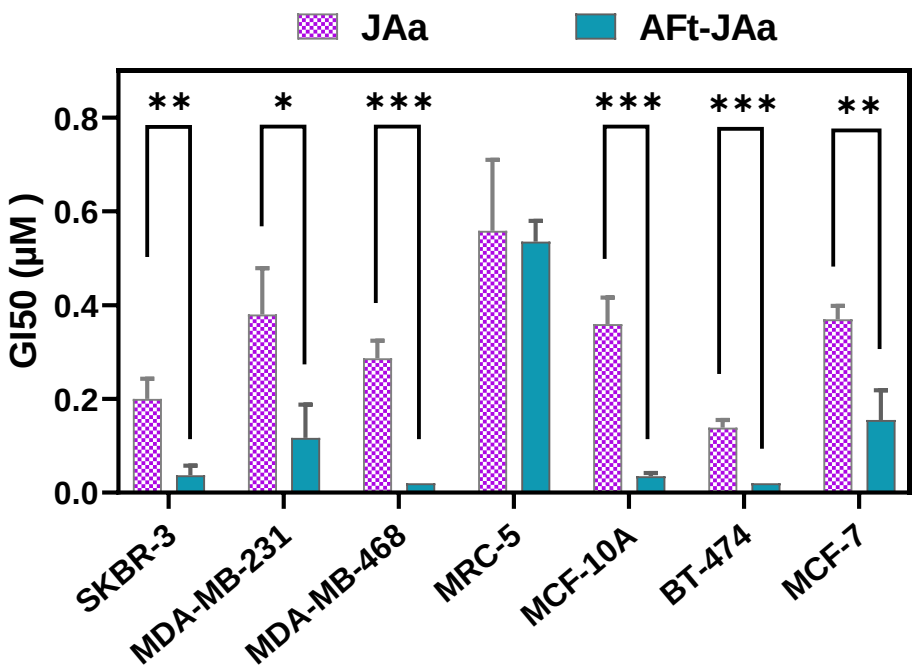


Figure 4.7: Growth inhibitory activity of JAa and its encapsulated form (AFt-JAa) represented by mean ± SEM GI_{50} values in seven cell lines. Data points represent GI_{50} mean ± SD (n ≥ 3); representative of 3 independent trials. 3-4 x 10^3 cells/well were exposed to test agents for 48 h. Significant differences were measured using multiple unpaired t-tests and expressed as *P < 0.05, **P < 0.01, and ***P < 0.001 in bracket.

A non-significant reduction of GI_{50} values was detected in TFR1-low expressing MRC-5 cells (p > 0.05) following the treatment with AFt-encapsulated JAa (**Figure 4.7**). This indicated enhanced selectivity in TFR1+ cells was supported by calculating their SI values to TFR1-low expressing MRC-5 cells (**Table 4.1**). After 48 h of exposure, AFt-encapsulated JAa inhibited the growth of all TFR1+ cells with high selectivity compared to the TFR1- low expressing cells; represented by SI values (~3.5 -~26.5). This selectivity can also be seen in the comparative growth inhibition profiles in **Figure 4.8** following the treatment of AFt-JAa even at low treated concentrations (≥ 0.02 µM).

In addition to the estimated GI_{50} values, the concentration of agent required to kill 50% of initially-treated cells (LC_{50}), and total growth inhibitory (*TGI*) values were estimated for all tested cells (**Table 4.1**). Data acquired from these two parameters also support the observation made with GI_{50} values. For example, estimated *TGI* values for all breast cells when treated with the encapsulated agent were lower than concentrations of naked JAa; corresponding to enhanced potency. On the other hand, the higher estimated *TGI* value (> 5 µM) when MRC-5 cells were exposed to encapsulated agent indicates its selectivity and confirms the potential of AFt-encapsulation to target TFR1-overexpressing cell lines.

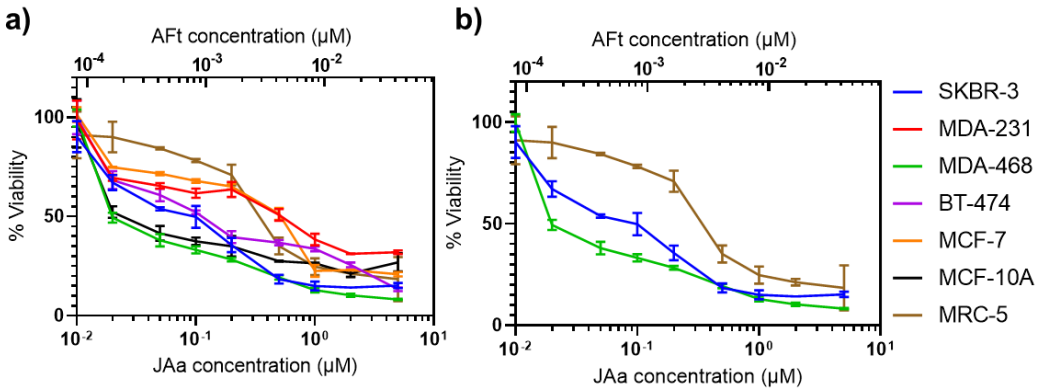


Figure 4.8: Representative MTT graphs from a single representative trial displaying **(a)** comparative growth-inhibitory profiles in all studied cell lines after treatment with AFt-JAa. **(b)** Representative enhanced selectivity of AFt-encapsulating JAa represented by higher growth inhibition at low concentrations of two selected TFR1+ cells (MDA-MB-468 and SKBR-3) compared to non-cancerous TFR1-low expressing MRC-5 cells. Cells were seeded in 96-well plates at a density of 3-5 x 10^3 cells/well. After allowing to adhere (24 h), all cell lines were treated and incubated for 48 h, except for BT-474 which was treated for 72 h. Mean ± SD of representative experiments are shown (n ≥ 3 per trial); MTT assays were repeated 3 times.

Of note, most tested cell lines show similar activities of JAa and its encapsulated form at high concentrations (≥ 2 µM JAa) as shown in **Figure 4.6**. We can speculate that at high concentrations of treated JAa, the tubulin-binding site of JAa can be saturated and no selectivity can be further detected between JAa and its encapsulated form. This also encourages the use of AFt NPs to safely deliver small doses of encapsulated agents and to reduce systemic toxicity.

4.3.3 *In vitro* cell viability effects of JAa and AFt-encapsulated JAa on breast cancer cell lines

The previous initial results for enhancing JAa activity upon its encapsulation inside AFt obtained from MTT assays were further validated using viable cell counting

assays. As outlined in Section 2.3.5, the MTT assay is associated with limitations, and specifically measures tetrazolium reduction by mitochondrial metabolic activity. Therefore, *in vitro* cell counting assays were conducted to evaluate the effects of JAa and its encapsulated form on cell proliferation and viability [441, 442].

The validation of MTT assay results was performed using three selected breast cancer cell lines; SKBR-3 (aggressive cells with high sensitivity to JAa treatment), MDA-MB-231 (highly aggressive cells with moderate sensitivity to JAa treatment), and MCF-7 (low aggressive cells with moderate sensitivity to JAa treatment) following 48 h exposure of cells to JAa, AFt-JAa (0.2 µM JAa), AFt (0.0017 µM) or appropriate media alone. This JAa concentration was selected as in MTT assays, and considerable differences in growth inhibition between naked- and AFt-encapsulated JAa were detected (**Figure 4.6**).

In SKBR-3 (one of the most sensitive cell lines to JAa treatment as detected from MTT assays) viable cell counting assays showed a significant reduction in viable cells following the treatment with both JAa and AFt-JAa ($P < 0.01$ compared to control) with fewer cells counted following exposure of cells to encapsulated JAa ($P < 0.01$ compared to cells treated with naked JAa) (**Figure 4.9a**). In MDA-MB-231 (a less sensitive cell line to JAa as detected in MTT assays), viable cell numbers comparable to control were counted following the treatment with the free agent (**Figure 4.9b**), however, a significant reduction of viable cells numbers was detected following their exposure to encapsulated JAa compared to naked JAa ($P < 0.05$). In MCF-7 cells lower but non-significant ($p > 0.05$) viable cell numbers were

counted with the free agent, but a significant reduction of viable cells numbers was counted following exposure to encapsulated JAa compared to control ($P < 0.05$) but non-significant when compared to the free agent ($p > 0.05$). Exposure of all cells to AFt alone (0.0017 µM) did not show any detrimental effect on viable cell numbers. In all cell lines, fewer viable cell numbers were evident following encapsulated JAa treatment, corroborating data obtained by MTT assay; indicating enhanced activity of JAa following delivery by AFt nanocarrier to the cells.

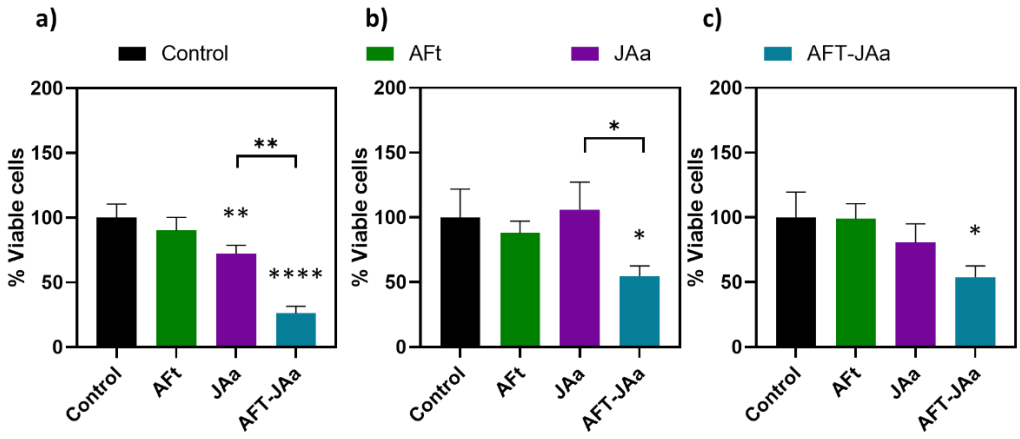


Figure 4.9: *In vitro* cell viability assays in **(a)** SKBR-3, **(b)** MDA-MB-231 and **(c)** MCF-7 following treatment with JAa, AFt-JAa (0.2 µM JAa), AFt (0.0017 µM) or media alone for 48 h. Cells (2 x 10^4 cells/well) were seeded in 6-well plates and incubated overnight before the treatment. Cells were harvested stained with trypan blue and counted by haemocytometer. Values are reported as mean ± SD ($n = 3$). Significant differences from the control for ≥ 3 independent trials are expressed as *P < 0.05, **P < 0.01, and ****P < 0.0001. Significant difference from JAa is expressed in brackets.

4.3.4 Effects of JAa and AFt-encapsulated JAa on colony formation of breast cancer cell lines

Following the validation of our initial results by cell counting assays, clonogenic assays were performed. Clonogenic assays were carried out to evaluate the ability of single breast cancer cells to survive a brief challenge with naked and

encapsulated JAa and retain their proliferative capacity to form progeny colonies. To mirror MTT assay treatment conditions, SKBR-3, MDA-MB-468, and MCF-7 were treated for 48 h and BT-474 for 72 h. *SF*% was calculated after cells were exposed to JAa, AFt-JAa (0.2 μM and 0.4 μM JAa), and AFt (0.0033 μM) equivalent to the highest concentration of AFt in AFt-JAa used in the assay.

As illustrated in **Figure 4.10** and **Figure 4.11**, comparable colony formation resulted with both control (medium alone) and AFt treatment in all tested cell lines corroborating the biocompatible nature of AFt delivery vehicle. The inhibition of colony formation with JAa and AFt-JAa was significant and dose-dependent in all treated cell lines. In SKBR-3 cells, JAa at concentrations of 0.2 μM and 0.4 μM inhibited colony formation by ~33% and ~81% respectively (**Figure 4.10.a**). SKBR-3 cells were more sensitive to encapsulated JAa; colony inhibition by ~83% and ~93% at concentrations of 0.2 μM and 0.4 μM respectively. Of interest, inhibition of colony formation with AFt-JAa (0.2 μM JAa) was equivalent to the inhibition of colony formation produced by 0.4 μM naked JAa, in agreement with cells' growth inhibition detected in MTT profiles at these treatment concentrations (**Figure 4.6**). AFt-encapsulated JAa demonstrated significantly enhanced activity at a concentration of 0.2 μM JAa ($P < 0.5$) and 0.4 μM ($P < 0.01$) compared to naked JAa (**Figure 4.10.a**), corroborating MTT results.

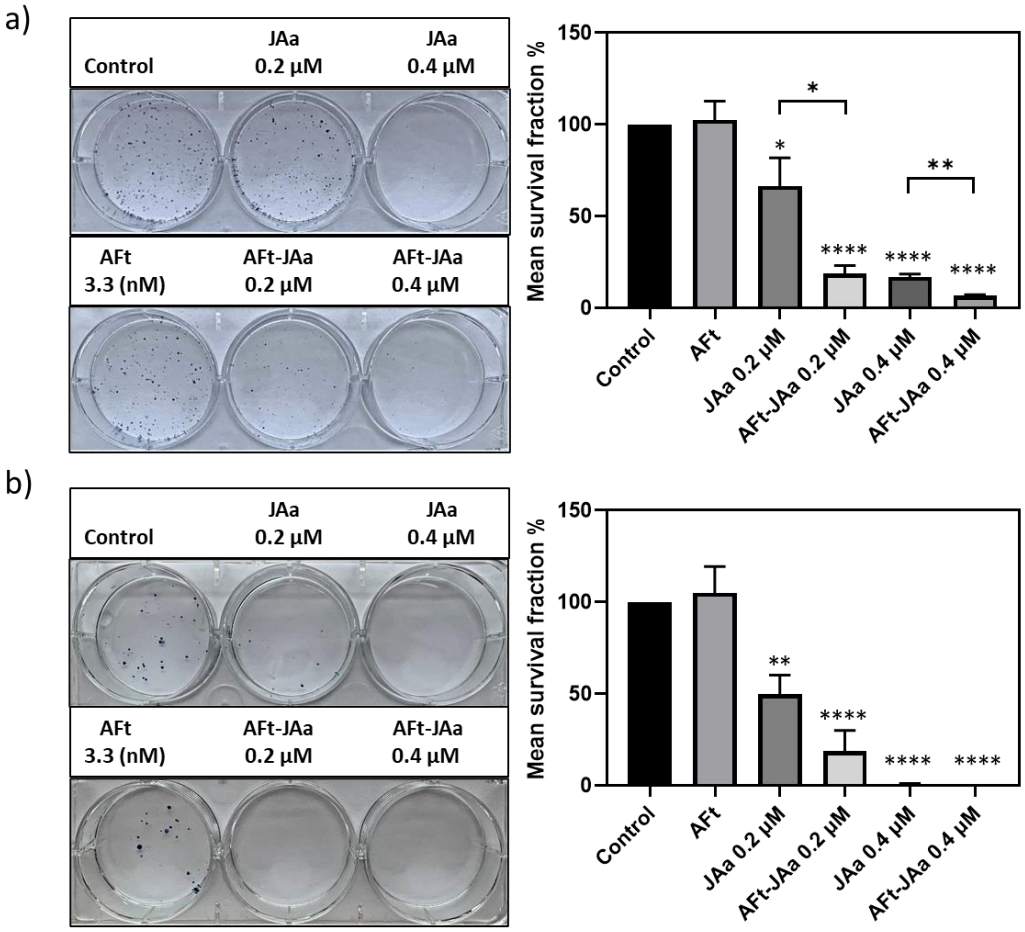


Figure 4.10: Representative images of the clonogenic assays and their percentage survival fractions (*SF*%) conducted on **(a)** SKBR-3 and **(b)** MDA-MB-468 for 48 h treatment with JAa, AFt-JAa (0.2 µM and 0.4 µM JAa), AFt (0.0033 µM) or media alone. Values are reported as mean ± SEM (*n* = 3). Significant differences from the control for ≥ 3 independent trials are expressed as *P < 0.05, **P < 0.01, and ****P < 0.0001. Significant differences from JAa are expressed in brackets.

In MDA-MB-468 at a low concentration of 0.2 µM JAa, significant inhibition of colony formation with naked JAa by ~50% (P < 0.01) and with AFt-JAa by ~81% (P < 0.0001) from control were detected (**Figure 4.10.b**). At 0.4 µM JAa, both free and encapsulated agent showed a comparable significant reduction in colony formation (P < 0.0001) and almost abolished colony formation in all 3 independent

trials by > 99%, reflecting its similar and high potency detected in MTT assays (**Figure 4.6**).

BT-474 colony formation was significantly inhibited by 44% ($P < 0.01$) with free and by 69% ($P < 0.001$) with encapsulated JAa at a concentration of 0.2 µM. At 0.4 µM JAa, both free and encapsulated agent showed significant reductions in colony formation by 60% with the free JAa ($P < 0.001$) and 75% with the encapsulated agent ($P < 0.0001$), indicating dose-related inhibition of clonogenic *SF*% (**Figure 4.11.a**). Of interest at a concentration of 0.2 JAa, AFt-encapsulated JAa demonstrated significantly enhanced activity ($P < 0.5$) compared to naked agent, which again corroborates MTT assay data (**Figure 4.6**) and the thesis that AFt-encapsulation enhances JAa potency.

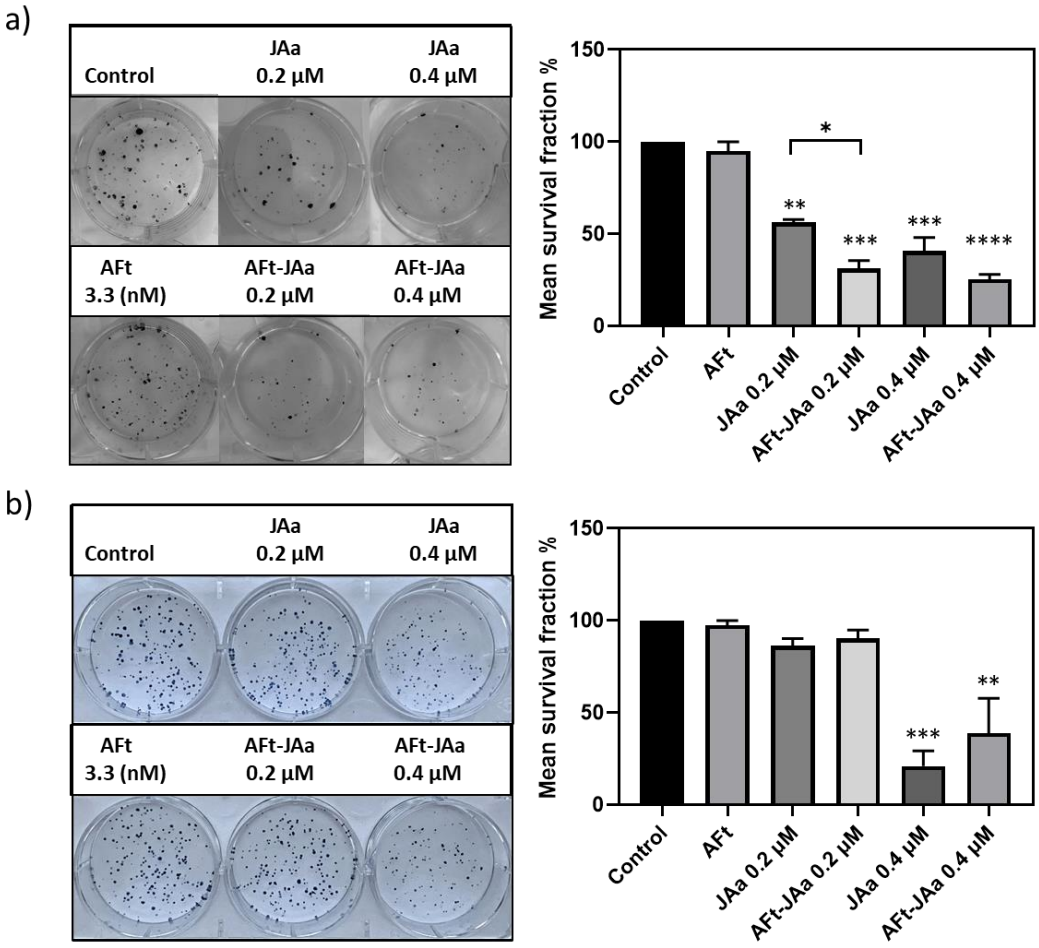


Figure 4.11: Representative images of the clonogenic assays and their percentage survival fractions (*SF*%) conducted on **(a)** BT-474 for 72 h treatment, and **(b)** MCF-7 for 48 h treatment. Cells were treated with JAa, AFt-JAa (0.2 µM and 0.4 µM JAa), AFt (0.0033 µM) or media alone. Values are reported as mean ± SEM (*n* = 3). Significant differences from the control for ≥ 3 independent trials are expressed as *P < 0.05, **P < 0.01, ***P < 0.001, and ****P < 0.0001. Significant difference from JAa is expressed in brackets.

At the lower-used concentration (0.2 µM), MCF-7 showed negligible sensitivity to JAa in clonogenic assays following exposure to both free and encapsulated agent ($p > 0.05$) as shown in **Figure 4.11.b**. These observations indicate that cells have neither been killed nor lost their ability to form progeny colonies. Dose-related inhibition of clonogenic *SF*% was detected; at a concentration of 0.4 µM, free and AFt-encapsulated JAa inhibited colony formation by 79% and 62% respectively.

However, this indicates that in MCF-7, encapsulated JAa at 0.4 µM showed unexpected lower activity compared to free agent and was unrelated to observations seen with other cell lines. This may be a consequence of the slow release of JAa from the core of AFt as discussed in Section 3.3.5. As demonstrated, JAa needed > 24 h to be fully released from the core of AFt. At the doubling time of MCF-7 cells (~18 h), cells will be exposed to a lower JAa amount when delivered within the AFt vehicle compared to the free agent. This will allow more cells to recover and double following treatment with encapsulated JAa and thus impact overall survival. In agreement with our observations, an earlier study reported that cells treated with H-AFt-encapsulated-gefitinib demonstrated higher *SF*% than cells treated with free gefitinib. Reduced potency, detected in clonogenic assays only but not MTT was related to gefitinib's sustained drug release from H-AFt [306]. Another study also showed that AFt encapsulation enhances platinum anticancer's uptake through a slow and sustained pattern [379]. On the other hand, acetate derivatives of jerantinines enhance their stability and hydrophobicity which impact their cellular permeability to and/or retention of jerantinines, in addition, to enhancing potency reported in assays necessitating continued exposure [439]. However, acetate forms are prodrugs, requiring bioactivation by cellular esterase cleavage to release active jerantinines [439]. The very low initial cell numbers in clonogenic assays (~250 cells/well of MCF-7) may produce cellular esterase concentrations below the threshold necessary to convert JAa to JA during the time of JAa exposure. On the other hand, when cells were seeded in higher numbers (700 cells/ well) for SKBR-3 and BT-474, and (400

cells/well) for MDA-MB-468, JAa potency was markedly potentiated by AFt-encapsulation corroborating observations seen from MTT assays.

In summary, significantly reduced colony formation in SKBR-3, BT-474, and MDA-MB-468 TFR1+ cells treated with AFt-encapsulated JAa corroborates enhanced activity seen with MTT and cell count assays.

Enhancing JAa's activity and selectivity in tested cell lines upon treatment with AFt-encapsulated JAa may be due to differences in TFR1 expression (**Figure 4.2**). TFR1 recognises the AFt H subunit and triggers its endocytosis which might further affect the accumulation of JAa inside the cells [113]. Further investigations were conducted to reveal whether the enhanced activity of JAa upon AFt delivery was i) related to enhanced cellular uptake of JAa, or ii) enhanced stability.

4.3.5 Cellular uptake study

The H-AFt cellular uptake study was conducted to correlate its intracellular accumulation with the expression of TFR1 (See Section 2.3.7.4). Intracellular accumulation of AFt will be considered when examining the enhanced activity and selectivity of JAa following AFt encapsulation. As AFt vehicle and JAa are not fluorophores, the study was done using AFt alone after conjugation with a fluorophore to reveal its internalisation by selected cells over time. The cellular uptake and internalisation study of AFt was done using H-AFt conjugated to 5-carboxyfluorescein at a concentration of 40 nM (equivalent to the highest concentration of AFt used in the MTT assay). Carboxyfluorescein was conjugated to the inner surface of H-AFt, as conjugation to AFt's outer surface might affect its

surface properties and thus its uptake mechanism by cells. Measurement of fluorescence signals was performed after washing the cells to exclude the effect of any extracellular AFt NPs on the final fluorescence signal. Intracellular uptake was measured quantitatively using flow cytometry in four TFR1+ cell lines (SKBR-3, MDA-MB-231, BT-474, and MCF-7) in addition to TFR1-low expression MRC-5 fibroblasts. Comparisons were made with control cells incubated with media alone.

Higher accumulation of H-AFt reflected by higher fluorescence signals was evident with time and was detected even at the shorter incubation time of 1 h in all tested cell lines (**Figure 4.12**). With longer exposure times (2.5 h, 4 h, 24) the accumulation of H-AFt started to noticeably vary between cells. For example, at 24 h the mean cellular accumulation of H-AFt increased by 564% and 900% in SKBR-3 and BT-474 respectively compared to their controls. Higher accumulations of H-AFt were also time-dependent in MDA-MB-231 and MCF-7 cells with the highest cellular accumulation detected after 24 h of exposure by 270 % and 340% for each cell line, respectively. Interestingly, following 24 h, MRC-5 cells measured the lowest cellular accumulation of H-AFt compared to other cells.

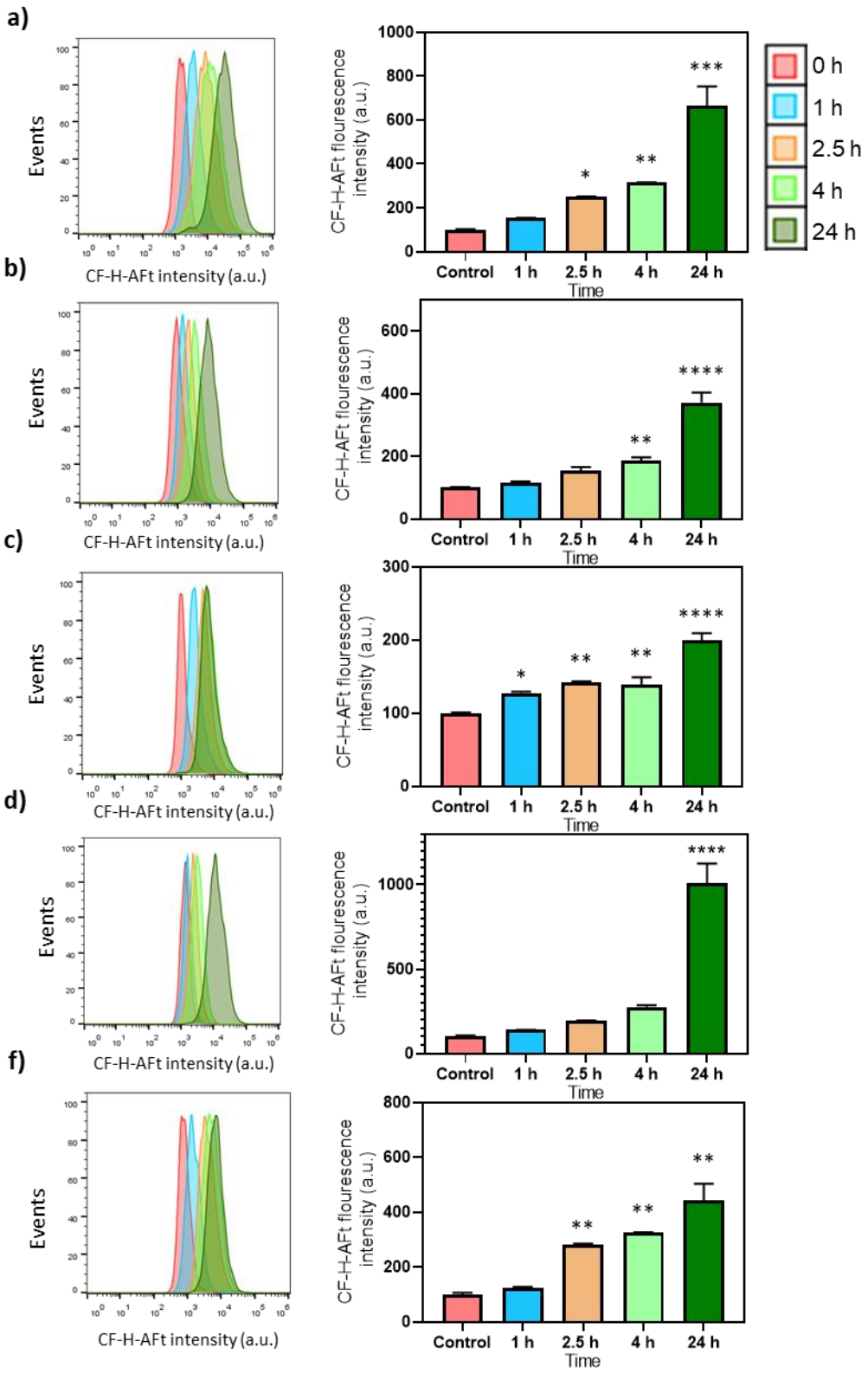


Figure 4.12: Cellular uptake study in **(a)** SKBR-3, **(b)** MDA-MB-231, **(c)** MRC-5, **(d)** BT-474 cells and **(f)** MCF-7 of 5-carboxyfluorescein-conjugated-human-apoferritin (CF-H-AFt, 40 nM) following 1 h, 2:30 h, 4 h and 24 h of exposure. Representative flow cytometry plots showing the shift in H-AFt fluorescence intensity indicating

its cellular uptake (on the left side) and statistical analyses of H-AFt uptake with time compared to control at (0 h) of exposure for each cell line (on the right side). Data are reported as median ± SD (*n* = 3) and repeated 3 times. Significant differences from the control are expressed as *P < 0.05, **P < 0.01, ***P < 0.001 and ****P < 0.0001.

Further statistical analysis of the mean fluorescence intensities performed between TFR1+ cells and TFR1-low expression MRC-5 fibroblasts showed that substantial differences in the accumulation of H-AFt started to emerge after 2.5 h (**Figure 4.13**). For instance, significantly higher H-AFt accumulations by SKBR-3 cells (P < 0.05) and MCF-7 cells (P < 0.01) were detected compared to MRC-5 after 2.5 h of exposure. While a significantly higher H-AFt accumulation with other cells MDA-MB-231 (P < 0.001) and BT-474 (P < 0.01) were detected at longer exposure times of 4 h and 24 h respectively.

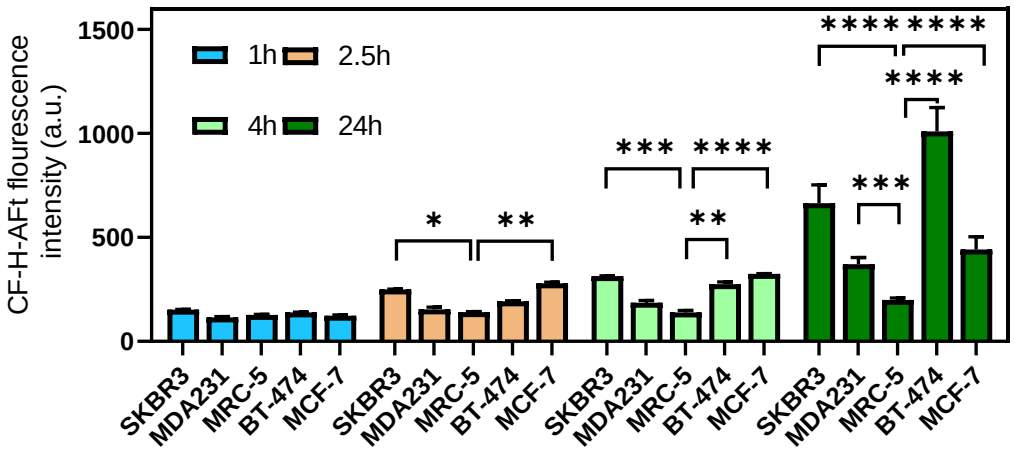


Figure 4.13: Cellular uptake study in TFR1+ cells (SKBR-3, MDA-MB-231, MRC-5, MCF-7 and BT-474) of 5-carboxyfluorescein-conjugated-human-apoferritin (CF-H-AFt, 40 nM) following 1h, 2:30 h, 4 h and 24 h of exposure. statistical analyses of H-AFt uptake with time of TFR1+ cells compared to TFR1-low expression MRC-5 fibroblasts at all exposure times. Data are reported as median ± SD (*n* = 3) and repeated 3 times. Significant differences from the MRC-5 are expressed as *P < 0.05, **P < 0.01, ***P < 0.001 and ****P < 0.0001.

The enhancement in H-AFt accumulation in these TFR1+ breast cancer cell lines is irrefutable and correlates with their higher expression of TFR1 compared to MRC-5. As mentioned earlier, the binding of Ft is mediated by the cellular TFR1, which recognises the Ft H chain and internalises it through clathrin-coated pit-mediated endocytosis [113]. As the H-chain comprises the whole of H-AFt and ~ 10% of horse spleen AFt [376, 395], we can use the uptake results of H-AFt to predict the uptake of horse spleen AFt used to encapsulate JAa. Moreover, we can speculate that H-AFt may be recognised more readily by TFR1, therefore the use of H-AFt may further enhance cancer-selectivity.

The cellular uptake study of AFt that revealed a higher accumulation of H-AFt in TFR1+ cells was followed by studying the accumulation of JAa in these cells under one treatment condition; To correlate their cellular uptake of AFt-encapsulated agent to the detected enhanced activity under these conditions (see Section 2.3.8). SKBR-3 and MDA-MB-231, MCF-7 and BT-474 cells were exposed to JAa, AFt-JAa (0.4 µM JAa), AFt (0.0033 µM) or appropriate media alone for 72 h (n = 6). Intra and extracellular samples (see Section 2.4.1) were analysed by LC-HRMS to detect both JAa and its hydrolysed form JA. After 72 h treatment, LC-HRMS analyses revealed greater intracellular JAa levels, by 7%, 13%, and 15% in SKBR-3, MDA-MB-231, and BT-474 cells respectively following treatment with AFt-JAa compared to the treatment with naked JAa (**Figure 4.14**). While in MCF-7, the levels of JAa and JA were below the limit of detection. This may be related to the higher proliferation of MCF-7 (doubling time of ~18 h) compared to other tested cell lines, which may result in higher degradation/metabolism of agent following 72 h exposure.

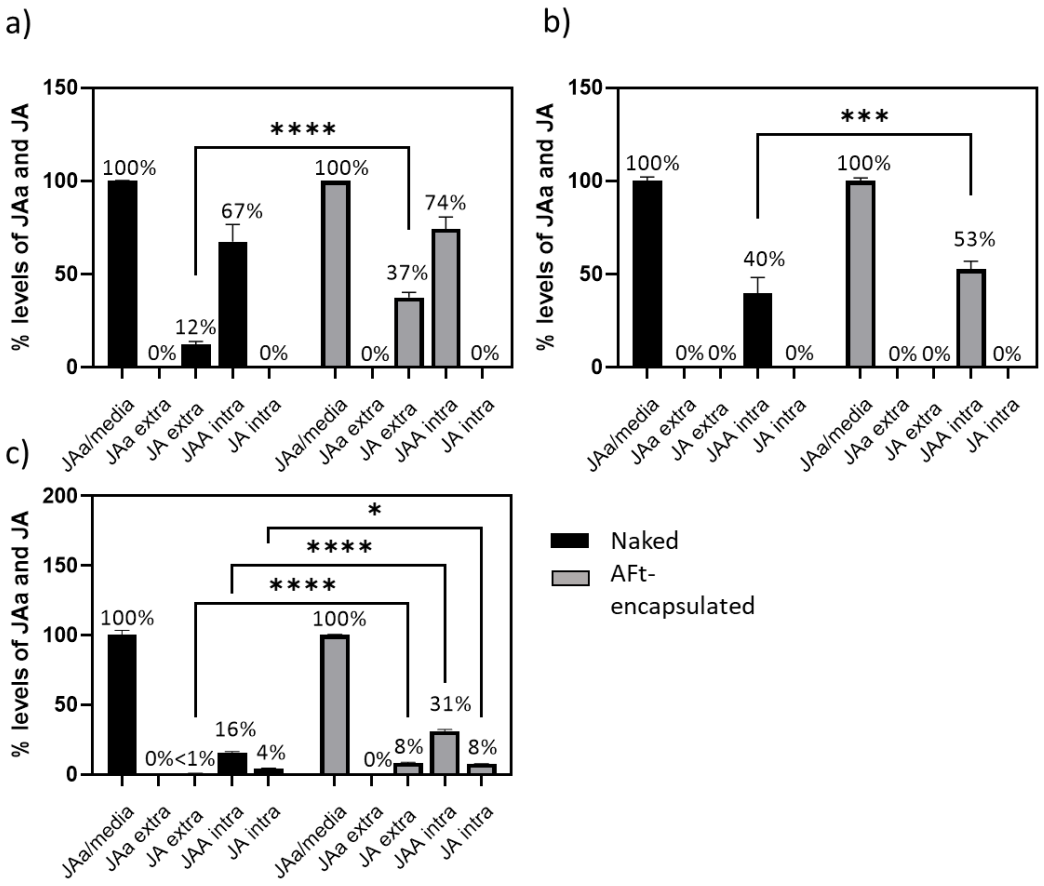


Figure 4.14: Intra and extracellular levels of JAa and its hydrolysed form following 72 h, 0.4 µM exposure of free and AFt-encapsulated JAa in **(a)** SKBR-3, **(b)** MDA-MB-231 and **(c)** BT-474. Data are represented as mean ± SD (*n* = 3) for 7 independent trials. Significant differences from naked JAa are expressed as *P < 0.05, ***P < 0.001 and ****P < 0.0001.

The greater intracellular JAa levels detected with AFt encapsulation support a role for TFR1 receptor-mediated cellular uptake of AFt, resulting in enhanced growth inhibition observed following exposure of these cancer cells to AFt-encapsulated JAa.

On the other hand, results show that ~25% and ~7% higher levels of extracellular JA were detected in SKBR-3 and BT-474 cells respectively following AFt-

encapsulation compared with naked JAa (**Figure 4.14a, c**). As higher levels of encapsulated agent might be related to better stability, the stability of naked and encapsulated JAa under the treatment conditions (24 h, 48 h, and 72 h at 37 ºC) was evaluated. The levels of JAa and JA were detected using LC-HRMS following incubation in different media. The detected levels of JAa with AFt encapsulation at 24 h exposure were ~0.4-fold higher than levels detected with free JAa (**Figure 4.15**). While the levels detected at 48 h and 72 h were ~1.2-fold higher with AFt encapsulation. These results indicate enhanced stability of JAa with AFt encapsulation under the treatment conditions, which further contributed to enhanced activity of AFt-JAa in various breast cancer cell lines.

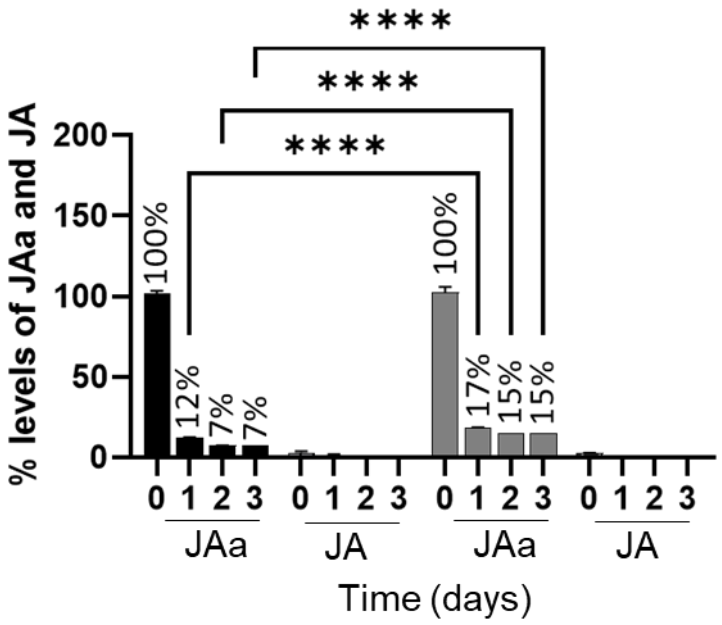


Figure 4.15: Levels of free and AFt-encapsulated JAa following incubation with different media for 24 h, 48 h and 72 h at 37 ºC. Data are represented as mean ± SD (*n* = 3) for 3 independent trials. Significant differences from free JAa are expressed as ****P < 0.0001 in brackets.

The overall enhanced selectivity and activity of encapsulated JAa in TFR1+ breast cells are therefore related to increased uptake/accumulation of AFt which results in greater cellular accumulation of JAa in addition to enhanced JAa stability under the treatment conditions. These observations are consistent with reports that the internalisation of H-AFt in TNBC cell lines (MDA-MB-231 and MDA-MB-468) was mediated through TFR1 followed by clathrin-dependent uptake [312]. Authors have shown that delivering curcumin within an AFt vehicle revealed better efficacy than delivering the drug alone [312]. Another study reported that platinum anticancer drugs delivered by AFt showed enhanced uptake and slow and sustained growth inhibition in a pheochromocytoma cell line [379]. The provided evidence indicates that the AFt vehicle enhances the activity of delivered agents as a result of enhanced uptake/accumulation of encapsulated agents in cells that overexpress the TFR1 receptor.

Although enhancing JAa's activity in breast cells is related to high expression of TFR1 that recognises AFt, drawing an absolute relationship between the expression of TFR1 and uptake of AFt or enhanced AFt-JAa potency was not achieved in our study (**Table 4.1**). This is a consequence of many reasons. First, the cellular accumulation pattern of H-AFt was not constant with time and varied from one cell line to another. As **Figures 4.16a, b** show, the accumulation pattern of AFt per h in the first 4 h of the study was higher and different than the accumulation seen in the subsequent 20 h exposure in SKBR-3, MDA-MB-231, and MCF-7 cells. On the other hand, the greater accumulation of AFt in the last 20 h of exposure compared to the first 4 h of the study seen with BT-474 cells might be related to a slower degradation of AFt compared to other cell lines. Indeed, the

accumulation of NPs is not exclusively related to intracellular uptake but also to the metabolic fate/state of cells [443]. Second, AFt is not exclusively sequestered by TFR1. AFt has been proved to recognise Chemokine (C-X-C motif) Receptor 4 (CXCR4), and SCARA5 which further contribute to the overall uptake of the protein and thus its biodistribution once inside the body [273].

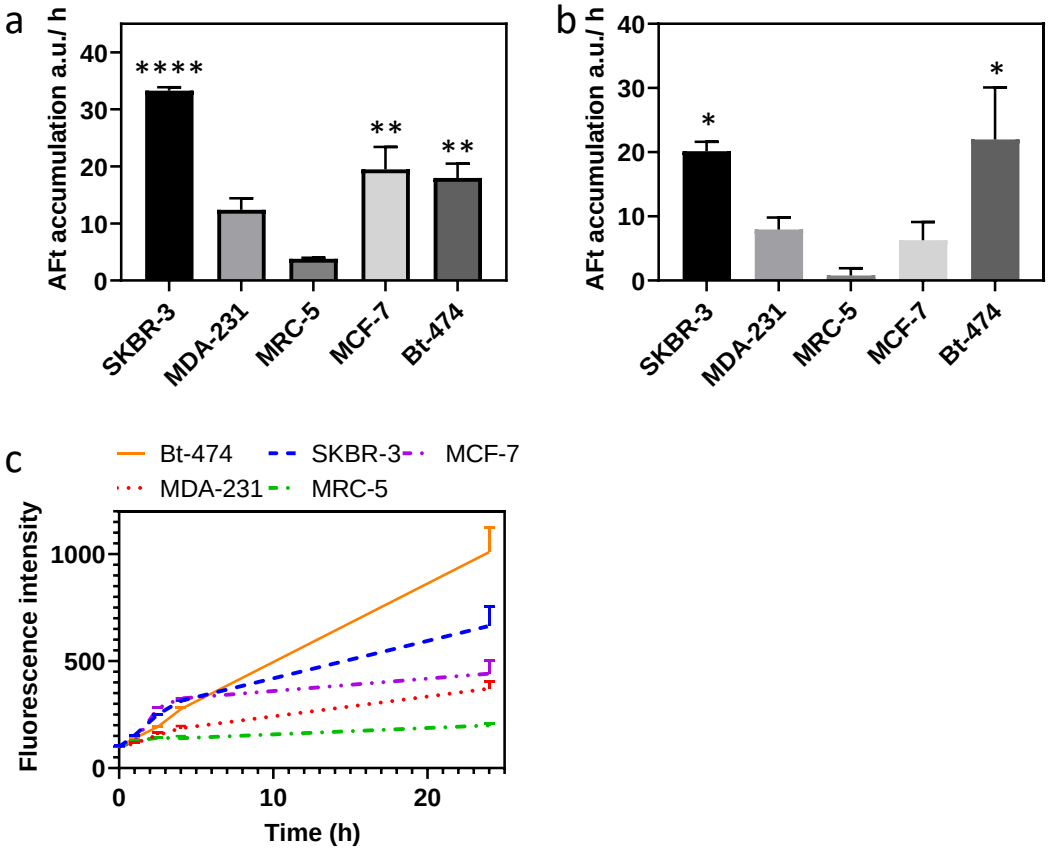


Figure 4.16: (c) Cellular accumulation pattern of 5-carboxyfluorescein-conjugated-human-apoferritin (40 nM) for 24 h in TFR1+ cells (SKBR-3, MDA-MB-231, MRC-5, MCF-7 and BT-474) and one TFR1-low expressing cells (non-cancerous MRC-5) during 24 h. **(a)** The accumulation levels per hour of H-AFt in all cells, during the first 4 h of study, and **(b)** the succeeding 20 h of study. Data are reported as median ± SD (*n* = 3) and repeated 3 times. Significant differences of accumulation pattern of H-AFt per hour in TFR1+ cells from MRC-5 cells are expressed as *P < 0.05, **P < 0.01 and ****P < 0.0001.

4.4 Conclusion

The present study was set out with the aim to deliver JAa efficiently and selectively to breast carcinoma cells. The high level of TFR1 detected using flow cytometry on the surface of cells of all subtypes of breast carcinoma supports previous findings [426] supporting its essential role to satisfy breast cancer cells' high iron demands [427, 432]. The low detected levels of TFR1 in normal MRC-5 fibroblasts further highlight the promising therapeutic benefits of actively targeting TFR1 in breast cancers. The high activity of JAa inhibiting the growth of all tested cells detected in MTT, cell counting, and clonogenic assays reflects its high potency but also non-selective targeting. This further supports the previously highlighted concerns of jerantinines and emphasises the importance of delivering JAa through AFt NPs to breast carcinomas [202, 203]. Following the delivery of AFt-JAa formulation, the reduction in GI_{50} values seen in MTT assays, the lower counted viable cells, and colonies formation in all TFR1+ cells but not TFR1-low expressing cells, revealed enhanced activity and selectivity of encapsulated JAa for breast cancer cells. Higher colonies detected in rapidly dividing MCF-7 cells (~18 h) following the treatment with encapsulated JAa may be related to the slow release of JAa. The slow release of JAa from AFt capsules that takes > 24 h (as shown in Chapter 3) endorses the premise of sustained drug release from AFt as an efficient DDS. Enhanced activity and selectivity of AFt-JAa formulation are shown to be correlated to the preferential enhanced uptake of H-AFt seen in TFR1+ cells over TFR1-low expressing cells, which recognise the Ft H chain of AFt and internalise it through clathrin-mediated endocytosis [23]. This further enhanced the uptake and

accumulation of intracellular JAa in treated breast cancer cell lines, in addition to enhancing its stability under the treatment conditions (37 ºC; ≤ 72 h) when encapsulated within AFt core. The treatment with AFt alone with the highest concentration used (40 nM) has a negligible effect on cells indicating a biocompatible delivery system.

4.5 Future work

1. To comprehensively understand the mechanism by which AFt is sequestered by cancerous cells and how it affects the activity of encapsulated agents more studies should be conducted:
    i. To verify different receptors responsible for AFt uptake (e.g, SCARA-5 and CXCR4).
    ii. To study the metabolomic profiles for different cells to understand the degradation/metabolism process of AFt and encapsulated agents.
    iii. Imaging studies to determine how AFt is trafficked through the cell.
2. The effectiveness of H-AFt formulation must be investigated; to better correlate its uptake to the expression of TFR1 only, in preference to horse spleen AFt that is also recognised by other receptors like SCARA-5 receptors through its L-chain.

5 Free and apoferritin encapsulated jerantinine A acetate perturb cell cycle and induce cell death of breast carcinoma cells

5.1 Introduction

A single molecule with multiple targets (also known as a hybrid molecule) in chemotherapy has many advantages over drug combinations, such as reducing possible drug interaction, adverse reactions and simplifying the drug regimen that enhances patient compliance [444]. Moreover, hybrid molecules have been shown to overcome acquired drug resistance and development of these agents has become a popular approach [445]. (−)-Jerantinines are multi-target antiproliferative alkaloids, demonstrating their *in vitro* potency by inhibiting tubulin polymerisation, PLK1 activity, generating ROS and arresting the cell cycle in G2/M phase in a panel of human cancer cell lines [198, 202, 203]. As a result of being multitargeted agents, jerantinines induce apoptosis in a caspase-dependent, as well as caspase 3-independent manner as in MCF-7 cells for example [202-204]. Jerantinines also share the advantage of other hybrid molecules and evade P-gp-mediated MDR for example in VCR resistant (VR) HCT-116 cells [203]. Jerantinines were also active against P-gp+ paediatric medulloblastoma cells [217] and therefore may represent a putative alternative to VCR in this disease. Besides being a multitargeted agent, JA has been exposed

as targeting the spliceosome in breast cancer cells leading to induction of cell death. The spliceosome is a pivotal protein complex comprised of small nuclear RNA (snRNA) involved in splicing immature mRNA; disturbing its function causes abnormal splicing patterns and ultimately cell death [204]. Therefore, it is crucial to preserve jerantinines' rich and diverse pharmacology while delivering them within AFt capsules in an attempt to enhance activity and selectivity as demonstrated previously in Chapter 4 with JAa.

5.2 Chapter aims

The goals of research described within this Chapter include:

- Evaluation of antiproliferative targets of free and AFt-encapsulated JAa in three subtypes of breast cancer cells (MCF-7 - luminal A, ER+; SKBR-3, HER2 overexpression; MDA-MB-231 - claudin-low; TNBC) by determining cell cycle perturbation.
- Evaluation of apoptosis in response to the treatment by investigating the changes in the expression of many proteins that play role in apoptosis and survival using western blots.
- Evaluation of possible targets and mechanisms perturbed by jerantinines in the treated aforementioned cell lines including PLK-1 and ROS generation.
- Corroboration of the biocompatibility of AFt against the aforementioned cell lines.

5.3 Results and discussion

5.3.1 Free and encapsulated JAa perturb cell cycle progression of breast cancer cell lines

As previously reported, jerantinines mediate their antiproliferative activity mainly by binding to the colchicine binding site of tubulin and destabilising its polymerisation [198, 201-203]. As a result of microtubule disruption, the transition of cells to the mitotic phase halts causing inhibition of cell growth, a consequence of profound G2/M events' accumulation.

To determine the effect of AFt-encapsulation of JAa on cell cycle progression, flow cytometry analyses were conducted on three selected cell lines: MCF-7 (luminal A; low proliferation rate with good prognosis), SKBR-3 (HER2-enriched; aggressive with intermediate prognosis) and MDA-MB-231 (triple-negative; most aggressive and poor prognosis) cells [60, 70]. Using the same treatment conditions adopted for clonogenic assays, cells were treated with JAa, AFt-JAa (0.2 µM and 0.4 µM JAa), AFt (0.0033 µM) and appropriate media alone for 48 h.

As described in Section 2.3.7.1, our method was adopted from Nicoletti [355], which further allows detection of two more subpopulations; pre-G1 (< 2N and known as hypoploid) and super G2 (> 4N number and known as hypertetraploid or aneuploid). Detecting the pre-G1 subpopulation is a good indication of apoptotic cells [446]. The used Triton X-100 detergent in this method allows the stain to permeabilise the cells. If the cells are going through apoptosis, many nucleases will be activated which will cause apoptotic cells to stain weaker than healthy cells.

Moreover, during the staining process, some of the fragmented DNA will be released from cells due to the hypotonic effect of the used buffer in this method which will weaken the stain of these cells [355]. The signal of DNA fragments is easily detected by flow cytometry following nucleic acid staining with propidium iodide. The weaker detected signal of propidium iodide will be shifted from the diploid subpopulation and appears in the hypodiploid (pre-G1) region.

In order to mathematically consider the pre-G1 and super-G2 subpopulations, suitable software analysis has to be chosen. Certain often-used software including Kaluza which use both Michael H fox and J.V. Watson algorithms, assume only the data within the G0/G1, S and G2/M peaks in the analysis [3]. However, FlowJo software analysis, which uses both J.V. Watson and Dean Jett Fox algorithms, considers pre-G1 and super-G2 subpopulations in the analysis and hence was used in our study.

In SKBR-3 cells (the cell line most sensitive to JAa, as indicated by MTT and viable cell counting assays, compared with MDA-MB-231 and MCF-7), a profound dose-dependent depletion of events in the G1 phase was detected (**Figure 5.1**). The depletion was accompanied by higher accumulation of events in G2/M and/or sub-G1 phases. Following treatment with the free agent, events' accumulation in the G2/M phase at a concentration of 0.2 µM JAa were comparable to the control (untreated) cells. While SKBR-3 revealed a significant cell cycle arrest in the G2/M phase at 0.4 µM JAa and higher events' accumulation by ~26% compared to the untreated cells ($p < 0.0001$). The treatment with the free agent at both 0.2 µM and 0.4 µM revealed a significant ($p < 0.001$) and dose-dependent increase of events

in the sub-G1 phase by ~145% and ~174% respectively. The significant accumulation of pre-G1 events in the affected populations indicates apoptosis. Interestingly, when JAa was delivered within AFt, higher events' accumulation at the G2/M phase was detected by ~13% at treated concentrations of 0.2 µM.

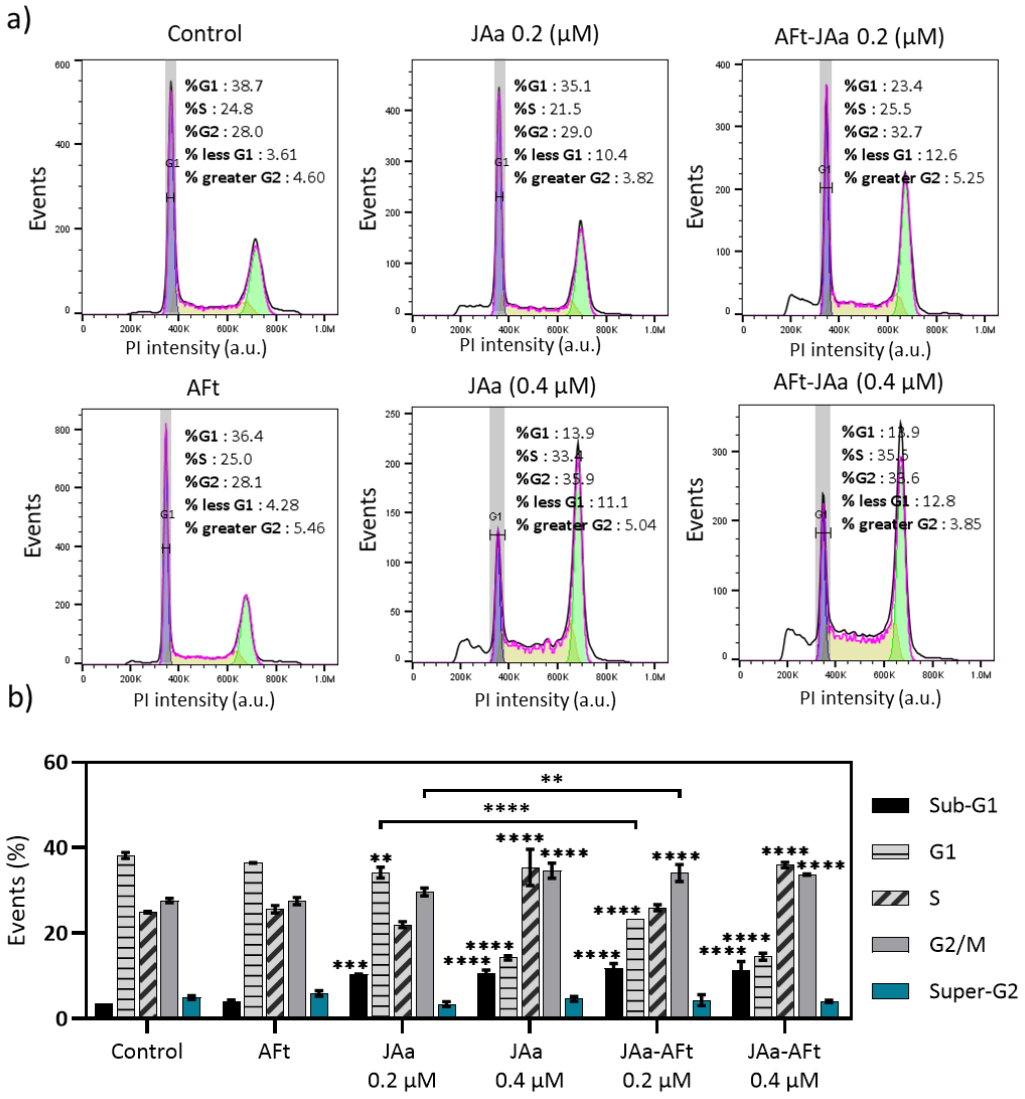


Figure 5.1: The effects of JAa and its encapsulated form AFt-JAa on the cell cycle of SKBR-3 cells. Cells were treated with JAa (0.2 µM, 0.4 µM), AFt-JAa (0.2 µM, 0.4 µM), AFt (0.0033) µM) for 48 h. **(a)** Representative cell cycle distribution and **(b)** their statistical analysis. Data are expressed as a percentage of median ± SD from 20,000 events from one trial (*n* = 2 per experiment) and repeated on 3 independent occasions. Significant differences are expressed as **P < 0.01, ***P < 0.001, ****P < 0.0001 from untreated control. Significant difference from JAa is expressed in brackets.

These results indicate that AFt encapsulation of JAa enhances activity of JAa at the lower used concentration of 0.2 μM, reflected by the significant higher depletion of G1 events ($p < 0.0001$) and G2/M events accumulation ($p < 0.01$). However, the effect of AFt encapsulation on the activity of JAa to perturb cell cycle progression at the higher used concentration was not significantly affected. These results further corroborate those described previously in Chapter 4, where MTT, cell count and clonogenic assays demonstrated the enhanced activity of JAa at the same used concentration (0.2 μM JAa), indicating enhanced delivery of JAa and consequently interaction with molecular target(s) following its AFt-encapsulation.

In MDA-MB-231 cells (less sensitive to JAa, as indicated by MTT and viable cell counting assays compared with SKBR-3 cells), the effect of JAa on cell cycle progression was also dose-dependent (**Figure 5.2**). Free JAa at 0.2 μM caused a significant G1 depletion ($p < 0.01$) compared to the control cells. Interestingly encapsulated JAa at the same concentration caused higher G1 depletion ($p < 0.0001$), and pre-G1 events' accumulation by 120% ($p < 0.01$). At a higher concentration of 0.4 μM, both free and encapsulated JAa caused a significant sub-diploid accumulation by ~204% with the free agent and 248% with AFt-JAa ($p < 0.0001$) compared to untreated cells. The cells also show dose-dependent accumulation of events in the S phase; which may indicate DNA damage (a possible consequence of ROS generation).

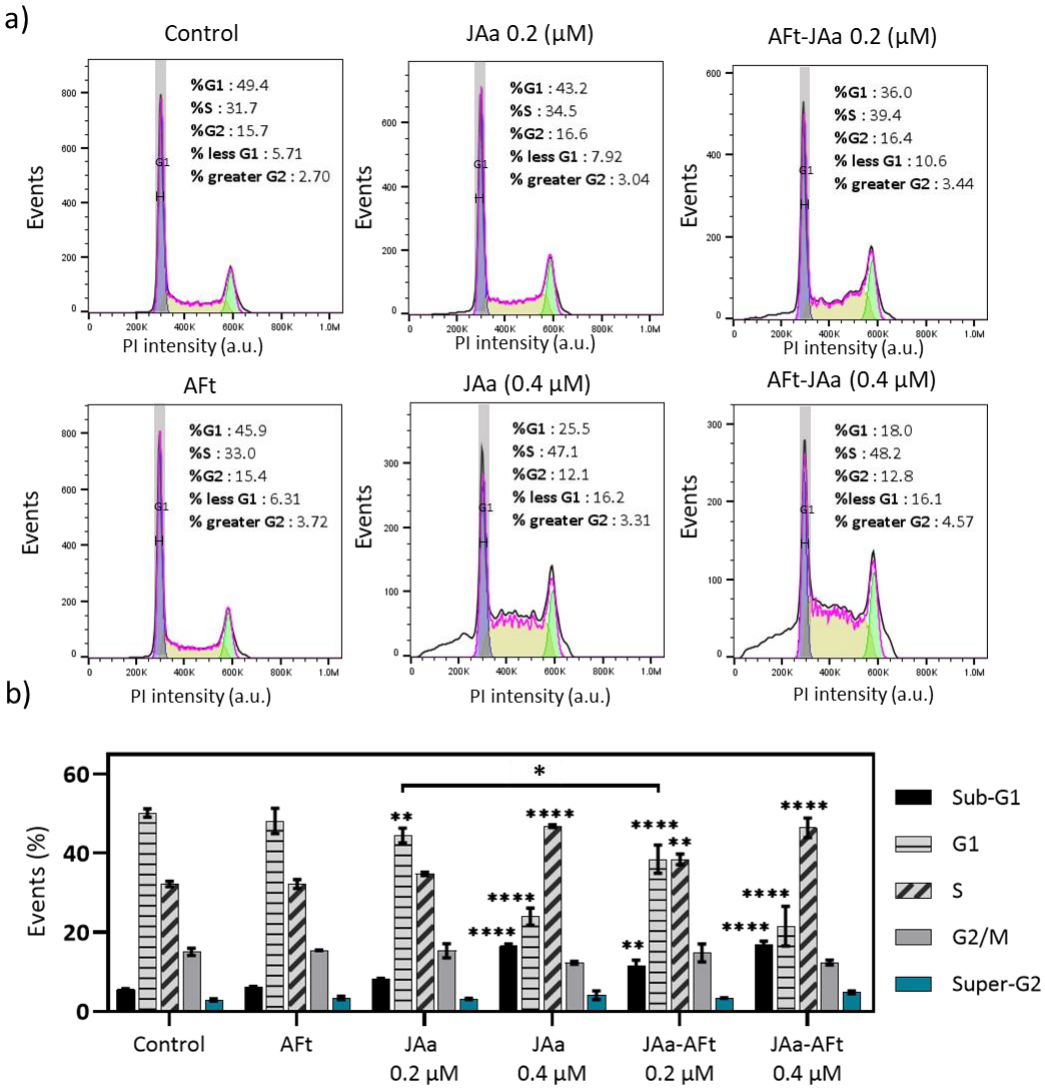


Figure 5.2: The effects of JAa and its encapsulated form AFt-JAa on the cell cycle of MDA-MB-231 cells. Cells were treated with JAa (0.2 µM, 0.4 µM), AFt-JAa (0.2 µM, 0.4 µM), AFt (0.0033) µM) for 48 h. **(a)** Representative cell cycle distribution and **(b)** their statistical analysis. Data are expressed as a percentage of median ± SD from 20,000 events from one trial (*n* = 2 per experiment) and repeated on 3 independent occasions. Significant differences are expressed as*P < 0.05, **P < 0.01, ****P < 0.0001 from untreated control. Significant difference from JAa is expressed in brackets.

Exhibiting lower sensitivity to JAa, MDA-MB-231 reveal less prominent changes to cell cycle distributions, however, results show enhanced perturbation of cell cycle for AFt-encapsulated agent, with a significant change of the G1 events ($p < 0.05$)

over treatment with 0.2 µM naked JAa). Enhanced activity is also indicated at 0.4 µM, as more numerous events were detected in the pre-G1 phase with encapsulated JAa; indicating apoptosis. These results are consistent with MTT and viable cell counting assays (see Section 4.3.2 and 4.3.3) demonstrating enhanced activity with AFt-encapsulated JAa at both concentrations.

In MCF-7 cells (less sensitive than SKBR-3 cells to JAa, as indicated by MTT and viable cell counting assays but equi-sensitive as MDA-MB-231), free and encapsulated JAa failed to significantly perturb the cell cycle progression at the lower used concentration of 0.2 µM ($p > 0.05$) as shown in **Figure 5.3**. Interestingly, encapsulated but not free JAa at a concentration of 0.4 µM revealed a significant depletion of G1 events ($p < 0.0001$). The treated cells showed a significant cell cycle arrest in the G2/M phase ($p < 0.05$) reflecting enhanced activity of encapsulated JAa at 0.4 µM. The same treated population also showed an accumulation of hypoploid events by ~10-fold ($p < 0.0001$); indicating apoptosis. The analysis also detected accumulation in pre-G1 events with 0.2 µM AFt-encapsulated JAa by 1.6-fold and with 0.4 µM free JAa by 2.7-fold. Those accumulations, although not statistically significant ($p > 0.05$), also indicate the presence of apoptotic populations.

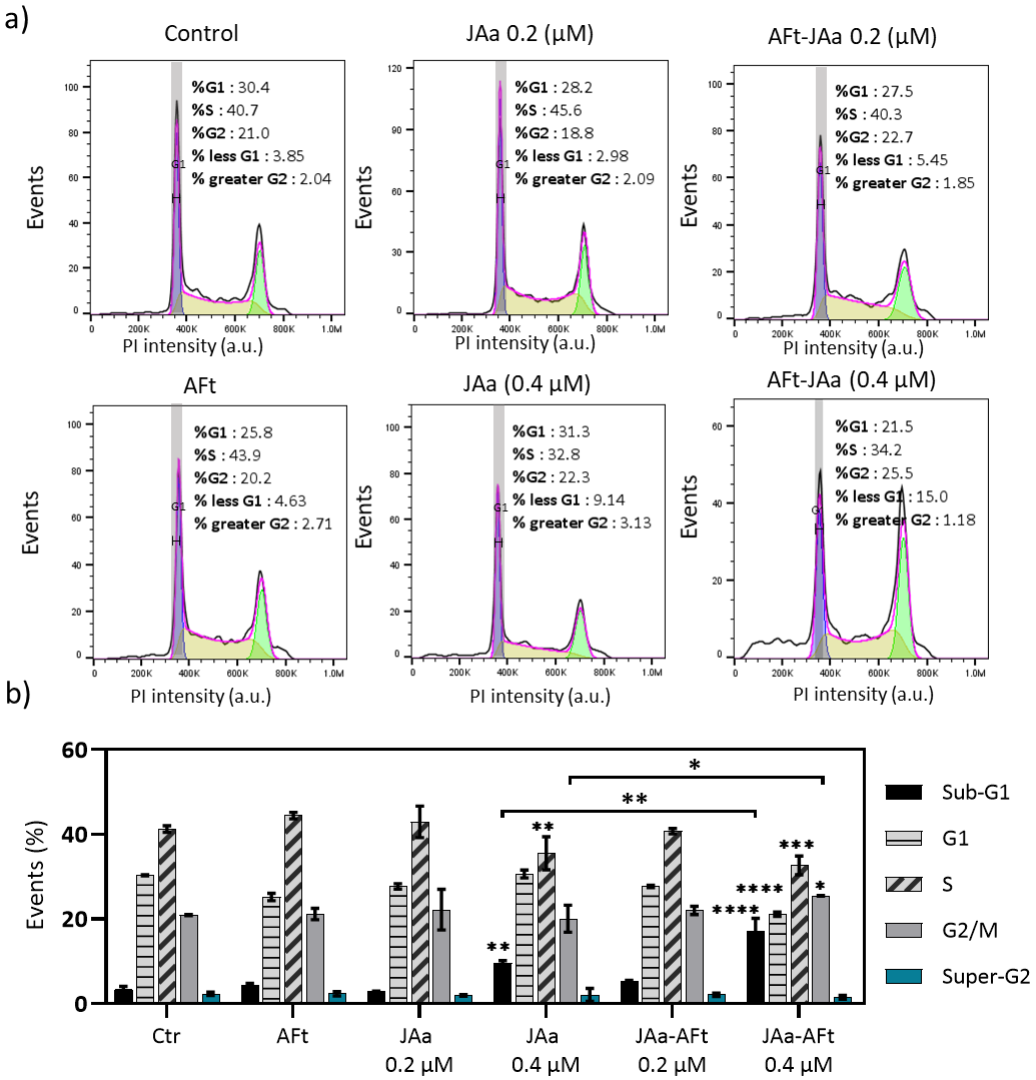


Figure 5.3: The effects of JAa and its encapsulated form AFt-JAa on the cell cycle of MCF-7 cells. Cells were treated with JAa (0.2 µM, 0.4 µM), AFt-JAa (0.2 µM, 0.4 µM), AFt (0.0033) µM) for 48 h. **(a)** Representative cell cycle distribution and **(b)** their statistical analysis. Data are expressed as a percentage of median ± SD from 20,000 events from one trial (*n* = 2 per experiment) and repeated on 3 independent occasions. Significant differences are expressed as *P < 0.05, **P < 0.01, ***P < 0.001, ****P < 0.0001 from untreated control. Significant difference from JAa is expressed in brackets.

Unlike MDA-MB-231 cells, significant perturbation of cell cycle analysis of MCF-7 is detected only with 0.4 AFt-JAa but not 0.2 µM AFt-JAa, reflecting lower sensitivity to free and encapsulated JAa. This further supports results reported in

Chapter 4, where the SI value of AFt-JAa was 3.5 in MCF-7 compared to the higher sensitivity detected with MDA-MB-231 with SI = 4.6 (see Section 4.3.2). The perturbation effect of encapsulated but not free JAa at a concentration of 0.4 µM, reflects the enhanced activity of JAa when delivered to the cells through AFt vehicle. This also supports the results from the previous Chapter 4, when MCF-7 shows enhancement in the SI of AFt-JAa.

The overall effect of JAa and its encapsulated form on G2/M cell cycle block implies arrest of cells from progression through mitosis. This indicates that the major mechanism of action of JAa – destabilisation of microtubules, is not affected by AFt encapsulation. AFt alone did not perturb cell cycle in any of the cell lines, further supporting the biocompatibility of AFt nano vehicle. Our results agree with Raja (2014) and Qazzaz (2016) [202, 203], who showed G2/M arrest of JA and JB as a sign of perturbing microtubules dynamics in diverse human carcinomas. JA and JB destabilise microtubules and reduce the expression of β-tubulin and as a result, inhibit tubulin polymerisation and mitosis in treated cells. Between the three treated cell lines, SKBR-3 cells; the most responsive cells to JAa as detected by MTT (refer to Section 4.3.2), also show the highest sensitivity to JAa treatment represented by a significant cell cycle perturbation and early apoptosis ($p < 0.0001$). The highest selectivity of AFt-JAa treatment indicated by SI value detected with SKBR-3 cells was further corroborated with greater and significant depletion of G1 events and apoptotic cells with AFt-JAa treatment ($p < 0.01$) compared to the free agent.

5.3.2 Free and encapsulated JAa induces apoptosis of breast cancer cell lines

Evading apoptosis is one of the main hallmarks of cancer, which results in cancer cell survival, proliferation, and resistance to the most common anticancer therapies. Thus inducing cancer cell apoptosis is the ultimate goal of non-surgical anticancer therapy [447]. Following treatment with free and AFt-encapsulated JAa, significant accumulation of events in the pre-G1 phase in breast cancer treated cells observed in the cell cycle analysis are a good indicator of apoptosis. Although cell cycle analysis was performed using the Nicoletti method, cell debris might also contribute to the pre-G1 signal [446]. Therefore, a distinction from apoptosis requires avoiding DNA shearing during preparation of the samples, or validation of results with another apoptosis test. In addition, the signal of apoptotic cells in late S or G2/M phases of cell cycle may not be detected as pre-G1 populations [448]. For these reasons, annexin V assays were carried out to validate apoptosis results indicated by previous cell cycle analysis.

Using the same treatment conditions as cell cycle analysis, SKBR-3, MDA-MB-231 and MCF-7 cells were prepared for apoptosis analysis by flow cytometry (see Section 2.3.7.2).

In this analysis, the signals detected from cells stained with propidium iodide and Annexin V were used to generate quadrant plots. The viable cells with no labelling are found in the lower left quadrant. The population of cells exclusively labelled with Annexin V are in the early apoptosis state and found in the lower right quadrant. This is due to the binding of Annexin V-FITC to the PS of the outer cell membrane of apoptotic cells [356]. The population exclusively labelled with propidium iodide represents the non-apoptotic, necrotic cells/debris and is found

in the upper left quadrant. This is due to the binding of propidium iodide to the DNA of the necrotic cells following its penetration of their ruptured/ highly porous cell membrane. While the population of cells with dual staining are in the late apoptosis state and found in the upper right quadrant.

Free and encapsulated JAa caused profound dose-dependent incidence of apoptosis in all tested cell lines (**Figure 5.4**, **5.5**, **5.6**). In the most sensitive cell line to JAa, a significant early SKBR-3 apoptosis ($p < 0.0001$) at 0.2 µM and 0.4 µM by ~3.2-fold and ~3.9-fold respectively was detected (**Figure 5.4**). While AFt-JAa induced early SKBR-3 apoptosis by ~3.9-fold and ~3.8-fold at a concentration of 0.2 µM and 0.4 µM respectively ($p < 0.0001$). Interestingly, the significantly higher apoptotic population ($p <0.001$) detected with AFt-JAa at 0.2 µM compared to the free agent, reflects its enhanced activity at this concentration and corroborates MTT, cell counting, and clonogenic assays. AFt-JAa at 0.2 µM demonstrated comparable activity to 0.4 µM naked JAa as demonstrated by apoptosis-induction, which corroborates results from the SKBR-3 clonogenic assay (as described previously in Chapter 4).

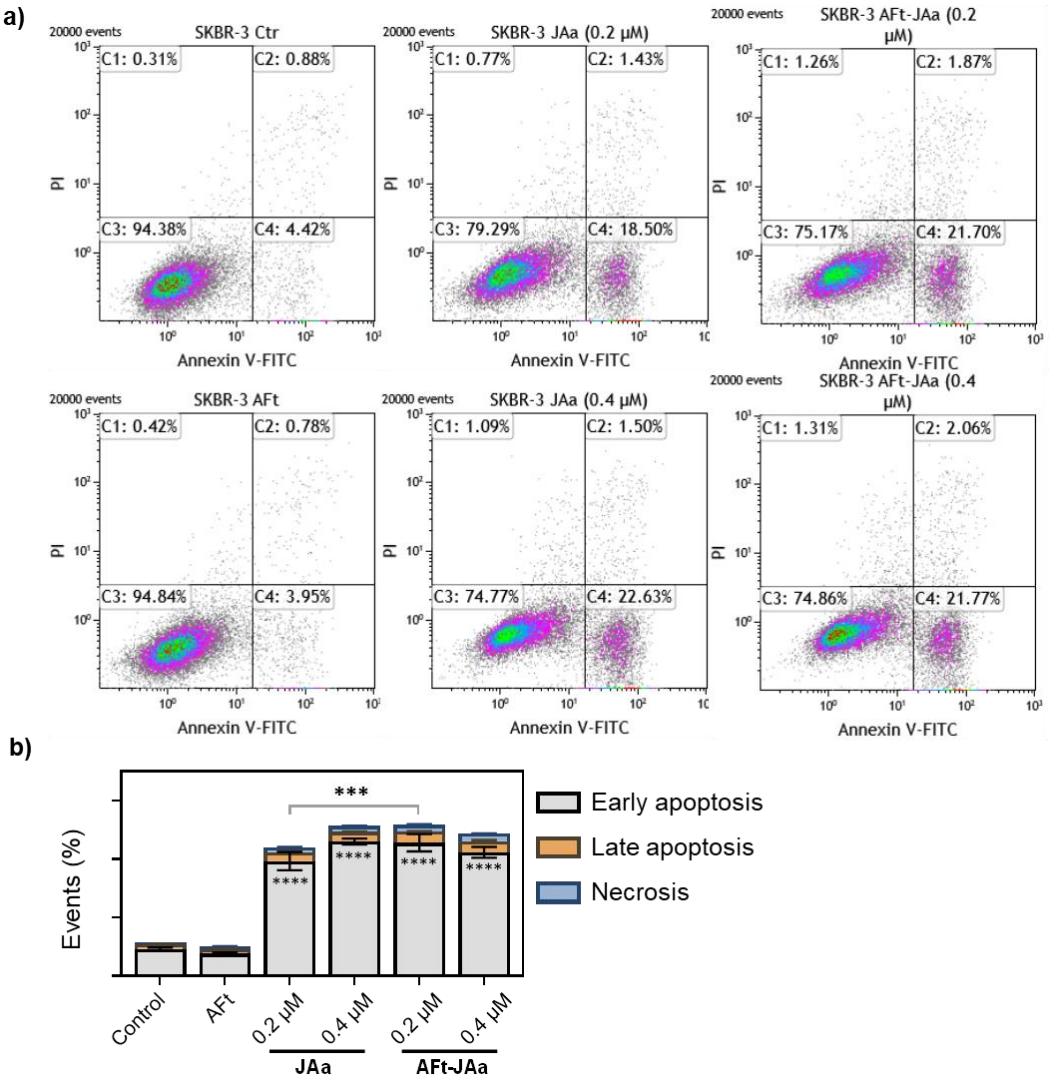


Figure 5.4: The effects of JAa and its encapsulated form AFt-JAa on the apoptosis of SKBR-3 cells. Cells were treated with JAa (0.2 µM, 0.4 µM), AFt-JAa (0.2 µM, 0.4 µM), AFt (0.0033) µM) for 48 h. **(a)** Representative quadrant scatter plots and **(b)** their statistical analysis. Data are expressed as a percentage of median ± SD from 20,000 events from one trial (*n* = 2 per experiment) and repeated on 3 independent occasions. Significant differences are expressed as ***P < 0.001, ****P < 0.0001 from untreated control. Significant difference from JAa is expressed in brackets.

MDA-MB-231 cells showed dose-dependent, significant late apoptosis with free and encapsulated JAa with all tested concentrations (**Figure 5.5**). Free JAa induced late MDA-MB-231 apoptosis by ~0.6-fold and ~2.2-fold at a concentration of 0.2 µM and 0.4 µM respectively. Interestingly higher late MDA-MB-231 apoptosis was

detected with AFt-encapsulated JAa by ~0.8-fold and ~2.7-fold at a concentration of 0.2 µM and 0.4 µM respectively. Of interest, comparable early apoptotic MDA-MB-231 events were detected after exposure to encapsulated 0.4 µM JAa, but significantly enhanced late phase apoptosis ($p < 0.05$) was detected compared to exposure to naked agent; reflecting enhanced activity of AFt-JAa at this concentration. In addition to the apoptotic cells, a profoundly significant accumulation of cells ($p < 0.01$) in the upper left quadrant was detected under all different conditions, indicative of non-apoptotic cell death.

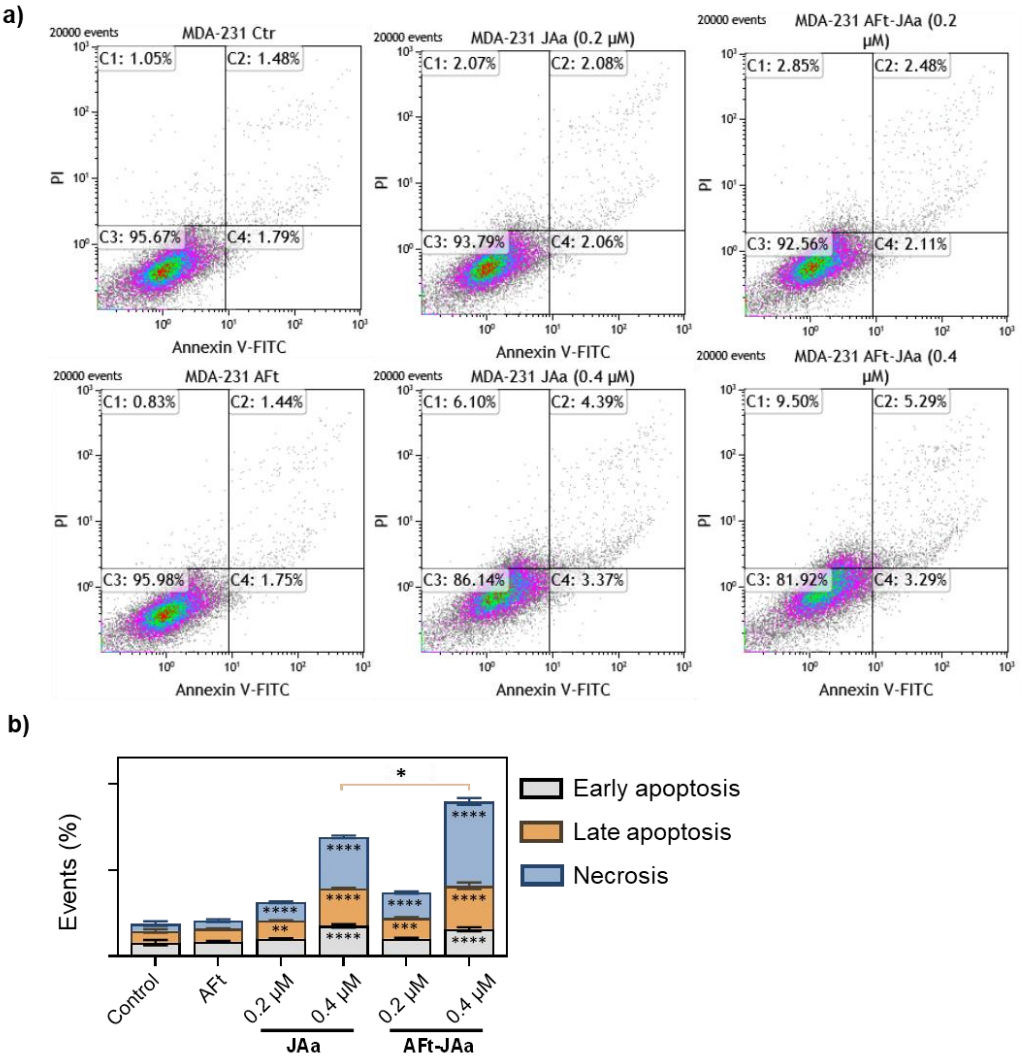


Figure 5.5: The effects of JAa and its encapsulated form AFt-JAa on the apoptosis of MDA-MB-231 cells. Cells were treated with JAa (0.2 µM, 0.4 µM), AFt-JAa (0.2 µM, 0.4 µM), AFt (0.0033) µM) for 48 h. **(a)** Representative quadrant scatter plots and **(b)** their statistical analysis. Data are expressed as a percentage of median ± SD from 20,000 events from one trial (*n* = 2 per experiment) and repeated on 3 independent occasions. Significant differences are expressed as *P < 0.05, **P < 0.01, ***P < 0.001, ****P < 0.0001 from untreated control. Significant difference from JAa is expressed in brackets.

In MCF-7 cells, Free JAa failed to cause significant annexin V+ apoptotic population at both used concentrations (**Figure 5.6**). Of interest, when JAa was delivered to cells within AFt, a significant incidence of apoptosis was detected ($p < 0.0001$) with the higher used concentration of 0.4 µM AFt-JAa; support enhancing activity with JAa and corroborating previously reported results from MTT, and cell counting assays.

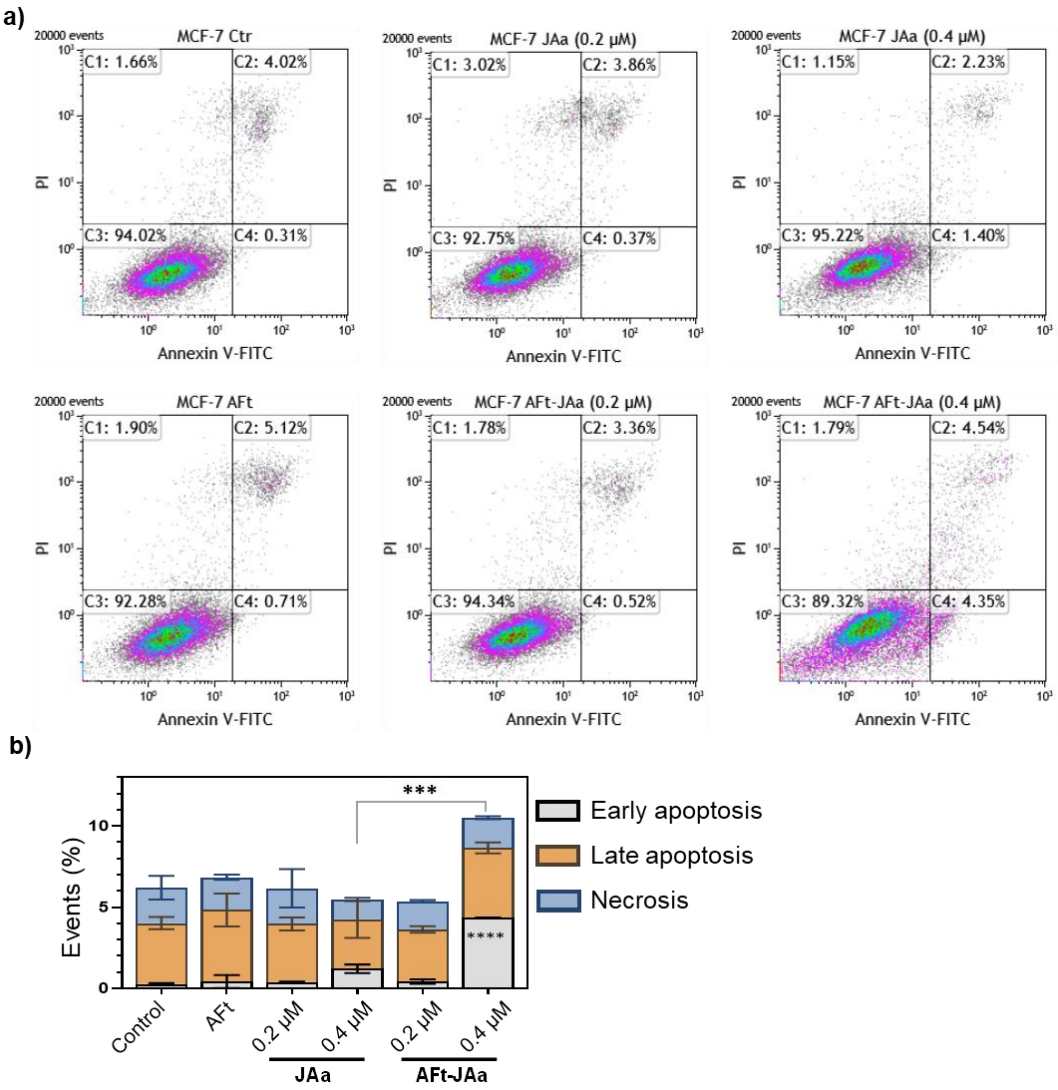


Figure 5.6: The effects of JAa and its encapsulated form AFt-JAa on the apoptosis of MCF-7. Cells were treated with JAa (0.2 µM, 0.4 µM), AFt-JAa (0.2 µM, 0.4 µM), AFt (0.0033) µM) for 48 h. **(a)** Representative quadrant scatter plots and **(b)** their statistical analysis. Data are expressed as a percentage of median ± SD from 20,000 events from one trial (*n* = 2 per experiment) and repeated on 3 independent occasions. Significant difference is expressed as ***P < 0.001, ****P < 0.0001 from untreated control. Significant difference from JAa is expressed in brackets.

In all treated cells, the apoptotic populations observed by the annexin V assays were consistent with findings of pre-G1 accumulation of cells provided by cell cycle analysis. Our results are also consistent with the findings of inducing apoptosis in cancer cells treated with JA and JB following cell cycle arrest in diverse human

cancer cell lines [202, 203]. AFt alone (0.0033 μM) indistinguishably affected apoptosis when compared with control in tested cell lines (**Figure 5.4**, **5.5**, **5.6**) supporting its applicability as a biocompatible delivery vehicle.

5.3.3 Free and encapsulated JAa change the expression of apoptotic and anti-apoptotic protein biomarkers

Evading apoptosis in cancer cells is related to their ability to inhibit apoptotic pathways by overexpressing antiapoptotic proteins and repressing proapoptotic ones [447]. Therefore, cell cycle perturbations and apoptosis-induction by JAa were further corroborated by investigating the expression of proteins possessing roles in mitosis, apoptosis, and cell survival including p53, Bcl-2, Mcl-1, PARP and PLK-1. P53 is a tumour-suppressor protein normally activated when cells are exposed to damage. When p53 is activated, it arrests the damaged cells to transit from the G1-to-S and the G2-to-M phase until the damage is repaired [10]. If the cells' damage cannot be repaired, p53 causes apoptosis by regulating the activity of the Bcl-2 family proteins [11, 23]. However, it is estimated that in 50% of cancers including breast cancer *TP53* gene mutations which encode p53, result in more aggressive disease and reduced survival [24]. The Bcl-2 protein family plays a key role in regulating intrinsic (mitochondrial) apoptosis. As a result of activating Bcl-2 pro-apoptotic family members and inhibiting Bcl-2 antiapoptotic family members, cytochrome c is released from mitochondria into the cytosol following MOMP resulting in apoptosome formation, caspase 3 activation and ultimately apoptosis [21]. Caspase 3 cleaves PARP as one of its targets, thus cleaved PARP functions as a biomarker of cells undergoing apoptosis [449]. The PARP enzymes'

superfamily are DNA damage sensors that play a key role in recruiting DNA repair proteins (see Section 1.3.3.2) [450]. Inhibition of PARP in BRCA-mutant/deficient tumours resulting in chromosomal instability, cell cycle arrest and subsequent apoptosis [174, 175].

PLK1 onco-protein is another important controller in cancer initiation and progression including driving mitotic events, and it is frequently highly expressed in human cancers [451-453]. PLK1 is a validated cancer target, and its inhibition leads to G2/M phase arrest resulting in apoptosis [452, 454-457].

Lysates of SKBR-3, MDA-MB-231 and MCF-7 cells, following 72 h exposure to free and encapsulated JAa (0.1-0.6 μM for SKBR-3 cells and 0.2-0.8 μM for the MCF-7 and MDA-MB-231 cells) were prepared and analysed using western blot (see Section 2.3.3).

A profound dose-dependent elevation in cleaved PARP accompanied abolished expression of antiapoptotic Mcl-1 protein in SKBR-3 lysates following treatment of cells with free and encapsulated JAa, indicating apoptosis (**Figure 5.7**). Interestingly, this was detected with encapsulated JAa at the lower concentration of 0.2 μM. Moreover, both free and encapsulated JAa caused significant dose-dependent decreases in the expression of p53 relative to control ($p < 0.01$).

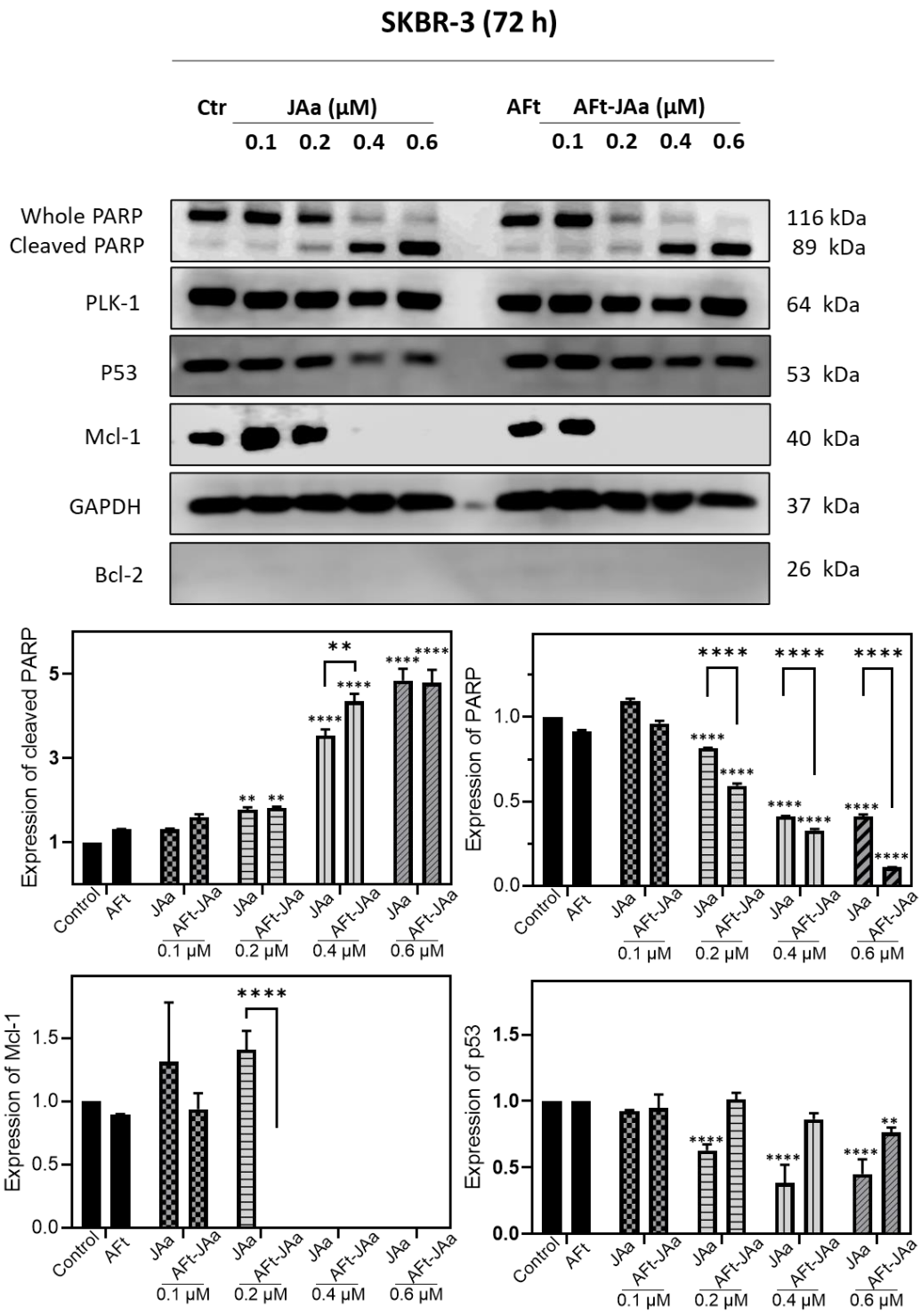


Figure 5.7: Protein expression in SKBR-3 cell lysates following 72 h exposure of cells to JAa, AFt-JAa at different concentrations, AFt (0.0068 μM) and media only. Collated densitometric measurement of cellular protein expression levels of PARP, cleaved PARP, Mcl-1 and p53 represented as mean ± SD and repeated on 3 independent occasions. Significant differences from untreated cells are expressed as **P < 0.01, ****P < 0.0001 from untreated control. Significant difference from JAa is expressed in brackets.

The highly detected levels of cleaved PARP accompanying treatment at higher concentrations are indicative of apoptosis. The detected cleavage of PARP in SKBR-3 lysates is consistent with high levels of caspase 3 [458]. It is known that PARP is cleaved upon the activation of caspase 3 [459]. Indeed, apoptosis was previously detected in MIA PaCa-2, HCT-116 and VR HCT-116 cells along with enhanced caspase 3 activity following their treatment with JA and JB; down-regulation of anti/apoptotic pro-apoptotic proteins Mcl-1 and Bcl-2 was also evident [202, 203]. Inducing apoptosis through the activation of caspase 3 is one of the mechanisms by which jerantinines affect the growth/viability of cancer cells. Moreover, it seems that the profound cleavage of PARP in SKBR-3 cells (the most sensitive cell line in the three cell line panel) may reflect their greater sensitivity to JAa over other cell lines. SKBR-3 cells harbour a mutated p53 protein [460]. Mutations in p53 produce a non-functional p53 protein or a protein with new functions that cause invasion, metastasis and chemoresistance [24, 461]. Thus, the interference with mutant p53 expression or activity reduces proliferation of cancer cells [462].

In MDA-MB-231, a greater reduction by AFt-JAa compared to naked JAa in the expression of tumour suppressor p53 was detected along with the expression of whole PARP and PLK1 at 0.8 μM, while the expression of these proteins remained stable at lower tested concentrations (**Figure 5.8**).

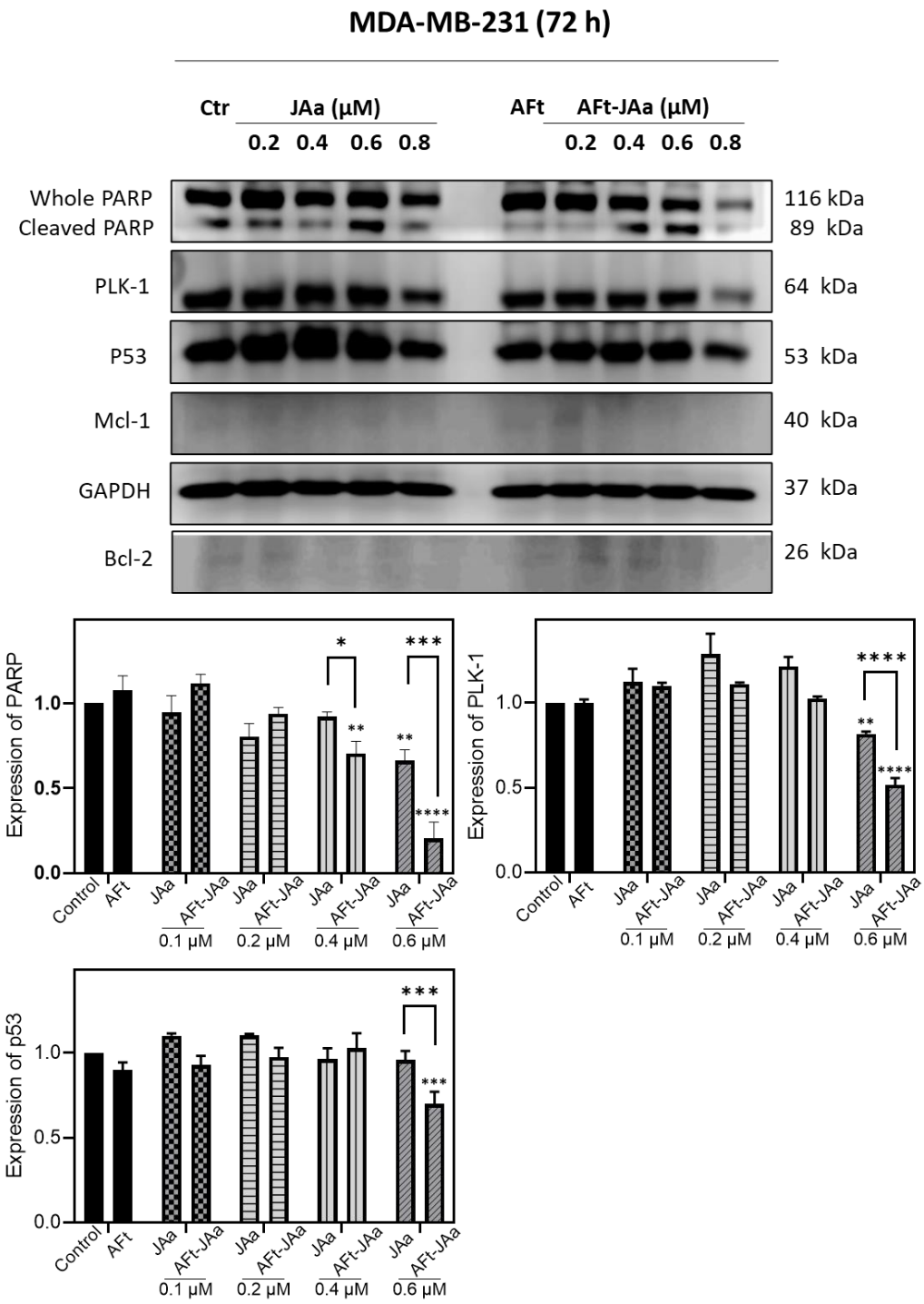


Figure 5.8: Protein expression in MDA-MB-231 cell lysates following 72 h exposure of cells to JAa, AFt-JAa at different concentrations, AFt (0.0068 µM) and media only. Collated densitometric measurement of cellular protein expression levels of PARP, PLK-1 and p53 represented as mean ± SD and repeated in 3 independent occasions. Significant differences from untreated cells are expressed as *P < 0.05, **P < 0.01, ***P < 0.001, ****P < 0.0001 from untreated control. Significant differences from JAa are expressed in brackets.

MDA-MB-231 also express caspase-3 [463], which upon its activation cleaves PARP. The reduction in PARP expression detected at higher concentrations of JAa is consistent with its lower sensitivity compared with SKBR-3; as shown in apoptosis assays (**Figure 5.5**). MDA-MB-231 cells also harbour another type of mutant p53. This mutation causes p53 to lose its ability to bind Bcl-xl and Bcl-2, resulting in losing cytochrome c release from mitochondria, and consequently cytoplasmic pro-apoptotic activity [464]. Thus, reduced expression of mutant p53 detected with JAa treatment at higher concentration (8 µM) is consistent with reduced proliferation of MDA-MB-231 cells detected with cell cycle arrest (**Figure 5.2**) and cell death (**Figure 5.5**). Of interest and in contrast to SKBR-3, JAa suppressed PLK1 protein in MDA-MB-231, indicating interference with mitotic entry, spindle assembly, anaphase entry and cytokinesis that results in apoptosis [452, 454-457]. Previously, JB has been shown to dose-dependently inhibit the expression and activity of PLK1 as one of multiple possible targets to interact with tubulin and accompanies G2/M arrest. Results suggest apoptosis-induction through different pathways in different cell lines and support the results of Annexin V assays.

In MCF-7 lysates, dose-dependent reduction in the expression of pro-survival Mcl-1 protein accompanied suppression of anti-apoptotic protein Bcl-2 and oncogenic kinase PLK-1 in parallel with up-regulation of p53 expression (**Figure 5.9**).

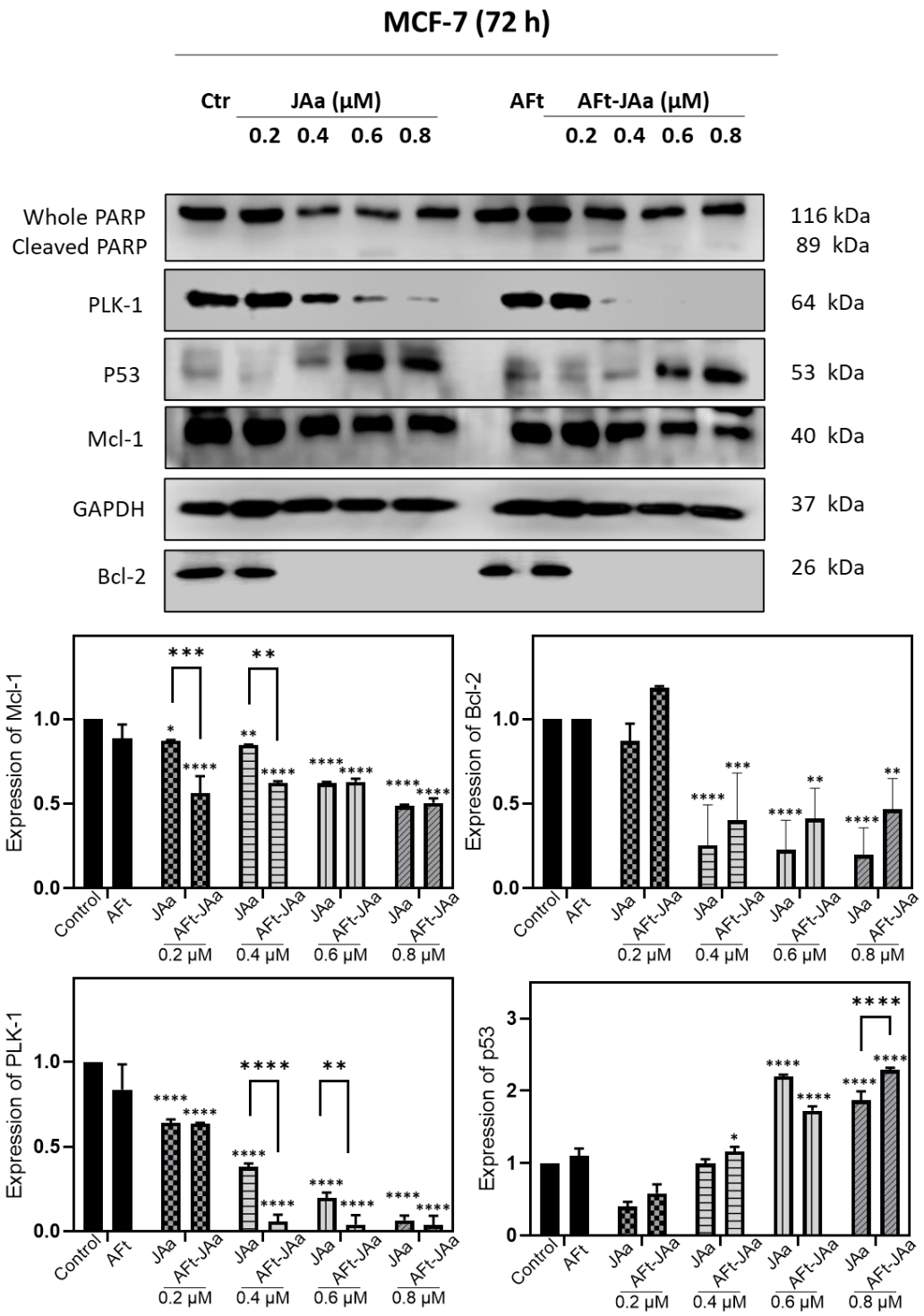


Figure 5.9: Protein expression in MCF-7 cell lysates following 72 h exposure of cells to JAa, AFt-JAa at different concentrations, AFt (0.0068 µM) and media only. Collated densitometric measurement of cellular protein expression levels of Mcl-1, Bcl-2, PLK-1 and p53 represented as mean ± SD and repeated in 3 independent occasions. Significant differences from untreated cells are expressed as *P < 0.05, **P < 0.01, ***P < 0.001, ****P < 0.0001 from untreated control. Significant differences from JAa are expressed in brackets.

The dose-dependent reduction in expression of anti-apoptotic/pro-survival proteins Mcl-1 and Bcl-2 indicate cell death and are consistent with apoptotic populations detected in Annexin V assays (**Figure 5.6**). Unlike the findings with SKBR-3 and MDA-MB-231, the relatively stable levels of PARP protein following the treatment is consistent with caspase 3 deficiency in MCF-7 cells [465]. Although caspase 3 activation and PARP cleavage predisposed apoptosis in diverse cancerous cells following the treatment with jerantinines [202, 203], it has been suggested that inducing apoptosis of MCF-7 following the treatment with JA might occur through caspase-independent pathways [466]. Indeed, MOMP results not only in releasing cytochrome c from mitochondria but also in other proteins such as apoptosis-inducing factor (AIF), proapoptotic mitochondrial serine protease (HtrA2/Omi) and endonuclease G which are known to promote caspase-independent death through mechanisms involving ROS production [467]. Such proteins might predispose the caspase-independent apoptosis pathways in MCF-7 but are yet to be investigated in a future study.

In contrast to the high expressed levels of mutant p53 found with SKBR-3 and MDA-MB-231 lysates, MCF-7 cells express low levels of wild type (WT) p53. This is consistent with the findings of lower total levels of WT p53 detected in breast cancer cells including MCF-7 compared with consistently higher levels of this protein in the breast cancer cell lines encoding mutant p53 [468]. Re-expressing p53 in cells retaining WT p53 activity results in restoring its anticancer activity and predisposes cancer cells to apoptosis or decreased proliferation [469]. Increasing levels of WT p53 in cancer cells treated with JA was detected previously along with down regulation of its inhibitor; Hdm2 [202]. Of interest, although increasing the

expression of WT p53 accompanied down regulation of PLK-1 in MCF-7, these cells show lower sensitivity to treatment compared to SKBR-3 and MDA-MB-231. Curiously, activation of functional but not mutant p53 has been found to protect cancer cells, including MCF-7, from the effects of PLK-1 inhibitors [451, 470]. Indeed, jerantinines target and inhibit PLK-1 as one of their multiple anticancer mechanisms [203]. Moreover, PLK1 is a direct transcriptional target of p53 and its inhibition results from the activation of WT p53 [471]. Alternatively, the inhibition of PLK1 may trigger DNA damage which activates functional p53 [451]. Either way, functional p53 has been found to lower cellular response to PLK1 inhibition by maintaining centrosome separation, this permits a proportion of treated cells to traverse mitosis and cytokinesis, and re-enter G1 phase in the cell cycle with a normal complement of chromosomes. Taken together, it may be suggested that the lower sensitivity to JAa detected in MCF-7 cells might be related to the protective effect of active WT p53 to PLK-1 inhibition. In contrast PLK1 inhibition in cancer cells that possess mutant p53, as seen in SKBR-3 and MDA-231 cells, might be advantageous with respect to jerantinine-sensitivity.

5.3.4 Free and encapsulated JAa Induce reactive oxygen species in breast cancer cell lines

ROS are highly reactive radicals, ions or molecules generated normally in cells and required for many cellular processes including immune response and progression of the cell cycle [358, 359]. However, these free radicals are destructive to cellular proteins and DNA; therefore, their cellular levels are managed with cellular antioxidants [361, 472]. Uncontrolled high levels of ROS lead to oxidative stress

resulting in degenerative diseases, and sometimes oncogenic transformation [360]. In cancer cells, the elevated rates of ROS promote tumourigenesis, angiogenesis and tumour invasion [360, 361].

Both environmental and internal mechanisms lead to the elevation of ROS levels [473], including high cellular levels of iron. As mentioned earlier (Section 1.6.2) iron plays a pivotal role in the occurrence of tumours and the disorder of its metabolism further facilitates tumour progression [474]. Due to their higher demand for iron, tumour cells import high levels of iron through the highly expressed TFR1 (Section 1.2.5.1). The high level of iron induces lipid peroxidation, a process that also results in ROS production. Iron-dependent excessive increased intracellular ROS lead to detrimental consequences including DNA damage and cell cycle arrest [361]. Cell death due to this process was recently discovered and is known as ferroptosis [472]. However, damaging high levels of intracellular ROS caused by chemotherapeutic agents results in ferroptosis in addition to other cell death mechanisms including apoptosis, necrosis and autophagy, which initiate caspase-dependent as well as caspase-independent cell death pathways [467, 475-477]. Cells undergoing ferroptosis do not share the morphological features of apoptosis: shrinkage of cells, formation of apoptotic bodies, chromatin condensation or formation of the cytoskeleton. Ferroptotic cells do not show swelling of cells or rupture of their cellular membrane like necrosis. Neither do ferroptotic cells demonstrate the formation of double-membraned autolysosomes detected in autophagy; they show a shrinkage of mitochondria and an increase in cell membrane density [478].

Some anticancer agents, notably natural oxygen-containing compounds (e.g., doxorubicin) also exert anticancer action via ROS generation, formed as by-products of oxygen metabolism. Due to their high metabolic turnover and genomic/chromosomal instability, cancer cells are highly sensitive to ROS; causing cellular death [479].

As previously indicated, treating MDA-MB-231 cells with JAa, resulted in accumulation of events in the S phase, which may indicate DNA damage as a possible consequence of ROS-generation. In addition, suggested cellular death that might trigger caspase 3-independent apoptosis pathways in MCF-7 might also involve ROS production. Therefore, measuring the levels of H_2O_2 was conducted to investigate whether JAa, AFt-JAa (0.4 µM JAa) and AFt (0.0033 µM) increase the levels of ROS in MDA-MB-231 and MCF-7 cells following 24 h exposure (see Section 2.3.9).

Free JAa evoked significantly increased ROS production in MDA-MB-231 (112%) and MCF-7 (135%) following 24 h exposure to cells compared to the control cells ($p < 0.01$) (**Figure 5.10**). AFt-JAa also showed a clear increase in ROS production in MDA-MB-231 (119%) and MCF-7 (127%), compared to the control ($p < 0.0001$) but not compared to free JAa ($p > 0.05$). AFt alone induces comparable levels of ROS to untreated cells in both cell lines ($p > 0.05$).

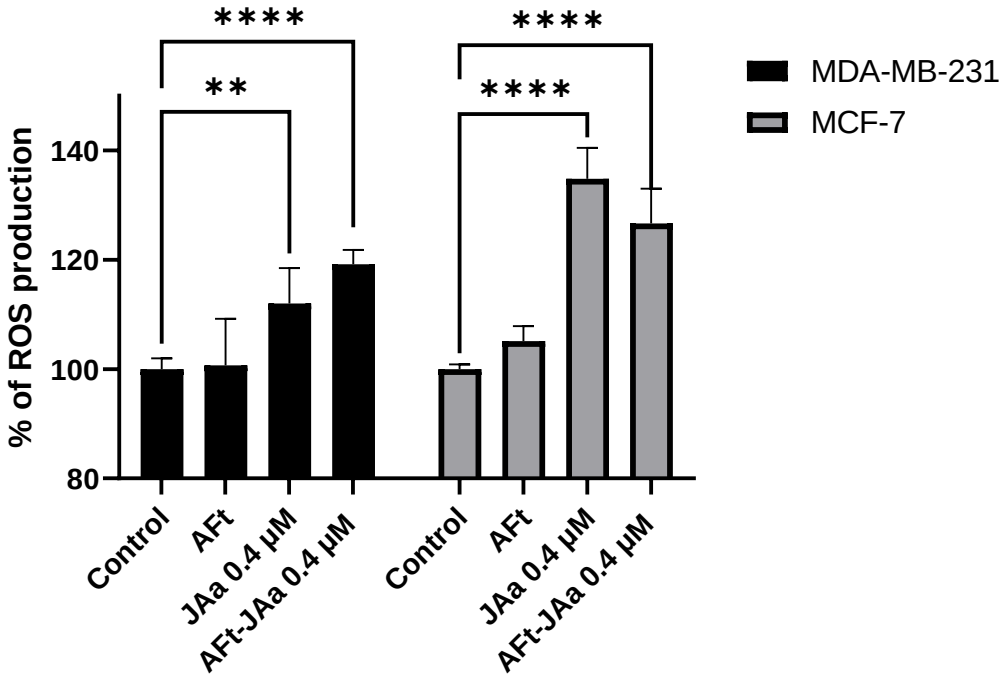


Figure 5.10: Free and AFt-encapsulated JAa (0.4 µM JAa for 24 h) potently increased ROS production in MDA-MB-231 and MCF-7 cells compared to their levels without treatment. While the levels of ROS production following AFt treatment (0.0033 µM) were comparable to untreated cells. Data are expressed as a percentage of Mean ± SEM in three independent trials (*n* = 2 per trial). Significant differences are expressed as **P < 0.01 and ****P < 0.0001.

Increased levels of ROS in treated cells indicate their contribution to cell death detected in previous *in vitro* assays (**Figure 5.5**, **5.6**), and support their suggested role in caspase-independent apoptosis [204], exemplified in caspase 3 deficient MCF-7 cells [463]. In MDA-MB-231 cells, ROS generation may contribute to apoptosis through caspase-dependent apoptosis, consistent with S phase accumulation and DNA damage in treated cells. Although sub-lethal doses of ROS production might be mutagenic, jerantinines show their cytotoxic effects at low doses due to their multitarget effects. In accordance with these results, a previous study has demonstrated that as one of its mechanisms, JB induces apoptosis

through the production of high levels of ROS in treated cells including HCT-116 and MIA PaCa-2 [203]. Moreover, the authors showed that JB overcomes P-gp mediated VCR resistance In VR HCT-116 cells by increasing the levels of ROS. Indeed, jerantinines were suggested to act as other natural products and induce apoptosis *via* ROS following the oxidation of mitochondrial pores, resulting in the release of cytochrome c and activation of caspases, inducing apoptosis [203, 480-482].

In contrast to results obtained with other conducted *in vitro* assays that indicate higher activity of encapsulated JAa, AFt-JAa shows comparable levels of ROS to levels induced with naked JAa. This is consistent with the fact that AFt-JAa formulation competes with Ft internalisation through binding to TFR1. This will further reduce intracellular iron levels and ROS induction through lipid peroxidation.

One interesting observation following treatment of MDA-MB-231 with JAa is related to the non-apoptotic population found in the upper left quadrant in Annexin V apoptosis assays (**Figure 5.5**). As the dead cells from ferroptosis do not go through the apoptosis process, they appear in the upper left quadrant of annexin V apoptosis assay along with necrotic populations [483]. Therefore, in MDA-MB-231, the high levels of ROS and non-apoptotic dead cells further suggest that the treatment with JAa might lead to ferroptosis cell death in these cells in addition to previously detected apoptosis. Moreover, it has been shown that p53 plays an important role in the regulation of ferroptosis, in addition to its role in the regulation of the Bcl-2 family. The relation between p53 and ferroptosis is not

yet fully established. However, previous studies have shown that although mutant p53 is associated with more aggressive and chemo-resistant cancers, it increases sensitivity to ferroptosis [484, 485]. In cancer cells, mutant p53 binding to antioxidant transcription nuclear factor erythroid 2–related factor 2 (NRF2) results in suppression of solute carrier family 7-member 11 (*SLC7A11*) expression. SLC7A11 is a constituent of the cystine/glutamate antiporter known as system x_c^- which mediates the internalisation of cystine, a precursor for glutathione (GSH) biosynthesis. GSH is one of the most important intracellular antioxidants that converts free radicals into harmless molecules such as converting H_2O_2 into water. Therefore, inhibition of system x_c^- results in lowering antioxidant capacity and increases sensitivity to oxidative stress and ferroptosis [484-486]. This might further explain the superior response to JAa treatment of MDA-MB-231 cells (harbouring mutant p53) compared to MCF-7 (harbouring WT p53) cells as observed with other *in vitro* assays (e.g., MTT and cell cycle perturbation). The overall findings of a non-apoptotic population in treated MDA-MB-231 along with ROS induction and mutant p53 stabilisation at the lower-used JAa concentration, support the possibility of ferroptosis-induction in these cells following JAa treatment. Further investigation of jerantinines' activity in TNBC cell lines harbouring mutant p53 should be examined to determine whether this cancer phenotype, typically associated with poor prognosis and ill-defined molecular targets for therapy, possesses greater sensitivity to jerantinines than WT p53 cancer cells.

5.4 Conclusion

The main goal of the current study was to examine mechanisms and molecular targets of JAa in three subtypes of breast cancer cells; SKBR-3, MDA-MB-231 and MCF-7, and to investigate the effect of AFt-encapsulation on targets affected by JAa in light of observed enhanced anticancer activity *in vitro*. Following treatment, G2/M events' accumulation confirmed the main mechanism of JAa as a microtubule destabilising agent as previously reported [198, 201-203]. As a result of prolonged arrest, cell death highlighted by the accumulation of cells in the pre-G1 phase was identified in all tested cells. The detected apoptotic population in SKBR-3 and MCF-7 cells, in addition to non-apoptotic, non-viable population in MDA-MB-231 suggests that several pathways may be targeted (rich and diverse pharmacology) and highlights the significance of JAa as a hybrid agent. As evidence for apoptosis, repression of survival, anti-apoptotic proteins Mcl-1, Bcl-2, and cleaved PARP were confirmed. Inhibition of PLK-1 and ROS induction following JAa treatment further highlight its multi-targeted capacity, consistent with previous reports [202, 203]. Our study exposes a new advantage of using JAa in the treatment of diverse breast carcinomas. JAa significantly increased the levels of functional WT p53 expression in MCF-7 while suppressing mutant p53 in SKBR-3 and MDA-MB-231 cells. Due to the relation between p53 mutations and oncogenicity, compounds that degrade mutant p53 without affecting WT p53 are valuable for cancer therapy [487]. Therefore, JAa's effect on the expression levels of p53 is a new promising therapeutic finding that is worthy of future investigations. Of interest inhibiting mutant p53 along with ROS production

accompanied by apoptotic and non-apoptotic cell death populations in MDA-MB-231 suggest ferroptosis as a new non-investigated mechanism of death triggered by JAa and AFt-JAa. This offers potential for use of JAa to treat TNBC, typically associated with poor prognosis. However, further mechanistic validation is required. Furthermore, our study confirms that the multiple pathways targeted by JAa were not affected upon its encapsulation with the biocompatible AFt delivery vehicle, rather enhanced activity was consistently detected.

5.5 Future work

3. Further investigations are needed to reveal apoptotic mechanisms triggered by JAa in caspase 3-deficient MCF-7 cells. This will include changes in the expression of proteins that might activate caspase-independent apoptosis pathways such as AIF, HtrA2/Omi, and endonuclease G proteins.
4. To comprehensively understand the mechanism by which non-apoptotic populations in MDA-MB-231 cells are produced following treatment with JAa. This will include changes in target genes and pathways regulating lipid peroxidation in ferroptosis such as i) GSH production ii) ROS detoxification iii) iron metabolism and their master transcriptional factors such NFE2L2.
5. Further investigations are needed to reveal how jerantinines increase the expression of WT p53 but in contrast, reduce/stabilise mutant p53 expression, and how this might be relevant to the (differences in) response to treatment.
6. Examining the levels of ROS in breast cancer cell lines treated with encapsulated and naked jerantinines following shorter exposure periods (e.g., 6 h), to further validate AFt-encapsulated formulation.
7. Confocal microscopy to examine morphological changes to microtubules caused by AFt-JAa; further interrogation of morphology associated with ferroptosis.

6 General discussion, conclusion and future directions

6.1 General discussion and conclusion

This study highlights the importance of investigating a new therapeutic approach to enhance breast cancer patients' quality of life and reduce mortality. Two major obstacles in breast cancer therapy - drug resistance and chemotherapeutic toxicity were addressed in this study by using one of the most attractive endogenous nanocarriers, AFt protein [60-62, 488]. JAa demonstrates promising high potency, multi-target effects and the ability to overcome MDR *in vitro* [202-204, 217]. However, it also shows poor cancer selectivity indicated by cytotoxicity against non-cancerous foetal lung fibroblast cells (MRC-5) [202]. Poor cancer-selectivity was addressed in this study by targeting JAa delivery to breast cancer cells using AFt. The nanoreactor and the self-assembly methods were both investigated to encapsulate JAa. Nanoreactor encapsulation of JAa was achieved only by mixing low volumes over extended time intervals (10 µL, 10 mM) every 30 min indicating the slow encapsulation of JAa into AFt. Indeed, JAa, a relatively large molecule with a MWt of 424, may require more time to diffuse through AFt's pores (0.3-5 nm) [387]. Not allowing sufficient time for JAa to diffuse into the core of AFt by adding higher amounts in shorter intervals increases the opportunity for unwanted intra- and inter-molecular interactions to develop, which are reflected in high aggregation as demonstrated by the large hydrodynamic size of AFt-JAa >

100 nm following nanoreactor route encapsulation. Enhancing the encapsulation of JAa was achieved by diffusing JAa at pH lower than its pKa (~7) to allow greater relaxation of AFt cages under acidic conditions [380], and to protonate JAa molecules that facilitate its movement into the negative inner surface of the AFt cage [382]; the interior high negative charge of AFt chains (specifically L–chain), works as a draining force to entrap cations inside the core of AFt at concentrations significantly higher than bulk concentration [407]. However, the inconsistency in EE% when increasing the ratio of JAa:AFt during encapsulation, and the large lateral dimensions of JAa (0.96 X 1.26 nm) suggest that using the nanoreactor method might not be the best route to encapsulate JAa. Moreover, the only encapsulation success by diffusion of a large molecule (maltose, with a lateral dimension of 1.3 nm) through the AFt channels was achieved in conjunction with relaxation of the cage by proton NMR [309]. All other successful nanoreactor route encapsulations without cage relaxation included agents with either relatively small with MWt < 250 [118, 307], or lateral dimensions ≤ 0.3 nm [306]. Therefore, complete dissociation of the AFt cage to ensure the encapsulation of JAa was investigated and optimised. The varied reports for the evaluation of the self-assembly method highlighted the importance of optimising and uniting the parameters controlling the efficiency of this method [310], to produce a reproducible and validated method with a high PR% yield. During the evaluation of the type of acidic solution used to dissociate AFt subunits, the disappearance of the horse spleen AFt band at ~480 in the native gel seen with HCl only, indicated the significance of solution types used to dissociate the horse spleen AFt cage rather than pH-alteration alone. This is explained by the impact of the Hofmeister

effect of ion type and their ability to salt in (structure-breaking ions) or salt out (structure-making ions) proteins. Accordingly, Cl^- is a better structure-breaking ion needed for salting in AFt subunits and keeping them separate at pH 2 compared to acetate [394]. On the other hand, the successful dissociation of H-AFt using both HCl and glycine acetate indicates the need for a weaker structure-breaking ion to disassemble AFt and thus supports its reported lower stability compared to horse spleen AFt [395]. The varied and different PR% produced upon adopting different reassembly methods reflect the importance of producing an efficient reassembled formulation at this step. Contrary to disassembly, AFt reassembly needed better structure making ions (salt out) to give the AFt subunits the required intermolecular hydrophobic forces, thus the ability to refold their native structure [282, 398]. This was achieved by both sustaining the reassembly solution with high ionic strength throughout the reassembly process and quickly avoiding the PI of AFt (4.1- 5.1) to restore subunits' reassembly properties [393]. The failure of producing the required hydrodynamic size of AFt (< 12 nm) when using basic solution rather than buffers, supports the significance of using buffers to bind to native proteins and increase the conformational stability of proteins with no impact on the denatured or unfolded state [400]. The characterisation of AFt-encapsulated large MWt agents including VCR and RB besides JAa through the self-assembly method, produced formulations with comparable size, charge and integrity to AFt stock used. Comparable size and charge cage to AFt post-encapsulation indicates the negligible effect of cargo type on the properties of reassembled AFt, and thus validates its use as cage, and the reassembly method we have optimised for encapsulating other agents with high MWt regardless of

their type. Our optimised self-assembly method encapsulated ~120 JAa molecules inside the core of horse spleen AFt, which robustly recovered ~77% and ~70% of protein without and with JAa encapsulation. The formulation was stable for 10 months at storage conditions (pH 7.4; 4 ºC) and showed rapid release of JAa at 37 ºC in the first 6 h with ~40% and 60% release at pH 5.3 and 7.4 respectively, followed by a more controlled release for > 24 h under both pH conditions.

AFt can be targeted to the tumour tissues due to its recognition by, and overexpression of TFR1 on tumour cells' outer surface. TFR1 recognise the Ft H chain of AFt and internalises it through clathrin-mediated endocytosis [23]. Thus, in this study, the significant high expression of membrane-bound TFR1 ($P < 0.0001$) measured in six breast cell lines (MCF-7 - luminal A, ER+; BT-474 - luminal B, HER2+; SKBR-3, HER2 overexpression; MDA-MB-468 - basal-like, TNBC; MDA-MB-231 - claudin-low, TNBC) compared to MRC-5 that expressed very low TFR1 levels, validated their targeting with AFt. In MTT assays JAa demonstrated high growth inhibitory effects in all used cell lines including non-transformed MCF-10A and MRC-5. GI_{50} cells values between 0.14 and 0.56 µM reflect its high potency, but also non-selective targeting. MTT assays demonstrated that delivering JAa within AFt NPs significantly reduced GI_{50} values ($P < 0.05$) only in cell lines that overexpress TFR1, irrespective of their phenotype, while no significant change in MRC-5 GI_{50} values following their exposure to naked or AFt-encapsulated JAa was encountered. The significantly lower counted viable cells, and colonies' formation in all TFR1+ cells further support enhanced activity of the AFt-JAa formulation and further inspire use of AFt as a TFR-1-targeted drug delivery vehicle for breast carcinoma. The enhanced selectivity of AFt-JAa formulation is shown to be

correlated to the preferential enhanced uptake of H-AFt seen in TFR1+ cells over TFR1-low expressing cells. The enhanced potency of the AFt-JAa nanoformulation was found to be related to increased intracellular accumulation of JAa in cells overexpressing TFR1, as reflected by significantly higher accumulation of JAa in TFR1+ over naked JAa in tested cells (SKBR-3, MDA-MB-231 and BT-474). The AFt formulation also enhanced the stability of JAa, which further contributes to the observed enhanced activity. This was reflected by higher detected levels of JAa in culture media without cells under the treatment conditions (T= 37 ^{o}C; ≤ 72 h) following AFt encapsulation compared to naked agent.

The subsequent supporting *in vitro* tests in SKBR-3, MDA-MB-231 and MCF-7 cells confirmed enhanced the activity of encapsulated JAa without altering its mechanism of action. Cell cycle analyses showed varied but significant cell cycle arrest with G2/M phase and pre-G1 events' accumulation following treatment with free JAa. This confirmed that JAa exhibits potent antiproliferative activity by arresting the cell cycle in the G2/M phase and indicates that a major molecular target of jerantinines, mitotic microtubules' destruction, was not affected (indeed, was enhanced) following delivery of the agent by AFt NPs [198, 201-203]. Consistent with the accumulation of pre-G1 events, apoptosis-induction in the three tested cell lines was also confirmed by Annexin V apoptotic assays. Western blotting demonstrated that inducing apoptosis in treated cells is related to repression of anti-apoptotic survival proteins; Mcl-1 in SKBR-3 and MCF-7 in addition to Bcl-2 in the latter. This was accompanied by cleaved PARP in SKBR-3 and MDA-MB-231 cells. In addition, enhanced expression of WT p53 in MCF-7 ($p < 0.0001$) and repression/stabilisation of mutant p53 in SKBR-3 (0.01) and MDA-

MB-231 respectively were detected at concentrations of ≥ 0.6 µM for both naked and encapsulated JAa. Indeed, destabilising tubulin polymerisation results in profound G2/M arrest and activates the mitotic checkpoint [489]. This results in the activation of tumour suppressor p53 which prohibits damaged cells transiting from the G2-to-M phase until the damage is repaired [10]. Cells with prolonged exposure to microtubule-disrupting agents, fail to go through cytokinesis and might transit to G1-like phase with double the number of normal chromosomes [490]. This will further activate G1 checkpoints which upon their activation further activate p53 in an attempt to repair the damaged DNA. As a result of unrepaired damage, activated p53 causes apoptosis by regulating the activity of Bcl-2 family proteins [11, 23]. The significant up-regulation of p53 protein following treatment of WT p53 MCF-7 cells with JAa was evident. In contrast, stabilisation of mutant p53 expression was detected in SKBR-3 and MDA-MB-231 cells at ≥ 0.2 µM and interestingly inhibited at 0.6 µM in SKBR-3. Indeed, mutants of p53 are detected in 50% of cancers which results in more aggressive disease and impaired survival [24]. Thus, inhibiting its expression by anticancer agents is of high interest. Western blotting revealed a reduction in the expression of anti-apoptotic/pro-survival Bcl-2 and Mcl-1 proteins which regulate mitochondrial apoptosis. As a result of their inhibition cytochrome c is released from mitochondria into the cytosol resulting in apoptosome formation, caspase 3 activations (this can also occur independently of caspase activation) and ultimately apoptosis, which was presented in the pre-G1 events' accumulation and the emergence of apoptosis populations detected by Annexin V assays [21]. Active caspase 3 cleaves PARP as one of its targets [449], this was evident in the lysates of treated SKBR-3 and MDA-

MB-231 cells. In contrast, the non-significant reduction of PARP when MCF-7 cells were treated with JAa, indicates that cleaving PARP is not a main mechanism of inducing apoptosis. This is consistent with the absence of caspase 3 in MCF-7 cells [491]. JAa-encapsulation within AFt did not change its multi-target capacity, indeed JAa still demonstrated high potency as a PLK1 inhibitor in treated MCF-7 and MDA-MB-231 cells before and after AFt-encapsulation. However, previously it has been found that activation of functional p53 protects cancer cells from the effect of PLK-1 inhibitors [451, 470], which further explains the lower sensitivity to JAa in MCF-7 cells but not cells with mutant p53; SKBR-3 and MDA-MB-231 and may further suggest a new specificity of jerantininines in treating cells with mutant p53. Moreover, mutant p53 might expose differences in response to the treatment through a different mechanism. In cancer cells, mutant p53 binding to antioxidant transcription factor NRF2 results in inhibition of system x_{C^-} which reduces antioxidant capacity and increases sensitivity to oxidative stress [484-486]. As detected in our results JAa induce ROS in both MDA-MB-231 cells (harbouring mutant p53) and MCF-7 (harbouring WT p53) and might further explain the better response to JAa treatment exhibited in MDA-MB-231 cells compared to MCF-7. Besides, in the three tested cell lines, the diverse apoptotic response could be related to many other reasons. The different sensitivity of treated cells to JAa treatment can be related to varied expression levels of certain proteins, indeed it has been supposed that the variation in the Bcl-2 protein content within the mitochondria affect the response levels of cells with different phenotypes to apoptosis [492]. Of interest, AFt did not show any detrimental effect on tested cells as indicated from all used *in vitro* assays including MTT, cell

count, clonogenic, cell cycle analysis, annexin V apoptosis, or western blotting expression of apoptotic/antiapoptotic proteins.

The overall enhanced activity of encapsulated JAa within AFt nanocarrier in TFR1+ cells showed in this study further supports previous research reporting enhanced activity of other clinical and experimental anticancer agents such as doxorubicin [321, 493], temozolomide [118], and benzothiazole prodrugs [307, 494]. This study confers a robust AFt-reassembly route to JAa-encapsulation which achieved a significant degree of cancer-selectivity in breast cancer cells expressing enhanced TFR1 versus TFR1-low MRC5 cells and provides evidence that AFt-JAa offers a potential treatment for intractable, drug-resistant mammary carcinomas, and supports using AFt as a safe and biocompatible nanocarrier of anticancer agents, worthy of further preclinical development.

6.2 Future directions

- LC-MS-based cellular metabolomics study is to be further conducted to identify key metabolites affected by naked and encapsulated JAa. Involved metabolites are to be further analysed by MetaboAnalyst and MetExplore analysis tools to comprehensively reveal several affected pathways involved in carcinogenesis and to investigate the potential nanotoxicity at the cellular and molecular levels [495].
- The development of affibody-conjugated AFt delivery capsules that target proteins overexpressed in certain mammary tumours, remains a goal of current research, ultimately to enhance survival rates and improve prognoses in breast cancer patients. However, the benefits of actively targeting AFt should be strictly evaluated versus the benefits of using passive targeting of AFt as presented in this study. As it has been reported previously that small polymers showed a better tumour accumulation when compared to their actively targeted larger form conjugated to antibodies, binding of affibody, which is part of monoclonal antibodies but with smaller size is to be investigated. In addition to the conflicts reported with their affinity; active targeting may tend to bind tightly to the cells on the surface of the tissue rather than penetration the core of the cancerous tissue [249].
- This study demonstrated enhanced potency and selectivity of encapsulated JAa, in addition to supporting the biocompatibility of used AFt nanocarrier. However, comprehensive future *in vivo* studies including

tolerability and efficacy of tested agents are needed to integrate these results into the clinical routine.

- As a non-P-gp substrate evading MDR efflux, previous reports presented jerantinines as a potential alternative to VCR in the treatment of paediatric medulloblastoma [217]. However, as the anticancer mode of action of jerantinines operating *via* microtubule disruption resulting from binding at the colchicine site, interestingly, colchicine is also a P-gp substrate [201, 496], a future study should be conducted to examine any cross-resistance between jerantinines and colchicine. This will be performed using two variant breast carcinoma lines derived from MDA-MB-231 and MCF-7 that demonstrate acquired resistance to colchicine.

7 References

1. Vogelstein, B. and K.W. Kinzler, *The multistep nature of cancer.* Trends in Genetics, 1993. **9**(4): p. 138-141.
2. Maman, S. and I.P. Witz, *A history of exploring cancer in context.* Nature Reviews Cancer, 2018. **18**(6): p. 359-376.
3. Siegel, R.L., et al., *Cancer Statistics, 2021.* CA: A Cancer Journal for Clinicians, 2021. **71**(1): p. 7-33.
4. Maringe, C., et al., *The impact of the COVID-19 pandemic on cancer deaths due to delays in diagnosis in England, UK: a national, population-based, modelling study.* The Lancet Oncology, 2020. **21**(8): p. 1023-1034.
5. Hanahan, D. and Robert A. Weinberg, *Hallmarks of Cancer: The Next Generation.* Cell, 2011. **144**(5): p. 646-674.
6. Hanahan, D. and R.A. Weinberg, *The hallmarks of cancer.* Cell, 2000. **100**(1): p. 57-70.
7. Senga, S.S. and R.P. Grose, *Hallmarks of cancer-the new testament.* Open Biol, 2021. **11**(1): p. 200358.
8. Nurhanan, M., et al., *Anti-proliferative activities of 32 Malaysian plant species in breast cancer cell lines.* Journal of Tropical Forest Science, 2008: p. 77-81.
9. Momand, J., H.-H. Wu, and G. Dasgupta, *MDM2 — master regulator of the p53 tumor suppressor protein.* Gene, 2000. **242**(1): p. 15-29.
10. Vogelstein, B., D. Lane, and A.J. Levine, *Surfing the p53 network.* Nature, 2000. **408**(6810): p. 307-310.
11. Gottlieb, T.M. and M. Oren, *p53 and apoptosis.* Seminars in Cancer Biology, 1998. **8**(5): p. 359-368.
12. Chiasson-MacKenzie, C., et al., *NF2/Merlin mediates contact-dependent inhibition of EGFR mobility and internalization via cortical actomyosin.* Journal of Cell Biology, 2015. **211**(2): p. 391-405.
13. Morrow, K.A., et al., *Loss of Tumor Suppressor Merlin in Advanced Breast Cancer Is due to Post-translational Regulation *.* Journal of Biological Chemistry, 2011. **286**(46): p. 40376-40385.
14. Lee, S., et al., *The Role of Merlin/NF2 Loss in Meningioma Biology.* Cancers, 2019. **11**(11): p. 1633.
15. Yan, G., M. Elbadawi, and T. Efferth, *Multiple cell death modalities and their key features (Review).* World Acad Sci J, 2020. **2**(2): p. 39-48.
16. Galluzzi, L., et al., *Molecular mechanisms of cell death: recommendations of the Nomenclature Committee on Cell Death 2018.* Cell Death & Differentiation, 2018. **25**(3): p. 486-541.
17. Letai, A., *Apoptosis and Cancer.* Annual Review of Cancer Biology, 2017. **1**(1): p. 275-294.
18. Wang, K., et al., *BID: a novel BH3 domain-only death agonist.* Genes Dev, 1996. **10**(22): p. 2859-69.
19. Letai, A., et al., *Distinct BH3 domains either sensitize or activate mitochondrial apoptosis, serving as prototype cancer therapeutics.* Cancer Cell, 2002. **2**(3): p. 183-192.
20. Kim, H., et al., *Stepwise activation of BAX and BAK by tBID, BIM, and PUMA initiates mitochondrial apoptosis.* Mol Cell, 2009. **36**(3): p. 487-99.
21. Bleicken, S., et al., *Structural model of active Bax at the membrane.* Mol Cell, 2014. **56**(4): p. 496-505.

22. D'Amelio, M., V. Cavallucci, and F. Cecconi, *Neuronal caspase-3 signaling: not only cell death.* Cell Death & Differentiation, 2010. **17**(7): p. 1104-1114.
23. Nakano, K. and K.H. Vousden, *PUMA, a novel proapoptotic gene, is induced by p53.* Molecular cell, 2001. **7**(3): p. 683-694.
24. Gasco, M., S. Shami, and T. Crook, *The p53 pathway in breast cancer.* Breast Cancer Research, 2002. **4**(2): p. 70.
25. Radha, G. and S.C. Raghavan, *BCL2: A promising cancer therapeutic target.* Biochimica et Biophysica Acta (BBA) - Reviews on Cancer, 2017. **1868**(1): p. 309-314.
26. Yaswen, P., et al., *Therapeutic targeting of replicative immortality.* Seminars in cancer biology, 2015. **35 Suppl**(Suppl): p. S104-S128.
27. Nishida, N., et al., *Angiogenesis in cancer.* Vascular health and risk management, 2006. **2**(3): p. 213-219.
28. Saman, H., et al., *Inducing Angiogenesis, a Key Step in Cancer Vascularization, and Treatment Approaches.* Cancers, 2020. **12**(5): p. 1172.
29. Baeriswyl, V. and G. Christofori, *The angiogenic switch in carcinogenesis.* Semin Cancer Biol, 2009. **19**(5): p. 329-37.
30. Zhang, P., et al., *Inhibition of VEGF Expression by Targeting HIF-1α with Small Interference RNA in Human RPE Cells.* Ophthalmologica, 2007. **221**(6): p. 411-417.
31. Goel, H.L. and A.M. Mercurio, *VEGF targets the tumour cell.* Nat Rev Cancer, 2013. **13**(12): p. 871-82.
32. Rak, J., et al., *Mutant ras oncogenes upregulate VEGF/VPF expression: implications for induction and inhibition of tumor angiogenesis.* Cancer Res, 1995. **55**(20): p. 4575-80.
33. Meadows, K.L. and H.I. Hurwitz, *Anti-VEGF therapies in the clinic.* Cold Spring Harb Perspect Med, 2012. **2**(10).
34. Mohajeri, A., et al., *The Challenges of Recombinant Endostatin in Clinical Application: Focus on the Different Expression Systems and Molecular Bioengineering.* Adv Pharm Bull, 2017. **7**(1): p. 21-34.
35. Nagy, J.A., et al., *Why are tumour blood vessels abnormal and why is it important to know?* British Journal of Cancer, 2009. **100**(6): p. 865-869.
36. Yuan, F., et al., *Microvascular permeability of albumin, vascular surface area, and vascular volume measured in human adenocarcinoma LS174T using dorsal chamber in SCID mice.* Microvascular research, 1993. **45**(3): p. 269-289.
37. Jain, R.K., *Transport of molecules across tumor vasculature.* Cancer and Metastasis Reviews, 1987. **6**(4): p. 559-593.
38. Izci, M., et al., *The Use of Alternative Strategies for Enhanced Nanoparticle Delivery to Solid Tumors.* Chemical Reviews, 2021. **121**(3): p. 1746-1803.
39. Tahtamouni, L., et al., *Molecular Regulation of Cancer Cell Migration, Invasion, and Metastasis.* Analytical Cellular Pathology, 2019. **2019**: p. 1356508.
40. Talmadge, J.E. and I.J. Fidler, *AACR centennial series: the biology of cancer metastasis: historical perspective.* Cancer research, 2010. **70**(14): p. 5649-5669.
41. Yu, W., et al., *Cadherin Signaling in Cancer: Its Functions and Role as a Therapeutic Target.* Frontiers in Oncology, 2019. **9**(989).
42. Meirson, T., H. Gil-Henn, and A.O. Samson, *Invasion and metastasis: the elusive hallmark of cancer.* Oncogene, 2020. **39**(9): p. 2024-2026.
43. Ward, Patrick S. and Craig B. Thompson, *Metabolic Reprogramming: A Cancer Hallmark Even Warburg Did Not Anticipate.* Cancer Cell, 2012. **21**(3): p. 297-308.

44. Medina, M.Á., *Metabolic Reprogramming is a Hallmark of Metabolism Itself.* BioEssays, 2020. **42**(10): p. 2000058.
45. Yu, M., et al., *The prognostic value of GLUT1 in cancers: a systematic review and meta-analysis.* Oncotarget, 2017. **8**(26): p. 43356-43367.
46. Marbaniang, C. and L. Kma, *Dysregulation of Glucose Metabolism by Oncogenes and Tumor Suppressors in Cancer Cells.* Asian Pacific journal of cancer prevention : APJCP, 2018. **19**(9): p. 2377-2390.
47. Eriksson, M., et al., *Effect of Mutant p53 Proteins on Glycolysis and Mitochondrial Metabolism.* Molecular and Cellular Biology, 2017. **37**(24): p. e00328-17.
48. Gonzalez, H., C. Hagerling, and Z. Werb, *Roles of the immune system in cancer: from tumor initiation to metastatic progression.* Genes & development, 2018. **32**(19-20): p. 1267-1284.
49. Pandya, P.H., et al., *The Immune System in Cancer Pathogenesis: Potential Therapeutic Approaches.* Journal of Immunology Research, 2016. **2016**: p. 4273943.
50. Vajdic, C.M. and M.T. van Leeuwen, *Cancer incidence and risk factors after solid organ transplantation.* International journal of cancer, 2009. **125**(8): p. 1747-1754.
51. Gonçalves, P.H., T.S. Uldrick, and R. Yarchoan, *HIV-associated Kaposi sarcoma and related diseases.* AIDS (London, England), 2017. **31**(14): p. 1903-1916.
52. Pérez-Valencia, J.A., et al., *Angiogenesis and evading immune destruction are the main related transcriptomic characteristics to the invasive process of oral tongue cancer.* Scientific Reports, 2018. **8**(1): p. 2007.
53. Guha, T. and D. Malkin, *Inherited TP53 Mutations and the Li-Fraumeni Syndrome.* Cold Spring Harb Perspect Med, 2017. **7**(4).
54. Watson, A. and J. Galloway, *Heartburn, Barrett's oesophagus and cancer: implications for primary care.* The British journal of general practice : the journal of the Royal College of General Practitioners, 2014. **64**(620): p. 120-121.
55. Zhang, X.-Y., P.-Y. Zhang, and M.A.M. Aboul-Soud, *From inflammation to gastric cancer: Role of Helicobacter pylori.* Oncology letters, 2017. **13**(2): p. 543-548.
56. Sung, H., et al., *Global Cancer Statistics 2020: GLOBOCAN Estimates of Incidence and Mortality Worldwide for 36 Cancers in 185 Countries.* CA: A Cancer Journal for Clinicians, 2021. **71**(3): p. 209-249.
57. Heer, E., et al., *Global burden and trends in premenopausal and postmenopausal breast cancer: a population-based study.* The Lancet Global Health, 2020. **8**(8): p. e1027-e1037.
58. International Agency for Research on Cancer. *Global cancer statistics 2020*. 2020 24/10/2021]; Available from: https://gco.iarc.fr/today/online-analysis-dual-bars-2.
59. Mutebi, M., et al., *Breast cancer treatment: A phased approach to implementation.* Cancer, 2020. **126**(S10): p. 2365-2378.
60. Harbeck, N., et al., *Breast cancer.* Nature Reviews Disease Primers, 2019. **5**(1): p. 66.
61. Ward, R.A., et al., *Challenges and Opportunities in Cancer Drug Resistance.* Chemical Reviews, 2021. **121**(6): p. 3297-3351.
62. Zhao, J., *Cancer stem cells and chemoresistance: The smartest survives the raid.* Pharmacol Ther, 2016. **160**: p. 145-58.
63. Zucca-Matthes, G., C. Urban, and A. Vallejo, *Anatomy of the nipple and breast ducts.* Gland surgery, 2016. **5**(1): p. 32-36.
64. Cserni, G., *Histological type and typing of breast carcinomas and the WHO classification changes over time.* Pathologica - Journal of the

Italian Society of Anatomic Pathology and Diagnostic Cytopathology, 2020. **112**(1): p. 25-41.
65. Nascimento, R. and K. Otoni, *Histological and molecular classification of breast cancer: what do we know?* Mastology, 2020. **30**.
66. Feng, Y., et al., *Breast cancer development and progression: Risk factors, cancer stem cells, signaling pathways, genomics, and molecular pathogenesis.* Genes & diseases, 2018. **5**(2): p. 77-106.
67. Fragomeni, S.M., A. Sciallis, and J.S. Jeruss, *Molecular Subtypes and Local-Regional Control of Breast Cancer.* Surg Oncol Clin N Am, 2018. **27**(1): p. 95-120.
68. Perou, C.M., et al., *Molecular portraits of human breast tumours.* Nature, 2000. **406**(6797): p. 747-752.
69. Sorlie, T., et al., *Repeated observation of breast tumor subtypes in independent gene expression data sets.* Proc Natl Acad Sci U S A, 2003. **100**(14): p. 8418-23.
70. Holliday, D.L. and V. Speirs, *Choosing the right cell line for breast cancer research.* Breast Cancer Research, 2011. **13**(4): p. 215.
71. Prat, A., et al., *Phenotypic and molecular characterization of the claudin-low intrinsic subtype of breast cancer.* Breast Cancer Res, 2010. **12**(5): p. R68.
72. Lukong, K.E., *Understanding breast cancer - The long and winding road.* BBA Clin, 2017. **7**: p. 64-77.
73. Howlader, N., et al., *Differences in Breast Cancer Survival by Molecular Subtypes in the United States.* Cancer Epidemiol Biomarkers Prev, 2018. **27**(6): p. 619-626.
74. Brisken, C., *Progesterone signalling in breast cancer: a neglected hormone coming into the limelight.* Nat Rev Cancer, 2013. **13**(6): p. 385-96.
75. Nik-Zainal, S., et al., *Landscape of somatic mutations in 560 breast cancer whole-genome sequences.* Nature, 2016. **534**(7605): p. 47-54.
76. Dai, X., et al., *Breast Cancer Cell Line Classification and Its Relevance with Breast Tumor Subtyping.* Journal of Cancer, 2017. **8**(16): p. 3131-3141.
77. Nwabo Kamdje, A.H., et al., *Signaling pathways in breast cancer: Therapeutic targeting of the microenvironment.* Cellular Signalling, 2014. **26**(12): p. 2843-2856.
78. Brown, M., L. Cato, and R. Jeselsohn, *Chapter 29 - Hormone-Responsive Cancers*, in *Yen and Jaffe's Reproductive Endocrinology (Eighth Edition)*, J.F. Strauss and R.L. Barbieri, Editors. 2019, Elsevier: Philadelphia. p. 717-741.e8.
79. Fan, S., et al., *Role of direct interaction in BRCA1 inhibition of estrogen receptor activity.* Oncogene, 2001. **20**(1): p. 77-87.
80. Montalto, F.I. and F. De Amicis, *Cyclin D1 in Cancer: A Molecular Connection for Cell Cycle Control, Adhesion and Invasion in Tumor and Stroma.* Cells, 2020. **9**(12): p. 2648.
81. Russo, J., et al., *Pattern of distribution of cells positive for estrogen receptor alpha and progesterone receptor in relation to proliferating cells in the mammary gland.* Breast Cancer Res Treat, 1999. **53**(3): p. 217-27.
82. Stark, G.R. and J.E. Darnell, Jr., *The JAK-STAT pathway at twenty.* Immunity, 2012. **36**(4): p. 503-14.
83. Lanning, N.J. and C. Carter-Su, *Recent advances in growth hormone signaling.* Rev Endocr Metab Disord, 2006. **7**(4): p. 225-35.
84. Haricharan, S. and Y. Li, *STAT signaling in mammary gland differentiation, cell survival and tumorigenesis.* Mol Cell Endocrinol, 2014. **382**(1): p. 560-569.

85. Greenwood, C., et al., *Stat1 and CD74 overexpression is co-dependent and linked to increased invasion and lymph node metastasis in triple-negative breast cancer.* J Proteomics, 2012. **75**(10): p. 3031-40.
86. Koromilas, A.E. and V. Sexl, *The tumor suppressor function of STAT1 in breast cancer.* JAK-STAT, 2013. **2**(2): p. e23353-e23353.
87. Magkou, C., et al., *Prognostic significance of phosphorylated STAT-1 expression in premenopausal and postmenopausal patients with invasive breast cancer.* Histopathology, 2012. **60**(7): p. 1125-32.
88. Barbieri, I., et al., *Constitutively active Stat3 enhances neu-mediated migration and metastasis in mammary tumors via upregulation of Cten.* Cancer Res, 2010. **70**(6): p. 2558-67.
89. Marotta, L.L., et al., *The JAK2/STAT3 signaling pathway is required for growth of $CD44^{+}CD24^{-}$ stem cell-like breast cancer cells in human tumors.* J Clin Invest, 2011. **121**(7): p. 2723-35.
90. Lee, M. and I. Rhee, *Cytokine Signaling in Tumor Progression.* Immune Network, 2017. **17**: p. 214.
91. Wee, P. and Z. Wang, *Epidermal growth factor receptor cell proliferation signaling pathways.* Cancers, 2017. **9**(5): p. 52.
92. Arteaga, Carlos L. and Jeffrey A. Engelman, *ERBB Receptors: From Oncogene Discovery to Basic Science to Mechanism-Based Cancer Therapeutics.* Cancer Cell, 2014. **25**(3): p. 282-303.
93. Garrett, T.P.J., et al., *The Crystal Structure of a Truncated ErbB2 Ectodomain Reveals an Active Conformation, Poised to Interact with Other ErbB Receptors.* Molecular Cell, 2003. **11**(2): p. 495-505.
94. Schwartz, R.S. and J.K. Erban, *Timing of metastasis in breast cancer.* New England Journal of Medicine, 2017. **376**(25): p. 2486-2488.
95. Li, G., et al., *Frizzled7 promotes epithelial-to-mesenchymal transition and stemness via activating canonical Wnt/β-catenin pathway in gastric cancer.* International journal of biological sciences, 2018. **14**(3): p. 280.
96. Song, J.L., et al., *microRNA regulation of Wnt signaling pathways in development and disease.* Cellular signalling, 2015. **27**(7): p. 1380-1391.
97. Yang, K., et al., *The evolving roles of canonical WNT signaling in stem cells and tumorigenesis: implications in targeted cancer therapies.* Laboratory Investigation, 2016. **96**(2): p. 116-136.
98. Nusse, R. and H. Clevers, *Wnt/β-Catenin Signaling, Disease, and Emerging Therapeutic Modalities.* Cell, 2017. **169**(6): p. 985-999.
99. Gustafson, C.T., et al., *Molecular strategies for modulating Wnt signaling.* Front Biosci (Landmark Ed), 2017. **22**: p. 137-156.
100. Gwak, H., et al., *Metformin induces degradation of cyclin D1 via AMPK/GSK3β axis in ovarian cancer.* Molecular Carcinogenesis, 2017. **56**(2): p. 349-358.
101. Rahmani, F., et al., *Role of regulatory miRNAs of the Wnt/ β-catenin signaling pathway in tumorigenesis of breast cancer.* Gene, 2020. **754**: p. 144892.
102. Cai, J., et al., *MicroRNA-374a activates Wnt/β-catenin signaling to promote breast cancer metastasis.* The Journal of clinical investigation, 2013. **123**(2).
103. Schade, B., et al., *β-Catenin signaling is a critical event in ErbB2-mediated mammary tumor progression.* Cancer Res, 2013. **73**(14): p. 4474-87.
104. Khramtsov, A.I., et al., *Wnt/β-Catenin Pathway Activation Is Enriched in Basal-Like Breast Cancers and Predicts Poor Outcome.* The American Journal of Pathology, 2010. **176**(6): p. 2911-2920.
105. Castagnoli, L., E. Tagliabue, and S.M. Pupa, *Inhibition of the Wnt Signalling Pathway: An Avenue to Control Breast Cancer*

Aggressiveness. International Journal of Molecular Sciences, 2020. **21**(23): p. 9069.
106. Murphy, L.C., et al., *Inducible upregulation of oestrogen receptor-beta1 affects oestrogen and tamoxifen responsiveness in MCF7 human breast cancer cells.* J Mol Endocrinol, 2005. **34**(2): p. 553-66.
107. Wei, Y.C., et al., *Upregulation and activation of δ-opioid receptors promotes the progression of human breast cancer.* Oncol Rep, 2016. **36**(5): p. 2579-2586.
108. Pizzamiglio, S., et al., *Expression of Iron-Related Proteins Differentiate Non-Cancerous and Cancerous Breast Tumors.* International journal of molecular sciences, 2017. **18**(2): p. 410.
109. Campisi, A., et al., *Gene Silencing of Transferrin-1 Receptor as a Potential Therapeutic Target for Human Follicular and Anaplastic Thyroid Cancer.* Molecular Therapy - Oncolytics, 2020. **16**: p. 197-206.
110. Dev, S. and J.L. Babitt, *Overview of iron metabolism in health and disease.* Hemodial Int, 2017. **21 Suppl 1**(Suppl 1): p. S6-s20.
111. Silvestri, L., et al., *The extrahepatic role of TFR2 in iron homeostasis.* Frontiers in pharmacology, 2014. **5**: p. 93.
112. Miyazawa, M., et al., *Regulation of transferrin receptor-1 mRNA by the interplay between IRE-binding proteins and miR-7/miR-141 in the 3'-IRE stem-loops.* Rna, 2018. **24**(4): p. 468-479.
113. Li, L., et al., *Binding and uptake of H-ferritin are mediated by human transferrin receptor-1.* Proceedings of the National Academy of Sciences, 2010. **107**(8): p. 3505-3510.
114. Tao, J., et al., *Hypoxia: dual effect on the expression of transferrin receptor in human melanoma A375 cell line.* Exp Dermatol, 2007. **16**(11): p. 899-904.
115. Rohner, F., et al., *Adjusting soluble transferrin receptor concentrations for inflammation: Biomarkers Reflecting Inflammation and Nutritional Determinants of Anemia (BRINDA) project.* The American journal of clinical nutrition, 2017. **106**(Suppl 1): p. 372S-382S.
116. Wan, Q., et al., *Transferrin Receptor 1-Associated Iron Accumulation and Oxidative Stress Provides a Way for Grass Carp to Fight against Reovirus Infection.* International Journal of Molecular Sciences, 2019. **20**(23): p. 5857.
117. Daniels, T.R., et al., *The transferrin receptor and the targeted delivery of therapeutic agents against cancer.* Biochim Biophys Acta, 2012. **1820**(3): p. 291-317.
118. Bouzinab, K., et al., *Delivery of Temozolomide and N3-Propargyl Analog to Brain Tumors Using an Apoferritin Nanocage.* ACS Appl Mater Interfaces, 2020. **12**(11): p. 12609-12617.
119. Horniblow, R.D., et al., *BRAF mutations are associated with increased iron regulatory protein-2 expression in colorectal tumorigenesis.* Cancer science, 2017. **108**(6): p. 1135-1143.
120. Holmström, P., et al., *Expression of iron regulatory genes in a rat model of hepatocellular carcinoma.* Liver Int, 2006. **26**(8): p. 976-85.
121. Johnson, I.R., et al., *Altered endosome biogenesis in prostate cancer has biomarker potential.* Mol Cancer Res, 2014. **12**(12): p. 1851-62.
122. Zhu, X., et al., *Mechanisms of gambogic acid-induced apoptosis in non-small cell lung cancer cells in relation to transferrin receptors.* J Chemother, 2009. **21**(6): p. 666-72.
123. Scott, C.S., et al., *Membrane transferrin receptor (TfR) and nuclear proliferation-associated Ki-67 expression in hemopoietic malignancies.* Leukemia, 1988. **2**(7): p. 438-42.
124. Basuli, D., et al., *Iron addiction: a novel therapeutic target in ovarian cancer.* Oncogene, 2017. **36**(29): p. 4089-4099.

125. Habashy, H.O., et al., *Transferrin receptor (CD71) is a marker of poor prognosis in breast cancer and can predict response to tamoxifen.* Breast Cancer Research and Treatment, 2009. **119**(2): p. 283.
126. Singh, M., et al., *Differential expression of transferrin receptor (TfR) in a spectrum of normal to malignant breast tissues: implications for in situ and invasive carcinoma.* Appl Immunohistochem Mol Morphol, 2011. **19**(5): p. 417-23.
127. Buas, M.F., et al., *Candidate early detection protein biomarkers for ER+/PR+ invasive ductal breast carcinoma identified using pre-clinical plasma from the WHI observational study.* Breast Cancer Res Treat, 2015. **153**(2): p. 445-54.
128. Lima, Z.S., et al., *Application of Imaging Technologies in Breast Cancer Detection: A Review Article.* Open access Macedonian journal of medical sciences, 2019. **7**(5): p. 838-848.
129. Koh, J. and M.J. Kim, *Introduction of a New Staging System of Breast Cancer for Radiologists: An Emphasis on the Prognostic Stage.* Korean journal of radiology, 2019. **20**(1): p. 69-82.
130. Tungsukruthai, S., N. Petpiroon, and P. Chanvorachote, *Molecular Mechanisms of Breast Cancer Metastasis and Potential Anti-metastatic Compounds.* Anticancer Research, 2018. **38**(5): p. 2607.
131. Rahman, G.A., *Breast Conserving Therapy: A surgical Technique where Little can Mean More.* Journal of surgical technique and case report, 2011. **3**(1): p. 1-4.
132. McLaughlin, S.A., *Surgical management of the breast: breast conservation therapy and mastectomy.* Surg Clin North Am, 2013. **93**(2): p. 411-28.
133. Vila, J., S. Gandini, and O. Gentilini, *Overall survival according to type of surgery in young (≤40 years) early breast cancer patients: A systematic meta-analysis comparing breast-conserving surgery versus mastectomy.* Breast, 2015. **24**(3): p. 175-81.
134. Claessens, A.K.M., et al., *The role of chemotherapy in treatment of advanced breast cancer: an overview for clinical practice.* Critical Reviews in Oncology/Hematology, 2020. **153**: p. 102988.
135. Bese, N.S., et al., *Breast radiation therapy guideline implementation in low- and middle-income countries.* Cancer, 2008. **113**(8 Suppl): p. 2305-14.
136. Braunstein, L.Z., et al., *Breast-cancer subtype, age, and lymph node status as predictors of local recurrence following breast-conserving therapy.* Breast Cancer Res Treat, 2017. **161**(1): p. 173-179.
137. Moran, M.S., et al., *Society of Surgical Oncology-American Society for Radiation Oncology consensus guideline on margins for breast-conserving surgery with whole-breast irradiation in stages I and II invasive breast cancer.* Int J Radiat Oncol Biol Phys, 2014. **88**(3): p. 553-64.
138. McGale, P., et al., *Effect of radiotherapy after mastectomy and axillary surgery on 10-year recurrence and 20-year breast cancer mortality: meta-analysis of individual patient data for 8135 women in 22 randomised trials.* Lancet, 2014. **383**(9935): p. 2127-35.
139. Wang, S.L., et al., *Hypofractionated versus conventional fractionated postmastectomy radiotherapy for patients with high-risk breast cancer: a randomised, non-inferiority, open-label, phase 3 trial.* Lancet Oncol, 2019. **20**(3): p. 352-360.
140. Poortmans, P.M.P., M. Arenas, and L. Livi, *Over-irradiation.* Breast, 2017. **31**: p. 295-302.
141. Correa, C., et al., *Accelerated Partial Breast Irradiation: Executive summary for the update of an ASTRO Evidence-Based Consensus Statement.* Pract Radiat Oncol, 2017. **7**(2): p. 73-79.

142. Poortmans, P., *Postmastectomy radiation in breast cancer with one to three involved lymph nodes: ending the debate.* Lancet, 2014. **383**(9935): p. 2104-6.
143. Moo, T.-A., et al., *Overview of Breast Cancer Therapy.* PET clinics, 2018. **13**(3): p. 339-354.
144. Rastogi, P., et al., *Preoperative chemotherapy: updates of National Surgical Adjuvant Breast and Bowel Project Protocols B-18 and B-27.* J Clin Oncol, 2008. **26**(5): p. 778-85.
145. Fisher, B., et al., *Effect of preoperative chemotherapy on the outcome of women with operable breast cancer.* J Clin Oncol, 1998. **16**(8): p. 2672-85.
146. Bhattacharyya, G.S., et al., *Overview of Breast Cancer and Implications of Overtreatment of Early-Stage Breast Cancer: An Indian Perspective.* JCO Global Oncology, 2020(6): p. 789-798.
147. Peto, R., et al., *Comparisons between different polychemotherapy regimens for early breast cancer: meta-analyses of long-term outcome among 100,000 women in 123 randomised trials.* Lancet, 2012. **379**(9814): p. 432-44.
148. Francis, P.A., et al., *Tailoring adjuvant endocrine therapy for premenopausal breast cancer.* New England Journal of Medicine, 2018. **379**(2): p. 122-137.
149. Soll, J.M., R.W. Sobol, and N. Mosammaparast, *Regulation of DNA Alkylation Damage Repair: Lessons and Therapeutic Opportunities.* Trends Biochem Sci, 2017. **42**(3): p. 206-218.
150. Scholar, E., *Alkylating Agents*, in *xPharm: The Comprehensive Pharmacology Reference*, S.J. Enna and D.B. Bylund, Editors. 2007, Elsevier: New York. p. 1-4.
151. Anampa, J., D. Makower, and J.A. Sparano, *Progress in adjuvant chemotherapy for breast cancer: an overview.* BMC Medicine, 2015. **13**(1): p. 195.
152. Castillo, C. and N. Camejo, *Impact of breast cancer treatments on fertility and the importance of timing for a fertility preservation intervention.* Revista de Senología y Patología Mamaria, 2021.
153. Noll, D.M., T.M. Mason, and P.S. Miller, *Formation and repair of interstrand cross-links in DNA.* Chemical reviews, 2006. **106**(2): p. 277-301.
154. Oun, R., Y.E. Moussa, and N.J. Wheate, *The side effects of platinum-based chemotherapy drugs: a review for chemists.* Dalton Transactions, 2018. **47**(19): p. 6645-6653.
155. Ejlertsen, B., *Adjuvant chemotherapy in early breast cancer.* Dan Med J, 2016. **63**(5).
156. von Minckwitz, G., et al., *Trastuzumab Emtansine for Residual Invasive HER2-Positive Breast Cancer.* New England Journal of Medicine, 2018. **380**(7): p. 617-628.
157. Mills, C.C., E.A. Kolb, and V.B. Sampson, *Development of Chemotherapy with Cell-Cycle Inhibitors for Adult and Pediatric Cancer Therapy.* Cancer Res, 2018. **78**(2): p. 320-325.
158. Ejlertsen, B., et al., *Cyclophosphamide, methotrexate, and fluorouracil; oral cyclophosphamide; levamisole; or no adjuvant therapy for patients with high-risk, premenopausal breast cancer.* Cancer, 2010. **116**(9): p. 2081-2089.
159. Mitchell, J.D., D.B. Sawyer, and D.J. Lenihan, *46 - Cardio-Oncology and Heart Failure*, in *Heart Failure: a Companion to Braunwald's Heart Disease (Fourth Edition)*, G.M. Felker and D.L. Mann, Editors. 2020, Elsevier: Philadelphia. p. 665-673.e3.
160. Martins-Teixeira, M.B. and I. Carvalho, *Antitumour Anthracyclines: Progress and Perspectives.* ChemMedChem, 2020. **15**(11): p. 933-948.

161. Mackey, J.R., et al., *Long-term outcomes after adjuvant treatment of sequential versus combination docetaxel with doxorubicin and cyclophosphamide in node-positive breast cancer: BCIRG-005 randomized trial.* Annals of Oncology, 2016. **27**(6): p. 1041-1047.
162. Perez, E.A., *Microtubule inhibitors: Differentiating tubulin-inhibiting agents based on mechanisms of action, clinical activity, and resistance.* Mol Cancer Ther, 2009. **8**(8): p. 2086-95.
163. Tolaney, S.M., et al., *Seven-year (yr) follow-up of adjuvant paclitaxel (T) and trastuzumab (H) (APT trial) for node-negative, HER2-positive breast cancer (BC).* Journal of Clinical Oncology, 2017. **35**(15_suppl): p. 511-511.
164. Cardoso, F., et al., *4th ESO-ESMO International Consensus Guidelines for Advanced Breast Cancer (ABC 4)†.* Ann Oncol, 2018. **29**(8): p. 1634-1657.
165. Masoud, V. and G. Pagès, *Targeted therapies in breast cancer: New challenges to fight against resistance.* World journal of clinical oncology, 2017. **8**(2): p. 120-134.
166. *Tamoxifen for early breast cancer: an overview of the randomised trials. Early Breast Cancer Trialists' Collaborative Group.* Lancet, 1998. **351**(9114): p. 1451-67.
167. Jordan, V.C., *Molecular mechanisms of antiestrogen action in breast cancer.* Breast Cancer Res Treat, 1994. **31**(1): p. 41-52.
168. Miller, W.R., *Aromatase inhibitors: mechanism of action and role in the treatment of breast cancer.* Semin Oncol, 2003. **30**(4 Suppl 14): p. 3-11.
169. Robertson, J.F., et al., *A good drug made better: the fulvestrant dose-response story.* Clin Breast Cancer, 2014. **14**(6): p. 381-9.
170. Gradishar, W., *Landmark trials in endocrine adjuvant therapy for breast carcinoma.* Cancer, 2006. **106**(5): p. 975-81.
171. Cardoso, F., et al., *70-Gene Signature as an Aid to Treatment Decisions in Early-Stage Breast Cancer.* New England Journal of Medicine, 2016. **375**(8): p. 717-729.
172. Slamon, D.J., et al., *Use of chemotherapy plus a monoclonal antibody against HER2 for metastatic breast cancer that overexpresses HER2.* N Engl J Med, 2001. **344**(11): p. 783-92.
173. Pernas, S. and S.M. Tolaney, *HER2-positive breast cancer: new therapeutic frontiers and overcoming resistance.* Therapeutic advances in medical oncology, 2019. **11**: p. 1758835919833519-1758835919833519.
174. Bryant, H.E., et al., *Specific killing of BRCA2-deficient tumours with inhibitors of poly(ADP-ribose) polymerase.* Nature, 2005. **434**(7035): p. 913-7.
175. Farmer, H., et al., *Targeting the DNA repair defect in BRCA mutant cells as a therapeutic strategy.* Nature, 2005. **434**(7035): p. 917-21.
176. Armstrong, N., et al., *A systematic review of the international prevalence of BRCA mutation in breast cancer.* Clinical epidemiology, 2019. **11**: p. 543-561.
177. Nakai, K., M.-C. Hung, and H. Yamaguchi, *A perspective on anti-EGFR therapies targeting triple-negative breast cancer.* American journal of cancer research, 2016. **6**(8): p. 1609-1623.
178. Lev, S., *Targeted therapy and drug resistance in triple-negative breast cancer: the EGFR axis.* Biochemical Society Transactions, 2020. **48**(2): p. 657-665.
179. Abourehab, M.A.S., et al., *Globally Approved EGFR Inhibitors: Insights into Their Syntheses, Target Kinases, Biological Activities, Receptor Interactions, and Metabolism.* Molecules, 2021. **26**(21).

180. Harvey, A.L., *Natural products in drug discovery.* Drug discovery today, 2008. **13**(19-20): p. 894-901.
181. Hassan, H.M., *A Short History of the Use of Plants as Medicines from Ancient Times.* Chimia (Aarau), 2015. **69**(10): p. 622-3.
182. Barr, J., *Vascular medicine and surgery in ancient Egypt.* Journal of Vascular Surgery, 2014. **60**(1): p. 260-263.
183. Levitsky, D.O. and V.M. Dembitsky, *Anti-breast Cancer Agents Derived from Plants.* Natural products and bioprospecting, 2014. **5**(1): p. 1-16.
184. McChesney, J.D., S.K. Venkataraman, and J.T. Henri, *Plant natural products: back to the future or into extinction?* Phytochemistry, 2007. **68**(14): p. 2015-2022.
185. Koehn, F.E. and G.T. Carter, *The evolving role of natural products in drug discovery.* Nature reviews Drug discovery, 2005. **4**(3): p. 206.
186. Newman, D.J. and G.M. Cragg, *Natural Products as Sources of New Drugs over the Nearly Four Decades from 01/1981 to 09/2019.* J Nat Prod, 2020. **83**(3): p. 770-803.
187. Da Rocha, A.B., R.M. Lopes, and G. Schwartsmann, *Natural products in anticancer therapy.* Current Opinion in Pharmacology, 2001. **1**(4): p. 364-369.
188. Du, Q., et al., *Docetaxel increases the risk of severe infections in the treatment of non-small cell lung cancer: a meta-analysis.* Oncoscience, 2018. **5**(7-8): p. 220-238.
189. Ho, M.Y. and J.R. Mackey, *Presentation and management of docetaxel-related adverse effects in patients with breast cancer.* Cancer Manag Res, 2014. **6**: p. 253-9.
190. Antonarakis, E.S. and A.J. Armstrong, *Evolving standards in the treatment of docetaxel-refractory castration-resistant prostate cancer.* Prostate Cancer Prostatic Dis, 2011. **14**(3): p. 192-205.
191. Sampath, D., et al., *Pharmacodynamics of cytarabine alone and in combination with 7-hydroxystaurosporine (UCN-01) in AML blasts in vitro and during a clinical trial.* Blood, 2006. **107**(6): p. 2517-24.
192. Mansoori, B., et al., *The Different Mechanisms of Cancer Drug Resistance: A Brief Review.* Advanced pharmaceutical bulletin, 2017. **7**(3): p. 339-348.
193. Jones, D., et al., *Laboratory practice guidelines for detecting and reporting BCR-ABL drug resistance mutations in chronic myelogenous leukemia and acute lymphoblastic leukemia: a report of the Association for Molecular Pathology.* J Mol Diagn, 2009. **11**(1): p. 4-11.
194. Barinaga, M., *From bench top to bedside.* Science, 1997. **278**(5340): p. 1036-9.
195. Harvey, A.L., *Medicines from nature: are natural products still relevant to drug discovery?* Trends in Pharmacological Sciences, 1999. **20**(5): p. 196-198.
196. Iwamoto, T., *Clinical application of drug delivery systems in cancer chemotherapy: review of the efficacy and side effects of approved drugs.* Biological and Pharmaceutical Bulletin, 2013. **36**(5): p. 715-718.
197. Lim, K.-H., et al., *Jerantinines A− G, cytotoxic Aspidosperma alkaloids from Tabernaemontana corymbosa.* Journal of natural products, 2008. **71**(9): p. 1591-1594.
198. Frei, R., et al., *Total Synthesis and Biological Evaluation of Jerantinine E.* Angewandte Chemie International Edition, 2013. **52**(50): p. 13373-13376.
199. Huber, T., et al., *Development of a β-C–H Bromination Approach toward the Synthesis of Jerantinine E.* The Journal of organic chemistry, 2017. **82**(14): p. 7410-7419.

200. Wang, N., et al., *Asymmetric Total Syntheses of (−)-Jerantinines A, C, and E,(−)-16-Methoxytabersonine,(−)-Vindoline, and (+)-Vinblastine.* Organic letters, 2017. **20**(1): p. 292-295.
201. Smedley, C.J., et al., *Sustainable Syntheses of (−)-Jerantinines A & E and Structural Characterisation of the Jerantinine-Tubulin Complex at the Colchicine Binding Site.* Scientific Reports, 2018. **8**(1): p. 10617.
202. Raja, V.J., et al., *Novel antitumour indole alkaloid, Jerantinine A, evokes potent G2/M cell cycle arrest targeting microtubules.* Investigational new drugs, 2014. **32**(5): p. 838-850.
203. Qazzaz, M.E., et al., *In vitro anticancer properties and biological evaluation of novel natural alkaloid jerantinine B.* Cancer Letters, 2016. **370**(2): p. 185-197.
204. Chung, F.F.-L., et al., *Jerantinine A induces tumor-specific cell death through modulation of splicing factor 3b subunit 1 (SF3B1).* Scientific Reports, 2017. **7**(1): p. 42504.
205. Holland, J.F., et al., *Vincristine Treatment of Advanced Cancer: A Cooperative Study of 392 Cases.* Cancer Research, 1973. **33**(6): p. 1258.
206. Wu, L.-T., et al., *Treatment of advanced medullary thyroid carcinoma with a combination of cyclophosphamide, vincristine, and dacarbazine.* Cancer, 1994. **73**(2): p. 432-436.
207. Jackson Jr, D.V., et al., *Treatment of advanced non-Hodgkin's lymphoma with vincristine infusion.* Cancer, 1984. **53**(12): p. 2601-2606.
208. Yang, Y.-X., et al., *Proteome analysis of multidrug resistance in vincristine-resistant human gastric cancer cell line SGC7901/VCR.* PROTEOMICS, 2006. **6**(6): p. 2009-2021.
209. Leonard, G.D., T. Fojo, and S.E. Bates, *The role of ABC transporters in clinical practice.* Oncologist, 2003. **8**(5): p. 411-24.
210. Glavinas, H., et al., *The role of ABC transporters in drug resistance, metabolism and toxicity.* Curr Drug Deliv, 2004. **1**(1): p. 27-42.
211. Fojo, T., *Multiple paths to a drug resistance phenotype: mutations, translocations, deletions and amplification of coding genes or promoter regions, epigenetic changes and microRNAs.* Drug Resist Updat, 2007. **10**(1-2): p. 59-67.
212. Keppler, D., *Multidrug resistance proteins (MRPs, ABCCs): importance for pathophysiology and drug therapy.* Handb Exp Pharmacol, 2011(201): p. 299-323.
213. Wind, N.S. and I. Holen, *Multidrug Resistance in Breast Cancer: From In Vitro Models to Clinical Studies.* International Journal of Breast Cancer, 2011. **2011**: p. 967419.
214. Clarke, R., F. Leonessa, and B. Trock, *Multidrug Resistance/P-Glycoprotein and Breast Cancer: Review and Meta-Analysis.* Seminars in Oncology, 2005. **32**: p. 9-15.
215. Riordan, J.R., et al., *Amplification of P-glycoprotein genes in multidrug-resistant mammalian cell lines.* Nature, 1985. **316**(6031): p. 817-9.
216. Yang, C.H., et al., *BCRP/MXR/ABCP expression in topotecan-resistant human breast carcinoma cells.* Biochem Pharmacol, 2000. **60**(6): p. 831-7.
217. Roper, S.J., et al., *MBRS-46. JERANTININE: A NOVEL TUMOUR-SPECIFIC ALKALOID FOR THE TREATMENT OF PAEDIATRIC MEDULLOBLASTOMA.* Neuro-Oncology, 2018. **20**(suppl_2): p. i138-i138.
218. Godin, B., et al., *Emerging applications of nanomedicine for the diagnosis and treatment of cardiovascular diseases.* Trends Pharmacol Sci, 2010. **31**(5): p. 199-205.

219. Poirot-Mazères, I., *Legal aspects of the risks raised by nanotechnologies in the field of medicine.* J Int Bioethique, 2011. **22**(1): p. 99-118, 212.
220. Ferrari, M., *Cancer nanotechnology: opportunities and challenges.* Nature Reviews Cancer, 2005. **5**(3): p. 161-171.
221. Seigneuric, R., et al., *From nanotechnology to nanomedicine: applications to cancer research.* Curr Mol Med, 2010. **10**(7): p. 640-52.
222. Bawa, R., *Regulating nanomedicine - can the FDA handle it?* Curr Drug Deliv, 2011. **8**(3): p. 227-34.
223. Matsumura, Y. and H. Maeda, *A New Concept for Macromolecular Therapeutics in Cancer Chemotherapy: Mechanism of Tumoritropic Accumulation of Proteins and the Antitumor Agent Smancs.* Cancer Research, 1986. **46**(12 Part 1): p. 6387.
224. Dvorak, A.M., et al., *The vesiculo-vacuolar organelle (VVO): a distinct endothelial cell structure that provides a transcellular pathway for macromolecular extravasation.* J Leukoc Biol, 1996. **59**(1): p. 100-15.
225. Nagy, J.A., et al., *Permeability properties of tumor surrogate blood vessels induced by VEGF-A.* Laboratory Investigation, 2006. **86**(8): p. 767-780.
226. Rosenblum, D., et al., *Progress and challenges towards targeted delivery of cancer therapeutics.* Nature Communications, 2018. **9**(1): p. 1410.
227. Wilhelm, S., et al., *Analysis of nanoparticle delivery to tumours.* Nature Reviews Materials, 2016. **1**(5): p. 16014.
228. Sevick, E.M. and R.K. Jain, *Viscous resistance to blood flow in solid tumors: effect of hematocrit on intratumor blood viscosity.* Cancer Res, 1989. **49**(13): p. 3513-9.
229. Bertrand, N., et al., *Cancer nanotechnology: The impact of passive and active targeting in the era of modern cancer biology.* Advanced Drug Delivery Reviews, 2014. **66**: p. 2-25.
230. Prabhakar, U., et al., *Challenges and key considerations of the enhanced permeability and retention effect for nanomedicine drug delivery in oncology.* Cancer Res, 2013. **73**(8): p. 2412-7.
231. Shi, J., et al., *Cancer nanomedicine: progress, challenges and opportunities.* Nature Reviews Cancer, 2017. **17**(1): p. 20.
232. Kipp, J.E., *The role of solid nanoparticle technology in the parenteral delivery of poorly water-soluble drugs.* International Journal of Pharmaceutics, 2004. **284**(1): p. 109-122.
233. Whitehead, K.A., R. Langer, and D.G. Anderson, *Knocking down barriers: advances in siRNA delivery.* Nature Reviews Drug Discovery, 2009. **8**(2): p. 129-138.
234. Kocbek, P., S. Baumgartner, and J. Kristl, *Preparation and evaluation of nanosuspensions for enhancing the dissolution of poorly soluble drugs.* International Journal of Pharmaceutics, 2006. **312**(1): p. 179-186.
235. Gagliardi, A., et al., *Biodegradable Polymeric Nanoparticles for Drug Delivery to Solid Tumors.* Frontiers in Pharmacology, 2021. **12**(17).
236. Mitchell, M.J., et al., *Engineering precision nanoparticles for drug delivery.* Nature Reviews Drug Discovery, 2021. **20**(2): p. 101-124.
237. *Let's talk about lipid nanoparticles.* Nature Reviews Materials, 2021. **6**(2): p. 99-99.
238. Sercombe, L., et al., *Advances and Challenges of Liposome Assisted Drug Delivery.* Front Pharmacol, 2015. **6**: p. 286.
239. Anselmo, A. and S. Mitragotri, *Nanoparticles in the clinic: an update. Bioeng Transl Med 4: e10143*. 2019.
240. Yang, W., et al., *Gold nanoparticle based photothermal therapy: Development and application for effective cancer treatment.* Sustainable Materials and Technologies, 2019. **22**: p. e00109.

241. Arias, L.S., et al., *Iron oxide nanoparticles for biomedical applications: a perspective on synthesis, drugs, antimicrobial activity, and toxicity.* Antibiotics, 2018. **7**(2): p. 46.
242. Rideau, E., et al., *Liposomes and polymersomes: a comparative review towards cell mimicking.* Chemical society reviews, 2018. **47**(23): p. 8572-8610.
243. Zhang, L., et al., *Microfluidic-assisted polymer-protein assembly to fabricate homogeneous functionalnanoparticles.* Materials Science and Engineering: C, 2020. **111**: p. 110768.
244. Caldorera-Moore, M., J.E. Vela Ramirez, and N.A. Peppas, *Transport and delivery of interferon-α through epithelial tight junctions via pH-responsive poly(methacrylic acid-grafted-ethylene glycol) nanoparticles.* J Drug Target, 2019. **27**(5-6): p. 582-589.
245. Strand, M.S., et al., *Precision delivery of RAS-inhibiting siRNA to KRAS driven cancer via peptide-based nanoparticles.* Oncotarget, 2019. **10**(46): p. 4761-4775.
246. van Vlerken, L.E., T.K. Vyas, and M.M. Amiji, *Poly (ethylene glycol)-modified nanocarriers for tumor-targeted and intracellular delivery.* Pharmaceutical research, 2007. **24**(8): p. 1405-1414.
247. Fenton, O.S., et al., *Advances in Biomaterials for Drug Delivery.* Advanced Materials, 2018. **30**(29): p. 1705328.
248. Manshian, B.B., et al., *Personalized medicine and follow-up of therapeutic delivery through exploitation of quantum dot toxicity.* Biomaterials, 2017. **127**: p. 1-12.
249. Shi, J., et al., *Cancer nanomedicine: progress, challenges and opportunities.* Nature reviews cancer, 2017. **17**(1): p. 20-37.
250. Cedervall, T., et al., *Understanding the nanoparticle–protein corona using methods to quantify exchange rates and affinities of proteins for nanoparticles.* Proceedings of the National Academy of Sciences, 2007. **104**(7): p. 2050.
251. Monopoli, M.P., et al., *Biomolecular coronas provide the biological identity of nanosized materials.* Nature Nanotechnology, 2012. **7**(12): p. 779-786.
252. Ke, P.C., et al., *A Decade of the Protein Corona.* ACS Nano, 2017. **11**(12): p. 11773-11776.
253. Mahmoudi, M., et al., *A new approach for the in vitro identification of the cytotoxicity of superparamagnetic iron oxide nanoparticles.* Colloids and Surfaces B: Biointerfaces, 2010. **75**(1): p. 300-309.
254. Mahmoudi, M., et al., *Protein−Nanoparticle Interactions: Opportunities and Challenges.* Chemical Reviews, 2011. **111**(9): p. 5610-5637.
255. Gordon, S. and P.R. Taylor, *Monocyte and macrophage heterogeneity.* Nature Reviews Immunology, 2005. **5**(12): p. 953-964.
256. Wu, T. and M. Tang, *Review of the effects of manufactured nanoparticles on mammalian target organs.* J Appl Toxicol, 2018. **38**(1): p. 25-40.
257. Patra, J.K., et al., *Nano based drug delivery systems: recent developments and future prospects.* Journal of nanobiotechnology, 2018. **16**(1): p. 1-33.
258. Hobbs, S.K., et al., *Regulation of transport pathways in tumor vessels: Role of tumor type and microenvironment.* Proceedings of the National Academy of Sciences, 1998. **95**(8): p. 4607.
259. Soo Choi, H., et al., *Renal clearance of quantum dots.* Nature Biotechnology, 2007. **25**(10): p. 1165-1170.
260. Dawidczyk, C.M., et al., *State-of-the-art in design rules for drug delivery platforms: lessons learned from FDA-approved nanomedicines.* J Control Release, 2014. **187**: p. 133-44.
261. Pant, K., et al., *Active targeting of dendritic polyglycerols for diagnostic cancer imaging.* Small, 2020. **16**(7): p. 1905013.

262. Yi, Y., et al., *Glucose-linked sub-50-nm unimer polyion complex-assembled gold nanoparticles for targeted siRNA delivery to glucose transporter 1-overexpressing breast cancer stem-like cells.* J Control Release, 2019. **295**: p. 268-277.
263. Ahmad, A., et al., *Precision Cancer Nanotherapy: Evolving Role of Multifunctional Nanoparticles for Cancer Active Targeting.* J Med Chem, 2019. **62**(23): p. 10475-10496.
264. Gabizon, A., H. Shmeeda, and Y. Barenholz, *Pharmacokinetics of pegylated liposomal Doxorubicin: review of animal and human studies.* Clin Pharmacokinet, 2003. **42**(5): p. 419-36.
265. Lynch, I., A. Salvati, and K.A. Dawson, *What does the cell see?* Nature Nanotechnology, 2009. **4**(9): p. 546-547.
266. Rodriguez, P.L., et al., *Minimal "Self" peptides that inhibit phagocytic clearance and enhance delivery of nanoparticles.* Science (New York, N.Y.), 2013. **339**(6122): p. 971-975.
267. Parodi, A., et al., *Synthetic nanoparticles functionalized with biomimetic leukocyte membranes possess cell-like functions.* Nat Nanotechnol, 2013. **8**(1): p. 61-8.
268. Hu, C.-M.J., et al., *Erythrocyte membrane-camouflaged polymeric nanoparticles as a biomimetic delivery platform.* Proceedings of the National Academy of Sciences, 2011. **108**(27): p. 10980.
269. Hu, C.M., et al., *Nanoparticle biointerfacing by platelet membrane cloaking.* Nature, 2015. **526**(7571): p. 118-21.
270. Björnmalm, M., et al., *Bridging Bio–Nano Science and Cancer Nanomedicine.* ACS Nano, 2017. **11**(10): p. 9594-9613.
271. Anselmo, A.C. and S. Mitragotri, *Nanoparticles in the clinic: An update.* Bioengineering & Translational Medicine, 2019. **4**(3): p. e10143.
272. Li, Z., et al., *Cancer drug delivery in the nano era: An overview and perspectives (Review).* Oncol Rep, 2017. **38**(2): p. 611-624.
273. Veroniaina, H., et al., *Apoferritin: a potential nanocarrier for cancer imaging and drug delivery.* Expert Review of Anticancer Therapy, 2021. **21**(8): p. 901-913.
274. Andrews, S.C., *Iron storage in bacteria.* Adv Microb Physiol, 1998. **40**: p. 281-351.
275. Drysdale, J.W., *Ferritin phenotypes: structure and metabolism.* Ciba Found Symp, 1976(51): p. 41-67.
276. Frolow, F., A.J. Kalb, and J. Yariv, *Structure of a unique twofold symmetric haem-binding site.* Nature Structural Biology, 1994. **1**: p. 453.
277. Arosio, P., M. Yokota, and J.W. Drysdale, *Structural and Immunological Relationships of Isoferritins in Normal and Malignant Cells.* Cancer Research, 1976. **36**(5): p. 1735-1739.
278. Caskey, J., et al., *Human ferritin gene is assigned to chromosome 19.* Proceedings of the National Academy of Sciences, 1983. **80**(2): p. 482-486.
279. Harrison, P.M. and P. Arosio, *The ferritins: molecular properties, iron storage function and cellular regulation.* Biochimica et Biophysica Acta (BBA) - Bioenergetics, 1996. **1275**(3): p. 161-203.
280. Worwood, M., *Serum ferritin.* CRC Crit Rev Clin Lab Sci, 1979. **10**(2): p. 171-204.
281. Zang, J., et al., *Ferritin cage for encapsulation and delivery of bioactive nutrients: From structure, property to applications.* Crit Rev Food Sci Nutr, 2017. **57**(17): p. 3673-3683.
282. Zhang, C., X. Zhang, and G. Zhao, *Ferritin Nanocage: A Versatile Nanocarrier Utilized in the Field of Food, Nutrition, and Medicine.* Nanomaterials (Basel), 2020. **10**(9).

283. Domínguez-Vera, J.M., B. Fernández, and N. Gálvez, *Native and synthetic ferritins for nanobiomedical applications: recent advances and new perspectives.* Future Medicinal Chemistry, 2010. **2**(4): p. 609-618.
284. Conrad, M.E., J.N. Umbreit, and E.G. Moore, *Iron absorption and transport.* The American journal of the medical sciences, 1999. **318**(4): p. 213-229.
285. Liu, X. and E.C. Theil, *Ferritins: dynamic management of biological iron and oxygen chemistry.* Acc Chem Res, 2005. **38**(3): p. 167-75.
286. Smith, J.L., *The Physiological Role of Ferritin-Like Compounds in Bacteria.* Critical Reviews in Microbiology, 2004. **30**(3): p. 173-185.
287. Knovich, M.A., et al., *Ferritin for the clinician.* Blood reviews, 2009. **23**(3): p. 95-104.
288. Holmes-Hampton, G.P., M.C. Ghosh, and T.A. Rouault, *Chapter Five - Methods for Studying Iron Regulatory Protein 1: An Important Protein in Human Iron Metabolism*, in *Methods in Enzymology*, S.S. David, Editor. 2018, Academic Press. p. 139-155.
289. Bang, S., et al., *Redox-inactive metal ions modulate the reactivity and oxygen release of mononuclear non-haem iron(III)–peroxo complexes.* Nature Chemistry, 2014. **6**(10): p. 934-940.
290. Eklund, H., et al., *Structure and function of the radical enzyme ribonucleotide reductase.* Progress in Biophysics and Molecular Biology, 2001. **77**(3): p. 177-268.
291. Jacobs, A., et al., *Serum ferritin concentration in early breast cancer.* British Journal of Cancer, 1976. **34**(3): p. 286-290.
292. Kew, M.C., et al., *Serum and tumour ferritins in primary liver cancer.* Gut, 1978. **19**(4): p. 294-299.
293. Nitti, D., et al., *Serum ferritin in pancreatic disease. An accurate test of malignancy?* Digestion, 1982. **25**(4): p. 258-62.
294. Shindelman, J.E., A.E. Ortmeyer, and H.H. Sussman, *Demonstration of the transferrin receptor in human breast cancer tissue. Potential marker for identifying dividing cells.* Int J Cancer, 1981. **27**(3): p. 329-34.
295. Winzerling, J.J. and D.Q.D. Pham, *Ferritin☆*, in *Reference Module in Life Sciences*. 2017, Elsevier.
296. Callens, C., et al., *Recent advances in adult T-cell leukemia therapy: focus on a new anti-transferrin receptor monoclonal antibody.* Leukemia, 2008. **22**(1): p. 42-8.
297. Shen, Y., et al., *Transferrin receptor 1 in cancer: a new sight for cancer therapy.* American journal of cancer research, 2018. **8**(6): p. 916-931.
298. Michaelis, L., C.D. Coryell, and S. Granick, *FERRITIN: III. THE MAGNETIC PROPERTIES OF FERRITIN AND SOME OTHER COLLOIDAL FERRIC COMPOUNDS.* Journal of Biological Chemistry, 1943. **148**(3): p. 463-480.
299. Michaelis, L., et al., *The original Michaelis constant: translation of the 1913 Michaelis-Menten paper.* Biochemistry, 2011. **50**(39): p. 8264-9.
300. Zhang, C., X. Zhang, and G. Zhao, *Ferritin Nanocage: A Versatile Nanocarrier Utilized in the Field of Food, Nutrition, and Medicine.* Nanomaterials, 2020. **10**(9): p. 1894.
301. Lin, X., et al., *Chimeric ferritin nanocages for multiple function loading and multimodal imaging.* Nano Letters, 2011. **11**(2): p. 814-819.
302. Zhao, J., et al., *Apoferritin protein nanoparticles dually labeled with aptamer and horseradish peroxidase as a sensing probe for thrombin detection.* Anal Chim Acta, 2013. **759**: p. 53-60.
303. Sana, B., E. Johnson, and S. Lim, *The unique self-assembly/disassembly property of Archaeoglobus fulgidus ferritin and its implications on molecular release from the protein cage.* Biochimica et Biophysica Acta (BBA)-General Subjects, 2015. **1850**(12): p. 2544-2551.

304. Simsek, E. and M. Akif Kilic, *Magic ferritin: A novel chemotherapeutic encapsulation bullet.* Journal of Magnetism and Magnetic Materials, 2005. **293**(1): p. 509-513.
305. Kilic, M.A., E. Ozlu, and S. Calis, *A novel protein-based anticancer drug encapsulating nanosphere: Apoferritin-doxorubicin complex.* Journal of biomedical nanotechnology, 2012. **8**(3): p. 508-514.
306. Kuruppu, A.I., et al., *An Apoferritin-based Drug Delivery System for the Tyrosine Kinase Inhibitor Gefitinib.* Advanced healthcare materials, 2015. **4**(18): p. 2816-2821.
307. Breen AF, S.D., Cassioli ML, Wells G, Thomas NR, Zhang J, Turyanska L, Bradshaw TD, *Protein Encapsulation of Experimental Anticancer Agents 5F 203 and Phortress: Towards Precision Drug Delivery. .* Int J Nanomedicine, 2019. **14:9525-9534**
308. Quilles Junior, J.C., et al., *Apoferritin encapsulation of cysteine protease inhibitors for cathepsin L inhibition in cancer cells.* RSC Advances, 2019. **9**(63): p. 36699-36706.
309. Yang, D. and K. Nagayama, *Permeation of small molecules into the cavity of ferritin as revealed by proton nuclear magnetic resonance relaxation.* Biochem J, 1995. **307 (Pt 1)**(Pt 1): p. 253-6.
310. Belletti, D., et al., *Protein cage nanostructure as drug delivery system: magnifying glass on apoferritin.* Expert Opinion on Drug Delivery, 2017. **14**(7): p. 825-840.
311. Jiang, Y., et al., *Preparation of hypocrellin B nanocages in self-assembled apoferritin for enhanced intracellular uptake and photodynamic activity.* Journal of Materials Chemistry B, 2017. **5**(10): p. 1980-1987.
312. Pandolfi, L., et al., *H-Ferritin Enriches the Curcumin Uptake and Improves the Therapeutic Efficacy in Triple Negative Breast Cancer Cells.* Biomacromolecules, 2017. **18**(10): p. 3318-3330.
313. Gomhor, J.A.H., et al., *Development and characterization of folic acid-functionalized apoferritin as a delivery vehicle for epirubicin against MCF-7 breast cancer cells.* Artif Cells Nanomed Biotechnol, 2018. **46**(sup3): p. S847-s854.
314. Dong, Y., et al., *ERK-Peptide-Inhibitor-Modified Ferritin Enhanced the Therapeutic Effects of Paclitaxel in Cancer Cells and Spheroids.* Molecular Pharmaceutics, 2021. **18**(9): p. 3365-3377.
315. Mazzucchelli, S., et al., *H-Ferritin-nanocaged olaparib: a promising choice for both BRCA-mutated and sporadic triple negative breast cancer.* Sci Rep, 2017. **7**(1): p. 7505.
316. Dostalova, S., et al., *Prostate-specific membrane antigen-targeted site-directed antibody-conjugated apoferritin nanovehicle favorably influences in vivo side effects of doxorubicin.* Scientific reports, 2018. **8**(1): p. 1-13.
317. Zhai, M., et al., *Glioma targeting peptide modified apoferritin nanocage.* Drug Delivery, 2018. **25**(1): p. 1013-1024.
318. Ghosh, S., et al., *Apoferritin Nanocage Delivers Combination of Microtubule and Nucleus Targeting Anticancer Drugs.* ACS Applied Materials & Interfaces, 2016. **8**(45): p. 30824-30832.
319. Bellini, M., et al., *Protein nanocages for self-triggered nuclear delivery of DNA-targeted chemotherapeutics in Cancer Cells.* Journal of Controlled Release, 2014. **196**: p. 184-196.
320. Xiong, K., et al., *Autophagy-Dependent Apoptosis Induced by Apoferritin–Cu(II) Nanoparticles in Multidrug-Resistant Colon Cancer Cells.* ACS Applied Materials & Interfaces, 2021. **13**(33): p. 38959-38968.

321. Mazzucchelli, S., et al., *Nanometronomic treatment of 4T1 breast cancer with nanocaged doxorubicin prevents drug resistance and circumvents cardiotoxicity.* Oncotarget, 2017. **8**(5): p. 8383-8396.
322. Ji, P., et al., *ROS-Mediated Apoptosis and Anticancer Effect Achieved by Artesunate and Auxiliary Fe(II) Released from Ferriferous Oxide-Containing Recombinant Apoferritin.* Adv Healthc Mater, 2019. **8**(23): p. e1900911.
323. Chen, Z., et al., *Apoferritin Nanocage for Brain Targeted Doxorubicin Delivery.* Molecular Pharmaceutics, 2017. **14**(9): p. 3087-3097.
324. Rizzuto, M.A., et al., *H-Ferritin nanoparticle-mediated delivery of antibodies across a BBB in vitro model for treatment of brain malignancies.* Biomaterials Science, 2021. **9**(6): p. 2032-2042.
325. Bradford, M.M., *A rapid and sensitive method for the quantitation of microgram quantities of protein utilizing the principle of protein-dye binding.* Analytical Biochemistry, 1976. **72**(1): p. 248-254.
326. Wittig, I., H.-P. Braun, and H. Schägger, *Blue native PAGE.* Nature Protocols, 2006. **1**(1): p. 418-428.
327. Stephens, R., *High-resolution preparative SDS-polyacrylamide gel electrophoresis: fluorescent visualization and electrophoretic elution-concentration of protein bands.* Analytical biochemistry, 1975. **65**(1-2): p. 369-379.
328. Raymond, S. and Y.-J. Wang, *Preparation and properties of acrylamide gel for use in electrophoresis.* Analytical Biochemistry, 1960. **1**(4): p. 391-396.
329. Feczkó, T., et al., *Optimization of protein encapsulation in PLGA nanoparticles.* Chemical Engineering and Processing: Process Intensification, 2011. **50**(8): p. 757-765.
330. Zhang, Z. and S.-S. Feng, *The drug encapsulation efficiency, in vitro drug release, cellular uptake and cytotoxicity of paclitaxel-loaded poly (lactide)–tocopheryl polyethylene glycol succinate nanoparticles.* Biomaterials, 2006. **27**(21): p. 4025-4033.
331. Govender, T., et al., *PLGA nanoparticles prepared by nanoprecipitation: drug loading and release studies of a water soluble drug.* Journal of Controlled Release, 1999. **57**(2): p. 171-185.
332. Mu, L. and S.-S. Feng, *PLGA/TPGS nanoparticles for controlled release of paclitaxel: effects of the emulsifier and drug loading ratio.* Pharmaceutical research, 2003. **20**(11): p. 1864-1872.
333. Tomaszewska, E., et al., *Detection limits of DLS and UV-Vis spectroscopy in characterization of polydisperse nanoparticles colloids.* Journal of Nanomaterials, 2013. **2013**.
334. Cho, T.J. and V.A. Hackley, *Fractionation and characterization of gold nanoparticles in aqueous solution: asymmetric-flow field flow fractionation with MALS, DLS, and UV–Vis detection.* Analytical and bioanalytical chemistry, 2010. **398**(5): p. 2003-2018.
335. Follens, L., et al., *Characterization of nanoparticles in diluted clear solutions for Silicalite-1 zeolite synthesis using liquid 29Si NMR, SAXS and DLS.* Physical Chemistry Chemical Physics, 2008. **10**(36): p. 5574-5583.
336. Cao, A., *Light Scattering. Recent Applications.* Analytical Letters, 2003. **36**(15): p. 3185-3225.
337. Bhattacharjee, S., *DLS and zeta potential – What they are and what they are not?* Journal of Controlled Release, 2016. **235**: p. 337-351.
338. Sapsford, K.E., et al., *Analyzing Nanomaterial Bioconjugates: A Review of Current and Emerging Purification and Characterization Techniques.* Analytical Chemistry, 2011. **83**(12): p. 4453-4488.
339. Masters, J.R.W., *Human cancer cell lines: fact and fantasy.* Nature Reviews Molecular Cell Biology, 2000. **1**(3): p. 233-236.

340. Geraghty, R.J., et al., *Guidelines for the use of cell lines in biomedical research.* Br J Cancer, 2014. **111**(6): p. 1021-46.
341. Hay, R.J., M.L. Macy, and T.R. Chen, *Mycoplasma infection of cultured cells.* Nature, 1989. **339**(6224): p. 487-488.
342. Mahmood, T. and P.-C. Yang, *Western blot: technique, theory, and trouble shooting.* North American journal of medical sciences, 2012. **4**(9): p. 429-434.
343. Bass, J.J., et al., *An overview of technical considerations for Western blotting applications to physiological research.* Scandinavian journal of medicine & science in sports, 2017. **27**(1): p. 4-25.
344. van Meerloo J., K.G.J.L., Cloos J, *Cell Sensitivity Assays: The MTT Assay*, in *Cancer Cell Culture.. Methods in Molecular Biology (Methods and Protocols)*, I. Cree, Editor. 2011, Humana Press.
345. Plumb, J.A., R. Milroy, and S.B. Kaye, *Effects of the pH dependence of 3-(4,5-dimethylthiazol-2-yl)-2,5-diphenyl-tetrazolium bromide-formazan absorption on chemosensitivity determined by a novel tetrazolium-based assay.* Cancer Res, 1989. **49**(16): p. 4435-40.
346. Bruggisser, R., et al., *Interference of plant extracts, phytoestrogens and antioxidants with the MTT tetrazolium assay.* Planta Med, 2002. **68**(5): p. 445-8.
347. Strober, W., *Trypan Blue Exclusion Test of Cell Viability.* Curr Protoc Immunol, 2015. **111**: p. A3.b.1-a3.b.3.
348. Alberts, D., et al., *In-vitro clonogenic assay for predicting response of ovarian cancer to chemotherapy.* The Lancet, 1980. **316**(8190): p. 340-342.
349. Plumb, J.A., *Cell sensitivity assays: clonogenic assay*, in *Cancer cell culture*. 2004, Springer. p. 159-164.
350. McKinnon, K.M., *Flow Cytometry: An Overview.* Current protocols in immunology, 2018. **120**: p. 5.1.1-5.1.11.
351. Pozarowski, P. and Z. Darzynkiewicz, *Analysis of cell cycle by flow cytometry*, in *Checkpoint controls and cancer*. 2004, Springer. p. 301-311.
352. Kim, H., et al., *A Mechanism for microRNA Arm Switching Regulated by Uridylation.* Mol Cell, 2020. **78**(6): p. 1224-1236.e5.
353. Nunez, R., *DNA Measurement and Cell Cycle Analysis by Flow Cytometry.* Current Issues in Molecular Biology, 2001. **3**(3): p. 67-70.
354. McCoy, J.P., *Flow Cytometry Software*, in *Pathobiology of Human Disease*, L.M. McManus and R.N. Mitchell, Editors. 2014, Academic Press: San Diego. p. 3664-3677.
355. Nicoletti, I., et al., *A rapid and simple method for measuring thymocyte apoptosis by propidium iodide staining and flow cytometry.* Journal of Immunological Methods, 1991. **139**(2): p. 271-279.
356. Vermes, I., et al., *A novel assay for apoptosis Flow cytometric detection of phosphatidylserine expression on early apoptotic cells using fluorescein labelled Annexin V.* Journal of Immunological Methods, 1995. **184**(1): p. 39-51.
357. Villas, B.H., *Flow cytometry: an overview.* Cell vision : the journal of analytical morphology, 1998. **5**(1): p. 56-61.
358. Covarrubias, L., et al., *Function of reactive oxygen species during animal development: passive or active?* Dev Biol, 2008. **320**(1): p. 1-11.
359. Zhang, J., et al., *ROS and ROS-Mediated Cellular Signaling.* Oxidative Medicine and Cellular Longevity, 2016. **2016**: p. 4350965.
360. Prieto-Bermejo, R., et al., *Reactive oxygen species in haematopoiesis: leukaemic cells take a walk on the wild side.* Journal of Experimental & Clinical Cancer Research, 2018. **37**(1): p. 125.
361. Liou, G.-Y. and P. Storz, *Reactive oxygen species in cancer.* Free radical research, 2010. **44**(5): p. 479-496.

362. Rong, L., et al., *Hydrogen peroxide detection with high specificity in living cells and inflamed tissues.* Regenerative biomaterials, 2016. **3**(4): p. 217-222.
363. Alfadda, A.A. and R.M. Sallam, *Reactive oxygen species in health and disease.* J Biomed Biotechnol, 2012. **2012**: p. 936486.
364. Clish, C.B., *Metabolomics: an emerging but powerful tool for precision medicine.* Cold Spring Harbor molecular case studies, 2015. **1**(1): p. a000588-a000588.
365. Wikoff, W.R., et al., *Metabolomics analysis reveals large effects of gut microflora on mammalian blood metabolites.* Proceedings of the National Academy of Sciences, 2009. **106**(10): p. 3698.
366. Johnson, C.H., et al., *Xenobiotic metabolomics: major impact on the metabolome.* Annu Rev Pharmacol Toxicol, 2012. **52**: p. 37-56.
367. Johnson, C.H. and F.J. Gonzalez, *Challenges and opportunities of metabolomics.* Journal of cellular physiology, 2012. **227**(8): p. 2975-2981.
368. Cuperlovic-Culf, M., et al., *Cell culture metabolomics: applications and future directions.* Drug Discov Today, 2010. **15**(15-16): p. 610-21.
369. León, Z., et al., *Mammalian cell metabolomics: Experimental design and sample preparation.* ELECTROPHORESIS, 2013. **34**(19): p. 2762-2775.
370. Tan, S.Z., et al., *Introduction to metabolomics and its applications in ophthalmology.* Eye, 2016. **30**(6): p. 773-783.
371. Sumner, L.W., et al., *Proposed minimum reporting standards for chemical analysis.* Metabolomics, 2007. **3**(3): p. 211-221.
372. Sumner, L.W., et al., *Proposed quantitative and alphanumeric metabolite identification metrics.* Metabolomics, 2014. **10**(6): p. 1047-1049.
373. Habashy, H.O., et al., *Transferrin receptor (CD71) is a marker of poor prognosis in breast cancer and can predict response to tamoxifen.* Breast Cancer Res Treat, 2010. **119**(2): p. 283-93.
374. Shen, Y., et al., *Transferrin receptor 1 in cancer: a new sight for cancer therapy.* Am J Cancer Res, 2018. **8**(6): p. 916-931.
375. Kilic, M.A., E. Ozlu, and S. Calis, *A novel protein-based anticancer drug encapsulating nanosphere: apoferritin-doxorubicin complex.* J Biomed Nanotechnol, 2012. **8**(3): p. 508-14.
376. Zhang, L., et al., *H-Chain Ferritin: A Natural Nuclei Targeting and Bioactive Delivery Nanovector.* Advanced Healthcare Materials, 2015. **4**(9): p. 1305-1310.
377. Lei, Y., et al., *Targeted tumor delivery and controlled release of neuronal drugs with ferritin nanoparticles to regulate pancreatic cancer progression.* J Control Release, 2016. **232**: p. 131-42.
378. Azzi, S., J.K. Hebda, and J. Gavard, *Vascular permeability and drug delivery in cancers.* Front Oncol, 2013. **3**: p. 211.
379. Xing, R., et al., *Characterization and cellular uptake of platinum anticancer drugs encapsulated in apoferritin.* Journal of Inorganic Biochemistry, 2009. **103**(7): p. 1039-1044.
380. Kim, M., et al., *pH-Dependent Structures of Ferritin and Apoferritin in Solution: Disassembly and Reassembly.* Biomacromolecules, 2011. **12**(5): p. 1629-1640.
381. Couvreur, P., et al., *Nanotechnologies for drug delivery: Application to cancer and autoimmune diseases.* Progress in Solid State Chemistry, 2006. **34**(2): p. 231-235.
382. Volkmer, D., *CRYSTALLIZATION | Biomineralization*, in *Encyclopedia of Separation Science*, I.D. Wilson, Editor. 2000, Academic Press: Oxford. p. 940-950.

383. Bryce, C.F. and R.R. Crichton, *The catalytic activity of horse spleen apoferritin. Preliminary kinetic studies and the effect of chemical modification.* The Biochemical journal, 1973. **133**(2): p. 301-309.
384. Dráb, T., et al., *Native Red Electrophoresis–A new method suitable for separation of native proteins.* Electrophoresis, 2011. **32**(24): p. 3597-3599.
385. Arosio, P., T.G. Adelman, and J.W. Drysdale, *On ferritin heterogeneity. Further evidence for heteropolymers.* J Biol Chem, 1978. **253**(12): p. 4451-8.
386. Hotze, E.M., T. Phenrat, and G.V. Lowry, *Nanoparticle aggregation: challenges to understanding transport and reactivity in the environment.* J Environ Qual, 2010. **39**(6): p. 1909-24.
387. Watt, G.D., D. Jacobs, and R.B. Frankel, *Redox reactivity of bacterial and mammalian ferritin: is reductant entry into the ferritin interior a necessary step for iron release?* Proceedings of the National Academy of Sciences of the United States of America, 1988. **85**(20): p. 7457-7461.
388. Gomhor J. Alqaraghuli, H., et al., *Development and characterization of folic acid-functionalized apoferritin as a delivery vehicle for epirubicin against MCF-7 breast cancer cells.* Artificial Cells, Nanomedicine, and Biotechnology, 2018. **46**(sup3): p. S847-S854.
389. Zhou, J., et al., *A "submunition" dual-drug system based on smart hollow NaYF4/apoferritin nanocage for upconversion imaging.* RSC Advances, 2016. **6**(40): p. 33443-33454.
390. Yang, Z., et al., *Encapsulation of platinum anticancer drugs by apoferritin.* Chemical Communications, 2007(33): p. 3453-3455.
391. Webb, B., et al., *Molecular Entrapment of Small Molecules within the Interior of Horse Spleen Ferritin.* Archives of Biochemistry and Biophysics, 1994. **309**(1): p. 178-183.
392. Domı, x, and J.M. nguez-Vera, *Iron(III) complexation of Desferrioxamine B encapsulated in apoferritin.* Journal of Inorganic Biochemistry, 2004. **98**(3): p. 469-472.
393. Stefanini, S., P. Vecchini, and E. Chiancone, *On the mechanism of horse spleen apoferritin assembly: a sedimentation velocity and circular dichroism study.* Biochemistry, 1987. **26**(7): p. 1831-1837.
394. Hofmeister, F., *Zur lehre von der wirkung der salze.* Archiv für experimentelle Pathologie und Pharmakologie, 1888. **24**(4-5): p. 247-260.
395. Stefanini, S., et al., *Thermal Stability of Horse Spleen Apoferritin and Human Recombinant H Apoferritin.* Archives of Biochemistry and Biophysics, 1996. **325**(1): p. 58-64.
396. Toyoda, K., et al., *H2O2 production by copper amine oxidase, a component of the ecto-apyrase (ATPase)-containing protein complex(es) in the pea cell wall, is regulated by an elicitor and a suppressor from Mycosphaerella pinodes.* Journal of General Plant Pathology, 2012. **78**(5): p. 311-315.
397. Eiler, S., et al., *Overexpression, purification, and crystal structure of native ER alpha LBD.* Protein Expr Purif, 2001. **22**(2): p. 165-73.
398. Jungwirth, P. and P.S. Cremer, *Beyond Hofmeister.* Nature Chemistry, 2014. **6**(4): p. 261-263.
399. R.R., C., *Ferritin*, in *Structure and Bonding*. 1973, Springer, Berlin, Heidelberg.
400. Zbacnik, T.J., et al., *Role of Buffers in Protein Formulations.* Journal of Pharmaceutical Sciences, 2017. **106**(3): p. 713-733.
401. Harrison, P.M. and D. Gregory, *Reassembly of apoferritin molecules from subunits.* Nature, 1968. **220**(5167): p. 578-580.

402. Wessely, Z., et al., *Identification of Mallory bodies with rhodamine B fluorescence and other stains for keratin.* Stain technology, 1981. **56**(3): p. 169-176.
403. Truant, J., W. Brett, and W. Thomas Jr, *Fluorescence microscopy of tubercle bacilli stained with auramine and rhodamine.* Henry Ford Hospital Medical Journal, 1962. **10**(2): p. 287-296.
404. Iijima, M. and H. Kamiya, *Surface modification for improving the stability of nanoparticles in liquid media.* KONA Powder and Particle Journal, 2009. **27**: p. 119-129.
405. Uchida, M., et al., *Targeting of cancer cells with ferrimagnetic ferritin cage nanoparticles.* Journal of the American Chemical Society, 2006. **128**(51): p. 16626-16633.
406. Liu, F., et al., *Binding properties of apoferritin to nicotinamide and calcium.* European Food Research and Technology, 2012. **235**(5): p. 893-899.
407. Uchida, M., et al., *The ferritin superfamily: Supramolecular templates for materials synthesis.* Biochimica et biophysica acta, 2010. **1800**(8): p. 834-845.
408. Worwood, M., et al., *The clearance of 131I-human plasma ferritin in man.* Blood, 1982. **60**(4): p. 827-33.
409. Johnson, E., et al., *Crystal Structures of a Tetrahedral Open Pore Ferritin from the Hyperthermophilic Archaeon Archaeoglobus fulgidus.* Structure, 2005. **13**(4): p. 637-648.
410. Lobert, S., B. Vulevic, and J.J. Correia, *Interaction of vinca alkaloids with tubulin: a comparison of vinblastine, vincristine, and vinorelbine.* Biochemistry, 1996. **35**(21): p. 6806-14.
411. Zhang, Z., et al., *Dose–response relationship in locoregional control for patients with stage II-III esophageal cancer treated with concurrent chemotherapy and radiotherapy.* International Journal of Radiation Oncology* Biology* Physics, 2005. **61**(3): p. 656-664.
412. Vassilomanolakis, M., et al., *First-line chemotherapy with docetaxel and cisplatin in metastatic breast cancer.* Breast, 2005. **14**(2): p. 136-41.
413. Perez, E.A., *Impact, mechanisms, and novel chemotherapy strategies for overcoming resistance to anthracyclines and taxanes in metastatic breast cancer.* Breast Cancer Res Treat, 2009. **114**(2): p. 195-201.
414. Longley, D.B. and P.G. Johnston, *Molecular mechanisms of drug resistance.* J Pathol, 2005. **205**(2): p. 275-92.
415. Lin, Z., et al., *Novel thermo-sensitive hydrogel system with paclitaxel nanocrystals: High drug-loading, sustained drug release and extended local retention guaranteeing better efficacy and lower toxicity.* Journal of Controlled Release, 2014. **174**: p. 161-170.
416. Mao, Y., et al., *Thermosensitive hydrogel system with paclitaxel liposomes used in localized drug delivery system for in situ treatment of tumor: better antitumor efficacy and lower toxicity.* Journal of pharmaceutical sciences, 2016. **105**(1): p. 194-204.
417. Lu, J., et al., *Mesoporous Silica Nanoparticles as a Delivery System for Hydrophobic Anticancer Drugs.* Small, 2007. **3**(8): p. 1341-1346.
418. Mishra, J., et al., *Evaluation of toxicity & therapeutic efficacy of a new liposomal formulation of amphotericin B in a mouse model.* The Indian journal of medical research, 2013. **137**(4): p. 767.
419. Radwan, M.A., et al., *Oral administration of amphotericin B nanoparticles: antifungal activity, bioavailability and toxicity in rats.* Drug delivery, 2017. **24**(1): p. 40-50.
420. Hu, K., et al., *Improved antitumor efficacy and reduced toxicity of liposomes containing bufadienolides.* Archives of Pharmacal Research, 2011. **34**(9): p. 1487.

421. Wang, Y., et al., *In vitro and in vivo anticancer activity of a novel puerarin nanosuspension against colon cancer, with high efficacy and low toxicity.* International journal of pharmaceutics, 2013. **441**(1-2): p. 728-735.
422. Yao, L., et al., *In vitro and in vivo evaluation of camptothecin nanosuspension: a novel formulation with high antitumor efficacy and low toxicity.* International journal of pharmaceutics, 2012. **423**(2): p. 586-588.
423. Ernsting, M.J., et al., *Preclinical pharmacokinetic, biodistribution, and anti-cancer efficacy studies of a docetaxel-carboxymethylcellulose nanoparticle in mouse models.* Biomaterials, 2012. **33**(5): p. 1445-1454.
424. Ryser, H., J. Caulfield, and J. Aub, *Studies on protein uptake by isolated tumor cells: I. Electron microscopic evidence of ferritin uptake by ehrlich ascites tumor cells.* The Journal of cell biology, 1962. **14**(2): p. 255-268.
425. Li, J.Y., et al., *Scara5 is a ferritin receptor mediating non-transferrin iron delivery.* Developmental cell, 2009. **16**(1): p. 35-46.
426. Calzolari, A., et al., *TfR2 localizes in lipid raft domains and is released in exosomes to activate signal transduction along the MAPK pathway.* Journal of Cell Science, 2006. **119**(21): p. 4486-4498.
427. Rychtarcikova, Z., et al., *Tumor-initiating cells of breast and prostate origin show alterations in the expression of genes related to iron metabolism.* Oncotarget, 2017. **8**(4): p. 6376-6398.
428. Lazaros, G., K. Antonatou, and D. Vassilopoulos, *The Therapeutic Role of Interleukin-1 Inhibition in Idiopathic Recurrent Pericarditis: Current Evidence and Future Challenges.* Front Med (Lausanne), 2017. **4**: p. 78.
429. Anderson, S.A., et al., *The IRP1-HIF-2α axis coordinates iron and oxygen sensing with erythropoiesis and iron absorption.* Cell Metab, 2013. **17**(2): p. 282-90.
430. Jiang, X.P., R.L. Elliott, and J.F. Head, *Manipulation of iron transporter genes results in the suppression of human and mouse mammary adenocarcinomas.* Anticancer Res, 2010. **30**(3): p. 759-65.
431. El Guerrab, A., et al., *Anti-EGFR monoclonal antibodies and EGFR tyrosine kinase inhibitors as combination therapy for triple-negative breast cancer.* Oncotarget, 2016. **7**(45): p. 73618-73637.
432. Wang, B., et al., *EGFR regulates iron homeostasis to promote cancer growth through redistribution of transferrin receptor 1.* Cancer Lett, 2016. **381**(2): p. 331-40.
433. Laughner, E., et al., *HER2 (neu) Signaling Increases the Rate of Hypoxia-Inducible Factor 1α (HIF-1α) Synthesis: Novel Mechanism for HIF-1-Mediated Vascular Endothelial Growth Factor Expression.* Molecular and Cellular Biology, 2001. **21**(12): p. 3995-4004.
434. Udensi, U.K., et al., *Proteomics-Based Identification of Differentially Abundant Proteins from Human Keratinocytes Exposed to Arsenic Trioxide.* Journal of proteomics & bioinformatics, 2014. **7**(7): p. 166-178.
435. Wrba, F., et al., *Transferrin receptor (TrfR) expression in breast carcinoma and its possible relationship to prognosis. An immunohistochemical study.* Virchows Arch A Pathol Anat Histopathol, 1986. **410**(1): p. 69-73.
436. Soule, H.D., et al., *Isolation and characterization of a spontaneously immortalized human breast epithelial cell line, MCF-10.* Cancer Res, 1990. **50**(18): p. 6075-86.
437. Campiglio, M., et al., *Inhibition of proliferation and induction of apoptosis in breast cancer cells by the epidermal growth factor receptor*

(EGFR) tyrosine kinase inhibitor ZD1839 ('Iressa') is independent of EGFR expression level. J Cell Physiol, 2004. **198**(2): p. 259-68.
438. Mosmann, T., *Rapid colorimetric assay for cellular growth and survival: application to proliferation and cytotoxicity assays.* J Immunol Methods, 1983. **65**(1-2): p. 55-63.
439. Qazzaz, M.E., *Anticancer properties and biological evaluation of natural alkaloid jerantinine B*, in *School of Pharmacy*. 2017, University of Nottingham.

: Nottingham.
440. Bézivin, C., et al., *Cytotoxic activity of compounds from the lichen: Cladonia convoluta.* Planta medica, 2004. **70**(9): p. 874-877.
441. Berridge, M.V., P.M. Herst, and A.S. Tan, *Tetrazolium dyes as tools in cell biology: new insights into their cellular reduction.* Biotechnology annual review, 2005. **11**: p. 127-152.
442. Berridge, M.V. and A.S. Tan, *Characterization of the cellular reduction of 3-(4, 5-dimethylthiazol-2-yl)-2, 5-diphenyltetrazolium bromide (MTT): subcellular localization, substrate dependence, and involvement of mitochondrial electron transport in MTT reduction.* Archives of biochemistry and biophysics, 1993. **303**(2): p. 474-482.
443. Piccolo, M., et al., *Exploring cellular uptake, accumulation and mechanism of action of a cationic Ru-based nanosystem in human preclinical models of breast cancer.* Scientific Reports, 2019. **9**(1): p. 7006.
444. Szumilak, M., A. Wiktorowska-Owczarek, and A. Stanczak, *Hybrid Drugs—A Strategy for Overcoming Anticancer Drug Resistance?* Molecules, 2021. **26**(9): p. 2601.
445. Musso, L., S. Dallavalle, and F. Zunino, *Perspectives in the development of hybrid bifunctional antitumour agents.* Biochemical pharmacology, 2015. **96**(4): p. 297-305.
446. Riccardi, C. and I. Nicoletti, *Analysis of apoptosis by propidium iodide staining and flow cytometry.* Nature Protocols, 2006. **1**(3): p. 1458-1461.
447. Pfeffer, C.M. and A.T.K. Singh, *Apoptosis: A Target for Anticancer Therapy.* International Journal of Molecular Sciences, 2018. **19**(2): p. 448.
448. Pozarowski, P. and Z. Darzynkiewicz, *Analysis of cell cycle by flow cytometry.* Methods Mol Biol, 2004. **281**: p. 301-11.
449. Oliver, F.J., et al., *Importance of poly (ADP-ribose) polymerase and its cleavage in apoptosis: lesson from an uncleavable mutant.* Journal of Biological Chemistry, 1998. **273**(50): p. 33533-33539.
450. Pines, A., et al., *Touching base with PARPs: moonlighting in the repair of UV lesions and double-strand breaks.* Trends Biochem Sci, 2013. **38**(6): p. 321-30.
451. Smith, L., et al., *The responses of cancer cells to PLK1 inhibitors reveal a novel protective role for p53 in maintaining centrosome separation.* Scientific reports, 2017. **7**(1): p. 16115-16115.
452. Liu, Z., Q. Sun, and X. Wang, *PLK1, A Potential Target for Cancer Therapy.* Translational oncology, 2017. **10**(1): p. 22-32.
453. Ikezoe, T., et al., *A novel treatment strategy targeting polo-like kinase 1 in hematological malignancies.* Leukemia, 2009. **23**(9): p. 1564-1576.
454. Degenhardt, Y. and T. Lampkin, *Targeting Polo-like Kinase in Cancer Therapy.* Clinical Cancer Research, 2010. **16**(2): p. 384.
455. Llamazares, S., et al., *polo encodes a protein kinase homolog required for mitosis in Drosophila.* Genes Dev, 1991. **5**(12a): p. 2153-65.

456. Sanhaji, M., et al., *Polo-like kinase 1 inhibitors, mitotic stress and the tumor suppressor p53.* Cell cycle (Georgetown, Tex.), 2013. **12**(9): p. 1340-1351.
457. Liu, X. and R.L. Erikson, *Polo-like kinase (Plk)1 depletion induces apoptosis in cancer cells.* Proceedings of the National Academy of Sciences, 2003. **100**(10): p. 5789.
458. Jelínek, M., et al., *The role of individual caspases in cell death induction by taxanes in breast cancer cells.* Cancer cell international, 2015. **15**(1): p. 8-8.
459. Lazebnik, Y.A., et al., *Cleavage of poly(ADP-ribose) polymerase by a proteinase with properties like ICE.* Nature, 1994. **371**(6495): p. 346-347.
460. Ghaleb, A., M. Padellan, and N. Marchenko, *Mutant p53 drives the loss of heterozygosity by the upregulation of Nek2 in breast cancer cells.* Breast Cancer Research, 2020. **22**(1): p. 133.
461. Hui, L., et al., *Mutant p53 in MDA-MB-231 breast cancer cells is stabilized by elevated phospholipase D activity and contributes to survival signals generated by phospholipase D.* Oncogene, 2006. **25**(55): p. 7305-7310.
462. Mantovani, F., L. Collavin, and G. Del Sal, *Mutant p53 as a guardian of the cancer cell.* Cell Death & Differentiation, 2019. **26**(2): p. 199-212.
463. Yang, S., Q. Zhou, and X. Yang, *Caspase-3 status is a determinant of the differential responses to genistein between MDA-MB-231 and MCF-7 breast cancer cells.* Biochimica et Biophysica Acta (BBA) - Molecular Cell Research, 2007. **1773**(6): p. 903-911.
464. Huovinen, M., et al., *Characterization of human breast cancer cell lines for the studies on p53 in chemical carcinogenesis.* Toxicology in Vitro, 2011. **25**(5): p. 1007-1017.
465. Pu, X., et al., *Caspase-3 and caspase-8 expression in breast cancer: caspase-3 is associated with survival.* Apoptosis : an international journal on programmed cell death, 2017. **22**(3): p. 357-368.
466. Vijay, R., *Biological Characterisation of a Novel and Naturally Isolated Indole Alkaloid*, in *School of Pharmacy*. 2015, University of Nottingham.
467. Kroemer, G. and S.J. Martin, *Caspase-independent cell death.* Nature Medicine, 2005. **11**(7): p. 725-730.
468. Ray, D., K.R. Murphy, and S. Gal, *The DNA binding and accumulation of p53 from breast cancer cell lines and the link with serine 15 phosphorylation.* Cancer biology & therapy, 2012. **13**(10): p. 848-857.
469. Lozano, G., *Restoring p53 in cancer: the promises and the challenges.* Journal of Molecular Cell Biology, 2019. **11**(7): p. 615-619.
470. Sur, S., et al., *A panel of isogenic human cancer cells suggests a therapeutic approach for cancers with inactivated p53.* Proc Natl Acad Sci U S A, 2009. **106**(10): p. 3964-9.
471. McKenzie, L., et al., *p53-dependent repression of polo-like kinase-1 (PLK1).* Cell Cycle, 2010. **9**(20): p. 4200-12.
472. Ray, P.D., B.-W. Huang, and Y. Tsuji, *Reactive oxygen species (ROS) homeostasis and redox regulation in cellular signaling.* Cellular signalling, 2012. **24**(5): p. 981-990.
473. Yang, H., et al., *The role of cellular reactive oxygen species in cancer chemotherapy.* Journal of Experimental & Clinical Cancer Research, 2018. **37**(1): p. 266.
474. Bogdan, A.R., et al., *Regulators of iron homeostasis: new players in metabolism, cell death, and disease.* Trends in biochemical sciences, 2016. **41**(3): p. 274-286.
475. Dixon, S.J., et al., *Ferroptosis: an iron-dependent form of nonapoptotic cell death.* Cell, 2012. **149**(5): p. 1060-1072.

476. Ravindran, J., et al., *Modulation of ROS/MAPK signaling pathways by okadaic acid leads to cell death via, mitochondrial mediated caspase-dependent mechanism.* Apoptosis, 2011. **16**(2): p. 145-161.
477. Shen, C., et al., *Aldehyde dehydrogenase 2 deficiency negates chronic low-to-moderate alcohol consumption-induced cardioprotecion possibly via ROS-dependent apoptosis and RIP1/RIP3/MLKL-mediated necroptosis.* Biochimica et Biophysica Acta (BBA) - Molecular Basis of Disease, 2017. **1863**(8): p. 1912-1918.
478. Xie, Y., et al., *Ferroptosis: process and function.* Cell Death Differ, 2016. **23**(3): p. 369-79.
479. Jia, P., et al., *The role of reactive oxygen species in tumor treatment.* RSC Advances, 2020. **10**(13): p. 7740-7750.
480. Circu, M.L. and T.Y. Aw, *Glutathione and modulation of cell apoptosis.* Biochimica et Biophysica Acta (BBA)-Molecular Cell Research, 2012. **1823**(10): p. 1767-1777.
481. Pallepati, P. and D.A. Averill-Bates, *Mild thermotolerance induced at 40 C protects HeLa cells against activation of death receptor-mediated apoptosis by hydrogen peroxide.* Free Radical Biology and Medicine, 2011. **50**(6): p. 667-679.
482. Lopez, J. and S.W. Tait, *Mitochondrial apoptosis: killing cancer using the enemy within.* Br J Cancer, 2015. **112**(6): p. 957-62.
483. Wu, C., et al., *Induction of ferroptosis and mitochondrial dysfunction by oxidative stress in PC12 cells.* Scientific reports, 2018. **8**(1): p. 574-574.
484. Chen, M.S., et al., *CHAC1 degradation of glutathione enhances cystine-starvation-induced necroptosis and ferroptosis in human triple negative breast cancer cells via the GCN2-eIF2α-ATF4 pathway.* Oncotarget, 2017. **8**(70): p. 114588-114602.
485. Liu, D.S., et al., *Inhibiting the system xC−/glutathione axis selectively targets cancers with mutant-p53 accumulation.* Nature Communications, 2017. **8**(1): p. 14844.
486. Lim, J.K.M., et al., *Cystine/glutamate antiporter xCT (SLC7A11) facilitates oncogenic RAS transformation by preserving intracellular redox balance.* Proceedings of the National Academy of Sciences, 2019. **116**(19): p. 9433.
487. Parrales, A. and T. Iwakuma, *Targeting Oncogenic Mutant p53 for Cancer Therapy.* Frontiers in Oncology, 2015. **5**: p. 288.
488. Veroniaina, H., et al., *Apoferritin: a potential nanocarrier for cancer imaging and drug delivery.* Expert Rev Anticancer Ther, 2021. **21**(8): p. 901-913.
489. Mukhtar, E., V.M. Adhami, and H. Mukhtar, *Targeting microtubules by natural agents for cancer therapy.* Molecular cancer therapeutics, 2014. **13**(2): p. 275-284.
490. Hayashi, M.T. and J. Karlseder, *DNA damage associated with mitosis and cytokinesis failure.* Oncogene, 2013. **32**(39): p. 4593-4601.
491. Jänicke, R.U., et al., *Caspase-3 is required for DNA fragmentation and morphological changes associated with apoptosis.* J Biol Chem, 1998. **273**(16): p. 9357-60.
492. Santos, L.C., et al., *Mitochondrial origins of fractional control in regulated cell death.* Nature Communications, 2019. **10**(1): p. 1313.
493. Bellini, M., et al., *Protein nanocages for self-triggered nuclear delivery of DNA-targeted chemotherapeutics in Cancer Cells.* Journal of Controlled Release, 2014. **196**: p. 184-196.
494. Breen, A.F., et al., *Development of novel apoferritin formulations for antitumour benzothiazoles.* Cancer Reports, 2019. **2**(4): p. e1155.
495. Lv, M., et al., *Metabolomics techniques for nanotoxicity investigations.* Bioanalysis, 2015. **7**(12): p. 1527-1544.

496. Silva, R., et al., *Colchicine effect on P-glycoprotein expression and activity: in silico and in vitro studies.* Chem Biol Interact, 2014. **218**: p. 50-62.
497. Eriksson, L., et al., *Multi- and Megavariate Data Analysis: Basic Principles and Applications*. Second ed. Vol. Part I. 2006, Umea: Umetrics AB.
498. Eriksson, L., et al., *Multi-and megavariate data analysis basic principles and applications*. Vol. 1. 2013: Umetrics Academy.

8 Appendices

8.1 Appendix I

This appendix provides the full gel images for AFt encapsulation of JAa presented in Chapter 3.

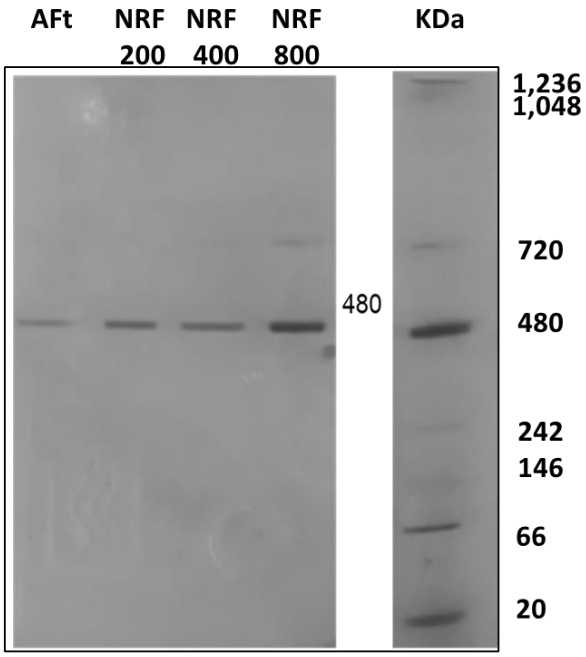


Figure 8.1: Characterisation of the integrity of AFt alone and AFt-JAa in different ratios (1:200; 1:400; 1:800) through nano-reactor route using (4-16%) native PAGE. Presented in **Figure 3.3**.

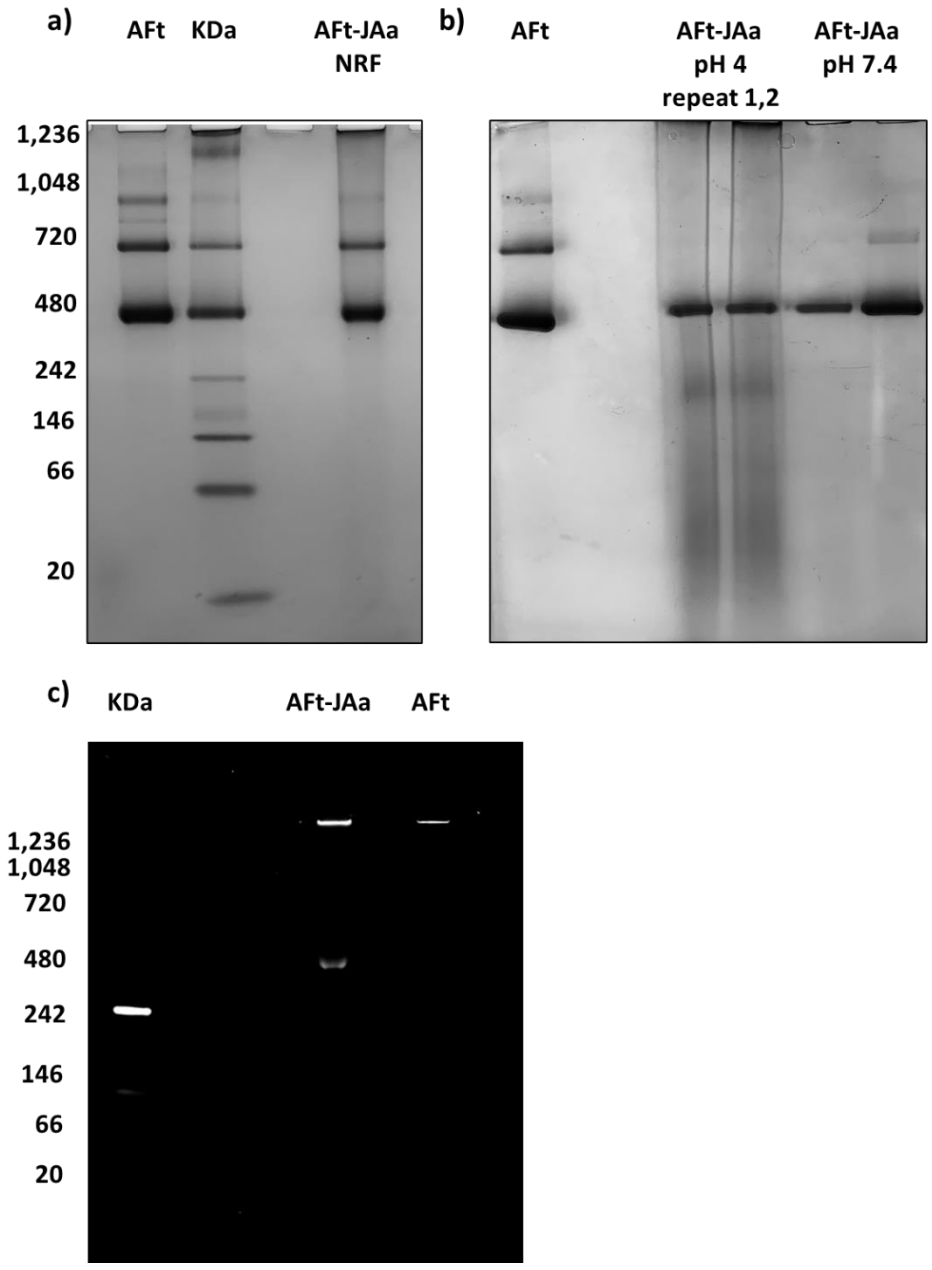


Figure 8.2: Blue (4-16%) polyacrylamide native gel electrophoresis of AFt-encapsulated-JAa (AFt-JAa) through the nano-reactor route (**a**) and reassembly route (**b**) presented in **Figures 3.5a** and **3.12b**.

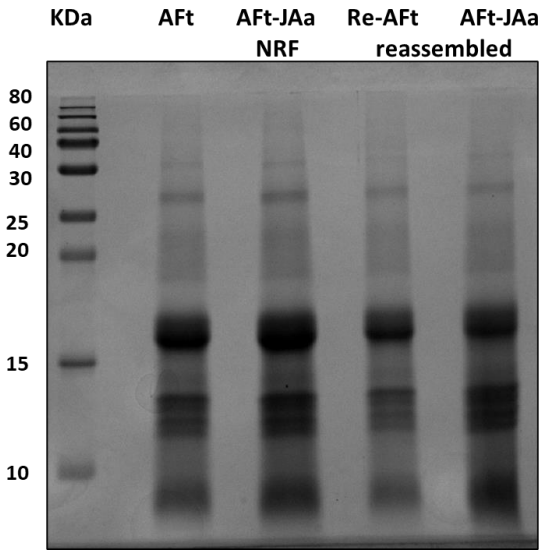


Figure 8.3: Sodium dodecyl sulfate-polyacrylamide gel electrophoresis (SDS-PAGE) of AFt-encapsulated-JAa (AFt-JAa) through the nano-reactor route and reassembly route presented in **Figures 3.5b**, **3.12c.**

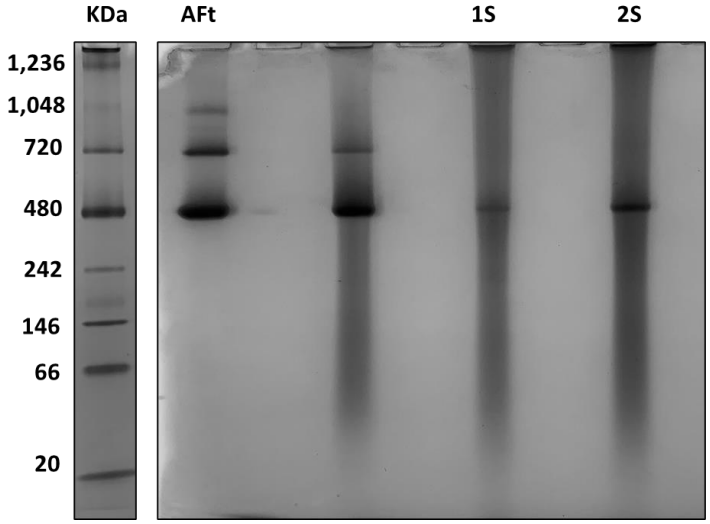


Figure 8.4: Blue (4-16%) polyacrylamide native gel electrophoresis of the AFt cage reassembly in one step (1S) from pH 2 to pH 7.4 vs raising the pH in two steps (2S) from pH 2 to pH 4 and then from pH 4 to pH 7.4 presented in **Figure 3.9**.

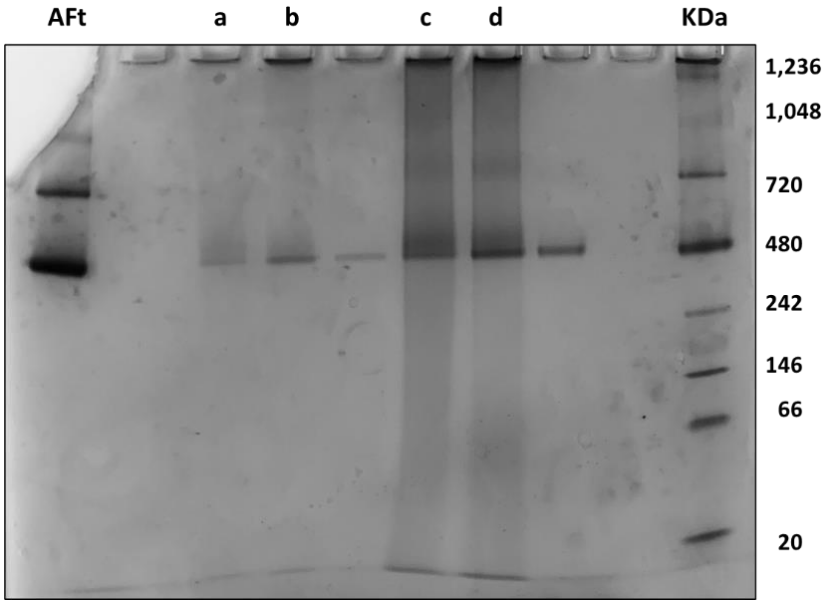


Figure 8.5: Blue (4-16%) polyacrylamide native gel electrophoresis of AFt cage reassembly through the study of the effect of initial AFt protein concentration on the outcomes of the reassembly method. (**a**) Native gel PAGE (pH 4) of ReM-1, (**b**) Native gel PAGE (pH 4) of ReM-2, (**c**) Native gel PAGE (pH 7.4) of ReM-1 and (**d**) Native gel PAGE (pH 7.4) of ReM-4 presented **Table 3.3**.

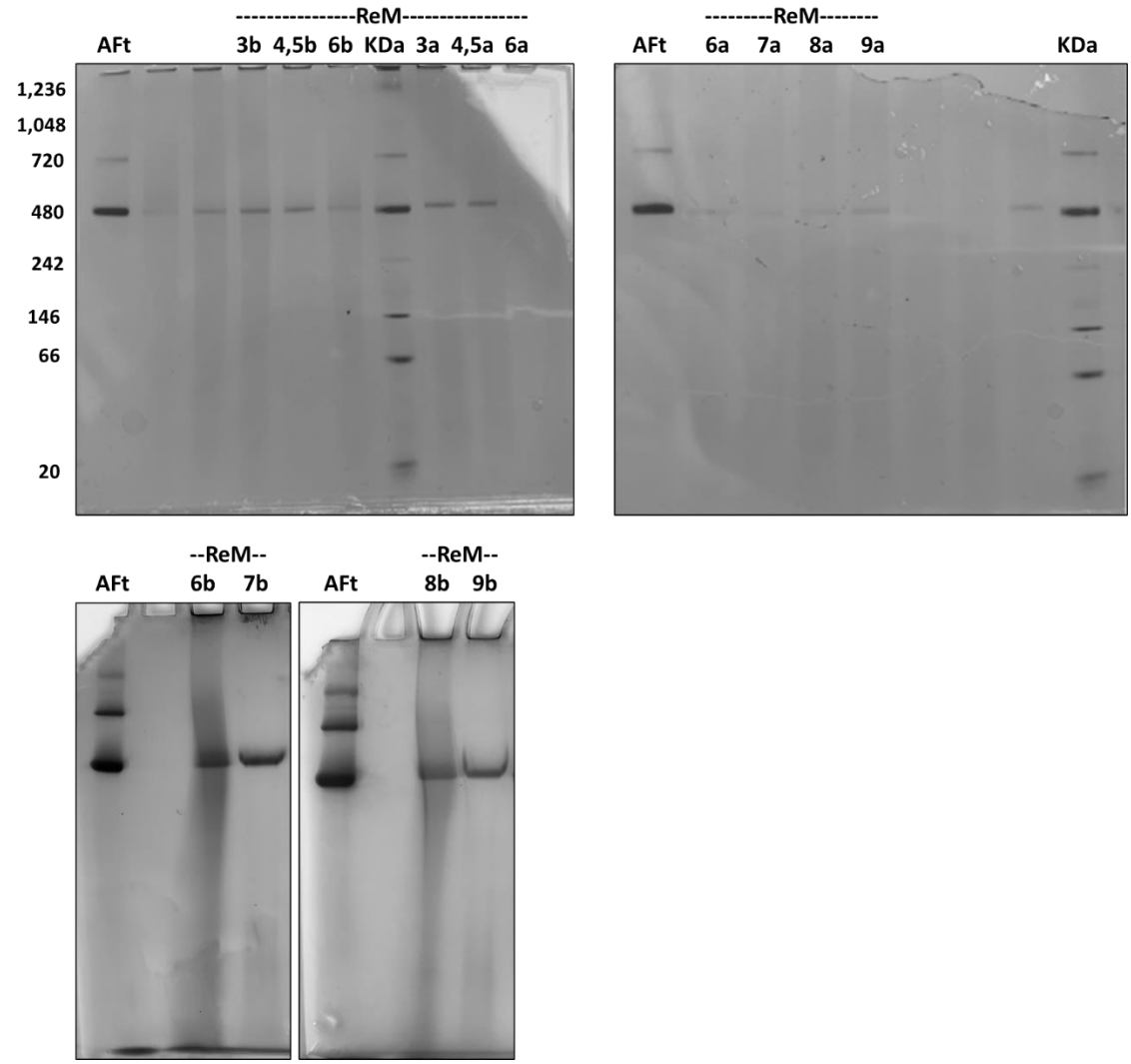


Figure 8.6: Blue (4-16%) polyacrylamide native gel electrophoresis of AFt cage reassembly optimisation study of the reassembly methods (ReM) 3-9; (**a**) reassembly at pH 4 and (**b**) reassembly at pH 7.4 presented in **Table 3.4**. and **Table 3.5**.

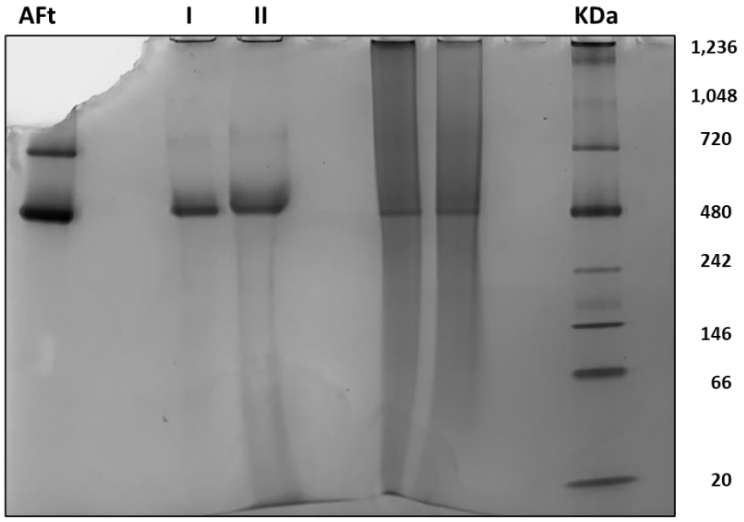


Figure 8.7: Blue (4-16%) polyacrylamide native gel electrophoresis of AFt cage reassembly optimisation of method ReM-5 evaluating the time and speed needed to purify the formulation. Reassembled AFt spin filtered for 10 min at 2000 rpm (I) or 15 min at 3000 rpm (II) presented in **Figure 3.10.**

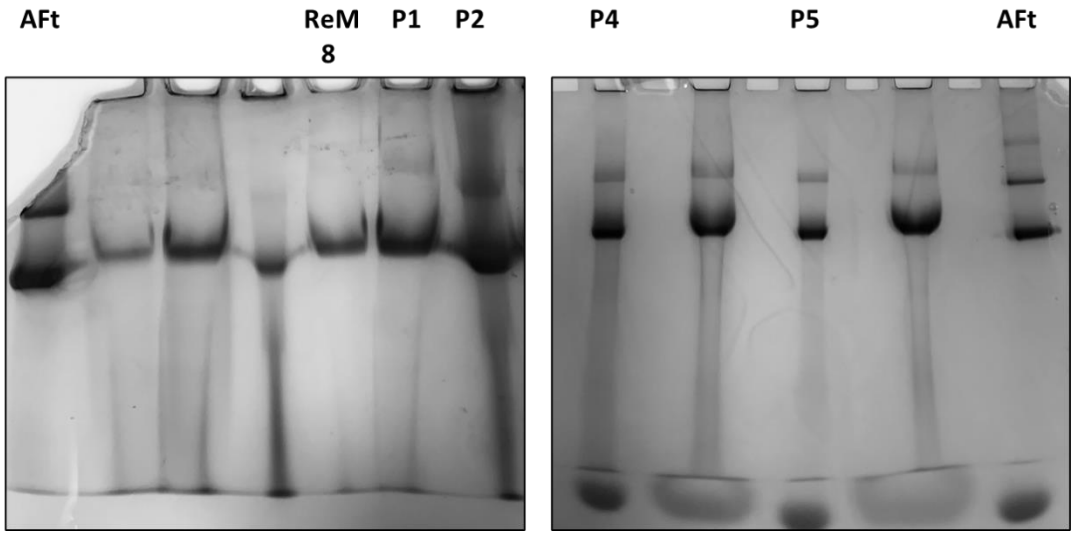


Figure 8.8: Blue (4-16%) polyacrylamide native gel electrophoresis of AFt cage purification methods of the reassembled AFt using 4 different methods. ReM-8 AFt was spin filtered for 15 min (P1), dialysed against 25 mM Trizma-acetate buffer then spin filtered for 15 min at 3000 rpm (P2), spin filtered for 15 min at 3000 rpm then dialysed against (100 mM) glycine NaOH buffer at pH=8.6 (P3) or spin filtered for 15 min then dialysed against 25 mM Trizma-acetate buffer at pH=7.4 (P4) presented in **Figure 3.11**.

8.2 Appendix II

This appendix provides the full gel images for TFR1 expression evaluated by western blot and presented in Chapter 4.

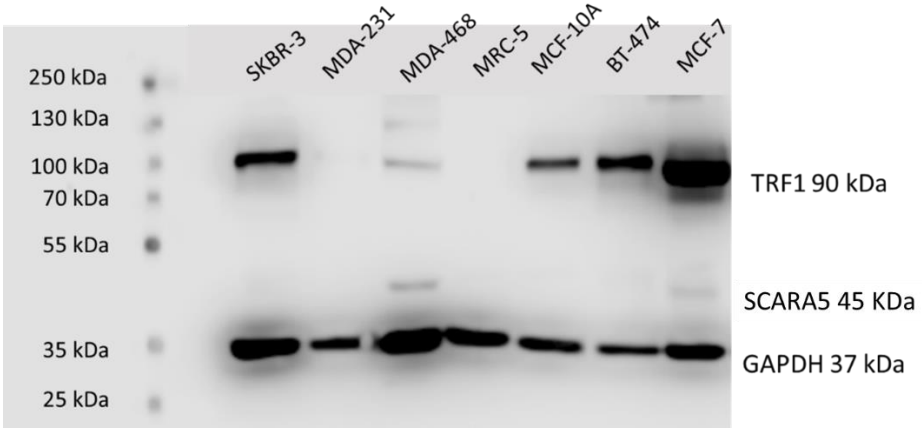


Figure 8.9: Expression of TFR1 and SCARA-5 in cell lines using immunoblotting technique of cell lysates containing 40 µg protein presented in **Figure 4.1a**. Densitometry analysis of TFR1 and SCARA-5 proteins normalised to the housekeeping gene (GAPDH).

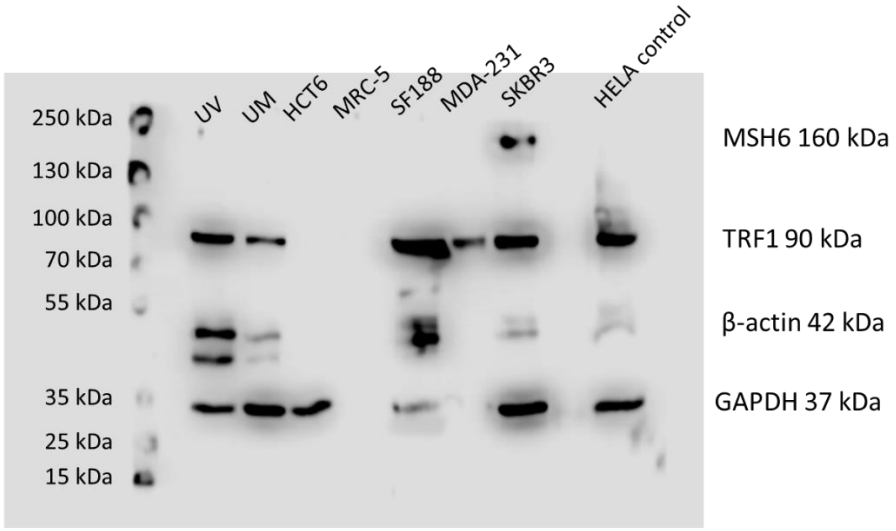


Figure 8.10: Expression of TFR1 in panel of cell lines including MDA-MB-231 using immunoblotting technique of cell lysates containing 50 µg protein presented in **Figure 4.1c**. Densitometry analysis of TFR1 protein normalised to the housekeeping gene (GAPDH).